

**Integration of microseismic and time-lapse seismic data with application to a heavy oil
reservoir**

by

Amna Feroz

A thesis submitted in partial fulfillment of the requirements for the degree of

Doctor of Philosophy

in

Geophysics

Department of Physics
University of Alberta

© Amna Feroz, 2021

Abstract

Thermal heavy oil extraction techniques are high temperature and pressure procedures to produce heavy oil. Elevated temperature and pressures alter the subsurface stresses, causing shear failure of rock within and surrounding the steam front. The steam also introduces volumetric changes at the reservoir level, and its impact may also propagate to the surface resulting in surface heaves. Furthermore, extraction of fluid/bitumen from the reservoir reduces the pore pressure and alters the petrophysical properties, ultimately causing reservoir compaction and surface subsidence.

The heavy oil fields in northern Alberta are under commercial production since 1986, several recovery methods have been applied to extract the bitumen cost-effectively. Grids of vertical injector/producer, horizontal injector/producers, CSS and SAGD have all been utilized. However, a horizontal well CSS strategy is being used in the most recently drilled pads. Despite applying several recovery operations and obtaining commercial-scale bitumen over the past 20 years, it is still unclear what exactly happens in the reservoir when steam is injected. It is also not certain how the steam moves laterally and vertically in the reservoir, thus adding uncertainty to the understanding of the recovery processes. Therefore a monitoring experiment was conducted, incorporating multiple remote sensing techniques, e.g., 2D and time-lapse reflection seismic data, microseismic data, production data, and tiltmeter recordings over a single CSS pad. The experiment recorded the data for four years to evaluate these technologies for field-wide monitoring. This experiment provided a testing ground to integrate several geophysical data to study the unknown associated with heavy oil extraction procedure.

The first aim of the thesis is to focus on microseismic data analysis and interpretation. The second part of the thesis aims to focus on time-lapse seismic data analysis and interpretation. The final part of the thesis links and integrates the observations from the two geophysical techniques by showing how one may help confirm or contradict the interpretation from each data.

A single deviated downhole microseismic monitoring array was installed at the pad of horizontal wells, to record the data. Before analyzing the recorded data, complete processing and quality workflow was proposed and applied to the recorded data to obtain event locations. As a result, approximately 2100 events were recorded during four cycles of steam injection and production. The spatial and temporal analysis and engineering data revealed that 95% of microseismicity is located in the overburden and recorded during the steam injection. I interpreted two fault planes in the overburden responsible for triggering the high number of microseismic activity.

I then focus on the time-lapse seismic data to process and identify time-lapse amplitude anomalies and isochrones time delays associated with the injection of a high volume of steam into the reservoir. The observations were integrated with surface tiltmeter data and temperature logs to interpret the spatial and vertical extent of the steam zones. It was concluded that the steam movement in the reservoir is non-homogenous; both spatially and vertically and several zones were identified where steam has partially or fully reached inside the reservoir.

Finally, the findings from several geophysical data sources were integrated to validate the proposed set of predictions. The validations of these predictions show that during the heavy oil recovery method, microseismic activity is more likely to occur in the overburden due to stress changes and the brittle nature of the rock. The reservoir also undergoes several changes due to high pressure and temperature, including dilation, compaction, and alterations of rock physics properties. These changes are interpreted by analyzing the time-lapse seismic data and surface tiltmeter data. The results also indicate that seismic reflection data highlight the changes at the reservoir level. In contrast, microseismic data would give a detailed picture of the changes in the overburden, and combining both is likely to give an elaborated insight of reservoir-caprock response to steam injection and the associated physical mechanisms.

To my Creator, for always holding my hand
To my Abu (father) and Ami (mother) for raising me to be the person I am today
To my husband and kids for their continuous support and patience

Acknowledgments

Foremost, I would like to express my sincere gratitude to my supervisor, Dr. Mirko van der Baan, for his continuous support, motivation, guidance, and patience during my Ph.D. His immense knowledge and enthusiasm helped me in all the time of research and writing of this thesis. He always motivated me to explore new scientific paths and upgrade my research skills. I could not have imagined having a better supervisor and mentor for my Ph.D. study.

Besides my supervisor, I would like to thank my supervisory committee: Dr. David Potter, Dr. Claire Currie, and Dr. Craig Heinke, for their feedback and insightful comments, which helped improve the quality of my thesis.

I want to thank all members of the microseismic industry consortium for their support. Special thanks to Melanie Grob (former Postdoc) for helping me settle in the group and answering all my questions every time I knocked on her office door. I would also like to thank my other colleagues Jean Baptist Tary, Robert Henry, V. Roche, and Hung Dinh. I would also like to thank an anonymous company for permission to use and show the data. I am also thankful to the sponsors of the Microseismic Industry Consortium for financial support during my Ph.D. I find myself fortunate to have the support of my work colleagues at CNOOC International Ltd when working on my thesis, especially Hamid Medjnoun, Kiersten Mohr, Doug Beringer, Jessica Budge, and Cheryl Hodgson.

I must thank Ruby, Mirko's wife, for welcoming us to her home for gatherings and celebrations and making sure we are settling in, well, socially and study-wise.

Above all, I am humbled to have such a supportive and loving family. I want to thank my parents for their unconditional love and support and the numerous sacrifices they made to help me succeed in my academic career. You are the best parents in the world. I want to thank my brothers (especially Mubasher and Umair), sisters (especially Saima), brother-in-law (Naseer Iqbal), sister-in-law (Sabiha Naz), and friend Huma Khalid for all their support and encouragement.

This whole journey wouldn't be possible without my husband (Naveed), son (Huzaifa), and daughter (Shanza) by my side, in good and bad times. I am blessed to have you, Huzaifa and Shanza; your laughter always kept me motivated.

Table of Contents

1	Introduction	1
1.1	Introduction.....	1
1.2	Problem statement.....	4
1.3	Research objective	6
1.4	Thesis outline and contribution.....	6
2	The Peace River monitoring project.....	8
2.1	Introduction.....	8
2.2	Geological setting	9
2.3	Depositional setting and stratigraphy.....	10
2.4	Peace River oil sands reservoir	12
2.4.1	History and reservoir characterization	13
2.4.2	Reservoir geology	14
2.4.3	Regional stresses	15
2.5	Project overview	16
2.5.1	Microseismic monitoring and steam cycles	17
2.5.2	Time-lapse seismic data	18
2.6	Road ahead.....	19
3	Geomechanics and rock physics of heavy oil extraction -An overview	20
3.1	Introduction.....	20
3.2	Geomechanical properties of rocks.....	21
3.2.1	Stress and strain	21
3.2.2	Deformation properties	22
3.2.3	Failure/strength properties	22
3.3	Thermally-induced stress changes	24
3.4	Geomechanical behavior of rock	26
3.4.1	Shearing and dilation	26
3.4.2	Shear at the shale caprock.....	27
3.4.3	Reservoir deformations	29
3.5	Correlation between seismic velocity and strength properties.....	30
3.6	Shale brittleness	34
3.7	The expected response of reservoir-caprock due to steam injection.....	35

3.8	Discussion	38
3.9	Summary	39
4	The impact of acquisition parameters and location techniques on microseismic event locations	41
4.1	Introduction.....	41
4.2	How events are located - Theory	42
4.2.1	P- wave method.....	43
4.2.2	P-S wave method	44
4.3	Synthetic Test.....	45
4.3.1	Test 1: Comparison of location method.....	45
4.3.2	Test 2: Impact of acquisition geometry on the location uncertainty	46
4.4	Results.....	46
4.4.1	Comparison of the location methods.....	46
4.4.2	Impact of acquisition geometry on location uncertainty.....	50
4.5	Discussion	52
4.6	Conclusion	54
5	Microseismic event locations and quality control workflow for Peace River data	55
5.1	Introduction.....	55
5.2	Event Location Workflow-Theory.....	55
5.3	Application to Peace River data.....	61
5.3.1	Data pre-processing.....	61
5.3.2	Event location	64
5.3.3	Quality control	65
5.4	Results.....	68
5.5	Discussion	70
5.6	Conclusion	73
6	Integration of microseismic and production data	74
6.1	Introduction.....	74
6.2	The Peace River CSS experiment	75
6.3	Data analysis strategy.....	76
6.3.1	The moment magnitude (M_w).....	77
6.3.2	Signal to noise ratio.....	78
6.3.3	Brittleness index.....	79

6.3.4	Assessing monitoring biases	79
6.3.5	Kaiser effect	81
6.4	Results.....	82
6.4.1	Spatial and temporal distribution	82
6.4.2	Moment magnitude	83
6.4.3	Integration of microseismic and engineering data	87
6.4.4	Brittleness index (<i>BI</i>)	88
6.5	Discussion	89
6.6	Conclusion	96
7	Time-lapse seismic data interpretation.....	98
7.1	Introduction.....	98
7.2	Workflow – time lapse analysis	99
7.2.1	Well to seismic tie.....	99
7.2.2	Data comparison	99
7.2.3	Time-lapse calibration.....	100
7.3	Results.....	103
7.3.1	Horizon interpretation	104
7.3.2	Time-lapse calibration.....	107
7.4	Time-lapse interpretation	113
7.4.1	Isochrone analysis	113
7.4.2	Amplitude anomaly.....	113
7.4.3	Difference volume.....	116
7.5	Discussion	117
7.5.1	Time-lapse processing.....	117
7.5.2	Additional observations	118
7.5.3	Time-lapse interpretation	119
7.6	Conclusion	124
8	Geomechanical behavior of the Peace River reservoir	126
8.1	Introduction.....	126
8.2	Reservoir response to steam injection.....	126
8.2.1	Observations	126
8.2.2	Theoretical analysis.....	129
8.2.3	Comparison of observations and theory.....	130

8.3	Caprock response to steam injection.....	133
8.3.1	Observations	133
8.3.2	Theoretical Analysis	134
8.3.3	Integrated Analysis	135
8.4	Caprock-reservoir response to production	138
8.4.1	Observations	138
8.4.2	Theoretical Analysis	139
8.4.3	Integrated Analysis	140
8.5	Comparisson of predictions with observations	141
8.5.1	Lessons Learned.....	141
8.5.2	Comparison with other models	143
8.6	Conclusions.....	145
9	Conclusion	146
9.1	Conclusion	146
9.2	Recommendation for future work.....	148
	Bibliography	149

List of Tables

Table 1.1 Original oil in place of crude bitumen as of December 31, 2014 (Alberta Energy Regulator 2015).
..... 2

Table 2.1 Bitumen reserves of the Peace River oil sand deposits (Hubbard 1999). 14

Table 5.1 Summary of data showing the number of events quality controlled, revisited, and disabled.....71

List of Figures

Figure 1-1: Location of the Canadian oil sand projects (reproduced with permission from Pacey, 2013). 1

Figure 2-1: Map showing the extent and main elements of the Western Canada Sedimentary Basin. The blue color shows the present extent of basin rocks and highlights the three sub-basins, e.g., Williston, Alberta, and Liard Basin (reproduced with permission from Wright et al., 1994). 8

Figure 2-2: Structural map of the foreland basin, showing some of the major structures in the basin (reproduced with permission from Mossop, 1988). 9

Figure 2-3: Peace River Stratigraphic column, showing sequence deposited during cretaceous (reproduced with permission from Hubbard, 1999). 10

Figure 2-4: Regional cross-section (A-A’) showing the presence and thickness variation of stratigraphic sequence in the basin from North to South. Different colors are indicative of different sequences (reproduced with permission from O’connell et al., 1994)..... 12

Figure 2-5: Map of Alberta, showing the location of Alberta oil sand, carbonate triangle, and heavy oil deposits (reproduced with permission from Machel 2010)..... 13

Figure 2-6: Schematic illustration of the orientation of fractures, with respect to the minimum (S_{hmin}) and maximum stress (S_{Hma}) direction (reproduced with permission from Zoback, 2010). 15

Figure 2-7: Map of Peace River area, showing maximum and minimum horizontal stress across the Peace River Arch and surface traces of Rocky Mountains thrust faults (reproduced with permission from Bell et al., 1994). 16

Figure 2-8: Acquisition geometry of CSS experiment, showing the treatment and observation wells on the pad. The horizontal wells are injectors and producers. A single deviated well is used for recording microseismic data (left). The base map on the right..... 17

Figure 2-9: Number of events over time, compared with injection/production history. Steam is injected in January of each year in increasing quantities (blue line). In the first year, a large number of events occur during steam injection (black line). Significantly few events are detected during extraction (water = green, oil = red)..... 18

Figure 3-1: Cylindrical sample under the influence of horizontal and vertical stresses along with Mohr’s diagram (τ - σ_n) and Mohr’s circle (Schön 2015). 23

Figure 3-2: Sketch of stress changes due to the heated zone. It shows that the increase in reservoir temperature (red circular zone) increases the horizontal stress along the vertical (B-B') and vertical stress along the horizontal profile (A-A'), the increase in the stress value is shown by the red line (reproduced with permission from Dusseault et al., 2007). 24

Figure 3-3: Sketch showing stress trajectories and shearing effects around the heated zone. The heated reservoir zone is shown as red; the induced stress anisotropy zone is developed in front of and above the expanding zone (thick black cross arrows). Vertical and horizontal thin black lines show the stress trajectories (reproduced with permission from Dusseault et al., 2007). 25

Figure 3-4: Schematic showing the stress changes, shear, and dilation zone ahead of the steam front (reproduced with permission from Dusseault & Collins, 2010). 26

Figure 3-5: Mohr circle showing an increase in pore pressure decreases the initial effective stresses (green circle), moving the circle to the left (red circle) and lowering the failure envelope (blue to red). The x-axis and y-axis represent normal and shear stress (Khan et al., 2011). 28

Figure 3-6: Zone of compression, shear, and extension above the reservoir due to hydrocarbon depletion (reproduced with permission from Dusseault et al., 2007). 29

Figure 3-7: Schematic cross-section showing surface deformation and faulting associated with fluid removal (Segall, 1989). 29

Figure 3-8: Schematic showing the surface distortion associated with volumetric (left) and shear (right) changes in the subsurface. The green oval and red triangle indicate the area of volumetric (ΔV) and shear (ΔS) changes, z is the depth, and the blue line shows the surface expression of the changes (reproduced with permission from Dusseault & Collins, 2010). 30

Figure 3-9: Plots of a) density variation with temperature and b) velocity variation with temperature, based on laboratory measurements (reproduced with permission from Chopra et al., 2010). 31

Figure 3-10: Compressional velocity as a function of temperature in saturated heavy oil sand. The velocity is measured at different pressure values ranging from 1MPa to 8 MPa (reproduced with permission from Eastwood, 1993). 32

Figure 3-11: Plot of a) measured bulk and shear moduli in heavy oil samples at different temperatures (reproduced with permission from Batzle et al., 2006). 32

Figure 3-12: Plot showing the relation between water saturation changes and relative P-wave velocity (reproduced with permission from Brisco, (2018)). 33

Figure 3-13: Plot of Young Modulus versus Poisson’s ratio separating ductile and brittle regions (reproduced with permission from Grieser & Bray, 2007)..... 35

Figure 3-14: Showing stress changes (σ) in response to the pore pressure, temperature (T), and volumetric (V) changes during steam injection (left) and hydrocarbon production (right). 37

Figure 4-1: Showing (a) Acquisition geometry used for the synthetic study, red stars are the synthetic sources, and black triangles are geophones, and (b) P- and S wave velocity model of the study area. 45

Figure 4-2: Map view (top) and a cross-sectional view (bottom) shows location uncertainties for downhole geophone array using the P-wave and P-S wave methods. The event is located approximately 400 m away from the center of the receiver array. Yellow triangles mark receivers. 47

Figure 4-3: Map (top) and cross-sectional (bottom) view show location uncertainties using the P-wave and P-S wave methods. The perturbed event locations shown in red are obtained from the Monte Carlo analysis. 48

Figure 4-4: Monte Carlo locations estimated for a single well (a-b) and dual well configuration (c-d) by using the P-wave and P-S wave methods. True, P-wave and P-S wave method Monte Carlo locations are denoted as the black star, blue, and red circles, respectively. The top figure (a-b) shows that perturbed event locations are much closer to the true event location when located using the P-S wave method in both the radial (a) and vertical direction (b) as compared to the P-wave method. However, (c-d) shows improvement in perturbed event locations by using multiple monitoring arrays..... 50

Figure 4-5: Standard deviation in Monte Carlo locations for events located in the caprock and reservoir interval for (a) single well and (b) two well-monitoring scenario estimated from P- and P-S wave methods. The RMS is plotted separately for caprock and reservoir rock. The x-axis is the distance between source and receiver, and the y-axis is the standard deviation. The blue and red lines show standard deviation in the P- and P-S wave methods, in the radial (solid) and vertical (dotted line) direction..... 50

Figure 4-6: Calculated PDF for 140m long geophone array placed in (a,d) deviated borehole, (b,e) vertical borehole, and (c,f) 100m long array in a vertical borehole, in cross-sectional (top row) and map view (bottom row). A solid black circle shows the true source location, and yellow triangles are the receivers..... 51

Figure 4-7: Calculated PDF for the event recorded by 140m long geophone array placed in a deviated borehole containing (a,d) eleven receivers, (b,e) six receivers, and (c,f) three receivers in cross-sectional (top) and map view (bottom). A solid black circle shows the true source location, and yellow triangles are the receivers. 52

Figure 5-1: Flowchart diagram illustrating the complete microseismic processing workflow employed in this study. 57

Figure 5-2: Illustration of the azimuth analysis, the dashed line represents the P –wave particle motion/ray path, the red star represents the microseismic source location, and grey triangles are the geophones..... 58

Figure 5-3: a) Perspective view of the field. The pad has horizontal wells to inject steam and produce hydrocarbon; geophones are lowered in the deviated observation well to record microseismic data. b) The figure on the right shows the P and S wave sonic logs and the 1D velocity model used in this project. 61

Figure 5-4: Waveforms showing a) raw and b) processed microseismic event recorded by a 10-level string of 3-component geophones during the 1st steam cycle. The two horizontal components are plotted in blue, and the vertical component is plotted in red..... 62

Figure 5-5: Showing different types of waveforms comprising the dataset in the study area. Different waveforms are labeled as Event1, 2, and 3 showing noise, a low amplitude event, and a good quality event, respectively. 63

Figure 5-6: Showing a) P- and S-wave arrival times picked on three-component waveforms followed by b) azimuthal analysis of the P- wave to remove the 180° ambiguity (the solid black lines indicate the preferred direction and grey lines are indicative of false azimuthal direction), and finally c) event locations, the red dot shows the event location of this particular microseismic event, whereas, the blue dots are all the events recorded during the 1st steam cycle in 2002. 64

Figure 5-7: Example showing the stepwise quality control of the individual event. a) Theoretical and observed P-and S-wave arrival times are superimposed on the event waveform (Black are the observed picks, and green are the theoretical picks). b) Hodogram at each receiver showing the P-wave polarization direction in the x-y plane, c, and d) Time and azimuth residual histograms. 66

Figure 5-8: An example of a revisited event during quality control. Initial (black) and updated (red) P -and S- wave picks are shown at each receiver (left), and corresponding P- and S- wave x-y hodograms (middle). The initial and final event locations are shown by black and red diamonds on the map view, the black triangles are the receivers, and black and gray lines are true and ambiguous azimuth directions (right). 67

Figure 5-9: Shows a map and depth view of the initial (left) and final event location after QC (left). Microseismic events are colored based on the steam cycle..... 67

Figure 5-10: Histogram showing S-P wave time residuals for initial event locations (left) and final event locations (right)..... 68

Figure 5-11: The separation distance vs. cross-correlation coefficient plot for a) Initial and b) final event locations. The red encircled area highlights the area where the most difference is evident..... 69

Figure 6-1: The pad well geometry in a) Cross-sectional view and b) Map view. Three laterals kick off from the central vertical well, with ten vertical injection-production wells and one deviated monitoring well. In the map view, the green color shows the perforated section of each well..... 76

Figure 6-2: Relationship of Brune-model parameters to far-field displacement spectrum (Eaton, 2014). 78

Figure 6-3: Magnitude-distance plot showing magnitude threshold (black dashed line) for a dataset. The green horizontal line indicates the detection sensitivity cut-off. The red and blue areas highlight the microseismic events excluded and included from the analysis, respectively (edited from Baig & Urbancic (2010)). 80

Figure 6-4: Schematic of landing height scenarios showing different depth coverage depending on whether the well is placed (a) lower or (b) higher in the section (reproduced with permission from Maxwell, 2014). 81

Figure 6-5: a) A map view of microseismic event location over the pad, b) Histogram of event count for each injection cycle, and c) Cross-section view and depth histogram of microseismic event distribution across the pad, horizontal colored lines indicate geological formations of interest, e.g., Falher Member, Wilrich Member, Bluesky, and Debolt Formations are shown as blue, yellow, red and purple colors, respectively. Microseismic events are colored based on their time of occurrence. Events that occurred during cycle 1, 2, 3, and 4 are colored as solid yellow, red, purple, and green circles, respectively..... 82

Figure 6-6: Histogram of calculated moment magnitudes of events recorded over four years. Different colors are used to show data from each cycle. 83

Figure 6-7: Magnitude versus distance plot for all data. The black line defines the magnitude detection limit for the data set, and the blue line indicates the detection-sensitivity cutoff. 84

Figure 6-8: Map view of a) The magnitude biased event map and b) Magnitude-limited event map of the pad..... 85

Figure 6-9: Time plot of injection pressure, microseismic event count, and production data over four years. The injected steam volume, water produced, oil produced, and injection pressure are shown in purple, blue, green, and red color, respectively. A dark red histogram shows the event frequency..... 86

Figure 6-10: The GR log, calculated Shear modulus, Young’s modulus, Poisson’s ratio, and Brittleness Index log for well 40-3, located on the western side of the pad. The histogram on the right shows the microseismicity occurrence at different depths. 88

Figure 6-11: Map view of a) landing height and b) magnitude threshold limit overlain by the magnitude limited event map over the pad. 90

Figure 6-12: Magnitude-distance plot of all the recorded events, data points are shown by different colors and sizes to indicate the time of occurrence and S/N ratio. A smaller size indicates a low S/N ratio, and a larger size indicates a high S/N ratio event..... 91

Figure 6-13: Schematic diagram showing two possible interpretations of microseismic event occurrence relative to surface pressure. The dark gray color shows the microseismic event histogram (reproduced with permission from Maxwell, 2014). 93

Figure 6-14: Time plot of simulation parameters (injection pressure, event count) and potential interpretation for cycle 1. The three time intervals are marked on the chart as phase **(a)**, **(b)**, and **(c)** (bottom) and corresponding time-stamped cross-sectional views of event locations (top). Pink line is the injection pressure, dark blue line shows the trend of microseismic histograms (light grey). 94

Figure 6-15: Interpreted fault/fracture planes in a) cross-sectional and b) map view overlay by the magnitude limited event locations. 95

Figure 6-16: The r-t plot of induced microseismic data, different colors indicate data recorded during different cycles, and vertically extended events are encircled in black. 96

Figure 7-1: Flow chart showing the time-lapse calibration workflow followed in this study.... 101

Figure 7-2: a) Basemap of the study area showing the location of seismic and well trajectories and b) stratigraphic section highlighting the geological formations of interest..... 104

Figure 7-3: Well to seismic correlation of well 40-3 from pad 40, showing a match between seismic reflectivity and synthetic seismogram for the three geological horizons of interest. The red and blue colors on seismic and synthetic log indicate negative (trough) and positive (peak) amplitude..... 104

Figure 7-4: East-west 2D seismic section displaying the seismic character for the top and bottom of the reservoir (Bluesky/Geth and Debolt Formation), caprock (top Wilrich), and a reference reflector ‘A’. 105

Figure 7-5: TWT difference map between monitor and baseline survey for reflector ‘A’ showing the time differences at shallow section (200ms above the reservoir). The horizontal lines are the seismic lines, and red dots are every 50th trace. 106

Figure 7-6: TWT maps for top Bluesky/Geth (top) and top Debolt (bottom) formation, generated from baseline (left) and monitor (right) surveys, highlighting the changes in TWT between the surveys. 107

Figure 7-7: a) NRMS, b) cross-correlation, and c) time-shift values along a 2D section, calculated from the baseline and monitor surveys before calibrating the monitor data. The horizons of interest are overlaid for analysis purposes. 108

Figure 7-8: Amplitude spectra for the baseline (blue), monitor (green), and calibrated monitor data after the shaping filter (orange). 109

Figure 7-9: NRMS attributes a) before calibration, b) after phase and time shift, c) after statics correction, and d) after time-variant shifts, showing the improvement in NRMS attribute after each subsequent calibration step is applied. 110

Figure 7-10: Cross-section showing the calculated a) cross-correlation coefficient and corresponding b) time shifts applied to the monitor data. The low cross-correlation values (0.5) and the largest time shifts (-7~-8ms?) are found to be within the reservoir interval. 111

Figure 7-11: Difference section a) after and b) before applying the calibration workflow. After calibration, changes occur predominantly within the reservoir. 112

Figure 7-12: Reservoir isochrone maps generated from a) baseline survey and b) monitor survey. The dashed rectangle encloses the area with substantial changes. 113

Figure 7-13: Comparison of a seismic line from the a) baseline and b) monitor surveys, highlighting areas undergoing amplitude changes. 114

Figure 7-14: Comparison of RMS amplitude maps for a) Top Bluesky/Geth (baseline), b) Top Bluesky/Geth (monitor), c) Top Debolt (baseline), and d) Top Debolt (monitor). 115

Figure 7-15: a) Amplitude difference section highlighting the changes within the reservoir and b) polygon showing the spatial trends of these changes over the pad. The blue and red polygons are representative of changes within the upper and lower reservoir interval, respectively. 116

Figure 7-16: Isochrone difference map for the reservoir (top) and temperature profiles from two observation wells at the pad. 118

Figure 7-17: Subsidence values recorded by tiltmeter during the 2nd cycle of steam injection (top) and production (bottom) between June 2004 to November 2004. The steam was injected from June to August 2004, and production started in September and continued till the end of November 2004..... 119

Figure 7-18: a) Observed and b) theoretical isochrones difference map for the reservoir interval, overlain by polygons bounding the changes in the upper (blue) and lower (red) reservoir interval. 121

Figure 7-19: Figure showing observed isochrone difference map overlain by the amplitude polygons (red and blue) and several interpreted zones (A, B, C, and D), where steam migrated vertically into different zones of the reservoir. 123

Figure 8-1: a) The cross-sectional view showing production-related microseismic event distributions across the pad. Horizontal colored lines indicate geological formations of interest. The Falher, Wilrich, Bluesky, and Debolt Formations are shown as blue, yellow, red, and purple colors, respectively. Microseismic events are colored based on their time of occurrence. Events that occurred during cycle 1, 2, 3, and 4 are colored as solid yellow, red, purple, and green circles, respectively. b,c) Comparison of a seismic line from the b) baseline and c) monitor surveys, highlighting areas undergoing amplitude changes. 127

Figure 8-2: Isochrone difference map for the reservoir (top) and temperature profiles from two observation wells at the pad. Different colors in the bottom indicate temperature values recorded at different times. 128

Figure 8-3: Subsidence values recorded by tiltmeters during the 2nd cycle of steam injection. The steam was injected from June to August 2004. The schematic diagram at the bottom shows the possible interpretation of the surface uplift during the injection cycle..... 129

Figure 8-4: Showing stress changes (σ) in response to the pore pressure, temperature (T), and volumetric (V) changes during steam injection (left) and hydrocarbon production (right). 130

Figure 8-5: Time plot of injection/production data volumes microseismic activity recorded during the steam injection cycles. The steam injection, hydrocarbon, and water production are shown in red, green, and purple colors. The microseismic event count is shown as dark red bars. 131

Figure 8-6: The GR log, calculated Shear modulus, Young’s modulus, Poisson ratio, and Brittleness index log for well 40-3, located on the western side of the pad. 133

Figure 8-7: Mohr’s circle plot showing a) initial stresses, b) reduction in minimum stress because of reservoir dilation, and c) increase in pore pressure in the overburden, causing slip failure. (reproduced with permission from Maxwell et al. (2015))..... 134

Figure 8-8: Possible Mohr circle changes responsible for microseismicity in the overburden during steam injection in the study area. The increased Mohr circle (dotted red) is caused by induced stress in the overburden due to steam injection into the reservoir. The solid blue lines are the failure criterion with a coefficient of friction (μ) 0.5 and 0.6 and cohesion (c) of 0 MPa. .. 136

Figure 8-9: Surface heave values recorded by tiltmeters during the 2nd cycle of hydrocarbon production. The hydrocarbon extraction was from September to November 2004. The schematic diagram at the bottom shows the possible interpretation of the surface subsidence during hydrocarbon production. 137

Figure 8-10: The cross-sectional view is showing production-related microseismic event distributions across the pad. Horizontal colored lines indicate geological formations of interest. The Falher, Wilrich, Bluesky, and Debolt formations are shown as blue, yellow, red, and purple colors, respectively. Microseismic events are colored based on their time of occurrence. Events that occurred during cycle 1, 2, 3, and 4 are colored as solid yellow, red, purple, and green circles, respectively. 139

Figure 8-11: Schematic diagram showing the reservoir a) before depletion and b) after reservoir depletion and expected faulting and fracturing in the surrounding of the depleted reservoir (reproduced with permission from Segall, 1989). 140

Figure 8-12: Schematic of the observed changes in the reservoir and overburden after four steam injection cycles and production at the pad. 142

1 Introduction

1.1 Introduction

Canada has one of the largest fossil fuel reserves in the world. It holds the third-largest reserves globally, after Venezuela and Saudi Arabia (Figure 1.1) (Pacey, 2013). Among all the Canadian provinces, Alberta has the largest oil reserves, and together with the Saskatchewan reserves, the deposits can supply the energy demands of North America for the next 100 years (Dusseault, 2002). According to Alberta Energy Regulator (2015), Alberta has over 1.8 trillion barrels of bitumen in place; however, less than 10% of it is considered as a reserve. The data also show that Alberta's bitumen volume is significantly larger than its conventional oil volume. Alberta bitumen has low API gravity (10° API), density greater than $1,000 \text{ kg/m}^3$, and viscosity of over 1 million cP. The majority of the bitumen reservoirs are at shallow depth, typically less than 1,000m (Chopra et al., 2010).



Figure 1-1: Location of the Canadian oil sand projects (reproduced with permission from Pacey, 2013).

Alberta has three major oil and sand production areas, Athabasca being the largest, Cold Lake is the second largest, and Peace River, the third largest deposit (Figure 1.1). Table 1.1 lists the original bitumen in place for different areas in Alberta. The average pay thickness varies between 5 to 25 meters, with average oil saturation of about 65% and 30% porosity. However, the

oil saturation of the Athabasca deposit can be as high as 90%. While oil sands have high oil saturation, the main challenge is the viscosity of the bitumen; the viscosities are too high to bring the bitumen to the surface through primary production. Therefore, the bitumen must be heated above 200°C to reduce the viscosity five times to move the oil under gravity and pressure (Mehrotra & Svrcek, 1986).

Table 1.1 Original oil in place of crude bitumen as of December 31, 2014 (Alberta Energy Regulator, 2015).

Oil sands area Oil sands deposit	Initial volume in-place (10 ⁶ m ³)	Area (10 ³ ha) ^a	Average pay thickness (m)	Average reservoir parameters		
				Mass (%)	Pore volume oil (%)	Average porosity (%)
Athabasca						
Upper Grand Rapids	5 817	359	8.5	9.2	58	33
Middle Grand Rapids	2 171	183	6.8	8.4	55	32
Lower Grand Rapids	1 286	134	5.6	8.3	52	33
Wabiskaw-McMurray (mineable)	20 823	375	25.9	10.1	76	28
Wabiskaw-McMurray (in situ)	131 609	4 694	13.1	10.2	73	29
Nisku	16 232	819	14.4	5.7	68	20
Grosmont	64 537	1 766	23.8	6.6	79	20
Subtotal	242 475					
Cold Lake						
Upper Grand Rapids	5 377	612	4.8	9.0	65	28
Lower Grand Rapids	10 004	658	7.8	9.2	65	30
Clearwater	9 422	433	11.8	8.9	59	31
Wabiskaw-McMurray	4 287	485	5.1	8.1	62	28
Subtotal	29 090					
Peace River						
Bluesky-Gething	10 968	1 016	6.1	8.1	68	26
Belloy	282	26	8.0	7.8	64	27
Debolt	7 800	258	25.3	5.1	66	18
Shunda	2 510	143	14.0	5.3	52	23
Subtotal	21 560					
Total	293 125					

^a ha = hectare.

The two main thermal recovery methods used in Alberta are CSS (Cyclic Steam Stimulation) and SAGD (Steam Assisted Gravity Drainage). CSS is a single well procedure; a targeted volume of steam (310°C) is injected into the formation at a pressure greater than the fracture pressure, typically greater than about 10 MPa (Butler, 1987; Gates & Larter, 2014; Stark, 2011). The injected steam heats the bitumen and fractures the reservoir. It increases the initial reservoir pressure,

reduces the viscosity of the bitumen near the well, thus mobilizing the oil to the well. Once the oil production rate drops below a defined threshold value, the cycle starts again with steam injection (Butler, 1987; Stark, 2011). In SAGD, two wells are placed parallel to each other in the targeted zone. The top well is the injection well; steam is injected into the formation. As the steam chamber grows outward, the oil is moved downward toward the lower well (production well) under the influence of gravity. The oil is produced continuously from the production well under the influence of gravity.

Both CSS and SAGD are excellent bitumen recovery processes for heavy oil operations, but both processes experience challenges. The injection pressure during CSS is kept higher than the fracturing pressure; thus, an intact cap rock is required to protect the formations above the reservoir. Inside the reservoir, the steam chambers are connected; therefore, when steam is injected, it flows along the connected channels between the injection wells and may not contribute much to the production at the well where the steam was injected; hence limiting the volume of recovered oil because of the distance oil needs to mobilize to get to the well. On the other hand, in SAGD operations, the steam is injected at a pressure substantially lower than the fracturing pressure; thus, any shale layers inside the reservoir formation become a major challenge as this introduces reservoir heterogeneity. Intact shale layers may reduce production since they create steam barriers (Gates & Larter, 2014).

The feasibility and efficiency of these underground extraction operations are sometimes questioned due to possible damage to the surrounding environment, particularly the seal (caprock) of the reservoir (Khazaei, 2016). In such types of underground injection operations, there is always a trade-off between the objective and economics of the project on the one hand and the safety of the process on the other hand. The safety of the operations is ensured by keeping the injection pressure low. Once the steam is injected into the reservoir, it induces stress changes in and around the reservoir, thus possibly creating fractures and providing a pathway for the fluid to reach the surface. It may compromise the caprock integrity, and cause surface damage, and, in severe cases, may cause a blowout. The damage to the caprock must be prevented because hydrocarbons are valuable resources and pose challenges with resource conservation (Khazaei, 2016). Therefore proper monitoring of these operations has become a major focus in western Canada and worldwide. Once the steam injection begins, reliable geophysical monitoring methods must be employed to

optimize the operation and achieve the objective. Valuable information on subsurface, surface, and oil production can be obtained by various geodetic and seismic techniques used in the industry. The most common techniques in the petroleum industry include seismic reflection surveying, microseismic monitoring, tiltmeter, and interferometric radar (InSAR) (Verdon et al., 2013).

Among these, seismic reflection surveying is commonly used to produce a time-lapse image of the reservoir undergoing steam injection and production. Injected steam alters the viscosity and density of the reservoir rock, thus affecting the velocity of the waves propagating through the impacted formation. Interpretation of these recorded changes directly or by impedance inversion can reveal the subsurface changes (Chopra et al., 2010). The earliest application of steam front detection was shown by Mummery (1985); he demonstrated the use of reflection seismic data to detect the steam front's movement. Several other studies have used time-lapse seismic data to generate images of amplitude anomalies corresponding to the changes in the reservoir (Eastwood et al., 1994; Kalantzis et al., 1996; Kalantzis, 1994).

Another effective imaging technique used in the petroleum industry is microseismic monitoring; it is the only technique that can image the geometry of the growing fractures (Maxwell, 2014). It refers to the recording of elastic waves due to microseismic events generated; because of material undergoing deformation. Therefore, it helps in understanding the rock response to the stress changes. The main advantage of microseismic monitoring is that rock damage can be evaluated continuously.

The goal of this thesis is to advance the application of microseismic and time-lapse seismic data to better understand the dynamics of the CSS by developing an integrated approach. An essential intent of the research is to demonstrate how the integration of several geophysical data reveals a complete picture of the subsurface changes in processes associated with CSS. The integration will help to establish cause and affect relationships between recorded data and physical changes/damage in the subsurface.

1.2 Problem statement

During thermal heavy oil extraction projects (CSS or SAGD), the injection pressure is intentionally kept low enough to build up the steam chamber only in the reservoir and to prevent any damage to caprock. The high temperature and pressure result in stress variation, volumetric

changes at the reservoir level, and shear failure within and surrounding the steam front. These subsurface changes may also propagate to the surface resulting in surface heaves (Collins, 2007; Nanayakkara & Wong, 2009). Furthermore, extraction of fluid/bitumen from the reservoir reduces the pore pressure and alters the petrophysical properties, ultimately causing reservoir compaction and surface subsidence (Waal & Smits, 1988; Finol & Ali, 1975; Muntendam-Bos & Fokker, 2009).

Many authors have contributed to the research to investigate and study the above effects. For example, Maxwell et al. (2007) combined microseismic and tiltmeter data to monitor the warm-up phase of a SAGD well pair. The integration of microseismic data and volumetric strains (inverted from surface deformation) helps delineate discrete deformation zones in the target area. Walters & Zoback (2013) integrated microseismic event locations and surface deformation data to better understand the spatio-temporal relation. The examined locations indicated the reactivation of shallow faults and brittle failure of rigid stringers within the reservoir. However, the study did not incorporate time-lapse surface seismic data, which can provide additional information and add to the current findings of the study. Schoofs et al. (2010) described an integrated workflow to monitor the steam distribution and caprock integrity in a fractured carbonate reservoir. The paper also emphasized the importance and need for the combined application of several geophysical technologies for monitoring purposes. Still, it did not contain an integrated analysis to explore the geomechanical behavior of the caprock-reservoir system.

As mentioned above, few attempts have been made to integrate limited geophysical data to monitor the steam front during heavy oil extraction. However, scientific papers that incorporate and jointly analyze large volumes of multidisciplinary data are rare to non-existent. This is unfortunate since it hampers our understanding of the dynamics of injection processes by linking unique observations from each type of data. For instance, in this thesis, it is shown that seismic reflection data highlight changes at the reservoir level. In contrast, microseismic data give a detailed picture of the changes in the overburden. The combination of both types of data enhances our insight into the reservoir-caprock response to steam injection and associated physical mechanisms because of the complementary information that can be derived from each data type.

1.3 Research objective

This research seeks to integrate microseismic, time-lapse surface seismic, production, and well data recorded during Cyclic Steam Stimulation (CSS) to achieve the following scientific objectives

- Understand the dynamics and evaluate the effectiveness of the CSS operation at growing the depletion chambers within the reservoir.
- Investigate the influence/ impact of steam injection on the reservoir-caprock system by integrating multidisciplinary geophysical data.
- Propose a set of geomechanical predictions and validate them with the help of multidisciplinary data observations.

1.4 Thesis outline and contribution

The thesis is organized into nine chapters:

Chapter 1 provides the background and scope of this research.

Chapter 2 presents an overview of the geology of the study area and a summary of the CSS experiment.

Chapter 3 reviews the current understanding of the geomechanical process associated with thermal heavy oil recovery processes.

Chapter 4 presents an uncertainty analysis for microseismic data focusing on the commonly used location methods, using data from a geophone array placed in a single deviated borehole. Synthetic data are used to demonstrate that microseismic uncertainty is dependent on the location method and acquisition geometry (well orientation, length, and density of geophone array).

Chapter 5 discusses the processing and quality control workflow for microseismic data recorded by a single monitoring borehole. First, a complete workflow is proposed and then applied to the real data recorded during the CSS experiment.

Chapter 6 presents the analysis and interpretation of recorded microseismic data. The data is first analyzed to examine the spatial and temporal trends to gain insight into the deformation associated with steam chamber growth. Later the results are integrated with the engineering data.

Chapter 7 discusses the time-lapse processing and interpretation of the seismic reflection data.

Chapter 8 highlights the integrated analysis of microseismic, surface seismic and engineering data observations and the likely physical mechanisms responsible for the geomechanical changes.

Chapter 9 concludes the research work and provides recommendations for further research.

The thesis provides the following main contributions to science:

- The first contribution of this thesis is the demonstration of microseismic event location uncertainty associated with two commonly used event location methods (P- and SP-method), using synthetic data from a geophone array placed in a single deviated borehole.
- Provide a workflow to process the microseismic data for the case of a single deviated observation well to produce a reliable event catalog for further analysis and interpretation. The workflow consists of three parts, namely pre-processing, event location, and quality control. The workflow also demonstrates the application of commonly used analysis methods to quality control the calculated microseismic event locations.
- Introduce a multidisciplinary data analysis approach to understand the geomechanics of heavy oil reservoirs undergoing cyclic steam stimulation—this involved interpretation and integration of microseismic, time-lapse seismic, surface tiltmeter, and production data.
- Emphasize the importance of unique information extracted from each geophysical data source (e.g., microseismic, time-lapse seismic data, and production data) to highlight the changes in and around the heated reservoir
- Reveal the presence of blind spots in some of the geophysical data, which may lead to incorrect interpretation of the subsurface image.

2 The Peace River monitoring project

2.1 Introduction

The Western Canada Sedimentary Basin (WCSB) is a vast sedimentary basin covering approximately 450,000 sq mi of Western Canada; it includes southwestern Manitoba, southern Saskatchewan, Alberta, northeastern British Columbia, and the southwest corner of the Northwest Territories (Figure 2.1). The Western Canada Sedimentary Basin can be described as a simple northeasterly tapering wedge of sedimentary rock. It extends from the Rocky Mountains west to the Canadian Shield in the east, having a thickness of 6 km under the Rocky Mountains but thins to zero at the eastern margins (Mossop & Shetsen, 1994).

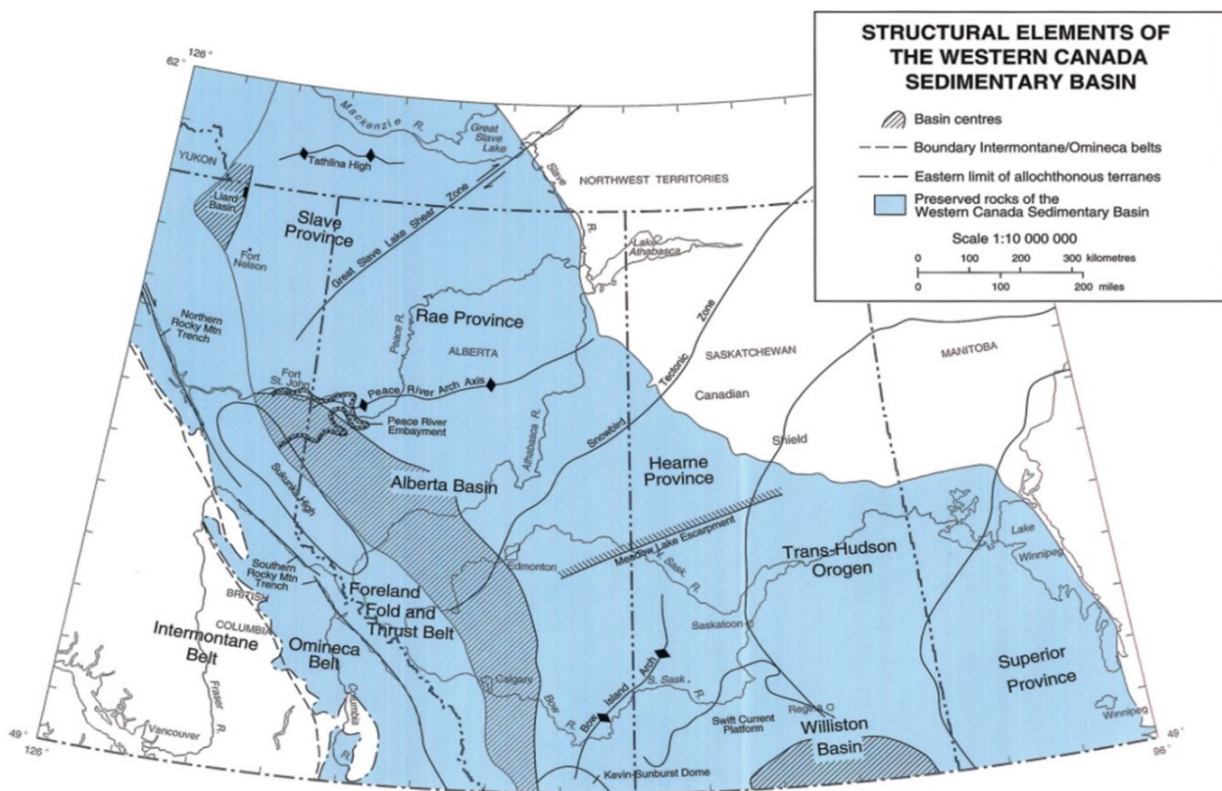


Figure 2-1: Map showing the extent and main elements of the Western Canada Sedimentary Basin. The blue color shows the present extent of basin rocks and highlights the three sub-basins, e.g., Williston, Alberta, and Liard Basin (reproduced with permission from Wright et al., 1994).

The variation in the shape and structure reveals a long and complex story of differential subsidence and uplift that resulted in the evolution and development of the WCSB (Porter et al., 1982). The structural evolution is related to the tectonic evolution of the Rocky Mountains. The three major structural elements of the WCSB are the Canadian Cordillera, cratonic Williston basin, and Alberta basin, as seen in Figure 2.2. The western margin is marked by the northwest-southeast

trending Cordilleran fold and thrust belt. The other two major features (Alberta basin and Williston basin) are separated by northeast-trending positive structural elements comprising the Bow island arch (Williams & Burk, 1964).

The study area of the Peace River oil sand deposit lies in north-central Alberta, as indicated by the red rectangle in Figure 2.2. The following sections will focus on the geology and reservoir potential of the study area.

2.2 Geological setting

The Peace River Arch (PRA), a cratonic uplift, lies in northwestern Alberta and northeastern British Columbia (Figure 2.1). Structurally, the PRA is east-northeasterly trending, and its preserved length is 750 km. Its western edge lies near the Alberta/British Columbia boundary. It is an asymmetrical structure with a steeply dipping northern flank and gently dipping southern flank. It is one of the four positive cratonic structures in the Western Canada Sedimentary Basin that developed at the western edge of North America. The other three positive cratonic features developed during the Paleozoic are; the West Alberta arch, the Tathlina High, and the Sweetgrass Arch (Figure 2.1). The Peace River Arch is the largest of these and records the longest history of tectonic activity (O'connell et al., 1994).

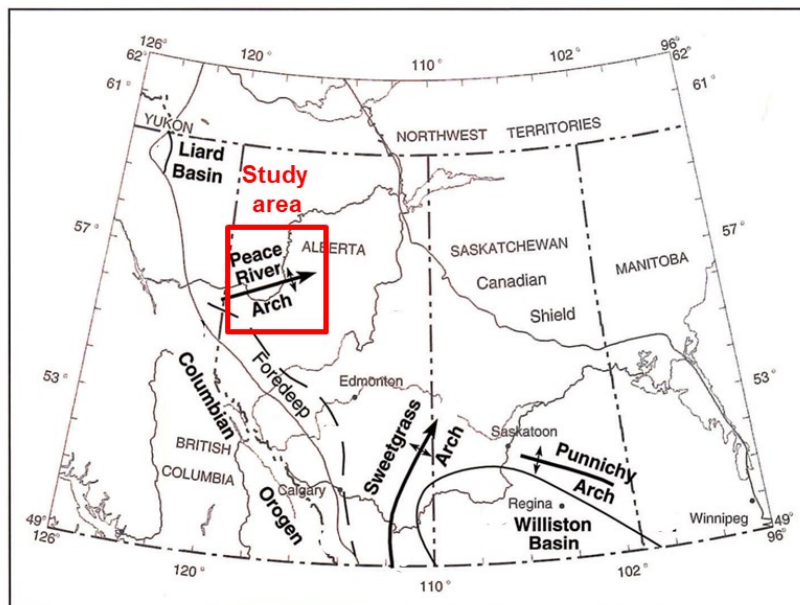


Figure 2-2: Structural map of the foreland basin, showing some of the major structures in the basin (reproduced with permission from Mossop, 1988).

2.3 Depositional setting and stratigraphy

The Western Canada Sedimentary Basin preserves a long history of deposition and structuring, ranging from the Sauk sequence (Precambrian–Cambrian age) to the Tejas sequence (Tertiary-Quaternary age) (Figure 2.3). Some of the sequences are well presented throughout the basin. In contrast, other sequences are restricted to a certain area of the Western Canada Sedimentary Basin (Figure 2.3), e.g., Ordovician and Silurian strata of the plains are preserved in the Williston basin, whereas the thickest Triassic sequence is found in the northwest part of the basin (O’Connell et al., 1994). Figure 2.3 shows a regional cross-section (A-A’) along the WCSB, displaying the deposition of different sequences. The deposited sequence is much thicker in the north as compared to the south of the basin. The Cambrian to Jurassic platform sequence is interrupted by several widespread unconformities (Figure 2.3).

The thickest sub-Jurassic rocks are found in the north of the Peace River Arch, and the thickest Cretaceous sequence is deposited in the Peace River area, as indicated by the red arrow on the cross-section. The detailed Peace River stratigraphic sequence of the Cretaceous is shown in Figure 2.4. The Cretaceous interval comprises the Bullhead group, Fort John group, and Smoky Group stratigraphic units (O’connell et al., 1994).

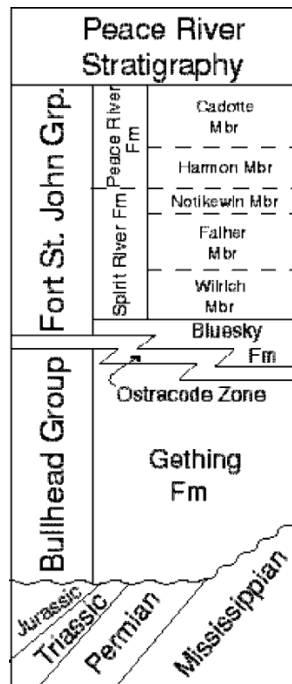


Figure 2-3: Peace River Stratigraphic column, showing sequence deposited during cretaceous (reproduced with permission from Hubbard, 1999).

Figure 2-4: Regional cross-section (A-A') showing the presence and thickness variation of stratigraphic sequence in the basin from North to South. Different colors are indicative of different sequences (reproduced with permission from O'connell et al., 1994).

The Bullhead group of lower Cretaceous unconformably overlies the Jurassic to Triassic deposits. It is composed of chert, quartz, and quartzite at the base and then grades to sandstone, siltstone, and mudstone. The Bullhead group is thickest in the northern Canadian Rockies (900m) and thins out in the Peace River area (100m). The Bullhead group contains the Bluesky, Gething, and Cadomin Formations. The Fort St. John Group is another Lower Cretaceous unit in the area. It comprises dark shale deposited in a marine environment and interbedded with sandstone, siltstone, and conglomerates. Its thickness varies between 700m to 2000 meters. It includes the Shaftesbury, Peace River, Spirit River, and Bluesky Formations, which conformably overlies the sandstone of the Dunvegan Formation. The younger strata of the Tertiary age have been eroded except the Paskapoo Formation. It is unconformably overlain by the Laurentide drift deposit of Quaternary age (Hubbard, 1999).

Heavy oil reservoirs in the Peace River area are found in Devonian and Cretaceous rocks. The heavy oil production in the study area is from the Bluesky/Gething Formation, which will be the subject of discussion in the next sections

2.4 Peace River oil sands reservoir

Trapped hydrocarbon reservoirs in the WCSB are classified into five types: (a) dry biogenic, (b) heavy oil; (c) sweet, light crude oil; (d) sweet gas and gas condensate; and (e) sour gas and gas condensate. These classes can be put into three groups based on the depth ranges, e.g. (a) and (b) are found at shallow depth or outcrop; (c) are found at intermediate depth (approximately 300-3500m) and (d) and (e) are found at deeper depth (> 3500m). Reefs are the most common type of trap in the area, and in some cases, a structural component is involved (Machel, 2010).

Most heavy oil reservoirs in the area are found in the Cretaceous sands and underlying Devonian carbonates. Heavy oil carbonates occur in the area called the "Carbonate Triangle" (Figure 2.5) at four stratigraphic levels, including Grosmont, Nisku, Shunda, and Debolt (Machel, 2010). These oil sands deposits are found at Athabasca, Cold Lake, and Peace River of northern Alberta. These deposits consist of bitumen-rich sands from the Gething Formation, Ostracode Zone, and Bluesky Formation, overlying the older strata of Paleozoic and Mesozoic age.

Hubbard (1999) revealed three deposition stages in the Peace River area based on the sedimentological analyses. The lithology of the Gething Formation indicates a terrestrial origin in the southeastern part, whereas, in the northeastern part, it changes to marine deposits. The Bluesky Formation corresponds to progradation deposition in the Boreal sea; it does not exceed a thickness of several meters. The maximum transgression of the Boreal sea is marked by the overlying Wilrich Member (Spirit River Formation) of the basal Cretaceous sequence at the Peace River.

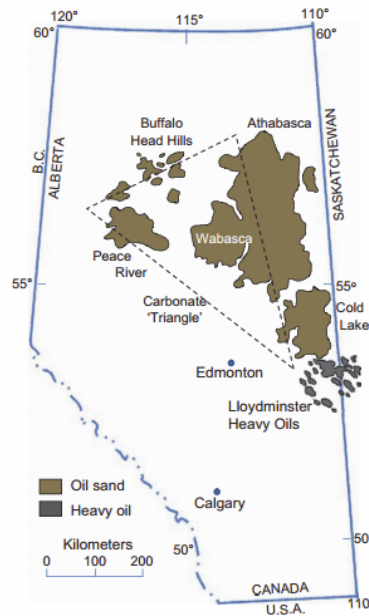


Figure 2-5: Map of Alberta, showing the location of Alberta oil sand, carbonate triangle, and heavy oil deposits (reproduced with permission from Machel 2010).

2.4.1 History and reservoir characterization

The Peace River sand deposits were discovered in the 1950s, located at a depth of 550 m. The oil sand deposits are found in the Bluesky/Gething Formation of Lower Cretaceous, Belloy Formation of Permian and Debolt, and Shunda Formations of Mississippian age, holding > 150 billion barrels of bitumen in place (table 2.1). But recoverable bitumen is restricted to late Cretaceous sand of the Bluesky/Gething Formation. Shell Canada initiated pilot projects in the 1970s and early 1980s, which lead to commercial production in the area. Since the API gravity of the bitumen is <10°, several different well designs have been employed with varying degrees of success, including a grid of vertical injectors and producers, horizontal injectors and producers, Steam-Assisted Gravity Drainage (SAGD), and cyclic steam stimulation(CSS). Initially, a series

of vertical wells are drilled from the main pad to the reservoir depth, and then horizontal wells are drilled laterally into the reservoir (McGillivray, 2005).

In the Peace River development area, the net pay average is 20 to 30 m in thickness, with average sandstone porosity of 28% and gas permeabilities (after bitumen extraction) range from 1 to 4 Darcy. The average bitumen saturation is 77% and may reach 88% in some areas (Hubbard, 1999; McGillivray, 2005).

Table 2.1 Bitumen reserves of the Peace River oil sand deposits (Hubbard, 1999).

Deposit	Areal Extent (10 ³ Ha)	Bitumen In Place	
		(10 ⁹ m ³)	(10 ⁹ bbls)
Bluesky/Gething (L. Cretaceous)	1153	14	88
Belloy (Permian)	26	0.3	1.8
Debolt (Mississippian)	302	7.8	49
Shunda (Mississippian)	143	2.5	15.8
Total:		24.6	154.6

2.4.2 Reservoir geology

Recoverable hydrocarbon reserves in the Peace River are deposited in the estuarine (tidal deltaic) sands of the Bluesky Formation. The localized fluvial-deltaic sand of the Ostracode Zone at Peace River is mud-dominated. The thickness of these sands overlain by the Bluesky Formation can reach up > 30 m. The thickest Lower cretaceous sediment zone is located at the paleo-lows on the underlying Mississippian surface.

The orogenic accretionary events in WCSB have resulted in stratigraphic and structural traps in the Peace River area. The regional structural dip of the reservoir strata in the area is southwest and

1. On the northern and eastern side of the Peace River arch, the up-dip seal is provided by the pinch out of the low permeability Mississippian carbonates.
2. Basinal shales of Wilrich Member and Bluesky Formation act as the top seal for the Bluesky Formation.
3. Estuarine mudstone provides a lateral east-southeast seal.

It is believed that bitumen at Peace River likely originated in the deep basin to the southwest and migrated to the current location up-dip through the Late Cretaceous and Tertiary (Hubbard, 1999; O'Connell et al., 1994).

The next section will summarize the regional stresses in the study area to better understand their impact on hydrocarbon exploration, particularly in the unconventional and fractured reservoir.

2.4.3 Regional stresses

Fractures tend to propagate in the direction of least resistance and widen in the direction that requires the least force. It means that tensile fractures will propagate in the direction of maximum principal stress and perpendicular to the least principal stress, as shown in Figure 2.6. Therefore, the key to understanding the fracture orientation in the area is first to understand the principle stress directions (Economides & Martin, 2007).

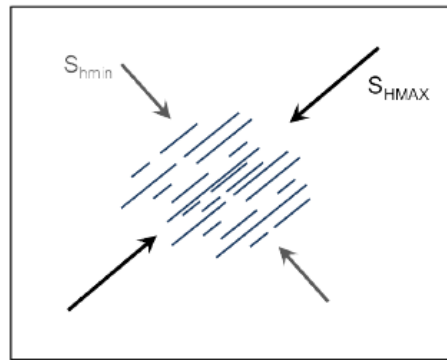


Figure 2-6: Schematic illustration of the orientation of fractures, with respect to the minimum (S_{hmin}) and maximum stress (S_{Hma}) direction (reproduced with permission from Zoback, 2010).

In western Canada, the current understanding of in situ stresses is interpreted from well logs, hydraulic fracture records, and production indicators (Bell et al., 1994). The WCSB is characterized by a NE-SW trending S_{Hmax} orientation (Adams & Bell, 1991; Zoback & Zoback, 1980). However, the Peace River Arch is an anomalous stress orientation region with the north-northeast-south-southwest S_{Hmax} trajectories. The slight deflection of the S_{Hmax} trajectories is seen in the map in Figure 2.7. In much of Alberta, the dominant fracture network is sub-vertical and mostly aligned in the NE-SW direction (Bell & Bachu, 2003). Based on micro and mini frac stress data from 41 wells in the Peace River area, it is found that the hydraulic fractures in the area will be approximately vertical, and the strike of the fractures will be parallel to the S_{Hmax} (Bell et al., 1994). This information will help predict the orientation of natural fractures in the study area during thermal recovery operations.

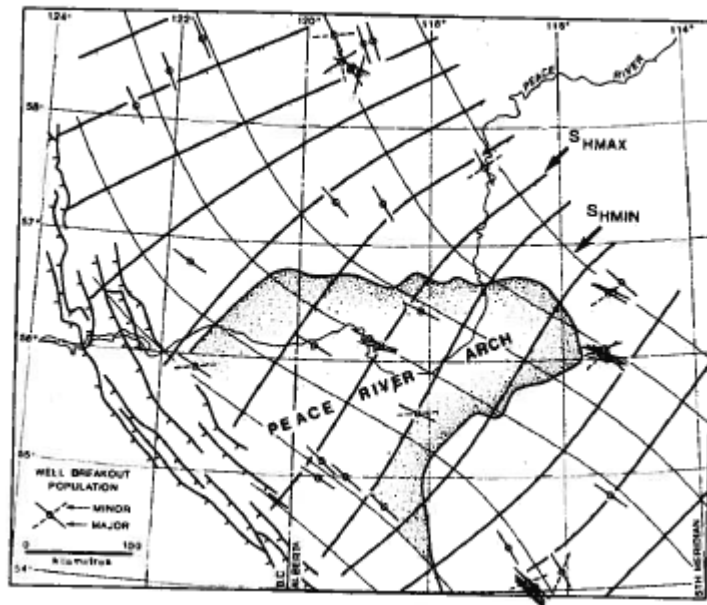


Figure 2-7: Map of Peace River area, showing maximum and minimum horizontal stress across the Peace River Arch and surface traces of Rocky Mountains thrust faults (reproduced with permission from Bell et al., 1994).

2.5 Project overview

The Peace River oil field in northern Alberta is under commercial production since 1986, several recovery methods have been applied to extract the bitumen cost-effectively. Grids of vertical injector/producer, horizontal injector/producers, CSS and SAGD have all been utilized. However, a horizontal well CSS strategy is being used in the most recently drilled pads. Several horizontal sections are drilled away from the vertical well into the reservoir, and steam is pumped through them. The steam is allowed to soak, reducing the bitumen's viscosity, and then the oil is pumped to the surface (McGillivray, 2005). Despite applying several recovery operations and obtaining commercial-scale bitumen over the past 20 years, it is still unclear what exactly happens in the reservoir when steam is injected. Although it is assumed that heat is transferred through a combination of dilation and thermal convection, uniformly outward from the well, it is still not known with certainty how the steam is distributed along the well path and moves laterally away from the well.

Additionally, it is also unclear how the steam moves vertically in the reservoir. This adds uncertainty to the understanding of steam recovery processes. Given the above unknowns, it is extremely important to investigate and understand what is happening in the subsurface/reservoir;

it will help optimize the operation. A monitoring experiment was conducted, incorporating multiple remote sensing techniques, e.g., 2D and time-lapse reflection seismic data, microseismic data, production data, and tiltmeter recordings over a single CSS pad. The experiment recorded the data for four years to evaluate these technologies for field-wide monitoring.

The monitoring experiment primarily focused on the application of time-lapse seismic and microseismic monitoring along with surface tiltmeter monitoring. The pad used in this thesis consists of horizontal wells. It uses a cyclic steam stimulation strategy (CSS) with a 50 level array of 3 component geophones cemented in the deviated well TH40-A for recording microseismic data. Figure 2.8 shows the geometry of the pad. A cross spread of permanent source locations was created by drilling 15 m deep holes for each shot. The resulting seismic reflection was recorded by the surface and borehole geophones, thus producing high fold 2D seismic lines and a sparse (one fold) surface 3D. In this thesis, I focus the analysis on the 2D seismic lines. When active survey is not recorded, the geophones (surface and borehole) were used to record microseismic data.

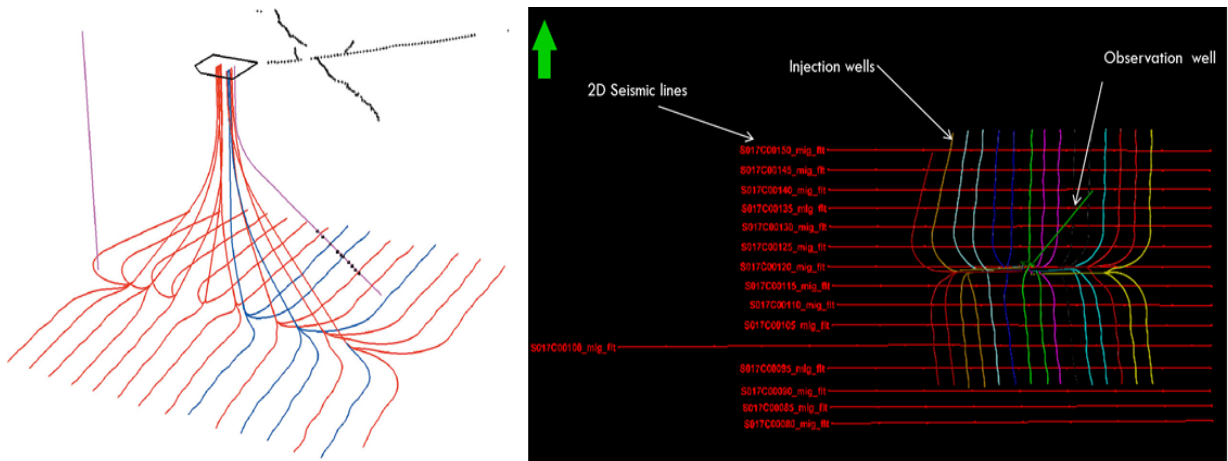


Figure 2-8: Acquisition geometry of CSS experiment, showing the treatment and observation wells on the pad. The horizontal wells are injectors and producers. A single deviated well is used for recording microseismic data (left). The base map on the right

2.5.1 Microseismic monitoring and steam cycles

The steam was injected into the reservoir through the ten horizontal wells (each further divided into three horizontal arms). Microseismic data were recorded by a single observation well at the pad (Figure 2.8). A total of four steam injection and production cycles were performed from

2002 to 2005. The microseismic data were recorded by ten 3C geophones placed inside the single deviated observation well. It consisted of approximately 3000 triggered files. The event occurrences and production history are shown in Figure 2.9. It will help to understand if events are related to steam injection or fluid extraction.

2.5.2 Time-lapse seismic data

The time-lapse surface seismic data were acquired at different times over the pad. The first 2D survey (baseline survey) was acquired in 2002 before injecting steam into the reservoir. The seismic survey (monitor survey) was acquired again after four cycles of steam injection/production. Both surveys are processed by following the same processing flow; therefore, any changes between the baseline/ monitor survey can be associated with changes in the reservoir.

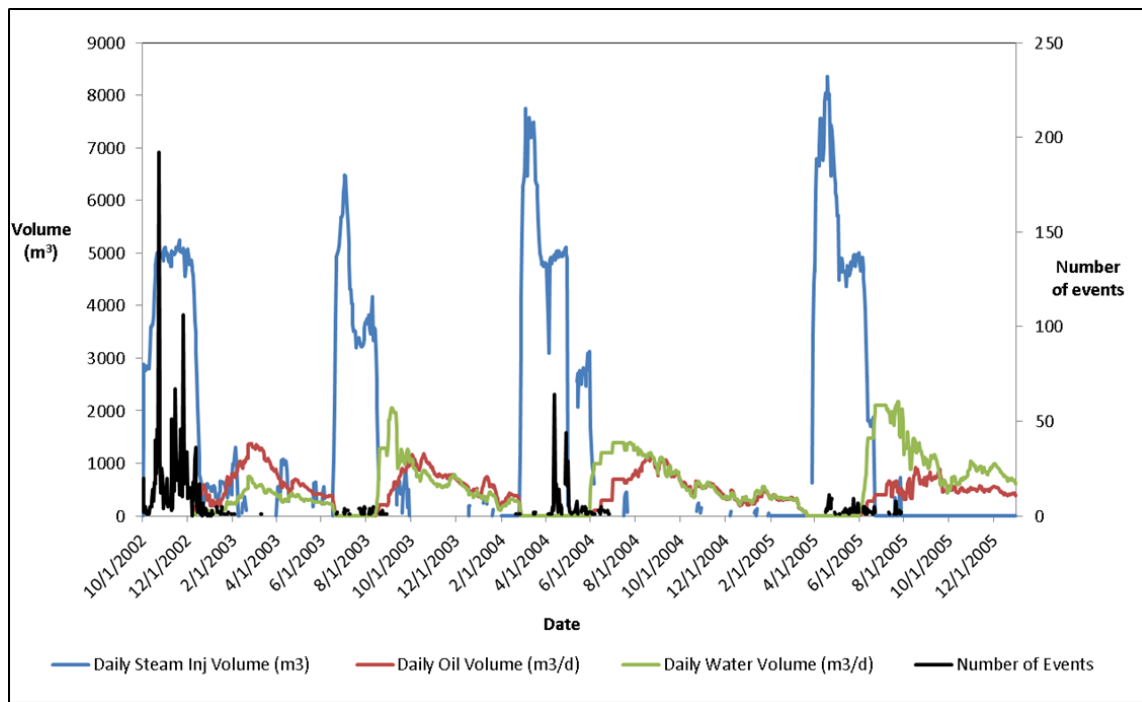


Figure 2-9: Number of events over time, compared with injection/production history. Steam is injected in January of each year in increasing quantities (blue line). In the first year, a large number of events occur during steam injection (black line). Significantly few events are detected during extraction (water = green, oil = red).

In addition to microseismic and time-lapse seismic data following data are also made available

- Well data
 - i. Geological well tops
 - ii. Well logs (sonic and density)

- iii. Temperature profiles
- Engineering data
 - i. Injection and production data
 - ii. Pressure data
- Tiltmeter observation

2.6 Road ahead

The previous section describes the experiment, geology, and available data for the research project. The multidisciplinary data will be utilized in a stepwise manner, as mentioned below, to achieve the research objectives described in chapter one.

- A set of geomechanical + rock physics predictions will be proposed based on the literature review.
- Then, raw microseismic data will be processed to obtain the microseismic event locations.
- Next, processed microseismic data will be analyzed and interpreted in conjunction with engineering data.
- It will be followed by time-lapse seismic data processing, analysis, and interpretation.
- Finally, the findings from surface seismic and microseismic data will be integrated to understand the CSS operation dynamics and validate the proposed geomechanical predictions.

3 Geomechanics and rock physics of heavy oil extraction -An overview

3.1 Introduction

When a thermal recovery method is used to extract heavy oil, the reservoir undergoes complex mechanisms absent in conventional reservoirs (Shafiei & Dusseault, 2013). In addition to thermal conduction and convection, the reservoir also experiences geomechanical changes. As a result, rock dilates, improving the permeability, porosity, and compressibility. It increases the vertical permeability and makes such operations economically feasible. On the other hand, thermal operations may also negatively affect stress/strain redistribution, reservoir deformation, ground surface heave, variation in rock properties, and deformation/disturbance in the overburden rock. All the above mechanisms occur in parallel as physical components of the thermal processes (Dusseault & Collins, 2010).

Researchers have been working for several decades to address thermal geomechanics and understand its impact on reservoir simulation, production mechanism, and prediction (Al-Aulaqi et al., 2011; Al-Hadhrami & Blunt, 2000; Civan, 2004; Karyampudi & Rao, 1995; Kumar & Verma, 2010; Schembre et al., 2006). Major factors leading to such studies have been the large vertical surface deformation, extensive microseismic activity, and the failure of conventional reservoir simulation to make predictions. The earliest attempt was made by Butler (1987) to investigate the thermal expansion of pore liquids and resultant pore pressure increase during steam injection operations. He concluded that during CSS, zones of high pore pressure might extend several meters into the reservoir. However, his approach did not invoke geomechanics. Later work on geomechanical modeling concluded that dilation might occur within a cold reservoir, between wells, and close to the thermal front (Chalaturnyk et al., 1991). It was also found that changes in the reservoir permeability and volume are dependent on temperature changes, effective pressure, and shear stress (Scott et al., 1994). Increasing the formation pressure to the threshold pressure causes irreversible shear dilation, thus permitting larger than expected injectivity and productivity (Singhal et al., 1998). The development of shear dilation in and around the steam chamber results from thermal jacking, developing a zone with compressive stresses leading to shearing and dilation of the reservoir. This increases the porosity from 28%-30% to 32%-34%, increasing the permeability from 1~2D to 5~8D (Collins et al., 2002). All this work has contributed extensively

to the current understanding resulting in successful thermal recovery operations (Collins et al., 2002; Collins, 2007).

This chapter cover two major objectives; (1) a review of the literature to better understand the impact of thermal recovery procedures on the geomechanical properties and behavior of the reservoir-caprock system and (2) the effect of these changes on geophysical parameters. These key learnings will be incorporated in future chapters to analyze geophysical data and interpret the key observations from a CSS experiment.

3.2 Geomechanical properties of rocks

Geomechanical properties are a specific group of petrophysical parameters directly measured in the laboratory using specific tests (Schön, 2015). These properties are of prime importance in the petroleum industry as they define how different rocks respond under different conditions (fluid injection and production) and help classify rocks. Some of the geomechanical properties are:

3.2.1 Stress and strain

When a rock is under the influence of stress, it experiences several kinds of deformation or strain. It may alter the linear dimension, volume, or shape of the rock, which may be elastic (reversible) or nonelastic (viscous, plastic, irreversible). The stresses can be vertical or horizontal; the vertical stress component is given by the weight of the overburden (Schön, 2015)

$$\sigma_{vertical} = g \cdot \int_0^z \rho(z) \cdot dz, \quad (3.1)$$

where g is the gravity acceleration, z is the depth, and ρ is the density at depth z . The horizontal component of stress is often approximated in the absence of tectonic forces as

$$\sigma_{horizontal} = \frac{\nu}{1-\nu} \cdot \sigma_{vertical} \quad (3.2)$$

where ν is Poisson's ratio.

In porous rocks, the concept of effective stress is introduced as

$$\sigma_{effective,ij} = \sigma_{ij} = \sigma_{total,ij} - \alpha \cdot \sigma_{pore} \cdot \delta_{ij}, \quad (3.3)$$

where

$\sigma_{total,ij}$ is the total stress tensor

α is the Biot-Willis effective stress parameter

δ_{ij} is the Kronecker delta.

Note that all the stresses mentioned here are effective stresses unless mentioned.

The failure behavior of rocks is described based on the principle of the effective stress component $\sigma_{11}, \sigma_{22}, \sigma_{33}$. To understand this, consider a cylindrical sample with equal horizontal stress components but different vertical stress components. The stress effects are described as

$$\text{mean effective stress } \sigma_{\text{mean}} = P = \frac{1}{3} \cdot (\sigma_{11} + \sigma_{22} + \sigma_{33}) \quad (3.4)$$

$$\text{shear stress } Q = \sqrt{3 \cdot I_2} \quad (3.5)$$

where $I_2 = \frac{1}{6}[(\sigma_{11} - \sigma_{22})^2 + (\sigma_{22} - \sigma_{33})^2 + (\sigma_{33} - \sigma_{11})^2]$ is the second invariant of the effective stress tensor.

When $\sigma_{11} = \sigma_{22} = \sigma_H$ and $\sigma_{33} = \sigma_v$, the above equations become

$$\sigma_{\text{mean}} = P = \frac{1}{3} \cdot (\sigma_v + 2 \cdot \sigma_H) = \frac{1}{3} \cdot (\sigma_{33} + 2 \cdot \sigma_{11}) \quad (3.6)$$

$$Q = \sigma_v - \sigma_H = \sigma_{33} - \sigma_{11} \quad (3.7)$$

3.2.2 Deformation properties

Deformation properties are mostly derived from a static compression test and include Young's modulus and Poisson's ratio. The Young's modulus is defined as the ratio of axial stress and the resulting axial strain:

$$E = \frac{\sigma}{\varepsilon} \quad (3.8)$$

The Young's modulus is stress-dependent and can also be derived from the linear portion of the stress-strain curve. It measures the stiffness of the rock, and its unit is $\text{N/m}^2 = \text{Pa}$ (pascal).

The other deformation parameter, Poisson's ratio, is defined as the relative change of radius (r) divided by the relative change of axial length (h)

$$v = \frac{\Delta r / r}{\Delta h / h}, \quad (3.9)$$

and varies between 0 and 0.5 (Schön, 2015).

3.2.3 Failure/strength properties

The strength describes the amount of force needed to bring the rock to failure; the force may be compressive, tensile, or shear in nature. The most commonly used and simple failure criterion was formulated by Coulomb in 1773. According to the criterion, the shear stress τ tending to cause failure across a plane is resisted by

- The cohesion (c) of the material,
- The normal stress σ_n across the plane times the coefficient of internal friction μ (or the angle of internal friction φ , where $\mu = \tan \varphi$):

$$\tau = c + \tan \varphi \cdot \sigma_n$$

Mohr's circle best illustrates the failure processes and strength properties; the principle is demonstrated in Figure 3.1:

- For a cylindrical sample, a constant lateral or radial stress ($\sigma_{11} = \sigma_{22}$) and axial stress (σ_{33}) increase until the rock ruptures.
- The rupture makes an angle (θ) with a weak shear plane.

Stress normal to the plane is

$$\sigma_n = \frac{\sigma_{11} + \sigma_{33}}{2} + \frac{\sigma_{11} - \sigma_{33}}{2} \cdot \cos(2\theta) \quad (3.10)$$

Shear stress parallel to the shear plane is

$$\tau = \frac{\sigma_{33} - \sigma_{11}}{2} \cdot \sin(2\theta) \quad (3.11)$$

The above equations are used to generate the $\tau - \sigma_n$ plot called Mohr's circle. A number of experiments are conducted to construct the failure envelope. The envelope indicates the stress condition of failure and maybe approximated as a straight line. This way, the cohesion (c , intercept with the vertical) and angle of internal friction (φ , the slope of the line) can be estimated (Schön, 2015).

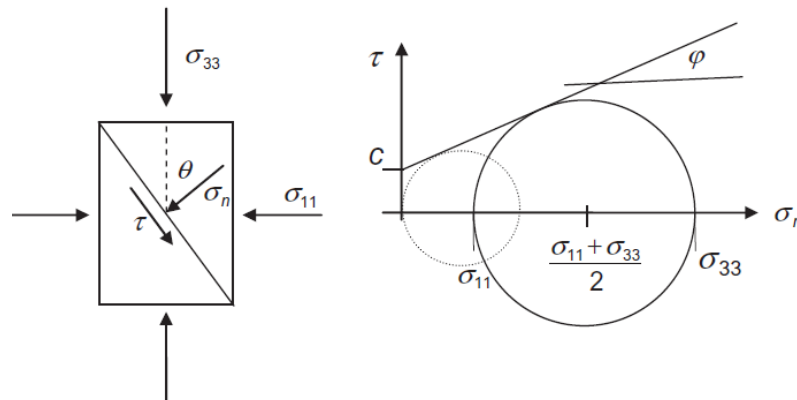


Figure 3-1: Cylindrical sample under the influence of horizontal and vertical stresses along with Mohr's diagram ($\tau - \sigma_n$) and Mohr's circle (Schön 2015).

The strength properties of rocks are generally controlled by the following:

- The type and mechanical quality of the bonding between the rock particles (cementation for clastic sedimentary rocks).
- The presence, distribution, and orientation of any previously present fractures or fissures in the rock.
- The internal rock structure (lamination, schistosity, anisotropy).
- Confining and pore-fluid pressure.

3.3 Thermally-induced stress changes

During thermal recovery processes, the temperature can rise to 350°C, resulting in a complex induced stress distribution zone around the reservoir. A qualitative sketch of expected changes in effective stress along horizontal and vertical sections near a steam chamber is shown in Figure 3.2.

The stresses in and around the steam chamber vary as:

- Within the heated zone, stresses increase in all directions due to thermal dilation.
- Along the horizontal section (A-A'), vertical stresses increase due to expansion, and horizontal stresses decrease due to extensional strain.
- Along the vertical section (B-B'), large horizontal stresses are developed next to the heated zone, whereas a decrease in vertical stresses is expected.

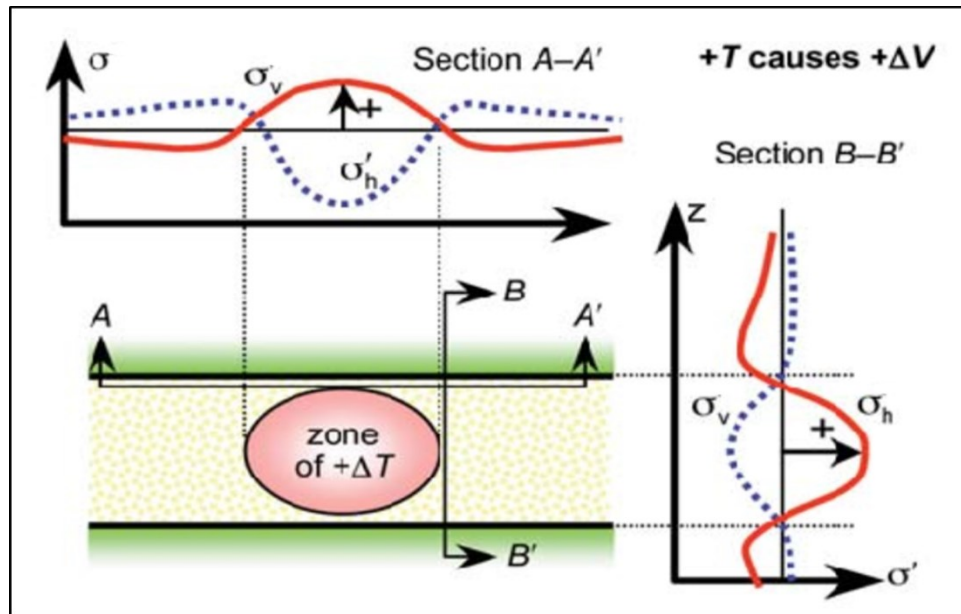


Figure 3-2: Sketch of stress changes due to the heated zone. It shows that the increase in reservoir temperature (red circular zone) increases the horizontal stress along the vertical (B-B') and vertical stress

along the horizontal profile (A-A'), the increase in the stress value is shown by the red line (reproduced with permission from Dusseault et al., 2007).

In short, stress anisotropy is induced around the heated zone. This can be easily visualized in the two dimensions using stress trajectories and small arrows for principle stresses (Figure 3.3). The heated reservoir may be assumed as a balloon (red zone) expanding outward within the brittle material. The stresses in the direction of expansion increase (shown by longer arrows perpendicular to the expanding zone), but stresses parallel to the balloon, in front of it (shown by shorter arrows parallel to the expanding zone) drop due to the stretching (Figure 3.3). It introduces large-scale stress anisotropy, leading to anisotropic changes in the P-(compressional) and S-(shear) wave velocities (Dusseault et al., 2007).

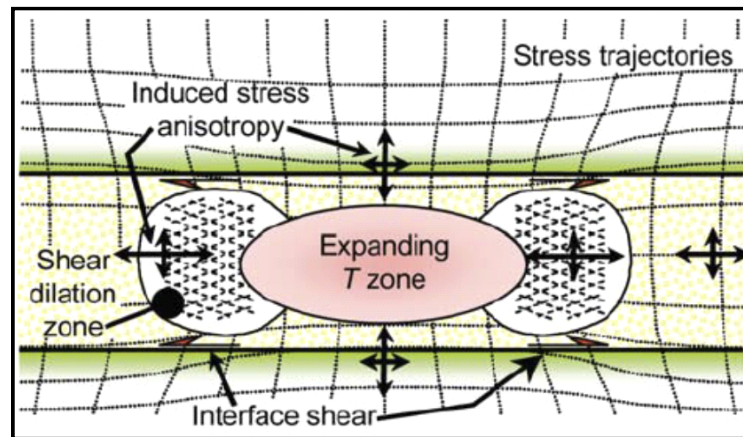


Figure 3-3: Sketch showing stress trajectories and shearing effects around the heated zone. The heated reservoir zone is shown as red; the induced stress anisotropy zone is developed in front of and above the expanding zone (thick black cross arrows). Vertical and horizontal thin black lines show the stress trajectories (reproduced with permission from Dusseault et al., 2007).

Increasing stress anisotropy means that shearing and shear dilation may take place. To shear, high porosity sandstone ($\phi > 0.25$), a principal effective stress ratio (σ_1 / σ_3) of more than 3.5-4.5, is needed, and simulation studies suggest that in weak sandstone, a temperature difference of (ΔT) 40-60°C is enough to cause shearing. Generally, steam injection elevates the reservoir temperature from 10-40°C to 200-325°C, enough to initiate massive shearing. It can beneficially result in a shear breach in thin shale barriers and dilate sandstone, increasing formation permeability, thus improving the production. It is now understood that all aggressive thermal operations enhance reservoir properties due to shearing, and tracking these changes (seismically or micro-seismically) can be of benefit to the geomechanical analysis (Dusseault et al., 2007).

Faulting or shearing around the steam front is an indication of high-stress anisotropy, and time-lapse measurements of changes in seismic attributes (e.g., amplitude and impedance) and microseismic monitoring could help locate and quantify these processes.

3.4 Geomechanical behavior of rock

The caprock overlying the oil sands consists of several low-permeability units that work together to act as the seal and limit the flow of fluid from the reservoir vertically upward. High temperature and pressure impact the geomechanics aspect of the caprock-reservoir system. This section will discuss a few of these effects.

3.4.1 Shearing and dilation

The thermal oil recovery process induces shearing; it is a failure mode that occurs when the anisotropic stresses exceed the frictional and cohesive strengths of the rock. As a result, several shearing zones are formed along which sliding occurs. In unconsolidated rocks, the sliding may further result in translation, rotation, and displacement of loose sand grains capable of causing a permanent disturbance, leading to dilation (an increase of bulk volume). Moreover, injection results in high differential thermal stresses, reducing the effective stresses, eventually shearing the shallow reservoir (Dusseault & Collins, 2010).

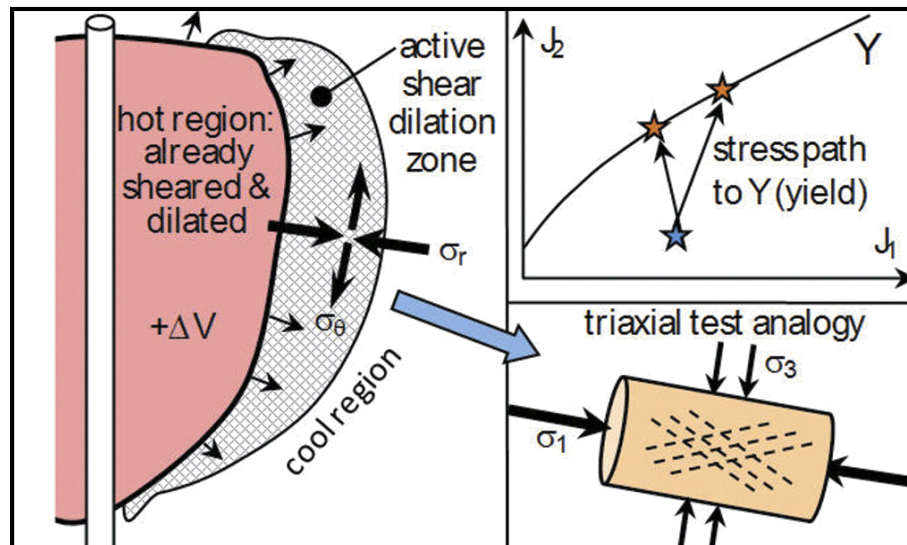


Figure 3-4: Schematic showing the stress changes, shear, and dilation zone ahead of the steam front (reproduced with permission from Dusseault & Collins, 2010).

Figure 3.4 shows a schematic of stress changes as the steam chamber propagates in the reservoir. The laterally propagating steam front will cause the effective horizontal stress (σ_h)

inside and outside the thermal zone to increase because of the lateral constraint. Meanwhile, the effective vertical stress (σ_v) decreases outside the thermal zone because of thermal jacking: unloading of some of the stresses in the cold reservoir by vertical extensional strains due to thermal expansion. For shallow reservoirs, these conditions make shearing favorable, and stiffer rock will attract higher stresses and eventually will be forced into its yielding condition. Hence, almost all the rock in advance of the propagating steam front will shear at low confining stresses. It means for competent sands, shear dilation potential is high, and minimal grain crushing is expected (Dusseault & Collins, 2010).

The strong dilation front of the heated zone results in an increase of absolute porosity of the reservoir by factor 2 to 10 and relative permeability by a factor of 10. Besides, the shearing will break up the thin clay dusting layer found between the bedding planes and beds. The shear dilation plays a significant part in the success of the thermal recovery processes as it enhances the transport flow (Dusseault & Collins, 2010).

3.4.2 Shear at the shale caprock

The caprock shales overlying the heavy oil reservoir are impermeable. During thermal expansion and dilation, a huge stress concentration is developed between the reservoir and the non-expanding overlying shales. During steam injection, shearing inside the reservoir is beneficial and intended for thermal recovery of heavy oil. However, if these fractures grow and extend to overlying shale layers, then it can lead to shear failure at the shale interface. One way to understand the cause of shearing is to analyze the effect of increased pressure and temperature using the Mohr-Coulomb criterion. The green circle represents the virgin state of stress before steam is injected, and the blue line represents the failure strength or, essentially, the shear strength of the rock (Figure 3.5). When steam injection starts, pore pressure increases, effective stresses decrease, causing the Mohr circle to move to the left. The reservoir is confined laterally by adjacent material, causing the total stress in the lateral direction to increase considerably, while vertical stress experiences little change as steam is injected. It causes the Mohr circle to become larger as it moves to the left (Figure 3.5). Since temperature changes also generate thermal stresses, this effect, combined with stress changes due to pore pressure, causes the Mohr circle to become even larger (Khan et al., 2011).

As the steam front continues to grow and high temperature touches the shale, it creates microfractures. These microfractures increase permeability. The steam enters the shale through

these microfractures, increasing the clay-bound water content in shale and drastically decreasing the cohesion and friction angle of shale. It will reduce the shear strength, as shown by the red line in Figure 3.5. In summary, the changes in pressure and temperature will enlarge the Mohr's circle diameter and move to the left, closer to the failure envelope, thus increasing the chance of shearing (Khan et al., 2011).

It is worth mentioning that when the steam front reaches the shale layer, the steam is condensed into water and absorbed by the shales. It causes the shale to swell and increase in lateral stresses, which considerably reduces Young's modulus and the peak strength (Bashbush et al., 2009), therefore facilitating the breakage of shale lamination.

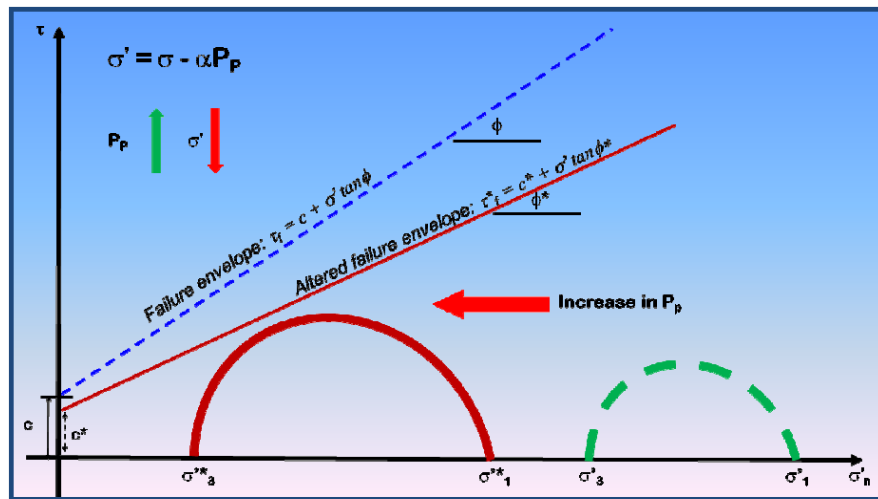


Figure 3-5: Mohr circle showing an increase in pore pressure decreases the initial effective stresses (green circle), moving the circle to the left (red circle) and lowering the failure envelope (blue to red). The x-axis and y-axis represent normal and shear stress (Khan et al., 2011).

Reservoir compaction and in situ stresses are induced by reservoir compaction. A sketch of induced stress above the depleting zone is shown in Figure 3.6. Directly above the center of the compacting reservoir, effective horizontal stress (σ_h) goes up but drops above the flanks. However, shear stress goes up above the shoulders, leading to the formation of shear planes due to the concentration of shear stresses on the interface (Figure 3.6). It has been observed in the Wilmington oil field in the 1950s, and '60s, where hundreds of wells above the shoulders of the gentle anticline reservoir were sheared. Similarly, hundreds of wells in Californian and Canadian thermal projects are sheared because of thermal expansion (Dusseault et al., 2007).

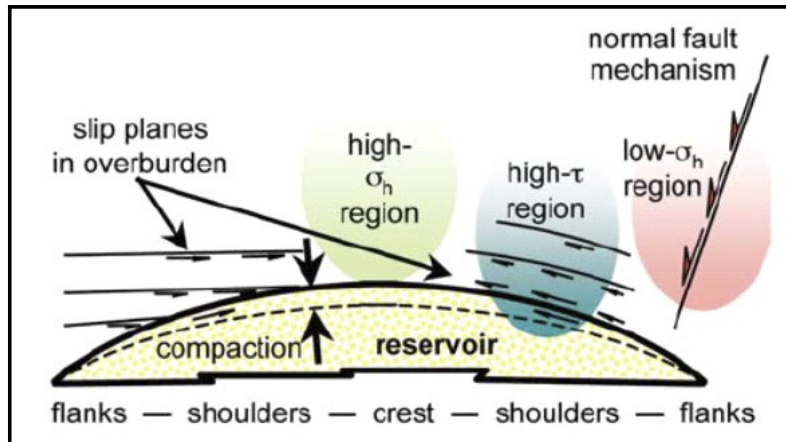


Figure 3-6: Zone of compression, shear, and extension above the reservoir due to hydrocarbon depletion (reproduced with permission from Dusseault et al., 2007).

3.4.3 Reservoir deformations

The deformations in the reservoir can cause deformations at the surface. Thermal recovery operations experience large vertical surface deformation (Δz). The thermal recovery processes between the depths of 200 to 500m can produce cumulative vertical surface deformations of up to 600 mm. The value of Δz is of economic importance, specifically at the late production cycles, because this is the dominant drive mechanism during late production. The recompaction drive effect increases the oil recovery rates and possibly the ultimate recovery factor as well.

The schematic cross-section in Figure 3.7 summarizes the surface deformation and faulting associated with fluid extraction. The fluid extraction from the reservoir causes subsidence and horizontal contraction of the center of the subsiding region and lesser extension at the flanks. Both normal and reverse faults may result during the extraction processes (Segall, 1989).

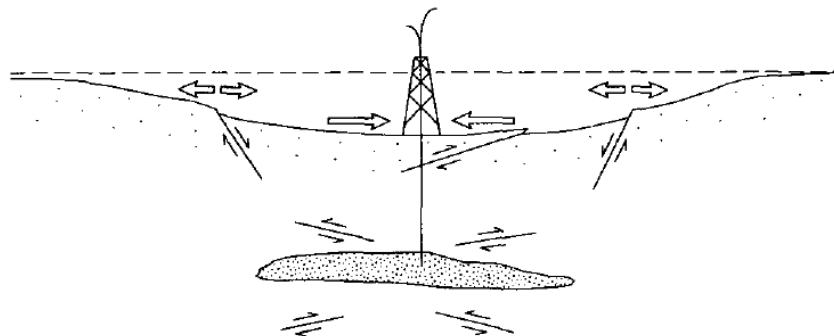


Figure 3-7: Schematic cross-section showing surface deformation and faulting associated with fluid removal (Segall, 1989).

During the injection phase, the reservoir distortion may be pure volumetric dilation or shearing related. It can give rise to monopolar or dipole surface deformation (Δz) distributions,

respectively, at the surface (Figure 3.8). The surface deformation field can be inverted to understand the volumetric or shear distortion at the reservoir level for a well-constrained case (single well operation at a constant depth). It has been used to help understand the production mechanism and predict possible casing failure due to steam injection (Dusseault & Collins, 2010).

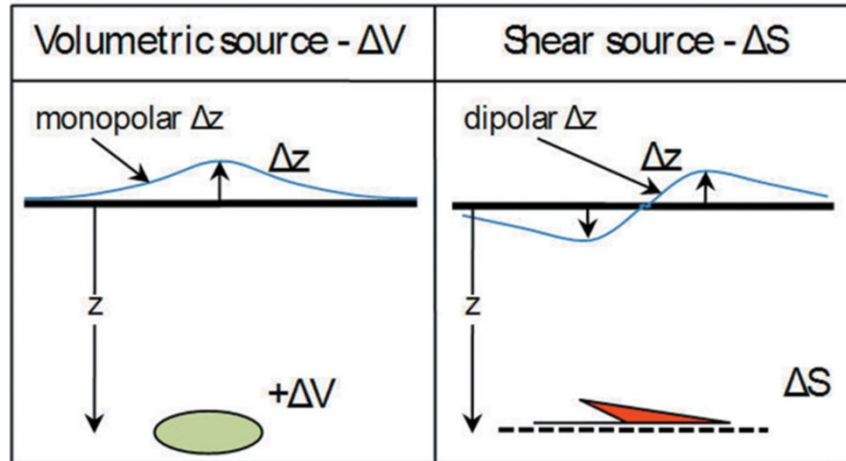


Figure 3-8: Schematic showing the surface distortion associated with volumetric (left) and shear (right) changes in the subsurface. The green oval and red triangle indicate the area of volumetric (ΔV) and shear (ΔS) changes, z is the depth, and the blue line shows the surface expression of the changes (reproduced with permission from Dusseault & Collins, 2010).

These volume changes at the reservoir level may be tracked indirectly by deformation inversion coupled with seismic data analysis. It can also help track the homogeneity of the injection processes, changes in permeability, and swept zones' distribution.

The geomechanical behavior of heavy oil reservoirs during thermal recovery can be better interpreted by analyzing the elastic properties (such as velocity, density, and impedance) of the reservoir-caprock system, emphasizing temperature variation. These properties will link the measured geophysical response and the geomechanical behavior of the geological system. This will be discussed in the next section.

3.5 Correlation between seismic velocity and strength properties

I have shown that during the thermal heavy oil recovery procedure, massive changes take place in the density and fluid saturation of the rock matrix due to temperature and also because of reservoir dilation (Schön, 2015). These changes greatly affect the seismic parameters such as (Isaac, 1998) velocity, amplitude, and frequency content.

Velocity is a crucial piece of information derived from seismic data. It depends on the material moduli through which the seismic wave propagates. The P-wave velocity is

$$V_P = \left[\frac{\left(K + \frac{4}{3}G \right)}{\rho} \right]^{1/2}, \quad (3.12)$$

where K is the bulk modulus, G is the shear modulus, and ρ is the density. The shear modulus is zero for most fluids, and the above equation is reduced to

$$V_{Pfluid} = \left[\frac{K}{\rho} \right]^{1/2}. \quad (3.13)$$

Seismic wave velocities within a rock are dependent on porosity, pore fluid, density, temperature, and effective pressure (Hicks & Berry, 1956; Isaac, 1998). The temperature dependency of velocity and density was investigated by Eastwood (1993). It was demonstrated that density varies with temperature changes, as shown in Figure 3.9a. The measurements were taken at the temperature range of 20°-250°C and a pressure range of 3.5-7 MPa. The experiment also investigated the impact of temperature on velocity in two bitumen samples (fluid only) (Eastwood, 1993).

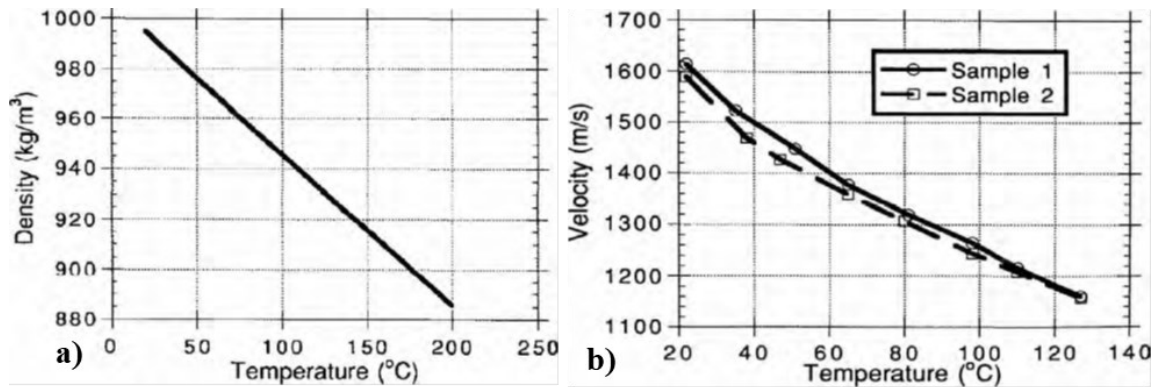


Figure 3-9: Plots of a) density variation with temperature and b) velocity variation with temperature, based on laboratory measurements (reproduced with permission from Chopra et al., 2010).

The plot in Figure 3.9b shows the temperature and compressional velocities (P-wave velocity) in two bitumen samples at a constant pressure of 0.1 mPa. The P-wave velocity decrease as the temperature increases from 22 to 127 C°; the decrease in velocity is approximately 30% relative to the velocity at 22°C (Eastwood, 1993). Velocity also exhibits pressure dependency; it decreases by 10% with a decrease of pressure (8MPa to 1MPa) at 22°C (Figure 3.10). It is seen that velocity and density both decrease with increased temperature for heavy oil (oil sand or bitumen). The magnitude of the decrease depends on temperature and differential pressure, which is the difference between the confining and pore pressure (Chopra et al., 2010).

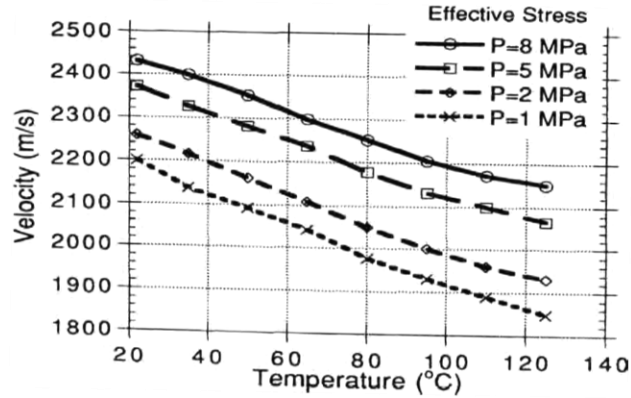


Figure 3-10: Compressional velocity as a function of temperature in saturated heavy oil sand. The velocity is measured at different pressure values ranging from 1MPa to 8 MPa (reproduced with permission from Eastwood, 1993).

As the viscosity of the heavy oil becomes high, the shear modulus becomes negligible. At low temperature (-12.5°C), a sharp shear-wave is detected because, at this temperature, oil is almost solid. As the temperature increases, both the bulk and shear moduli decrease almost linearly (Figure 3.11a). At a temperature of approximately 80°C the shear modulus approached zero (not shown in the figure). At room temperature, heavy oil supports shear waves, but as temperature increases, its shear modulus rapidly decreases until it becomes zero (Batzle et al., 2006).

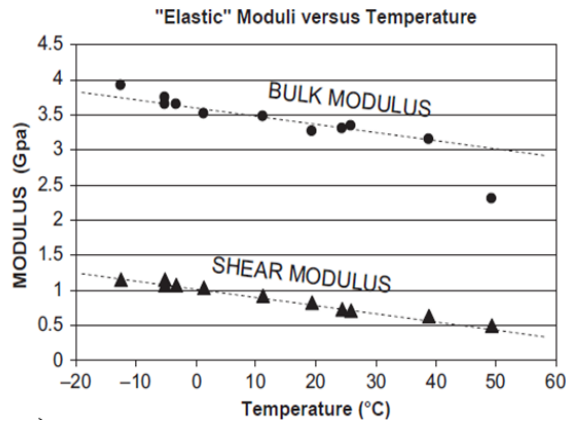


Figure 3-11: Plot of a) measured bulk and shear moduli in heavy oil samples at different temperatures (reproduced with permission from Batzle et al., 2006).

The seismic velocity is also affected by the fluid saturation changes in the rock. The effect of fluid substitution on the P-wave velocity of the fluid-saturated medium can be estimated (Jaeger et al., 2007):

$$V_P = \left[\frac{(K_{sat} + \frac{4}{3}G_{sat})}{\rho_{eff}} \right]^{1/2} \quad 3.14$$

where ρ_{eff} is the effective density and K_{sat} and G_{sat} are the effective bulk modulus and shear modulus of the saturated medium. The saturated elastic moduli can be estimated by using the Gassmann equation (Gassman & Smit, 1951).

$$K_{sat} = K_{dry} + \frac{\left(1 - \left(\frac{K_{dry}}{K_o}\right)\right)^2}{\frac{\phi}{K_{fluid}} + \frac{(1-\phi)}{K_o} \frac{K_{dry}}{K_o^2}}, \quad 3.15$$

where K_{dry} is the bulk modulus of dry rock, K_{fluid} is the bulk modulus of the pore fluid, K_o is the bulk modulus of the matrix, and ϕ is the porosity of the dry rock.

It is seen from the equation no 3.14 and 3.15 that the velocity of the medium will be inversely impacted by the fluid density and directly by the variation in the elastic moduli of the effective medium. The effect of fluid substitution on P wave velocity is shown in Figure 3.12. Increasing the water saturation in the rock will increase the effective density and bulk modulus. According to equation 3.14, the increase in effective density will decrease the velocity, whereas an increase in bulk modulus will increase the P-wave velocity. Figure 3.12 shows the effect of increasing the bulk modulus is dominant, thus results in a positive correlation between water saturation and P-wave velocity.

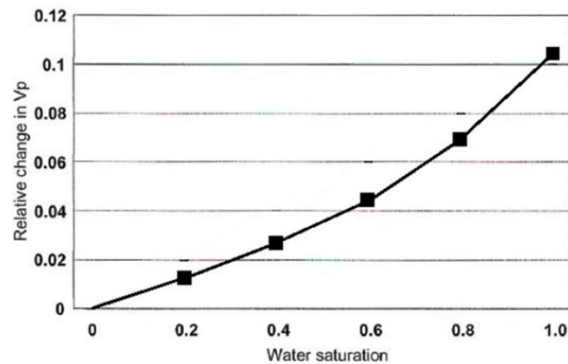


Figure 3-12: Plot showing the relation between water saturation changes and relative P-wave velocity (reproduced with permission from Brisco, (2018)).

Based on the above plots, I anticipate that

- Inside the reservoir, during steam injection, the temperature increases; therefore, the velocity will decrease. Whereas, during production, the reservoir cools down, increasing the P-wave velocity.
- Inside the caprock, the velocity remains the same as long the high temperatures do not reach the caprock. But, the velocity in the caprock may vary if 1) reservoir fluid leaks to the reservoir (increasing the P-wave velocity) or 2) if the caprock develops fractures during injection and production cycles (decreasing the P-wave velocity).

It is appropriate to anticipate that the temperature effects will be more dominant and important inside the reservoir interval, resulting in an increase in two-way time and impedance contrast. On the other hand, changes in the caprock will be primarily linked to induced stresses.

3.6 Shale brittleness

In addition to changes in heavy oil properties, the shale's brittleness is also important as it is likely to influence microseismic activity. The shales act as the caprock for heavy oil reservoirs, and their ability to fracture is of interest (King, 2010). The mechanical behavior of shale is important in hydraulic fracture stimulation, where brittleness indicates the ability to initiate and maintain long-term hydraulic conductivity (Schön, 2015). Brittle shales are more easily fractured than ductile shales. The brittleness index is used to differentiate different types of shales. Two types of criteria are used:

- A criterion based on shale mineralogy: The Brittleness index is calculated from the volume fraction of different minerals in the rock matrix (Rickman et al., 2008; Sondergeld et al., 2010):

$$\text{Brittleness index} = \text{Quartz} / (\text{Quartz} + \text{Carbonates} + \text{Clay}) \quad (3.14)$$

- A criterion based on Young's modulus and Poisson's ratio: Another way to characterize shales is to calculate the brittleness index from velocity and density logs. Shales with a Young modulus (E) > 34.5 MPa and Poisson ratio (ν) < 0.25 as brittle. A plot is usually plotted to separate the two types (Schön, 2015), as shown in figure 3.13.

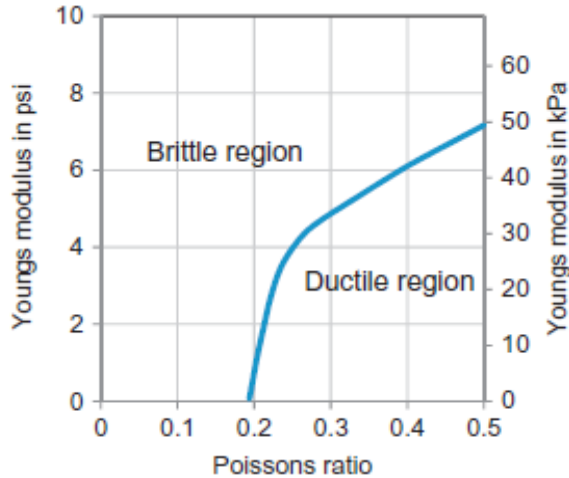


Figure 3-13: Plot of Young Modulus versus Poisson's ratio separating ductile and brittle regions (reproduced with permission from Grieser & Bray, 2007).

3.7 The expected response of reservoir-caprock due to steam injection

In response to steam injection, the reservoir and surrounding rocks experience a change in temperature (ΔT), pressure (Δp), and effective stresses ($\Delta \sigma'_{ij}$), resulting in shearing, dilation, and mechanical damage. Based on the key observations and learnings from the literature, a set of predictions is proposed, as illustrated in Figure 3.14. The schematic highlights the expected response of the caprock-reservoir system at high temperature and pressure during CSS.

When steam injection starts, several changes are expected; for example,

- I expect to observe surface uplift because steam injection at high temperature ($> 200^\circ\text{C}$) causes thermal expansion of the reservoir rock. Since the reservoir is shallow (depth 550m), the reservoir expansion will cause the overlying strata to elevate. This may be confirmed by analyzing the surface tiltmeter data, a ground-based heave measurement technique. Surface tiltmeters are traditionally used to monitor local deformation to understand the relationship between injection/production and resulting surface deformation (Maron et al., 2005; Maxwell et al., 2007; Walters & Zoback, 2013). I predict microseismic activity in the overburden instead of the reservoir during the steam injection cycles because of the induced stresses in the overlying brittle shales. The steam injection into the reservoir causes the reservoir to expand, exerting stress on the overlying shale. As the reservoir expands, new fractures may develop in the caprock, or faults/fractures may be reactivated. When this happens, microseismic

activity is recorded. The stress changes will also occur in the reservoir, but since shale is more brittle, I expect most of the microseismicity to be in the caprock. This brittle nature of the shale can be confirmed by calculating the brittle index using the velocity and density logs. Inside the reservoir, an increase in temperature is expected to decrease the velocity and density of the heated reservoir, thus decreasing the acoustic impedance. The decrease in acoustic impedance within the heated zone will result in a higher impedance contrast between the heated reservoir and the surrounding rock. This will cause the seismic reflection amplitude to increase. The decrease in velocity will impact the P-wave passing through the reservoir interval, thus increasing the two-way travel time (TWT). This is expected to be visible on the isochrone difference maps of the reservoir.

- Additionally, I do not anticipate changes in the seismic properties (amplitude and seismic arrival time) within the caprock interval because of minimal or no variation in rock physics properties. The steam is expected to stay within the reservoir interval unless there is 1) reservoir fluid leakage to the caprock altering the fluid saturation (increase in P-wave velocity) or 2) substantial fracturing/faulting (decrease in P-wave velocity), which are unlikely

Conversely, during the production cycle, the following changes are expected

- I expect surface subsidence during the production cycles because of the fluid (hydrocarbon and water) withdrawal from the reservoir. The extraction of fluid from the reservoir causes the reservoir to shrink, causing the overlying layers to drop, resulting in surface subsidence. Similar to surface uplift, surface subsidence is traditionally measured by placing tiltmeters on the surface.
- I expect microseismic activity in the overburden during production cycles because of the induced stresses. The induced stresses due to the fluid extraction, pore pressure reduction, and reservoir shrinkage may cause fracturing/faulting above the depleted reservoir in the overburden. This will result in the triggering of microseismic activity.

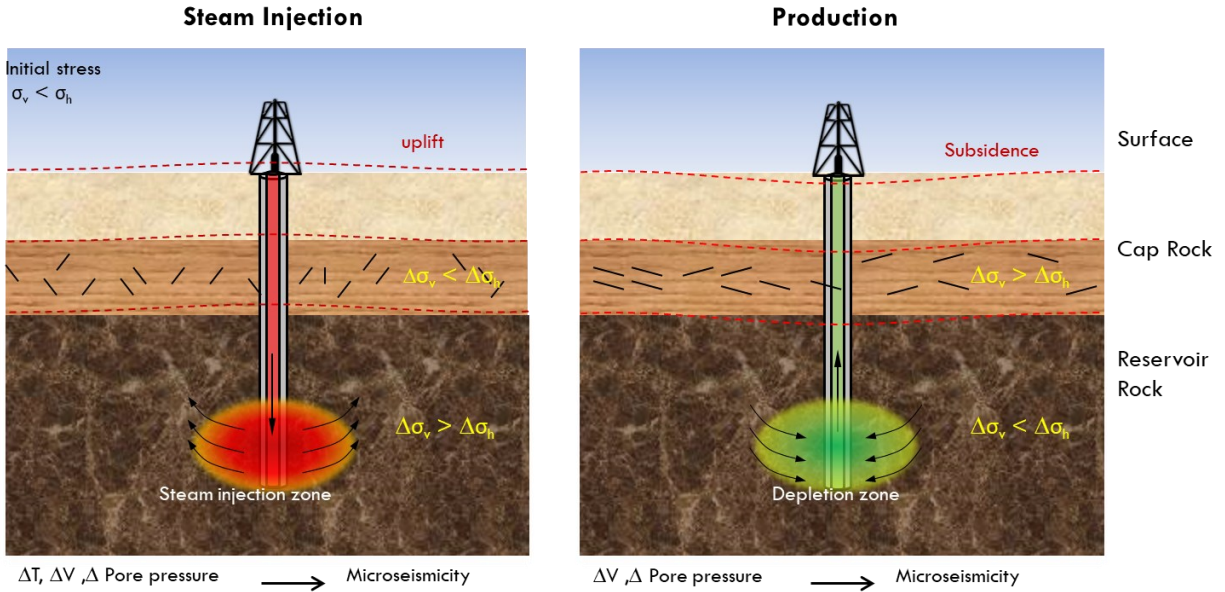


Figure 3-14: Showing stress changes (σ) in response to the pore pressure, temperature (T), and volumetric (V) changes during steam injection (left) and hydrocarbon production (right).

The above predictions will be validated by analyzing and interpreting the following geophysical data

- The first step is to analyze and interpret the recorded microseismic data recorded during the CSS experiment. The focus will be to examine the spatial and temporal trends of the microseismic data. These event locations are of key importance, as they will help validate or contradict the predictions. The above findings will be integrated with engineering data (pressure logs, injection, and production volumes) to differentiate injection and production-related microseismicity. This will help validate the prediction that microseismic may be recorded during injection and production cycles.
- The well log data (sonic and density logs) will be used to calculate the brittleness index to distinguish between brittle and ductile zones. The brittleness index will be compared with the depth trends of resulting microseismic events. This will help validate or contradict the prediction that the majority of the microseismic activity is expected to be in the overburden. It is expected to validate the depth trend of event locations.
- Next, time-lapse seismic reflection data will be used to analyze the seismic amplitude and reservoir isochrone difference between baseline and monitor surveys. This will

help validate the prediction that steam injection results in velocity reduction within the reservoir interval and no changes in the overburden.

- The surface tiltmeter data will be incorporated to examine any surface uplift and subsidence during steam injection and production, respectively. The surface uplift during injection will confirm the thermal expansion of the heavy oil reservoir, and surface subsidence will confirm reservoir contraction due to fluid production, thus validating the prediction.

3.8 Discussion

In this chapter, I have formulated a set of predictions to study the caprock-reservoir rock response to steam injection at high temperature and pressure. The schematic in figure 3.14 highlights some of the physical mechanisms and effects observed during the heavy oil recovery processes. The majority of these predictions agree with the fundamental mechanism argued by Dusseault & Collins (2010) and discussed in section 3.7. But, they do not incorporate the impact of higher temperature on rock physics properties. The temperature changes are also important and must be considered. The temperature change will alter the physical (density and velocity) and mechanical properties of the rocks (i.e., density, Young's modulus, Poisson's ratio, friction angle, and cohesion). For example, a temperature change can reduce the friction coefficient, resulting in the excitation of micro earthquakes (Miyazawa et al., 2008). The change in the P- and S-wave velocity is related to the changes in elastic properties of the pore fluid through Gassmann's equation. The model assumes that pore space is completely connected, and the rock is homogenous and isotropic. The Gassmann equations are most widely and commonly used to calculate seismic velocity changes due to different fluid saturations in the reservoir. This traditional technique cannot be applied to predict the moduli of rocks saturated with heavy oil, especially at low temperatures. At low temperatures, the heavy oil behaves like quasi-solid. The Gassmann model equation is inapplicable if the pore-filling material is a solid or a liquid whose shear modulus has a finite component. It has also been tested experimentally for a range of temperatures, and results indicate that as temperature decreases below 60°, heavy oil becomes dispersive and Gassmann estimates no longer match the data (Han et al., 2007). For the above reasons, I do not incorporate the Gassmann model to study the velocity changes in the reservoir. However, the Gassmann equations can model the fluid substitution in the caprock if there is fluid leaking into the caprock.

However, since I do not anticipate fluid leakage from the reservoir into the overburden rock, I ignore its application in this research study.

The predictions are based on the current scientific understanding of geomechanical processes (Dusseault, 2002; Dusseault et al., 2007; Dusseault & Collins, 2010) and established correlations between seismic properties and rock strength obtained from lab results (Batzle et al., 2006; Mavko et al., 1998). The predicted changes are limited to the geology of the study area and may need to be modified for different geology. For example, I anticipated microseismic activity in the overburden because caprock shales are more brittle than the heavy oil sand reservoir. The same may not be observed if the steam is injected into the carbonate heavy oil reservoir. For the carbonate reservoir, I expect a substantial amount of microseismic activity in the reservoir because carbonate is more brittle than the heavy oil sands. In addition, the prediction of surface uplift due to reservoir dilation is dependent on the depth of the reservoir. It will be obvious if the reservoir is shallow (<600m), as in the study area. However, if the reservoir is deep (>1000m), the reservoir will still experience thermal expansion but most of it will cause the overburden rock to compress, thus limiting the impact on the surface.

Some of these changes (surface subsidence, induce microseismicity, and velocity slowness) have been previously analyzed by several authors (Maron et al., 2005; Maxwell et al., 2007). However, what is novel in this study is the integration of the observations from multidisciplinary data to link these expected changes to the physical processes. The validation or contradiction of these predictions will improve the current understanding of the geomechanical processes and will reveal the complicated response of the seemingly simple CSS operation

3.9 Summary

This chapter summarizes the principles and physical mechanisms that may be observed during a thermal recovery process. The following changes are expected

- The effect of increased pressure and temperature during steam injection reduces the heavy oil's viscosity, thus easing the production from the reservoir.
- The effects of temperature and pressure extend beyond the reservoir interval and alter the stresses within and surrounding the reservoir interval during injection and production cycles.

- The rock above the reservoir is likely to experience shearing due to stress redistribution. However, shearing in the overburden is not desirable and may cause a caprock breach or well casing failure.
- The subsurface changes may result in surface uplift and subsidence during steam injection and hydrocarbon production, respectively. Substantial uplift or subsidence can result in containment challenges.

A better understanding and monitoring of thermal recovery processes can be made possible by incorporating several types of geophysical data, including but not limited to time-lapse seismic, well data, microseismic data, engineering data (production, injection, and temperature recordings), and surface tiltmeter data.

4 The impact of acquisition parameters and location techniques on microseismic event locations

4.1 Introduction

The microseismic acquisition involves continuous monitoring of passive seismic by placing geophones on the surface or in the borehole. The geophones may be mounted in several different possible configurations and are mostly deployed in the borehole. A range of different downhole recording geometries is used to monitor hydrocarbon reservoirs and hydraulic fracturing. These geophones can be installed permanently or temporarily, depending on the project's scope (Maxwell, 2014).

The common objective of any microseismic monitoring study is to obtain accurate locations of the microseismic events both in space and time. A microseismic event originates at an unknown time and location. In downhole monitoring, the determination of microseismic event locations may be viewed as an optimization problem, where the hypocenter is defined as the point with the minimum difference between observed and theoretical parameters (e.g., (Lee et al., 1981; Lee & Lahr, 1972)). It is achieved by arrival-time inversion (Gibowicz, 1994; Maxwell, 2014). The method involves minimizing the P- and/or S-wave arrival time differences at each sensor through a grid search (Prugger & Gendzwill, 1988) or linear iterative strategy (Geiger, 1912). The least-square solution can be used to determine microseismic locations for different geometries, including vertical, horizontal, deviated, and multiwell arrays, by inverting only P- (P-wave difference method) or P- and S-wave arrival times (P-S wave difference method) (Zhou et al., 2015).

In this study, I investigate uncertainties in the estimated locations of microseismic events by two commonly used location methods, using data from a geophone array placed in a single deviated borehole, using a grid search optimization procedure. The objective is to evaluate each method and select the one which results in the least location uncertainty for a deviated borehole geometry. The selected method is then used in the next chapter to locate microseismic events from the heavy oil monitoring experiment (Chapter 2). The analysis is further extended to investigate location uncertainties given various acquisition parameters, e.g., receiver array orientation (vertical or deviated), length of the array, and receiver density.

4.2 How events are located - Theory

For microseismic borehole surveys, most localization procedures require knowledge of P and S- wave arrival times and azimuth and dip information to compute event locations. In this study, I use a grid search to invert for the source location. First, a theoretical lookup table is calculated, given a velocity model. Each point in the table is denoted by X and defined by (x, y, z, t_p, t_s) , where t_p and t_s are the predicted P- and S- wave arrival times, and θ is the source azimuth. The x , y , and z are the easting, northing, and depth of the potential source location, respectively. A grid search then compares the differences between observed and predicted travel times for all receivers recording a specific event to determine the most likely source location. The following equation obtains the maximum likelihood estimate for the source location \mathbf{x}

$$P(X = \mathbf{x}|t_{p,obs}) = \exp^{-\frac{1}{2} \sum_{n=1}^N \frac{(t_{cal,n} - t_{obs,n})^2}{(\sigma_p^2 + \sigma_s^2)}}, \quad (4.1)$$

where N is the total number of receivers, t_{cal} and t_{obs} are theoretical and observed S - P arrival times at each receiver in the receiver array. P is the non-normalized probability density function (PDF) for the hypocenter location and σ_p and σ_s are the uncertainty in P- and S- wave arrival time picks.

Inversion based on travel times alone may not lead to unique solutions for geophones in a single well. Hence, in addition to travel time, source azimuth and incidence angle may also be needed to constrain the source location (Bayer et al., 2012). Both additional variables are usually estimated from polarization analysis of the P-wave arrival of the three-component data using covariance analysis. The auto and cross-variance of three-component data U_x , U_y , and U_z containing N_s time samples can be obtained from

$$C_{ij} = \frac{1}{N_s} \sum_{s=1}^{N_s} U_i(s) U_j(s), \quad (4.2)$$

where i and j are the component indices, and s is the index variable for a time sample. N_s is the total number of samples in the analysis window. The real-valued and symmetrical covariance matrix can then be written as

$$\mathbf{C} = \begin{pmatrix} C_{xx} & C_{xy} & C_{xz} \\ C_{xy} & C_{yy} & C_{yz} \\ C_{xz} & C_{yz} & C_{zz} \end{pmatrix}. \quad (4.3)$$

The covariance matrix \mathbf{C} represents the polarization ellipsoid with the best fit to the real data. The three eigenvalues $\lambda_1 \geq \lambda_2 \geq \lambda_3$ and corresponding eigenvectors $\bar{p}_1, \bar{p}_2, \bar{p}_3$ of the matrix \mathbf{C} are associated with the principal axes of the polarization ellipsoid. Azimuth, incident angle, and linearity are calculated from the eigenvalues and eigenvectors. The directional cosine of the first eigenvector corresponding to the largest eigenvalue defines the azimuth θ , given by

$$\theta = \text{atan} \left\{ \frac{p_1(y)}{p_1(x)} \right\}, \quad (4.4)$$

where azimuth (θ) is measured counterclockwise from the positive x-axis being the east direction (Bayer et al., 2012). $p_1(x)$, $p_1(y)$ and $p_1(z)$ are the x, y, and z components of the largest eigenvector p_1 .

Linearity (L) relates all three eigenvalues by $\left(\frac{\lambda_2 + \lambda_3}{2\lambda_1} \right)$. L ranges between zero and one; it is one for a perfectly linearly polarized wave and zero for an elliptically polarized wave.

The apparent incident angle can be given as

$$\phi = \text{atan} \left\{ \frac{p_1(z)}{\sqrt{[p_1(x)^2 + p_1(z)^2]}} \right\}. \quad (4.5)$$

It is zero for horizontal polarization and is defined to be positive in the positive z-direction. It defines the largest eigenvector orientation when combined with the azimuth (Bayer et al., 2012). The linearity and apparent incident angle will not be used further but are only mentioned here to define the complete covariance analysis.

A more accurate event location can be derived using a combined analysis of arrival times (S-P wave arrival time) and polarization parameters (source azimuth) by examining the likelihood of each trial location by the following methods:

4.2.1 P- wave method

The maximum likelihood may be estimated by minimizing the observed and predicted P-wave arrival times and azimuths for all combinations of receiver pairs. It is the most commonly used method when only a single phase is picked. The non-normalized probability density function

P for the grid point X to be the source location \mathbf{x} for the observed time $t_{p,obs}$ and azimuth θ_{obs} is calculated as follows

$$P(X = \mathbf{x}|t_{p,obs}, \theta_{obs}) = \exp\left(-\frac{1}{2}\left(\sum_{n=1}^N \frac{(\Delta t_{p,obs}^n - \Delta t_{p,cal(X)}^n)^2}{2\sigma_p^2} + \sum_{n=1}^r \frac{((\sin(\theta))_{obs}^n - (\sin(\theta))_{cal(X)}^n)^2}{2\sigma_{\sin(\theta)}^2}\right)\right) \quad (4.6)$$

where σ_p and $\sigma_{\sin(\theta)}$ are the relative uncertainty in P- wave arrival times and azimuth respectively, n is the number of observation ranging between 1 to N and r , N is the total number of observations defined as $(r(r-1)/2)$, r is the total number of receivers, $\Delta t_{p,obs}^n$ and $\Delta t_{p,cal(X)}^n$ are differential P- wave observed and predicted arrival times between two receivers, $(\sin(\theta))_{obs}^n$ and $(\sin(\theta))_{cal(X)}^n$ are observed and predicted source azimuth differences at every receiver. The azimuth is in radians in the above equation.

4.2.2 P-S wave method

An alternative is to compare the predicted and observed S-P wave arrival times and azimuths at each receiver in the array. The probability density function is then given by

$$P(X = \mathbf{x}|t_{sp,obs}^n, \theta_{obs}^n) = \exp\left(-\frac{1}{2}\left(\sum_{n=1}^r \frac{(t_{sp,obs}^n - t_{sp,cal(X)}^n)^2}{\sigma_p^2 + \sigma_s^2} + \sum_{n=1}^r \frac{((\sin(\theta))_{obs}^n - (\sin(\theta))_{cal(X)}^n)^2}{\sigma_{\sin(\theta)}^2}\right)\right), \quad (4.7)$$

where σ_p , σ_s and $\sigma_{\sin(\theta)}$ are the uncertainties in P-, S- wave arrival times and azimuths, respectively, n is the number of observations ranging from 1 to r , r is total the number of receivers, $t_{sp,obs}^n$ and $t_{sp,cal(X)}^n$ are observed and predicted S-P wave arrival times and $(\sin(\theta))_{obs}^n$ and $(\sin(\theta))_{cal(X)}^n$ are observed and predicted azimuth differences at the n^{th} receiver.

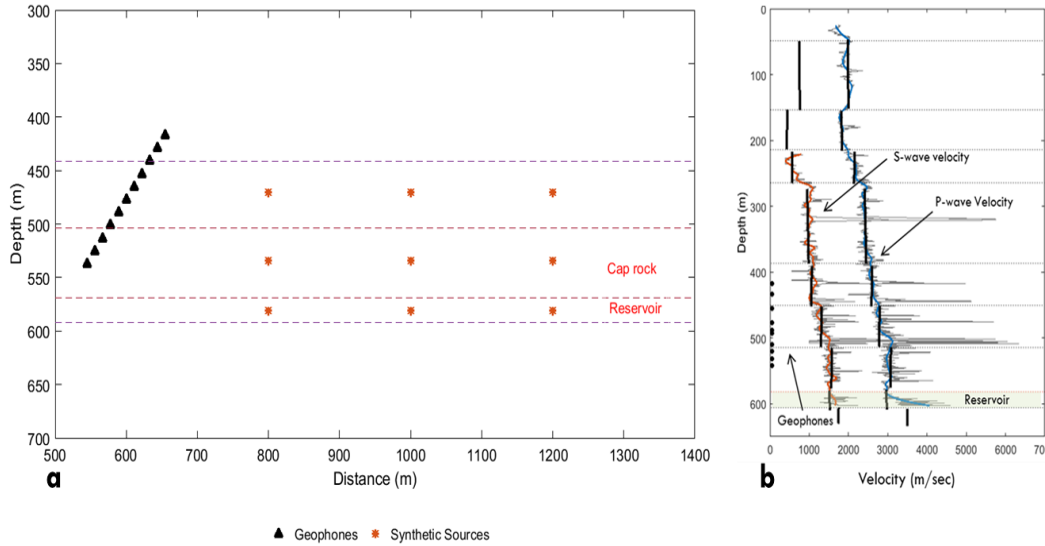


Figure 4-1: Showing (a) Acquisition geometry used for the synthetic study, red stars are the synthetic sources, and black triangles are geophones, and (b) P- and S wave velocity model of the study area.

4.3 Synthetic Test

Two simple synthetic tests are designed to investigate location uncertainty resulting from different location methods and acquisition geometries.

4.3.1 Test 1: Comparison of location method

Test 1 is designed to critically assess the hypocenter solution obtained by each of the two location methods (P-wave method and P-S wave method), recorded by a single geophone array placed in the deviated borehole. The monitoring setup of the heavy oil experiment (described in Chapter 2) is duplicated. A total of eleven 3C geophones are lowered in the borehole between 460 and 535 m depth, as shown in Figure 4.1a. The synthetic sources are intentionally placed at different depths (caprock and reservoir) and distances from the monitoring well, to thoroughly understand the uncertainty at different levels. Theoretical arrival times are calculated using a 1D velocity model of the area generated from P- and S- wave sonic logs (Figure 4.1b). The test first evaluates the methods using a single deviated borehole by calculating the non-normalized PDF using equations 4.6 and 4.7 and Monte Carlo simulations. The time and azimuth uncertainties are set to be 1 msec and 5 degrees, respectively. The uncertainty values are based on published work by Rutledge & Phillips (2003) and Eisner et al. (2011). The Monte Carlo analysis is performed by perturbing data (arrival times and azimuths) and inverting for event locations. The procedure is repeated 100 times.

The analysis is extended by adding another well 900 m away from the first well to evaluate the performance and limitations of each method for a multi-well monitoring setup.

4.3.2 Test 2: Impact of acquisition geometry on the location uncertainty

The second test is designed to inspect the influence of different acquisition parameters on location uncertainty by analyzing the non-normalized PDF of the location method selected from test 1 to evaluate the impact of

- Length and orientation of the receiver array
- Receiver density (number of receivers)

The test is expected to help understand the efficiency of the acquisition setup (single deviated borehole) compared to a vertical borehole.

4.4 Results

4.4.1 Comparison of the location methods

Figure 4.2 illustrates how the P- and P-S wave methods constrain estimated event depths and distances from a deviated well. The location uncertainty in the radial direction is largest for the P-wave method (Figure 4.2a) and is significantly reduced for the P-S wave method (Figure 4.2c). This is supported by comparing the size of the uncertainty in the cross-sectional view (Figures 4.2b,d). The perturbed event locations from the Monte Carlo simulation are plotted on the non-normalized PDF as solid red circles (Figure 4.3(a-d)). It is interesting to note that the event cloud overlaps the non-normalized PDF, indicating that location uncertainty calculated by PDF and Monte Carlo simulation are in good agreement with each other. The resulting locations form a cloud that defines the location uncertainty due to the arrival times and azimuth for each location method (Figure 4.3(a-d)). These event locations are expected to sample the random location uncertainty resulting from the input data uncertainties (Maxwell, 2009). The visual inspection of the shape and size of the PDF and Monte Carlo simulation indicate that the P-S wave method results in more accurate event locations compared to the P-wave method for a single borehole geometry.

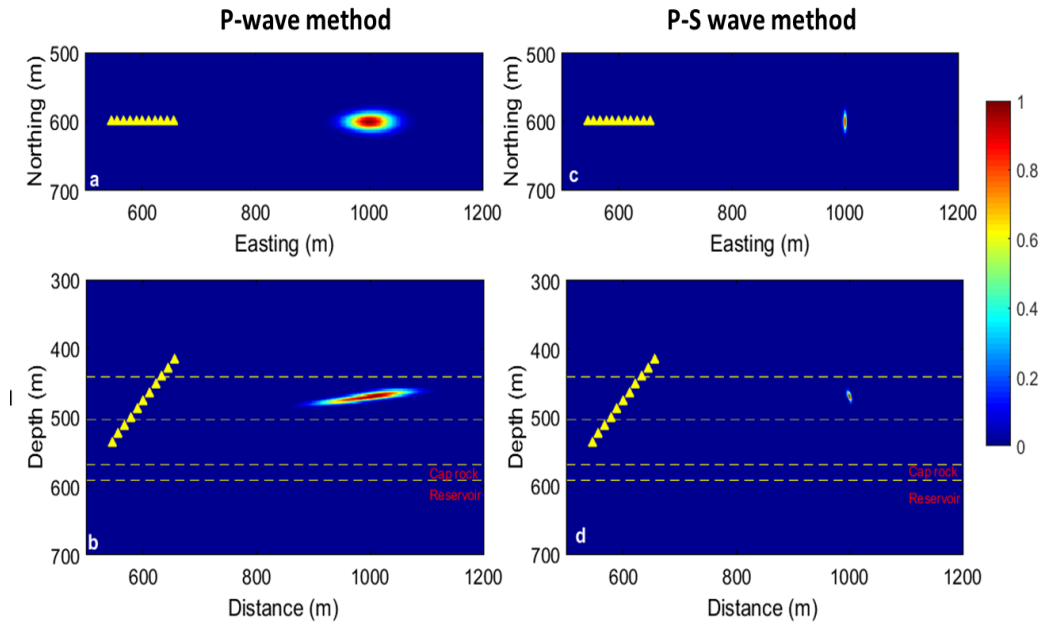


Figure 4-2: Map view (top) and a cross-sectional view (bottom) shows location uncertainties for downhole geophone array using the P-wave and P-S wave methods. The event is located approximately 400 m away from the center of the receiver array. Yellow triangles mark receivers.

Figure 4.4 a-b shows the Monte Carlo locations using the P-wave (blue circles) and P-S wave methods (red circles) for a deviated borehole with true events at different distances. The inclined trend and larger spread of blue events are apparent. The size and shape of the event clouds around the true location (black star) indicate that the P-S method results in more certain event locations than the P-wave method. The improvement in Monte Carlo locations is evident for both methods, particularly for dual well acquisition geometry (figure 4.4 b-c). The event cloud is much smaller and less scattered, indicating that location uncertainty is reduced when a dual well configuration is used. Nevertheless, a comparison of Figures 4.4 (a-b) and 4.4 (c-d) indicates that the P-S wave method still results in more certain locations. Figure 4.5 displays the summary of the resulting event location uncertainty for different location methods by varying errors in time and azimuth for single and multiple monitoring arrays. It is evident that the P-S wave method results in the least location uncertainty irrespective of the number of wells recording the event. Another obvious observation from the plots is that the P-wave method always results in maximum event location uncertainty in the radial/horizontal direction, as shown by the solid blue line in Figure 4.5 a-b.

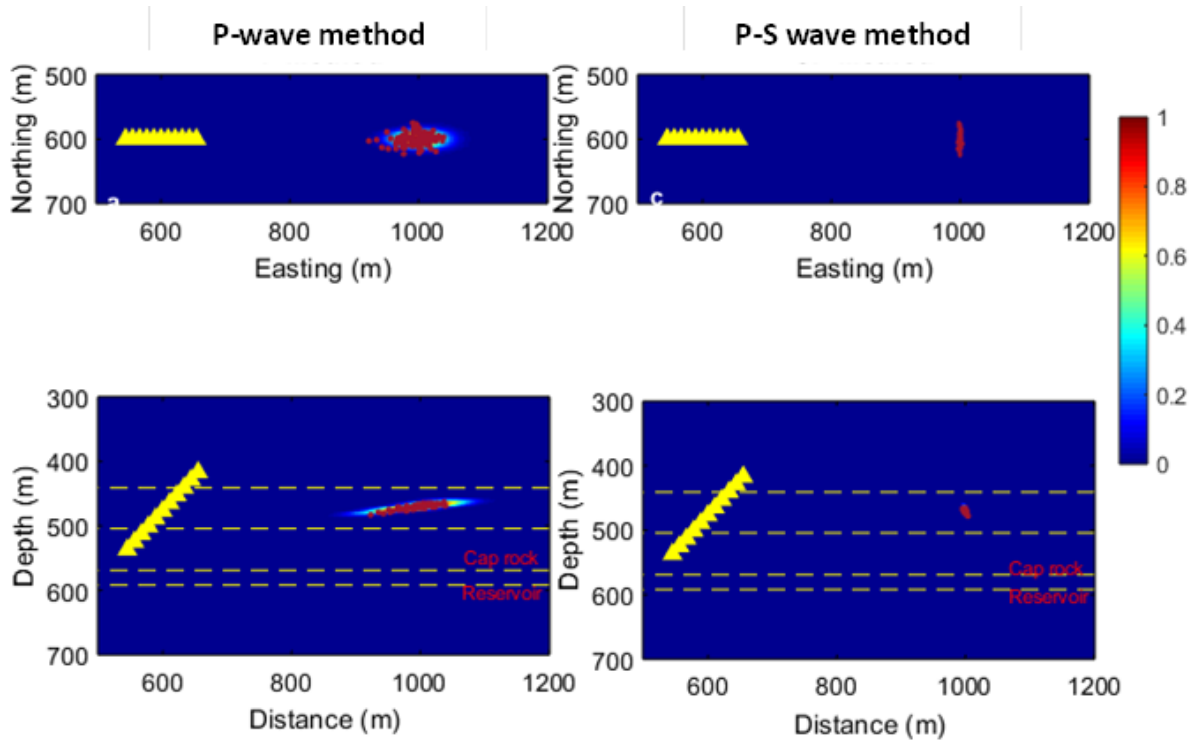
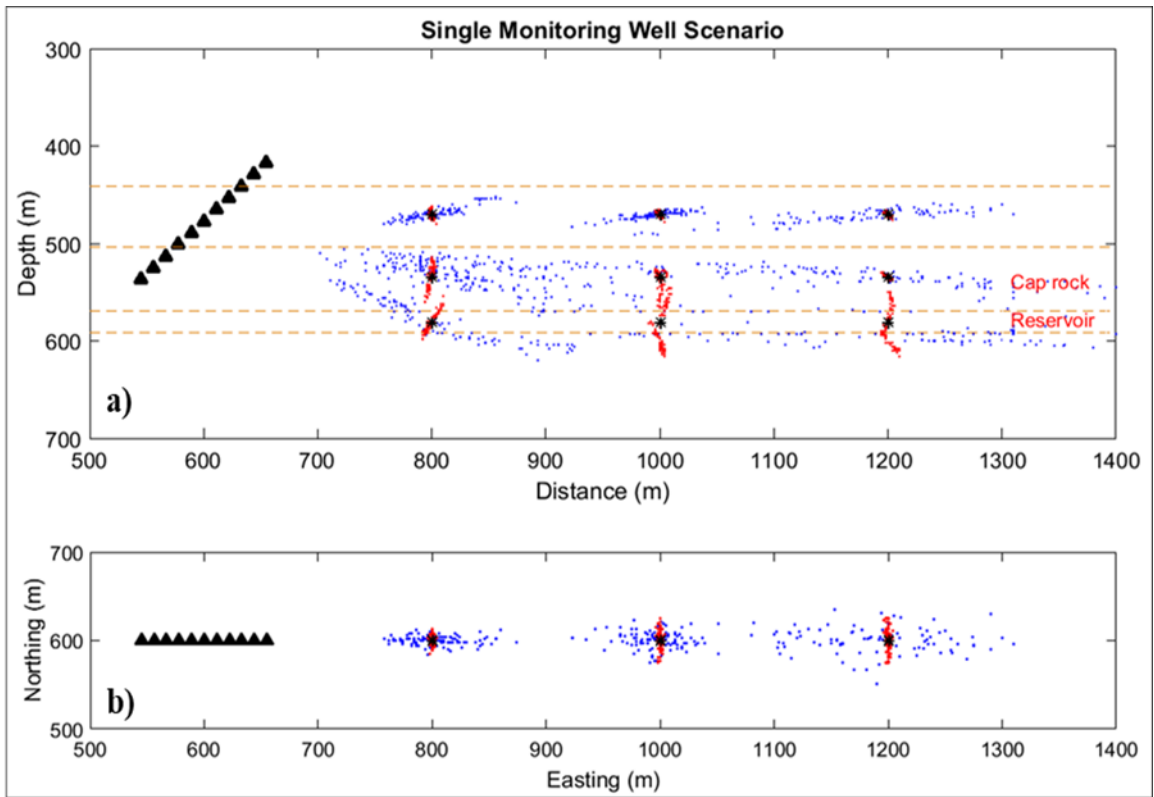


Figure 4-3: Map (top) and cross-sectional (bottom) view show location uncertainties using the P-wave and P-S wave methods. The perturbed event locations shown in red are obtained from the Monte Carlo analysis.



▲ Geophones - - - Geological Interface * Synthetic Sources · P-wave Method · P-S wave Method

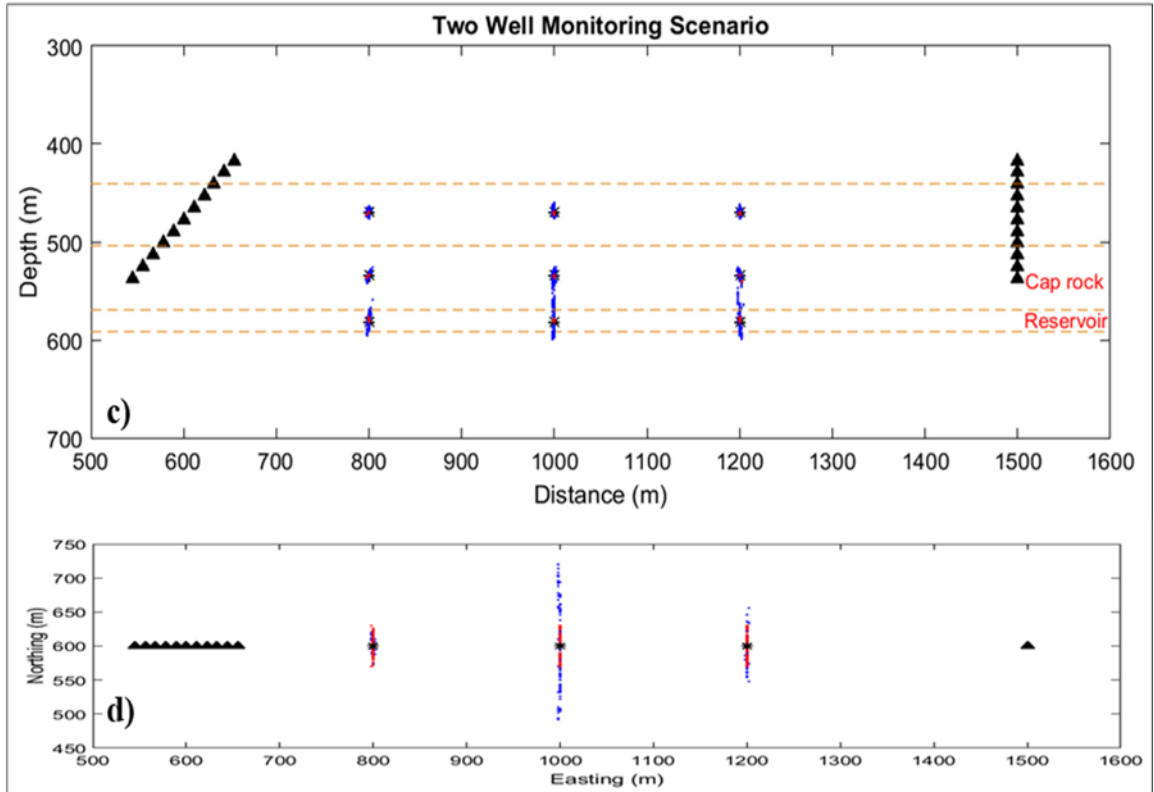


Figure 4-4: Monte Carlo locations estimated for a single well (a-b) and dual well configuration (c-d) by using the P-wave and P-S wave methods. True, P-wave and P-S wave method Monte Carlo locations are denoted as the black star, blue, and red circles, respectively. The top figure (a-b) shows that perturbed event locations are much closer to the true event location when located using the P-S wave method in both the radial (a) and vertical direction (b) as compared to the P-wave method. However, (c-d) shows improvement in perturbed event locations by using multiple monitoring arrays.

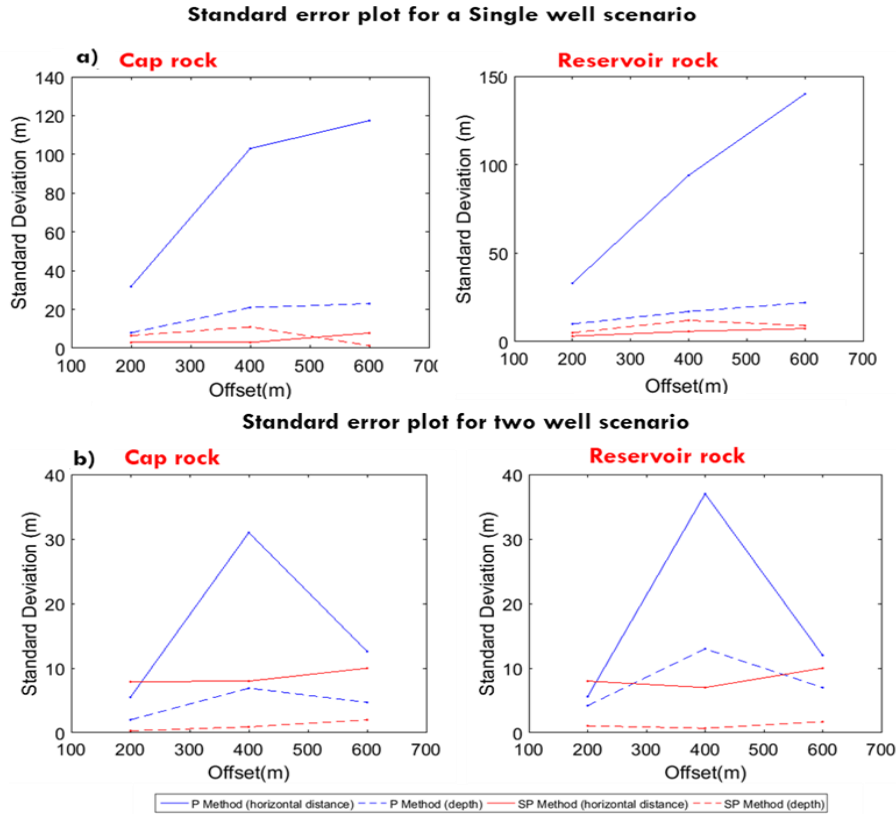


Figure 4-5: Standard deviation in Monte Carlo locations for events located in the caprock and reservoir interval for (a) single well and (b) two well-monitoring scenario estimated from P- and P-S wave methods. The RMS is plotted separately for caprock and reservoir rock. The x-axis is the distance between source and receiver, and the y-axis is the standard deviation. The blue and red lines show standard deviation in the P- and P-S wave methods, in the radial (solid) and vertical (dotted line) direction.

4.4.2 Impact of acquisition geometry on location uncertainty

Figure 4.6 illustrates how well an array of geophones constrains location depth and distance with varying array length. The location uncertainty is largest in the vertical direction and shorter array does not constrain locations well (Figure 4.6 a-c). The lateral distance of the located events is minimally affected, as indicated by the non-normalized PDF's size, shown in the map view of Figure 4.6 (a-c). Location uncertainty is smallest when the geophone array is deployed in the

deviated borehole instead of the vertical one (Figures 4.6 a & b). This indicates that the length and orientation of the geophone array strongly control the depth uncertainty.

Figure 4.7a-c illustrates the shape and size of the uncertainty for an event located using different receiver densities; note the increase in the size of the location uncertainty from left to right in the map (top) and depth views (bottom). The uncertainty is largely impacted in the radial direction and barely in terms of depth.

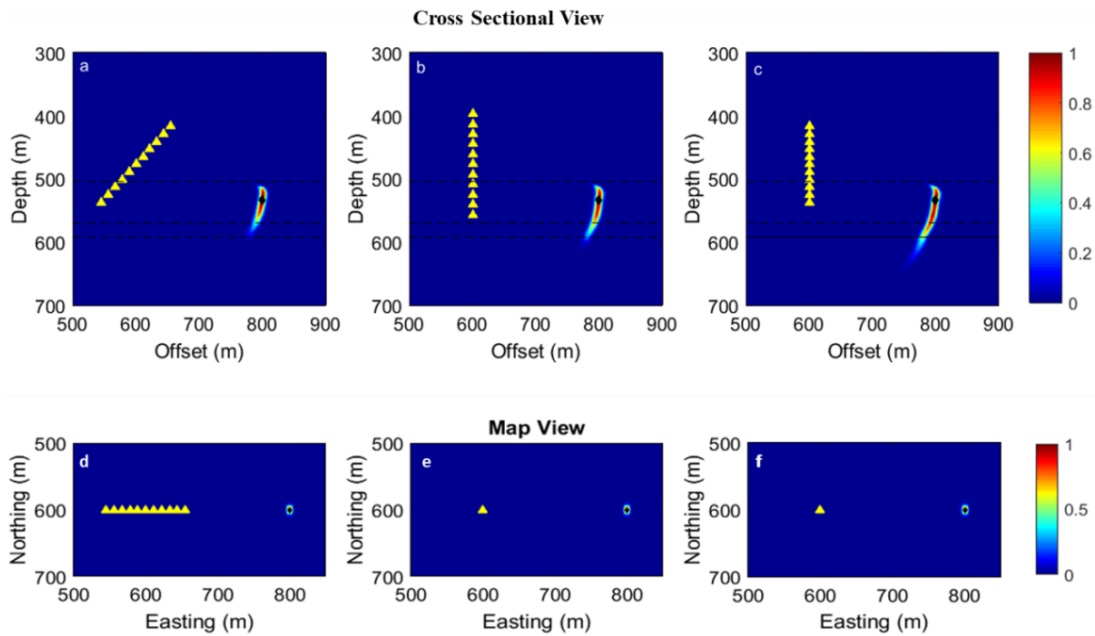


Figure 4-6: Calculated PDF for 140m long geophone array placed in (a,d) deviated borehole, (b,e) vertical borehole, and (c,f) 100m long array in a vertical borehole, in cross-sectional (top row) and map view (bottom row). A solid black circle shows the true source location, and yellow triangles are the receivers.

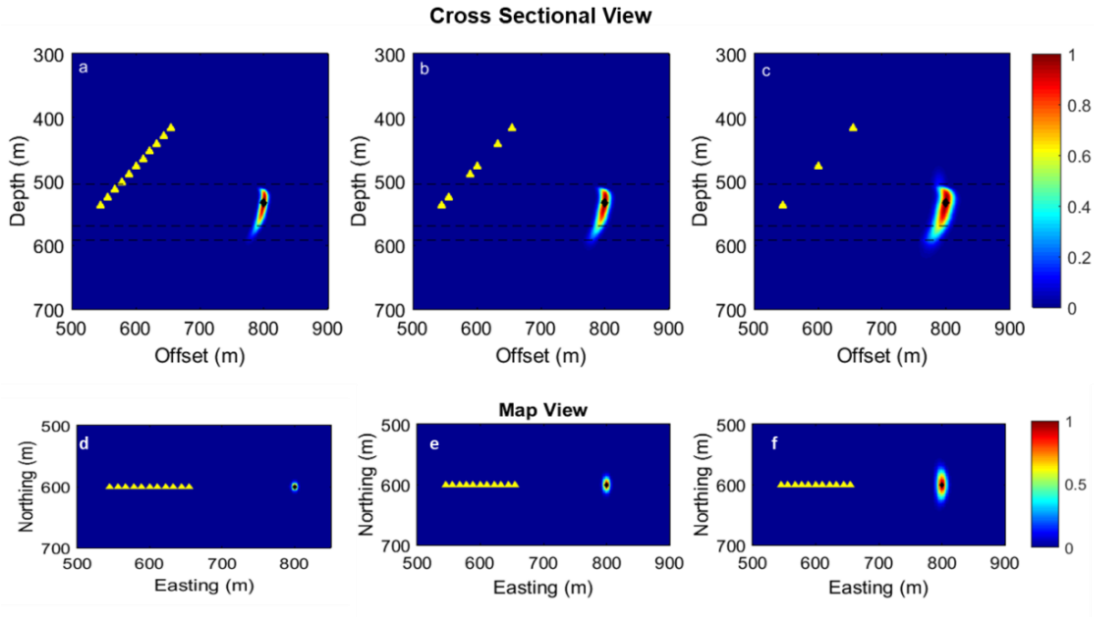


Figure 4-7: Calculated PDF for the event recorded by 140m long geophone array placed in a deviated borehole containing (a,d) eleven receivers, (b,e) six receivers, and (c,f) three receivers in cross-sectional (top) and map view (bottom). A solid black circle shows the true source location, and yellow triangles are the receivers.

4.5 Discussion

The study highlights the impact of two location algorithms on resulting location uncertainty for a single deviated monitoring borehole. The analysis is further extended to include the impact of different acquisition parameters (e.g., array orientation length and receiver density). My findings indicate that for a single deviated borehole array, the most accurate event locations are obtained when the P-S wave method is used to locate microseismic events instead of the P-wave method. The P-S wave method leads to closely clustered locations as predicted by both the PDFs and Monte Carlo simulation for both single and multiple receiver arrays.

The P-wave method determines event locations by incorporating the P-wave difference between every receiver pair. The receivers are closely spaced (10 to 20m apart). The resulting arrival time differences for each receiver pair are between 1 to 4ms. This is comparable to the commonly assumed picking error (1 to 2ms), which introduces a large uncertainty in the resulting event locations. On the contrary, the P-S wave method compares the S-P wave arrival time at each receiver rather than between each receiver pair. The S-P wave arrival times (40 to 50ms) are much higher than the assumed picking errors (1 to 2ms); thus, the resulting locations are better constrained.

Similar results are found by Zhou et al. (2015) and Maxwell (2009), demonstrating that it is difficult to locate microseismic events using only the P-wave phase in borehole monitoring because of the narrow aperture of the receiver array. However, this is not the case in surface microseismic monitoring (Chmiel & Bardainne, 2014) and earthquake seismology (Spence, 1980). The P-wave method has been successfully used to obtain the event location. The surface microseismic data is usually acquired using only vertical sensors because using 3C sensors increases the operation cost. This leads to using only P-wave to estimate the relative event location (Chmiel & Bardainne, 2014).

Similarly, in earthquake seismology, the P-wave difference method has been used successfully (Poiata et al., 2016; Ruiz et al., 2017; Spence, 1980), and many scientists have contributed to the P-wave method (Font et al., 2004; Geiger, 1912; Jones et al., 2014; Thurber & Engdahl, 2000; Zhou, 1994). The above is possible because geophones are placed on the surface in a pattern leading to a wider receiver aperture. This suggests that the accuracy of the P Method is dependent on the acquisition setup.

The findings from the second synthetic test suggest that location uncertainty is also controlled by the length of the receiver array, receiver density, and the orientation of the array. For a single borehole geometry, events are best constrained in the depth direction when the array is placed in a deviated borehole due to the wider aperture of the array compared to the vertical array. Thus, the above findings add to the understanding by Eisner et al. (2009), that only the length of the geophone array controls the depth resolution. The second synthetic test also indicates that location event uncertainty in the vertical direction is affected by geophone density in the array.

The above findings are of particular importance when planning/designing the acquisition geometry of the monitoring experiment. These findings give insight into several factors controlling the location uncertainty, especially for a deviated borehole geometry. The results from the synthetic study above help in quantifying the potential uncertainty associated with location methods and acquisition geometries for the study area. The P-S wave method is used in the next chapter to locate the microseismic events recorded over the heavy oil field.

The results presented in the chapter are based on the 1D isotropic velocity model and specific for the study area acquisition geometry. However, the analysis can be easily extended to evaluate/compare different acquisition geometries and parameters or incorporate a more sophisticated velocity model. The described modeling strategy helps to assess and select the right

location procedures to obtain accurate event locations. This is important during pre-survey planning to make recommended changes to obtain better event locations. If it is not possible to modify the acquisition geometry due to operational or financial constraints, then the methodology leads to an increased understanding of expected location uncertainties and hopefully avoiding incorrect interpretation of the calculated event locations.

4.6 Conclusion

In this chapter, the impact of event location methods and acquisition geometry on event location uncertainty is investigated. With the use of a simple synthetic example, it is illustrated how simple factors such as choice of location algorithm and acquisition parameters (array length, orientation, and geophone density) can introduce errors into the resulting event location. My analysis indicates the following:

- The P-S wave method is found to be preferable for the heavy-oil acquisition geometry. The P method appears to work well only when a good spatial coverage of geophones is present.
- The length and spatial spread of the receiver array control the depth accuracy. In contrast, the density of the receiver array highly impacts the location uncertainty in the radial direction but less so depth uncertainty.

5 Microseismic event locations and quality control workflow for Peace River data

5.1 Introduction

The first and most critical step in microseismic monitoring is to locate microseismic events accurately, both in time and space (Castellanos & van der Baan, 2012; De Meersman et al., 2009). Once accurate event locations are determined, a detailed analysis may be performed to understand and image the reservoir. These locations are commonly obtained by assuming a velocity model and minimizing the difference between the observed and predicted arrival times (Jones et al., 2010). Travel times suffice to locate earthquake hypocenters, but location methods adopted from earthquake seismology need more consideration before applying microseismic data because of substantial differences in acquisition configurations. Microseismic data are mostly recorded by a single array of geophones, unlike global seismology, where geophones are widely spread spatially (Jones et al., 2010). This forces the user to incorporate P- wave polarization information to constrain locations (De Meersman et al., 2009). There is also a 180° degree uncertainty in the resulting locations and may be removed if more than one monitoring array records the data, which is not common in microseismic monitoring experiments. Thus, extra constraints and attention are needed to remove the 180° degree uncertainty in event locations. Another important yet mostly overlooked procedure is the quality assessment of event locations and input data.

This chapter describes a complete workflow, including the processing of microseismic data and quality control of event locations. In the beginning, the 180° degree azimuthal uncertainty is removed by incorporating the spatial distribution of geophones placed in the deviated borehole. Then, the hypocenter location is obtained by inverting the S-P wave arrival times in a grid search manner. Next, I incorporate a combination of simple but effective strategies to quality check the results. I then apply the complete workflow to a data set recorded during the steam injection experiment over four years (2002-2005), as mentioned in chapter 2.

5.2 Event Location Workflow-Theory

Figure 5.1 summarizes the complete location workflow implemented in this study. The processes can be broadly divided into six steps: 1) data pre-processing, 2) arrival time picking, 3) P-wave polarization analysis, 4) removal of 180° uncertainty in azimuthal measurements, 5) event location, and 6) quality control of the event locations.

Step 1: Data Pre-processing

Microseismic data may be acquired on the surface or downhole using 3C geophones. The 3C geophone has two horizontal and one vertical component. When the tool is lowered down in the borehole, it rotates and tilts. This happens because it is not operationally possible to avoid the tool rotation and the deviation of the drilled borehole. The vertical component is affected by the well deviation. In contrast, the horizontal components are affected by rotation and well deviation, and recorded data must be corrected before processing. It is desirable to have the z-component vertically aligned and two horizontal components parallel to East and North directions. First, a correction is applied to account for well inclination by incorporating the well deviation survey. Next, the true position of horizontal components (h1 and h2) is determined by calculating the true azimuth of P-wave polarization relative to the North using a perforation shot (with known source position often called calibration shot). It is usually repeated for all the calibration shots, and the average rotation angle is calculated. The trace data is rotated, such that the h1 component is parallel to the East, and the h2 component is parallel to the North.

Raw data was mean corrected to remove any DC component; this is achieved by subtracting the mean from the data. The data are then filtered to reduce the noise; a bandpass filter is normally applied.

Step 2: Arrival time picking

Accurate phase picks are necessary for correct event locations as errors in arrival time picks have been identified as a major factor controlling location quality (Pavlis, 1986). Picking is often done manually for earthquake seismology. However, microseismic monitoring in the oil and gas industry collects and stores a large amount of data. Therefore, several automated procedures and tools have been developed to handle large data set and add consistency to the processes. Some of these techniques include; short-term average/long term average (STA/LTA) (Allen, 1978), envelope functions (Baer & Kradolfer, 1987), neural networks (Gentili & Michelini, 2006), and autoregressive methods (Rastin et al., 2013; Sleeman & Eck, 1999).

The most commonly used procedure is that by Earle & Shearer (1994). It compares the short-term average and long-term average of the signal. However, the method is inconsistent in placing the pick on the waveform, e.g., first break or peak and trough. Another picking procedure uses an iterative semi-automated method where a pilot trace is generated and is correlated with individual

waveforms, thus removing any phase lags (De Meersman et al., 2009; Rowe et al., 2002). However, this method can only be applied once the initial phase is picked. Irrespective of which method is applied, manual scanning and adjusting the picks cannot be ignored.

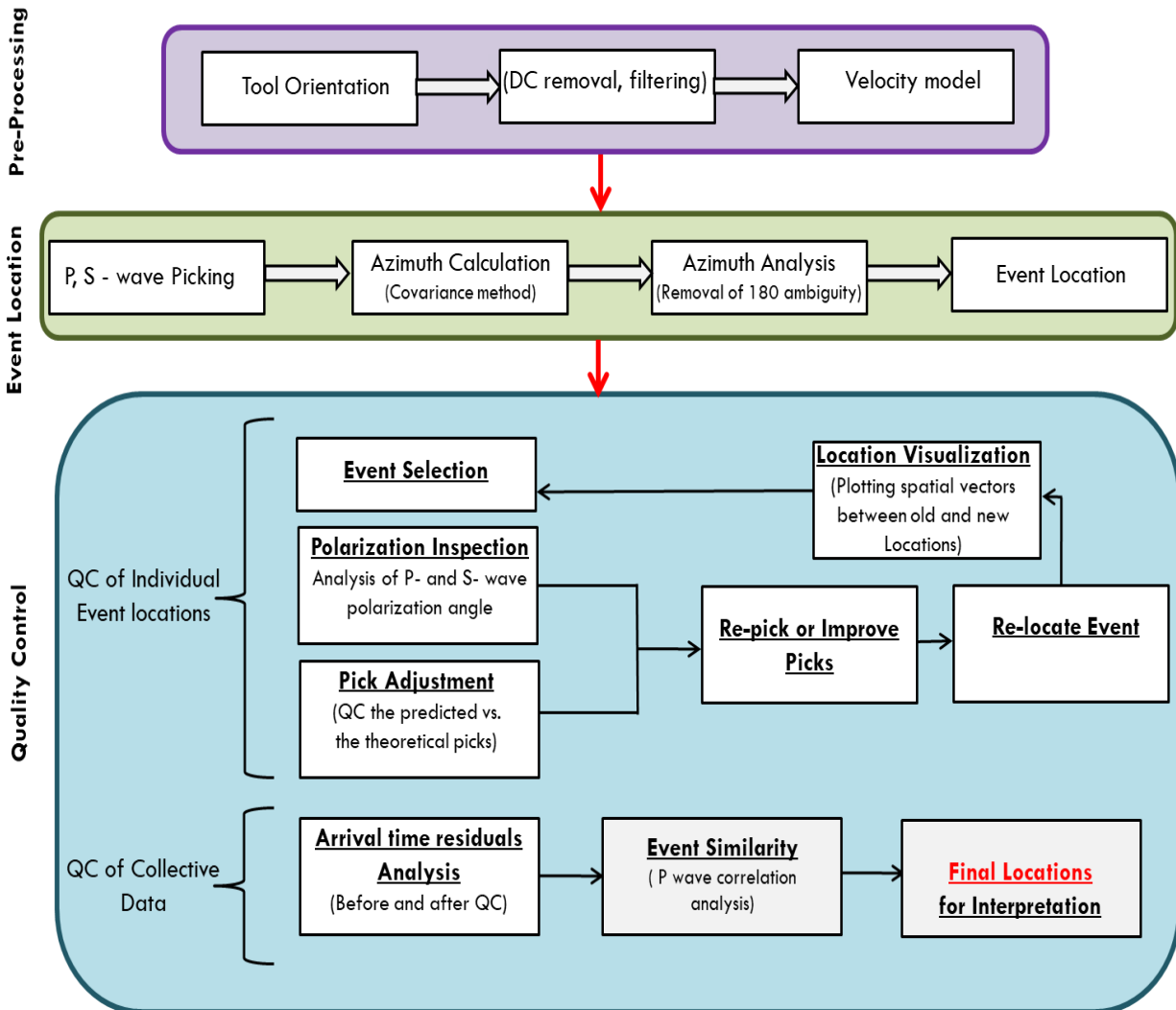


Figure 5-1: Flowchart diagram illustrating the complete microseismic processing workflow employed in this study.

Step 3: P wave polarization analysis - covariance method

A microseismic event generates different types of seismic waves. In general, the P-phase polarization is used to find the event back azimuth. The P-wave polarization is estimated using a covariance analysis of three-component data at each station (section 4.2, chapter 4). The method first calculates the auto and cross-variance using the three-component data, then estimates the P-

phase polarization (equations 4.2 to 4.5). A detailed discussion on the covariance method is provided in section 4.2, chapter 4.

Step 4: Azimuth analysis-removal of 180° ambiguity

The calculated azimuth values from the covariance analysis have a 180° degree ambiguity, which must be removed before inverting for event location. This is possible if 1) prior knowledge exists about which side of the monitoring array the microseismic activity is expected, or 2) the geophones are placed in multiple wells. The former is not always possible as most monitoring arrays are located in the middle of the field. The latter is very costly and thus rarely implemented.

We may take advantage of the spatial spread of geophones placed in a deviated or horizontal borehole. The azimuth calculated at each receiver location is used to resolve the azimuthal ambiguity. The calculated azimuths are plotted as straight ray paths at each receiver location and extended in both directions until they converge, thus indicating the possible correct side of the well where the event occurred. Azimuth information of at least two stations is required to remove 180° degree ambiguity. Figure 5.2 illustrates the method. This does not work for the vertical array because all the receivers are located at the same x-and y- coordinates.

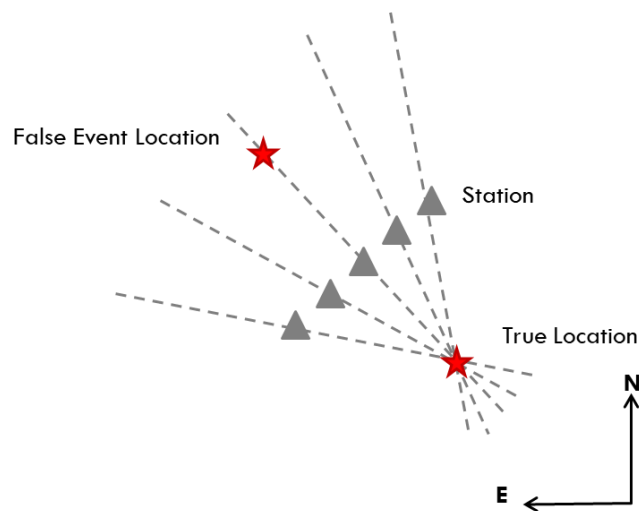


Figure 5-2: Illustration of the azimuth analysis, the dashed line represents the P –wave particle motion/ray path, the red star represents the microseismic source location, and grey triangles are the geophones.

Step 5: Event location

The fifth stage of the workflow is the location of microseismic events. The microseismic event locations may be obtained by using one of the following methods: Geiger's travel time inversion method (Geiger, 1912), the commonly used grid search method (Jones et al., 2014; Zhou et al., 2015), the migration based location approach (Haldorsen et al., 2013; Rentsch et al., 2007; Zhang & Zhang, 2013), the reverse-time imaging method (Artman et al., 2010) or the double-difference (DD) method (Castellanos & van der Baan, 2013; Zhou et al., 2010).

In this workflow, I use a 'grid search method' to invert for absolute event locations. The procedure consists of generating a grid with nodes associated with possible hypocenters. Next, theoretical P-, S-wave arrival times and P wave azimuths are calculated for each node and compared with observed values. This will yield a likelihood estimate at each node; the node with the maximum probability estimate is selected as the source location. Based on the synthetic results in chapter four, the SP Method is used in a grid search manner to locate the events.

Step 6: Quality control

Once initial event locations are estimated, the next step is to perform quality control of the event locations and input parameters. Quality control is extremely important to detect and remove any location artifacts or errors. These artifacts may be due to uncertainties in input parameters, velocity errors, and/or computational procedures.

The quality control procedure comprises of two parts. In the first part, each event is analyzed independently from the rest of the data. I start by comparing the observed and theoretical arrival time picks by overlaying them on the waveform. This simple step will instantly show if:

- 1) Observed and theoretical picks are in good agreement,
- 2) Observed picks have systematic and/or aleatoric errors and need to be re-picked,
- 3) Constant shifts occur between predicted and observed arrival times (possibly due to wrong origin time estimation) or,
- 4) Possibly, a wrong phase has been picked.

The proposed workflow incorporates the polarization information; therefore, while each waveform is being analyzed, a common strategy is to plot the x-y plane hodogram at each receiver. The P- and S-wave phases are polarized parallel and perpendicular to the wave propagation and can be examined from the hodogram. This will validate if correct P- and S-wave phases have been picked. Hodogram analysis can also help reveal if arrivals are very noisy and not linearly polarized. Based on the above, a decision is made to accept the event location or revise the P- and S-wave time pick. The procedure is repeated for each event.

The second part involves an analysis of all event locations at once. It is done by first plotting the original and improved event locations and histogram of azimuth and S-P wave residuals. The first will point out any event location trends that may be considered location artifacts, e.g., events aligned vertically or horizontally in a linear pattern. The histogram plot of differential S-P wave arrival time residuals will give an overall picture of how close the theoretical and observed parameters are. The theory behind this is simple: picking errors follow a random distribution with a mean zero. If the residuals are not centered around zero but instead skewed to the right or left, this indicates that the velocity model may need modification. Therefore, the residual histogram not only serves as a quality check of the locations but also the velocity model.

The last step is to analyze the similarity between events by calculating the P-wave cross-correlation coefficient. The main assumption of similarity analysis is that two waveforms will have a high correlation coefficient if both events have a very similar waveform and are closely located (Arrowsmith & Eisner, 2006; Castellanos & van der Baan, 2013; Geller & Mueller, 1980; Got et al., 1994; Poupinet et al., 1984), because the mechanism of closely located events is likely to be similar and follow the same ray path. These similar events are called doublets (Poupinet et al., 1984). For this reason, I begin the analysis by calculating the weighted average cross-correlation across all three components between all N possible event pairs in the dataset. The weighing is done according to the maximum amplitude at each component. The final cross-correlation value is obtained by averaging the cross-correlation coefficient over all the receivers. For more details, I refer to Arrowsmith & Eisner (2006). A plot of normalized event cross-correlation coefficient vs. the event separation distance is then plotted. It will allow a quick assessment of the location consistency between similar events.

5.3 Application to Peace River data

The proposed workflow is applied to recorded microseismic data in the study area. The acquisition geometry of the pad is shown in Figure 5.3a; the pad consists of several horizontal wells through which the steam is injected into the reservoir (a detailed description of the experiment is in chapter 2). The array consists of ten 3C geophones, lowered into the deviated monitoring well; the geophones are separated by approximately 10m and were placed above the reservoir. The data was recorded between 2002 and 2005. The field data was provided in the form of triggered events.

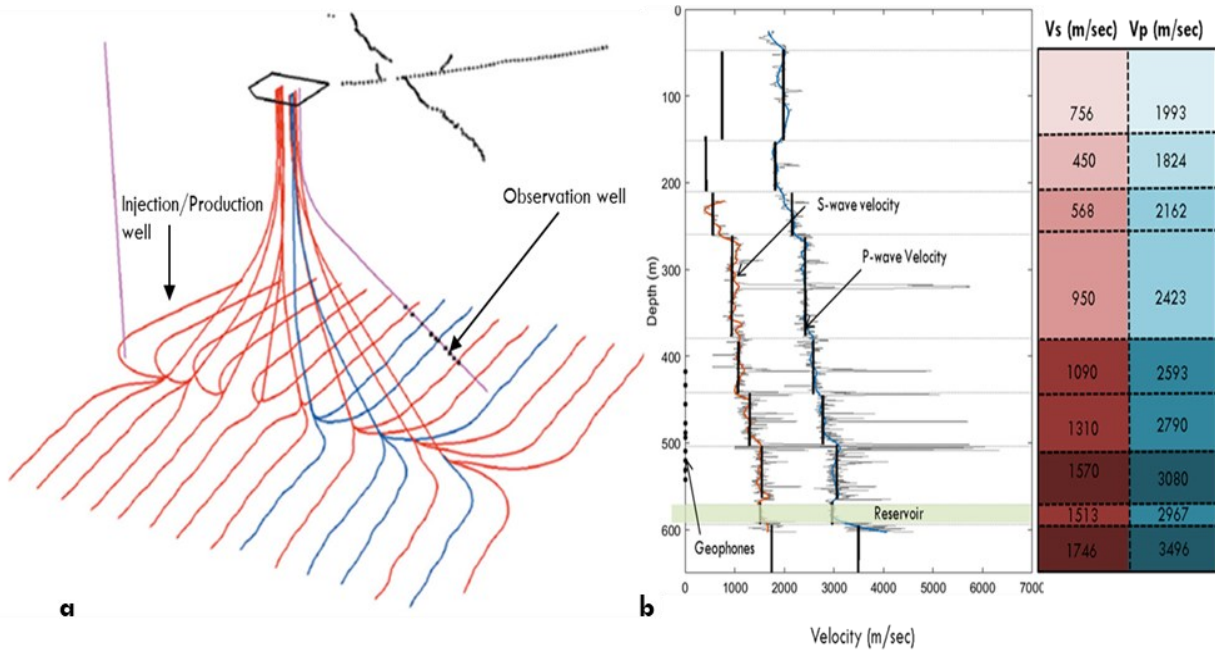


Figure 5-3: a) Perspective view of the field. The pad has horizontal wells to inject steam and produce hydrocarbon; geophones are lowered in the deviated observation well to record microseismic data. b) The figure on the right shows the P and S wave sonic logs and the 1D velocity model used in this project.

5.3.1 Data pre-processing

First, the receivers are oriented into E, N, and Z-directions by multiplying the three-component data by a (3×3) tool orientation matrix. The operator provided the tool orientation matrix. Once the data are oriented, the mean is removed, and the data are filtered using a bandpass filter of 45-60-170-180. A notch filter is also applied at 60Hz, where needed. Figure 5.4 shows the waveforms of a raw event (left) and the same event after receiver orientation and filtering (right). The noise is suppressed, and P- and S-wave arrivals are easily identifiable.

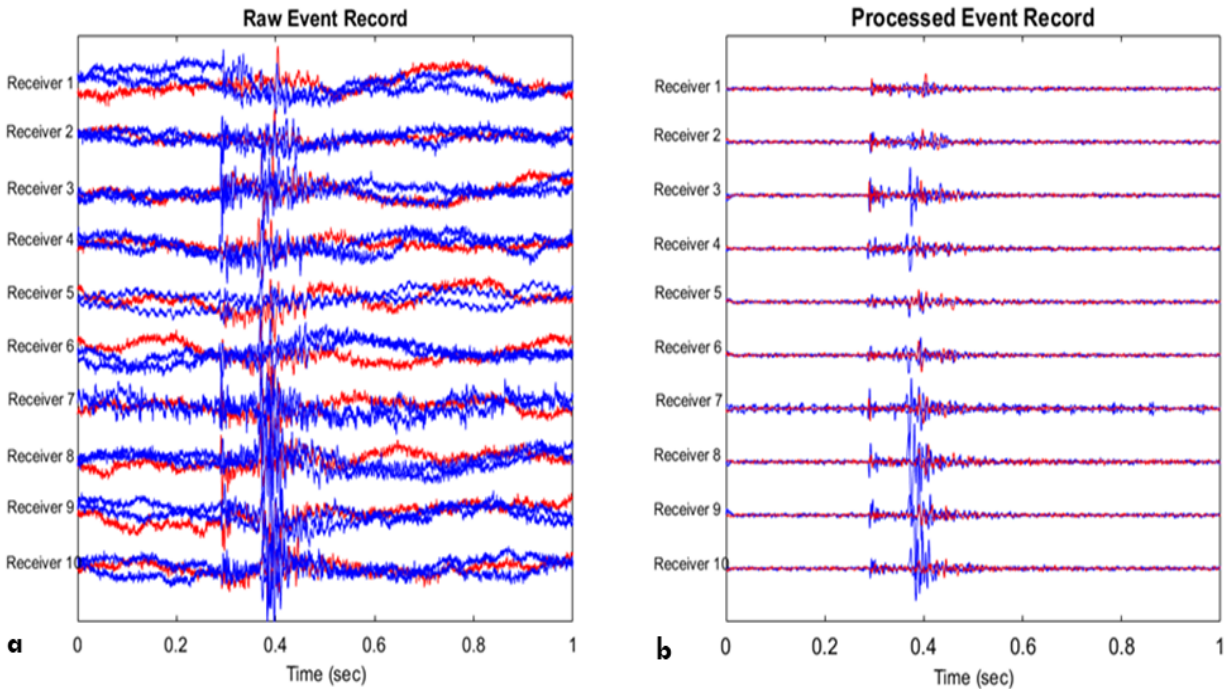


Figure 5-4: Waveforms showing a) raw and b) processed microseismic event recorded by a 10-level string of 3-component geophones during the 1st steam cycle. The two horizontal components are plotted in blue, and the vertical component is plotted in red.

Before proceeding further, a visual inspection of the filtered data was performed to understand the data quality. Figure 5.5 gives an example of recorded waveforms, labeled as Event 1, 2, and 3. The recorded data also contain waveforms, which may not be microseismic events, e.g., Event 1. Both the P- and S-wave phases may be visible (e.g., Event 3). Others may have a low P-wave amplitude (e.g., Event 2), thus making it difficult to pick the P-wave first arrivals accurately.

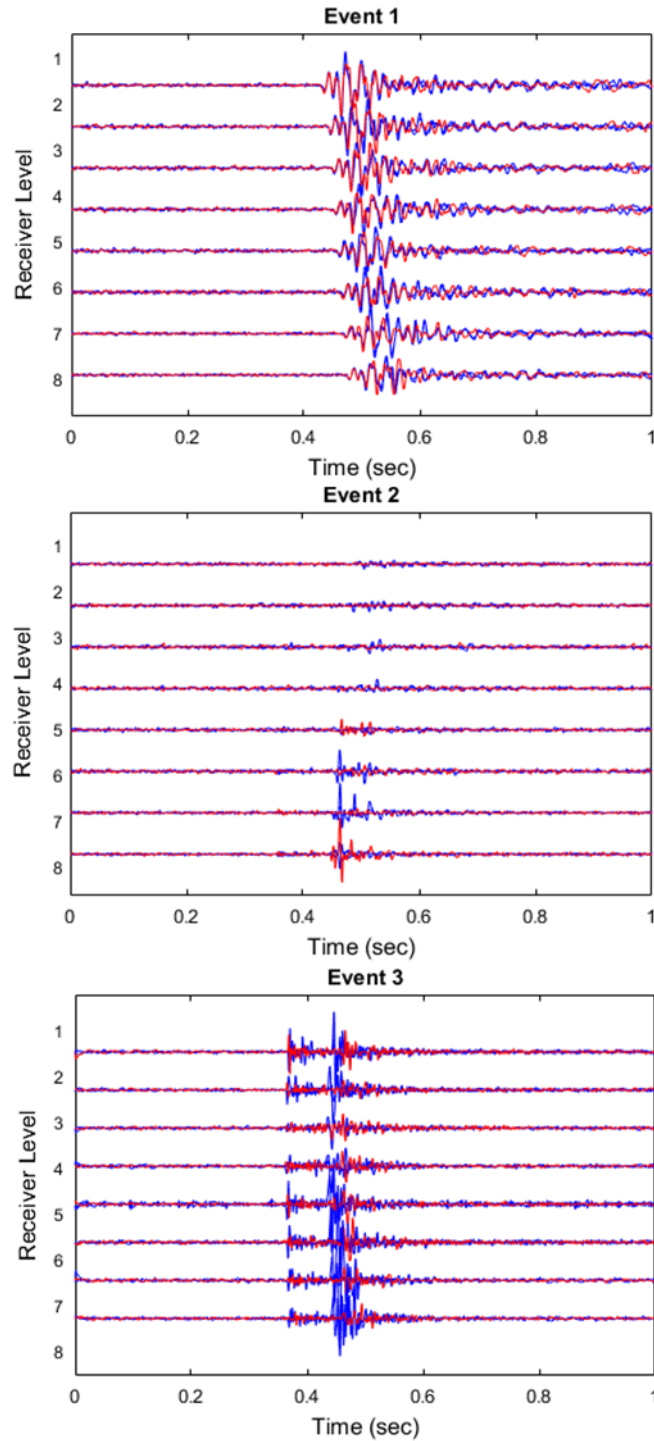


Figure 5-5: Showing different types of waveforms comprising the dataset in the study area. Different waveforms are labeled as Event1, 2, and 3 showing noise, a low amplitude event, and a good quality event, respectively.

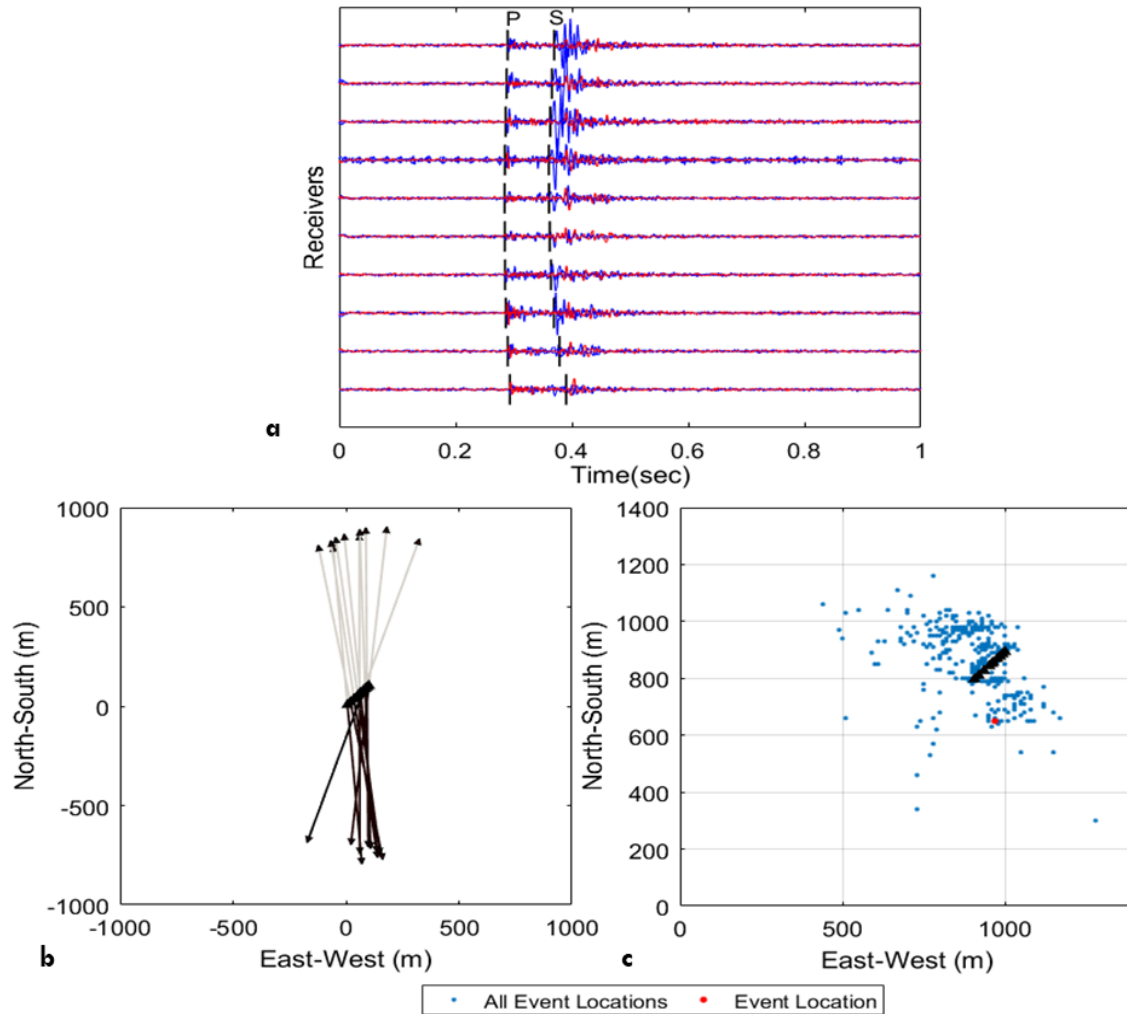


Figure 5-6: Showing a) P- and S-wave arrival times picked on three-component waveforms followed by b) azimuthal analysis of the P- wave to remove the 180° ambiguity (the solid black lines indicate the preferred direction and grey lines are indicative of false azimuthal direction), and finally c) event locations, the red dot shows the event location of this particular microseismic event, whereas, the blue dots are all the events recorded during the 1st steam cycle in 2002.

5.3.2 Event location

A velocity model is required to locate microseismic events. Therefore, a blocked 1D-velocity model is generated by using P- and S-wave logs. The resulting velocity model is shown in Figure 5.3b.

The next stage of the procedure is picking P- and S-wave arrival times. The microseismic waveforms are picked in chronological order using AR modeling and the Akaike Information Criterion (Sleeman & Eck, 1999), largely followed by manual re-picking. Once satisfactory picks

are obtained, the P-wave azimuth is calculated using the covariance method and corrected for the 180° ambiguity. The picked arrival times and azimuths are then used to calculate the hypocenter location in a grid search manner. The grid spans a horizontal offset range of 0 to 1400m and a depth range of 300 to 700, and each grid cell spacing is 10m in the horizontal and depth direction. The hypocenter location is then calculated for each event using equation 4.7 (chapter 4). The equation considers the uncertainties in P- and S- wave arrival time picks and azimuth. Arrival time and azimuth uncertainties are assumed to be 1 msec and 10°, respectively.

An example of an event showing the steps followed from arrival time picking to the event location is shown in Figure 5.6. The P- and S-wave arrival times are picked and overlaid on the event waveform (Figure 5.6a). Figure 5.6b shows how the azimuth is plotted. The optimal set of azimuth values is selected to locate the event. Then, the event location is calculated by incorporating the P- and S-wave arrival time picks along with the chosen azimuth (figure 5.6c).

The same steps are followed for each file in the data set, and all the events are located. While doing so, several data files were discarded, which were either only noise or very noisy waveforms such that P- and S- phases were difficult to pick. This resulted in 1046 event locations, which are then further quality controlled.

5.3.3 Quality control

As mentioned earlier, the proposed quality control workflow is comprised of two parts. In the first part, each location is revisited and analyzed. In doing so, some events may be in good agreement, and others may require adjustment to the input parameters, e.g., P- and S-wave arrival time picks and azimuth. For each file, a QC figure is displayed, showing the waveforms overlain by predicted and modeled arrival times, the horizontal hodogram at each receiver, and histograms of time and azimuth residuals. Then, a decision is made based on the visual inspection of the QC figure; whether the event location is accepted, or input parameters need to be adjusted. Figure 5.7 shows the QC figure for an event recorded during the 1st steam cycle. Note that the theoretical (green ticks) and observed (black ticks) P- and S- wave arrival times are almost similar at all receiver locations. However, this is not always the case; only 1225 out of 2270 events were marked as acceptable. Selected events were revisited, visually inspected, and re-located. Figure 5.8 shows an example of a revisited and re-located event with adjusted picks. Note that the difference in the initial (black ticks) and final (red ticks) P- and S-wave picks, hodograms, and the resulting event location. The difference between the initial and final picks is not substantial, and the resulting

hodograms appear to be relatively similar. However, the small difference in P- and S-wave picks did affect the resulting event location (red diamond).

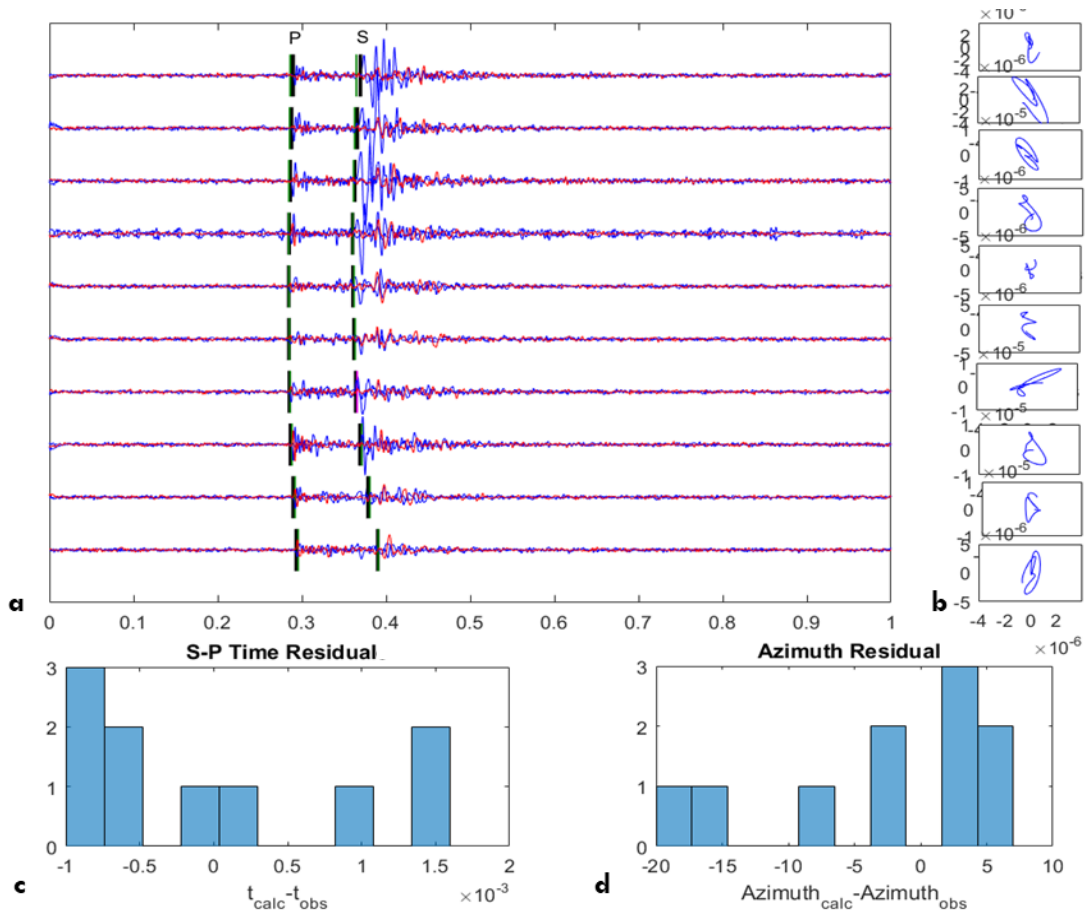


Figure 5-7: Example showing the stepwise quality control of the individual event. a) Theoretical and observed P- and S-wave arrival times are superimposed on the event waveform (Black are the observed picks, and green are the theoretical picks). b) Hodogram at each receiver showing the P-wave polarization direction in the x-y plane, c, and d) Time and azimuth residual histograms.

Each event is quality controlled similarly; then, all the events are collectively inspected. A plot of the initial and final locations is the fastest way to visualize the effect of the QC step and look for any location artifacts (e.g., linear trends in the data). Figure 5.9 shows the map and depth view of the initial (before QC) and final locations (after QC). Note the clustering of events after quality control, marked by a black arrow. Although both figures show mostly subtle differences, initial locations are more scattered, whereas the final locations are more focused.

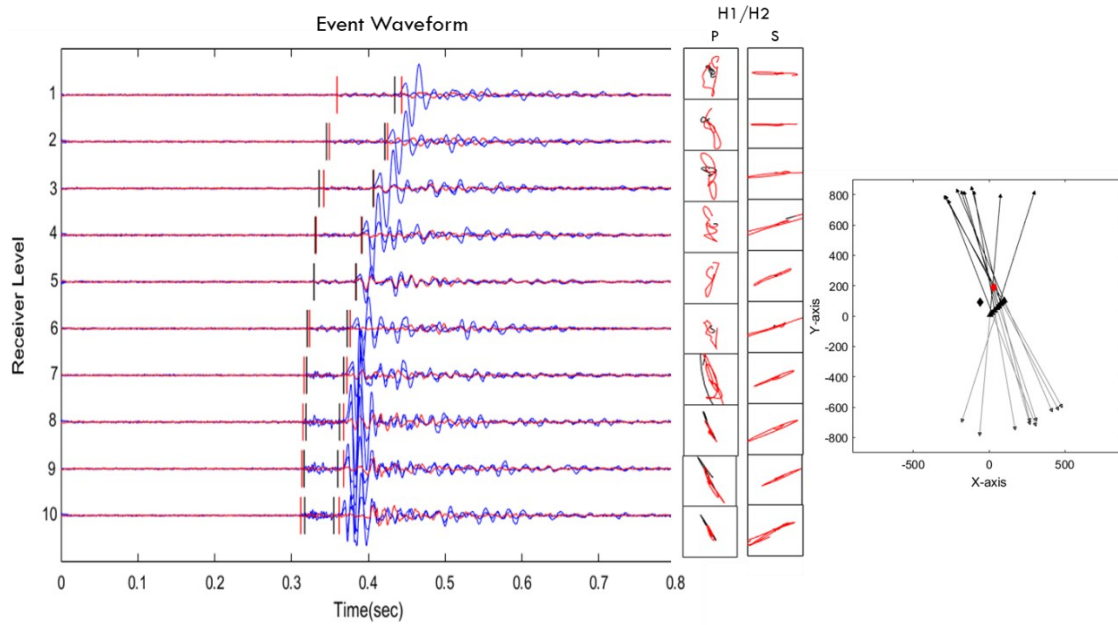


Figure 5-8: An example of a revisited event during quality control. Initial (black) and updated (red) P -and S- wave picks are shown at each receiver (left), and corresponding P- and S- wave x-y hodograms (middle). The initial and final event locations are shown by black and red diamonds on the map view, the black triangles are the receivers, and black and gray lines are true and ambiguous azimuth directions (right).

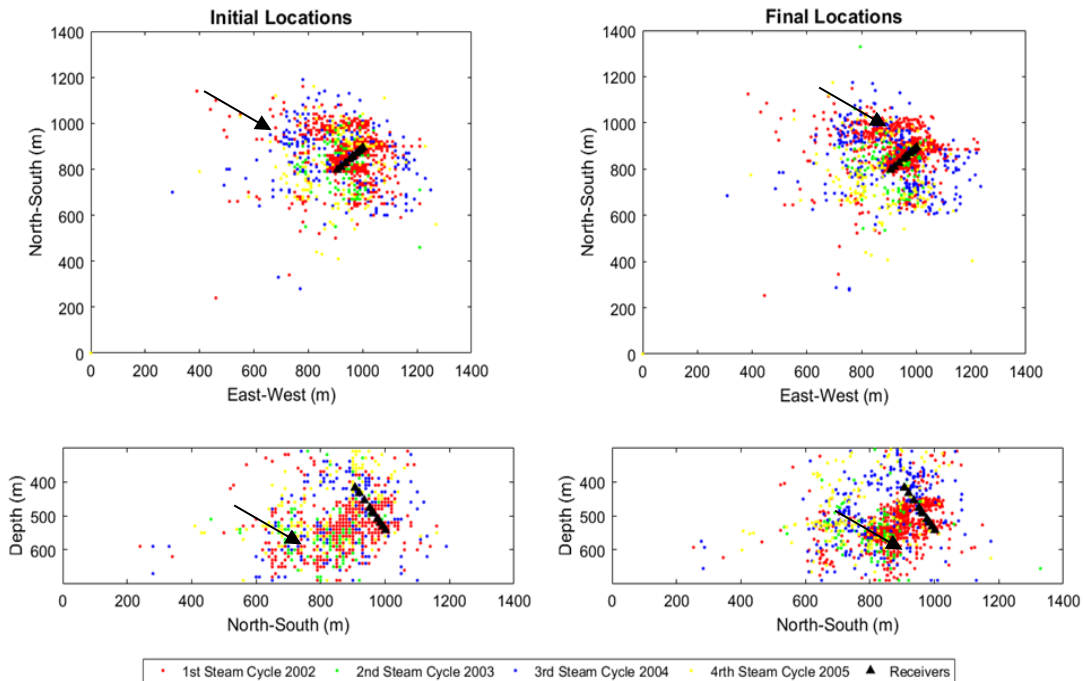


Figure 5-9: Shows a map and depth view of the initial (left) and final event location after QC (left). Microseismic events are colored based on the steam cycle.

Subsequently, I analyze all events together by plotting S-P wave arrival time residuals of initial and final locations (Figures 5.10a, b). The tightening of final travel time residuals compared to initial locations is a strong indicator of event location improvement. The residual histogram is expected to be symmetrical and centered around zero (mean zero). Both histograms are centered around zero, but the residuals of initial locations are skewed to the left. However, the same is not observed after quality control, and a higher peak is seen at zero. The above illustrates the effectiveness of the quality control workflow and improvement in the results.

I continue with the quality control analysis and analyze the cross-correlation coefficient and location distance between similar events. Figure 5.11 shows a plot of cross-correlation vs. separation distance for initial and final event locations; note the data point outlined in red. The data points with high cross-correlation were located 200m away from each other. In contrast, events with high cross-correlation coefficient should be located at much closer distances, as seen in the distance vs. correlation plot of quality-controlled events in Figure 5.11. Overall, the waveform similarity between events decreases as inter-event distance increases, as expected.

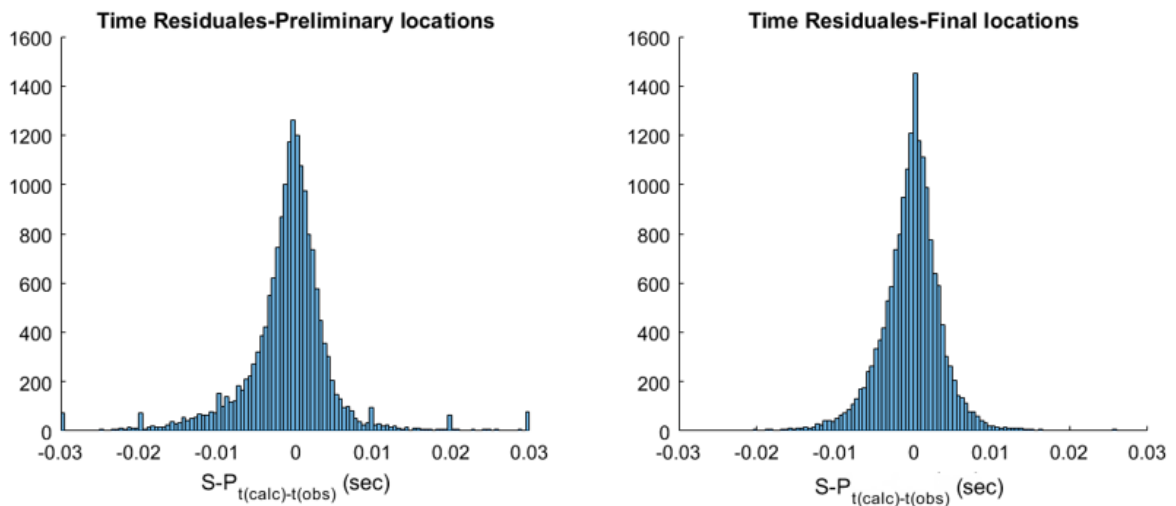


Figure 5-10: Histogram showing S-P wave time residuals for initial event locations (left) and final event locations (right).

5.4 Results

The data consisted of ~9,000 files, out of which 2271 files were extracted manually as possible events. The workflow was applied to the selected 2271 events, and 1225 events successfully passed the quality control workflow, whereas 1046 events were revisited and re-

located. The summary of the data is shown in Table 5.1. The inclusion of the azimuth analysis step appears to improve confidence in the event locations. The revision of selected events improved the individual event locations, and it is evident from Figure 5.9 that the workflow also tightened the event cluster.

It is a common scenario to have one or two noisy receivers or deal with low amplitude P- or S- wave signals, making it difficult for an automatic picker to detect the onset. In this study, around 70% of the events selected for revision only had minor picking errors, which needed a slight adjustment. The remaining events mostly had missing arrival time picks or one or more noisy receivers, which introduced large errors in the event locations. The event locations were improved by simply eliminating the noisy receiver.

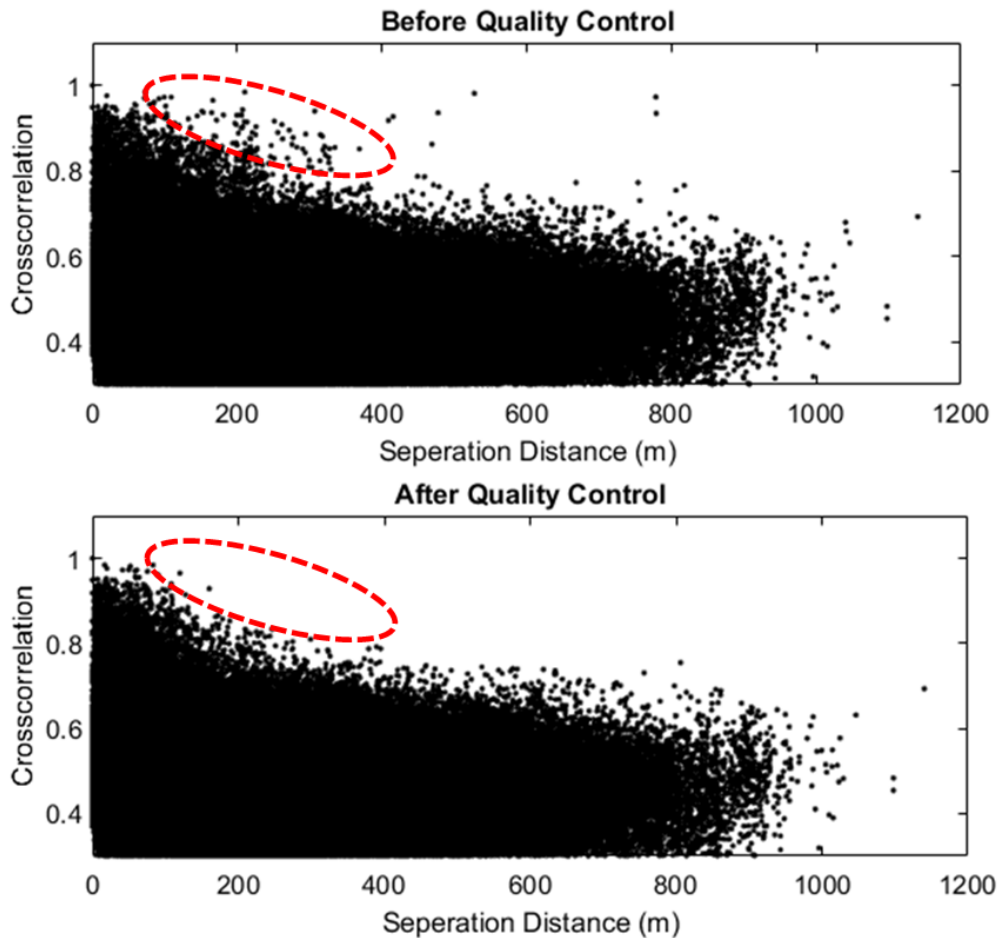


Figure 5-11: The separation distance vs. cross-correlation coefficient plot for a) Initial and b) final event locations. The red encircled area highlights the area where the most difference is evident.

Table 5.1 Summary of data showing the number of events quality controlled, revisited, and disabled.

Data Summary		
	Event Count	Comments
Total no. of Events	2271	Microseismic events recorded from 2002 to 2005.
QC passed Events	1225	Events located and passed the quality check.
Revisited Events	1046	Arrival times were revisited, azimuth re-calculated, and events relocated.
Disabled/discarded Events	~190	Limited no of picks, very noisy data

5.5 Discussion

In this study, I take advantage of commonly used techniques in a stepwise manner to reduce these errors. I proposed and applied a six-step procedure to locate microseismic event locations recorded by a single deviated borehole. The developed workflow first outlines the three important pre-processing steps that must be performed before estimating microseismic event locations, irrespective of acquisition geometry or size of the dataset. These include tool orientation, data filtering, and velocity model generation. The filter must be carefully selected to preserve the P- and S- wave signal after careful analysis of the dataset. It is followed by locating and quality control of the microseismic events.

In comparison with the previous processing workflow by Akram (2014) and Wang et al. (2016), most of the processing steps are similar, for example, pre-processing (tool orientation, filtering, and velocity model calibration) and event location. However, both workflows do not comment on the inherited 180° uncertainty (due to single borehole acquisition setup) and quality control of the microseismic events but rather outlines the standard procedure to process the data irrespective of different acquisition geometries (vertical, horizontal and deviated). The workflow

developed in this study is for a deviated borehole but is also applicable to a horizontal geometry. It may need additional constraints for a single vertical array, as mentioned by Jones et al., (2010). They presented and applied a five-step processing workflow for a vertical borehole and used dip angles to remove the 180° degree ambiguity associated with event locations. However, none of the published workflows incorporates the quality control procedure proposed in this study.

The acquisition geometry, velocity model, and inaccuracies in arrival time picks are major sources of errors in event locations (Akram, 2014). The results obtained by applying the proposed processing workflow to heavy oil data demonstrate that errors in P- and S-wave picking contribute significantly to errors in the microseismic event location. Similar results are obtained by Pavlis (1986) and Akram (2014). This is supported by the number of events selected for edit and relocation. The waveforms with poor picks were identified by inspecting the observed and theoretical arrival times and azimuths. These events are revisited, picks adjusted, and relocated. The improvement in event locations is explained by comparing the arrival time residual histogram and cross-correlation coefficient vs. distance plot. It also supports the effectiveness of the quality control procedure for improving absolute event locations.

The most important pre-processing step is velocity model generation; it can severely affect event locations. It is preferable to have a 3D velocity model that is closer to the true velocity model. On the scale length of the microseismic borehole survey, the velocity structure is often approximated as being 1D. In this study, the 1D velocity model is generated from the sonic well logs because a 3D velocity estimate is not possible using logs from a single well. However, the effect of the velocity model on event location accuracy is demonstrated by Maxwell (2009) and Yerkes & Castle (2011) and found that velocity model uncertainty tends to relate to results in systematic misallocation. Akram et al. (2013) investigated the impact of ignoring velocity anisotropy on event locations. It was found that there exists a systematic variation in the event locations and events are located closer to the receiver array (spatially), away from the true location. However, for this particular dataset, the inclusion of the anisotropic velocity model is not expected to affect the event locations drastically because events are already located very close to the monitoring well, thus changing the interpretation.

Another important step in this workflow is removing the inherent 180° ambiguity in azimuth using the spatially distributed receivers in a deviated borehole. Once done, the resulting locations

are more certain. However, this step can be neglected if the workflow is to be adopted for multiple monitoring wells because of the wider spread of the geophones.

The true event location can be attained by using arrival times only. Microseismic event locations are estimated by minimizing azimuthal and S-P wave arrival time differences at each receiver position in a grid search manner. Although, grid search-based procedure suffers from higher computational times than other procedures, e.g., global algorithms (Billings et al., 1994). Despite this, the grid search method is widely used because of its simplicity and robustness in implementation. Nonetheless, the computational time is reduced by carefully handling the grid size, e.g., by initially locating the events on a larger grid size (20m) and then narrowing down the search around the initial event location by generating another grid of smaller size (1m). It reduced the computational time and improved the location accuracy of the calculated event locations.

The proposed quality control takes advantage of commonly used techniques, e.g., cross-correlation vs. distance plot and residual histogram analysis. The residual histogram is a simple but effective quality control tool to evaluate the arrival time picks. If picking errors are random, the residuals will be centered on the mean. The improvement in the event locations is illustrated by a narrow histogram of arrival time residual (figure 5.10b). The improvement in arrival time picks ensures more confidence in the resulting microseismic locations. The residual histogram and the cross-correlation versus the distance plot show the applicability and efficiency of the quality control procedure for refined arrival picks on microseismic data. As a future implementation, the cross-correlation analysis can be extended to find multiplets in the data and calculate relative event locations (Castellanos & van der Baan, 2012; Kocon & van der Baan, 2012).

In a downhole microseismic monitoring experiment, it is common to have one or two noisy receivers, thus making it difficult for an automatic picker to detect the onset. The decision is made manually to improve or discard a particular trace from the analysis. In this dataset, 20% of the selected events for revision had one very noisy receiver and was discarded. The results of the manual inspection may be impacted by the processor's understanding and experience of the subject. Although it is a time-consuming process, it adds value by improving the quality of results; thus, it is still highly recommended. However, further work may be done to accelerate the processing time by automating some of the steps in the proposed workflow. To speed up the picking procedure, more than one automatic picker could be used to pick the majority of the P-

and S-wave phases. Next, instead of manually deciding if an event should be incorporated for further processing and analysis, a threshold can be set. Similarly, the correct azimuth can be selected automatically by finding the converging set of azimuth values. The threshold may be set in terms of the S/N ratio and the number of receivers with P- and S-phase picks. This will help eliminate some of the low-quality events, which otherwise will be located forcefully and result in uncertain event locations, thus affecting the resulting interpretation.

5.6 Conclusion

I have developed and applied a workflow to process and quality control microseismic events recorded by a single deviated borehole, using a 1D-velocity model. The procedure is a six-step approach consisting of 1) data pre-processing, 2) arrival time picking, 3) P-wave polarization analysis, 4) removal of the 180° uncertainty in azimuthal measurements, 5) event location, and 6) quality control of the event locations. The approach is tested on the heavy oil dataset. A total of 2271 events are processed, and 1046 events are revisited during the quality control. As a result, 2081 events are located and 190 discarded, essentially due to the inability to pick the P- or/and S-wave phases. Interpretation of the event locations is made in the next chapter.

6 Integration of microseismic and production data

6.1 Introduction

One of the microseismic monitoring applications is to image inelastic deformation associated with the injection of steam/water/gas for secondary recovery and production (Maxwell, 2009; Maxwell & Urbancic, 2001). Microseismic monitoring has been used in geothermal fields since the 1970s as a routine procedure to image the fracture network. Its use in the oil and gas industry is mostly related to hydraulic fracturing mapping (Albright & Hanold, 1976; Pearson, 1981). Imperial Oil first investigated the use of microseismic monitoring in heavy oil extraction processes in 1980. Since then, the microseismic monitoring system has been installed on more than 100 pads to monitor and detect thermal casing failure that may be associated with thermal stresses during cyclic steam injection at Cold Lake, Alberta (Smith et al., 2002). In 2002, Shell Canada initiated an integrated surveillance project to monitor CSS operation (McGillivray, 2005).

Microseismic monitoring during steam injection in heavy oil reservoirs has utilized the technique to track steam front movement within the reservoir, identify well casing failure, potential caprock integrity issues, and characterize activation of faults. Other advanced analyses, e.g., source parameter characterization, may help identify the stress transfer mechanism associated with steam chamber growth. Real-time monitoring of microseismic activity can help identify fracture development within or above the reservoir, the breach of caprock sealing capacity, the leak or damage in the well casing (Talebi & Boone, 1998). Unusual clustering of microseismic events or large magnitudes may indicate activation of a fault, alerting the operator to take proper measures to ensure the safety and integrity of the operation.

I analyzed and interpreted microseismic data from Alberta, Canada, where heavy oil is extracted using the CSS processes. Steam is pumped into the reservoir at high pressure and temperature, at a depth of approximately 565 m. As a result, microseismic events are generated in the overburden and also in the reservoir. McGillivray (2005) analyzed Peace River data to monitor steam front diffusion. He showed that the majority of the microseismic events are in the reservoir section. However, the potential of fractures and faults in unconsolidated reservoir sands is still poorly understood. I analyze the provided dataset, keeping in mind two objectives. First, understand and track the development of the steam chamber growth. Second, obtain detailed insight into the deformation associated with steam growth. To do this, I first examine the spatial

and temporal trends of microseismic events and analyze moment magnitude. Later the results are integrated with the engineering data.

6.2 The Peace River CSS experiment

As mentioned in the early chapters, the data for this study was acquired during the CSS experiment over four years. The microseismic array was deployed in September 2002, weeks before the steam injection started at the pad of horizontal wells. The CSS involved four injection-production cycles between September 2002 to December 2005. The geometry of the injectors and monitoring well is shown in Figure 6.1. The pad's design is such that it consists of ten main boreholes drilled down to the reservoir from the center. Then horizontal sections are drilled away from the main borehole into the reservoir. Therefore, each main well has three horizontal laterals extending in north and south directions. The steam is then pumped into all the wells simultaneously, allowed to soak, and followed by production. The production is also obtained simultaneously from all the wells. The microseismic data were recorded by 3C geophones placed in a single deviated borehole (TH40-A) located in the middle of the pad, deviated to the northeast. Ten receivers were placed in the well above the reservoir, between depths of 416 to 539m in TVD. The reservoir lies at a depth of 565m with an average thickness of 25~35m at the pad. It is important to know and understand the injection production geometry and strategy, as this may facilitate and investigate the recorded microseismic activity in the area.

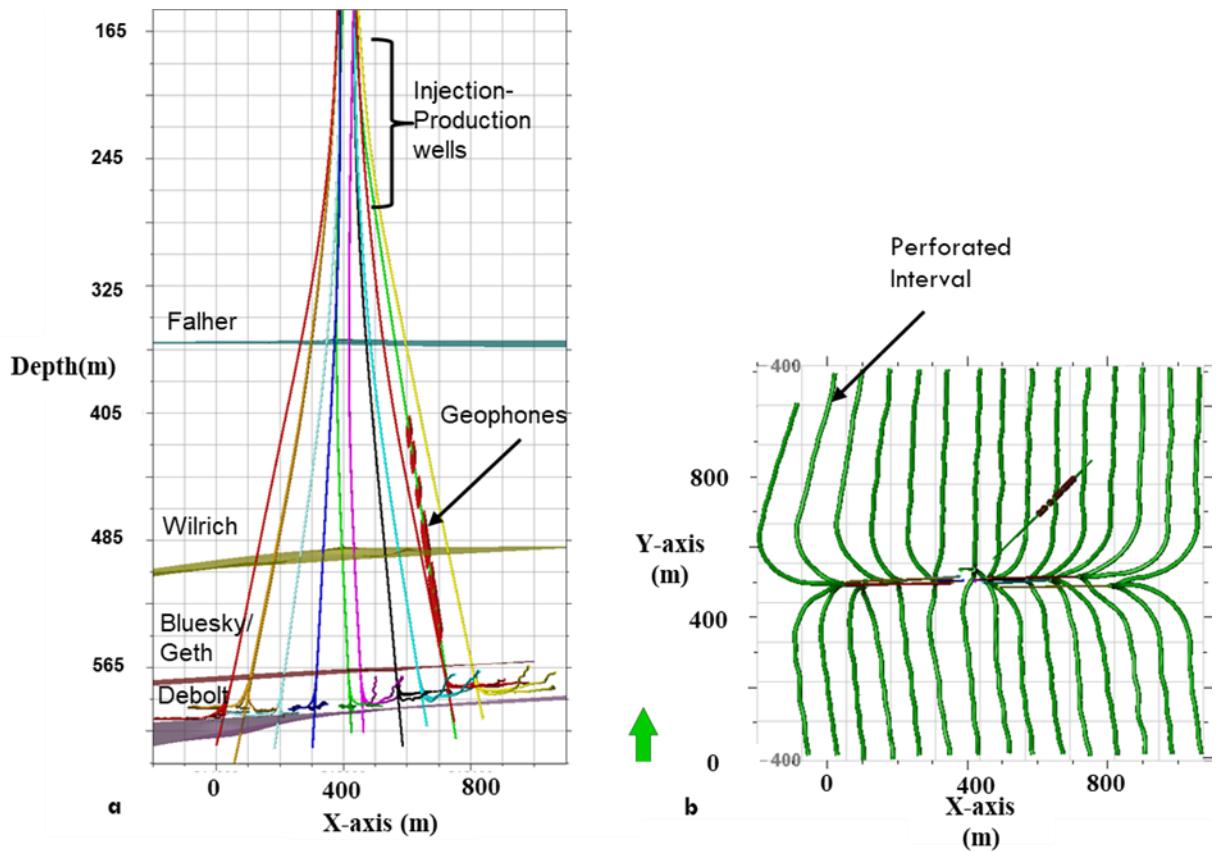


Figure 6-1: The pad well geometry in a) Cross-sectional view and b) Map view. Three laterals kick off from the central vertical well, with ten vertical injection-production wells and one deviated monitoring well. In the map view, the green color shows the perforated section of each well.

6.3 Data analysis strategy

It is a common practice to analyze the microseismic event locations to understand the rock deformation and infer the length and height of fractures from the size and shape of the events cloud (Maxwell, 2014). However, several other attributes (source parameters) may be estimated from the recorded data to advance the data analysis. In the current study, the moment magnitude and S/N ratio of each event are estimated from their waveforms to determine the data sensitivity. This is followed by evaluating the monitoring biases by inspecting the magnitude-distance plot and landing height at the monitoring pad. Once done, the influence of the Kaiser effect and brittleness of the subsurface rock on the spatial and temporal trends of the event locations is inspected. The following is the description of the estimated parameters.

6.3.1 The moment magnitude (M_w)

The moment magnitude (M_w) relates event magnitude to the physical fault model, as introduced by Kanamori, 1977. The moment magnitude of a microseismic event describes the event's strength (Baig & Urbancic, 2010). There are several methods to calculate the magnitude; the Brune model fit is used in this study (Brune, 1970). The seismic moment (M_0) measures the size of the microseismic event and is defined as the product of rupture area (A), shear modulus (μ), and average slip on the fault (d) (Aki & Richards, 2009; Hanks & Kanamori, 1979)

$$M_0 = \mu dA. \quad (6.1)$$

If density (ρ), velocity (V_p , V_s), and distance (r) are known, then the seismic moment can be expressed in terms of the Brune model. It relates stress released across the fault to the spectrum of shear radiation (Brune, 1970; Eaton, 2014)

$$M_0 = \frac{4\pi V^3 |A_0^v| r}{R_v}, \quad (6.2)$$

where $|A_0^v|$ is the low-frequency amplitude of the displacement spectrum, and R_v is the radiation constant. The lower frequency plateau may be generated from the displacement spectrum of a P- or S- wave. According to the Brune model, the amplitude of the frequency response is flat until the corner frequency is reached; after that, the amplitude falls at f^2 , as shown in Figure 6.2 (Brune, 1970). The corner frequency and magnitude of an event are empirically related. It is based on the relationship between seismic moment and the fault surface area: a larger fault surface will produce a larger wavelength signal (lower frequency), whereas a small fault will result in a smaller wavelength signal (higher frequency). Therefore, the corner frequency can be viewed as the characteristic frequency of the event (Baig & Urbancic, 2010).

The moment magnitude, M_w can then be calculated by using the empirical relationship between seismic moment (M_0) and moment magnitude (M_w) (Hanks & Kanamori, 1979)

$$M_w = \frac{2}{3} \log_{10} M_0 - 6. \quad (6.3)$$

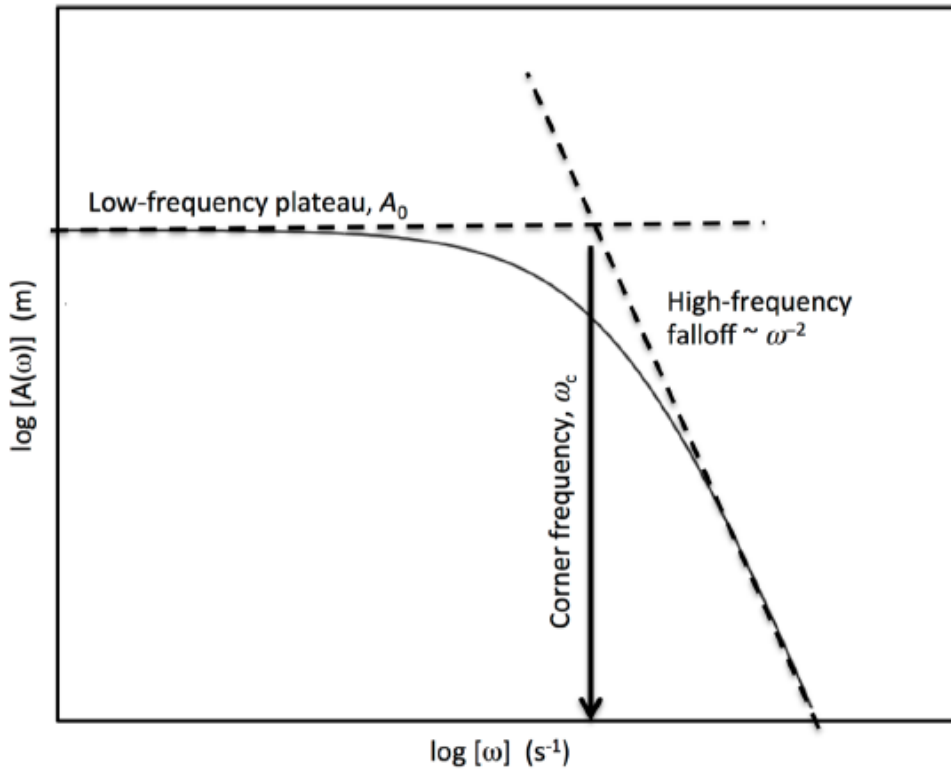


Figure 6-2: Relationship of Brune-model parameters to far-field displacement spectrum (Eaton, 2014).

6.3.2 Signal to noise ratio

Another way to characterize microseismic events is signal quality. The recorded signals are generally weak and low in amplitude, thus introducing more uncertainty in the microseismic trace attributes (Maxwell, 2009). It also impacts the confidence in the arrival time picks and the resulting locations irrespective of which acquisition or processing method is applied (Maxwell, 2014).

The S/N ratio may be defined as

$$S/N = \frac{A_P}{\sigma_n}, \quad (6.4)$$

where σ_n is the standard deviation of the noise, and A_P is the P-wave signal amplitude. For simplicity, I have considered the absolute value of the data samples in the selected P-wave window.

6.3.3 Brittleness index

The brittleness index (BI) is commonly used to characterize rocks under stress (Zhang et al., 2016). It defines the rock's ability to fail in a brittle manner. The P- and S-wave velocity and density logs are used to calculate the dynamic elastic moduli logs by (Mavko et al., 1998)

$$v = \frac{V_P^2 - 2V_S^2}{2(V_P^2 - V_S^2)}, \quad (6.5)$$

$$K = \rho \left(V_P^2 - \frac{4}{3} V_S^2 \right), \quad (6.6)$$

$$E = 3K(1 - 2v), \quad (6.7)$$

$$BI = \left(\frac{E_{norm} + v_{norm}}{2} \right). \quad (6.8)$$

In the above equations, v is the Poisson's ratio, K is the bulk modulus, E is the Young's modulus, and BI is the brittleness index. The common objective of calculating the BI is to differentiate the brittle and ductile zones. This will help predict the geological zones where more fracturing and microseismic activity may occur.

6.3.4 Assessing monitoring biases

- **Magnitude-distance plot**

Before interpreting the microseismic data, it is important to correct any monitoring biases. One of the common inherent biases is associated with the single-downhole monitoring setup; for instance, small magnitude events can be detected at close vicinity, but only larger events are detected at greater distances. Thus, the number of detectable events decreases with offset. Hence, a magnitude distance plot may be used to reveal a distance-dependent detection threshold, as illustrated by the dotted black line in Figure 6.3. The plot is also used to define the magnitude cut-off to remove or normalize the detection bias, illustrated by a green horizontal line in Figure 6.3. All the events below the green lines are excluded from further analysis. Though it will limit the number of fractures imaged in some parts of the experiment, it is essential to consider the detection threshold limit to evaluate the recorded data correctly. Therefore, a magnitude-distance plot is generated ahead of the interpretation.

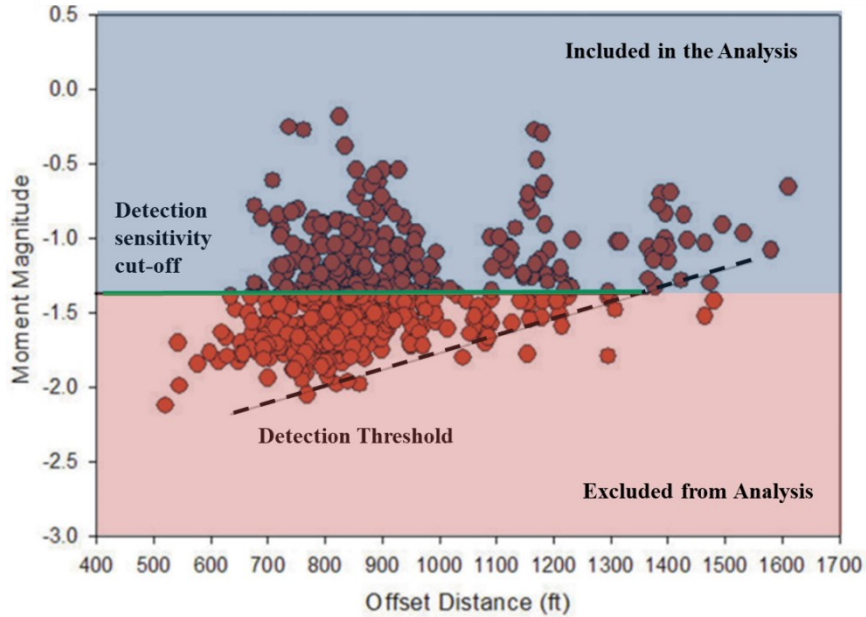


Figure 6-3: Magnitude-distance plot showing magnitude threshold (black dashed line) for a dataset. The green horizontal line indicates the detection sensitivity cut-off. The red and blue areas highlight the microseismic events excluded and included from the analysis, respectively (edited from Baig & Urbancic (2010)).

The event detection sensitivity may also vary with time during the microseismic monitoring experiment, mainly if noise increases, decreasing the detection sensitivity, and larger events need to be recorded to achieve a certain S/N ratio. The detection limit also affects the number of imaged events.

- **Landing height**

An important parameter that needs to be considered when drilling a horizontal well is deciding what depth to target and land the well (Figure 6.4). In an ideal situation with a massive homogenous reservoir, it is always desired and recommended to land the well at the bottom of the reservoir (Illustrated in Figure 6.4 a) so that steam can impact most of the reservoir interval (Maxwell, 2014). On the contrary, if the well is landed near the top of the reservoir, then it is most likely that steam will not be as effective as needed, as illustrated in Figure 6.4b. The landing height is defined as the difference between the reservoir top and depth at which the well lands in the reservoir. The landing height is calculated by

$$Landing\ Height\ (LH) = Top\ reservoir\ depth - Perforation\ depth \quad (6.9)$$

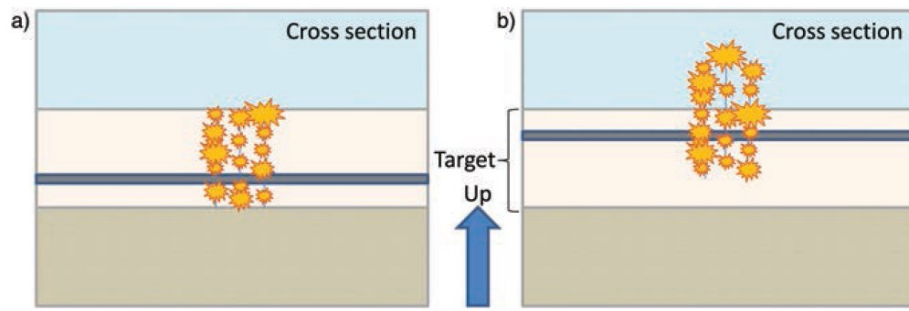


Figure 6-4: Schematic of landing height scenarios showing different depth coverage depending on whether the well is placed (a) lower or (b) higher in the section (reproduced with permission from Maxwell, 2014).

The purpose of calculating the landing height is to identify zones in the overburden closer to the injection point in the reservoir, thus, indicating areas in the caprock that are more susceptible to fracture growth.

6.3.5 Kaiser effect

The analysis of the microseismic activity in rocks during loading and unloading is of prime importance in the hydrocarbon industry to better understand the physics of the seismogenic processes. The Kaiser effect has been highlighted by different studies of microseismic and acoustic emissions in rocks under cyclic loading by applying stress or fluid injection (e.g., Baisch et al., 2002; Lockner, 1998; Zang et al., 2000; M. D. Zoback & Harjes, 1997). The Kaiser effect is characterized by the absence of acoustic emissions or seismic activity when the load/stress applied on the rock is less than the load/stress applied in previous cycles. Once the previous peak stress is exceeded, the seismic or acoustic emission activity increases rapidly. The phenomenon was first observed by Kaiser (1950) in metals and investigated in geosciences at the end of the 1970s (e.g., Kurita & Fujii, 1979; Tanimoto et al., 1978).

Microseismic activity in rocks is often associated with faulting as a result of hydraulic fracturing. The triggering mechanism for fluid-induced microseismicity is caused by perturbations of pore pressure and stress. In this chapter, I intend to evaluate if the trend of microseismic activity, recorded during steam injection and production cycles of heavy oil recovery experiment, correlates to injection pressure via the Kaiser effect.

The microseismic data are analyzed by calculating and integrating the attributes and parameters mentioned above. The next section will highlight the key findings and observations.

6.4 Results

6.4.1 Spatial and temporal distribution

The detection of spatial patterns in microseismic data is the first step to analyze the induced fracture geometry. Additionally, the spatial and temporal trends may provide further insight into the details of fracture growth. These patterns can be indicative of asymmetric fracture growth, screen outs, or fault reactivation. The histogram of event density and attributes can help visualize and interpret the variation of event locations in time and depth (Maxwell, 2014).

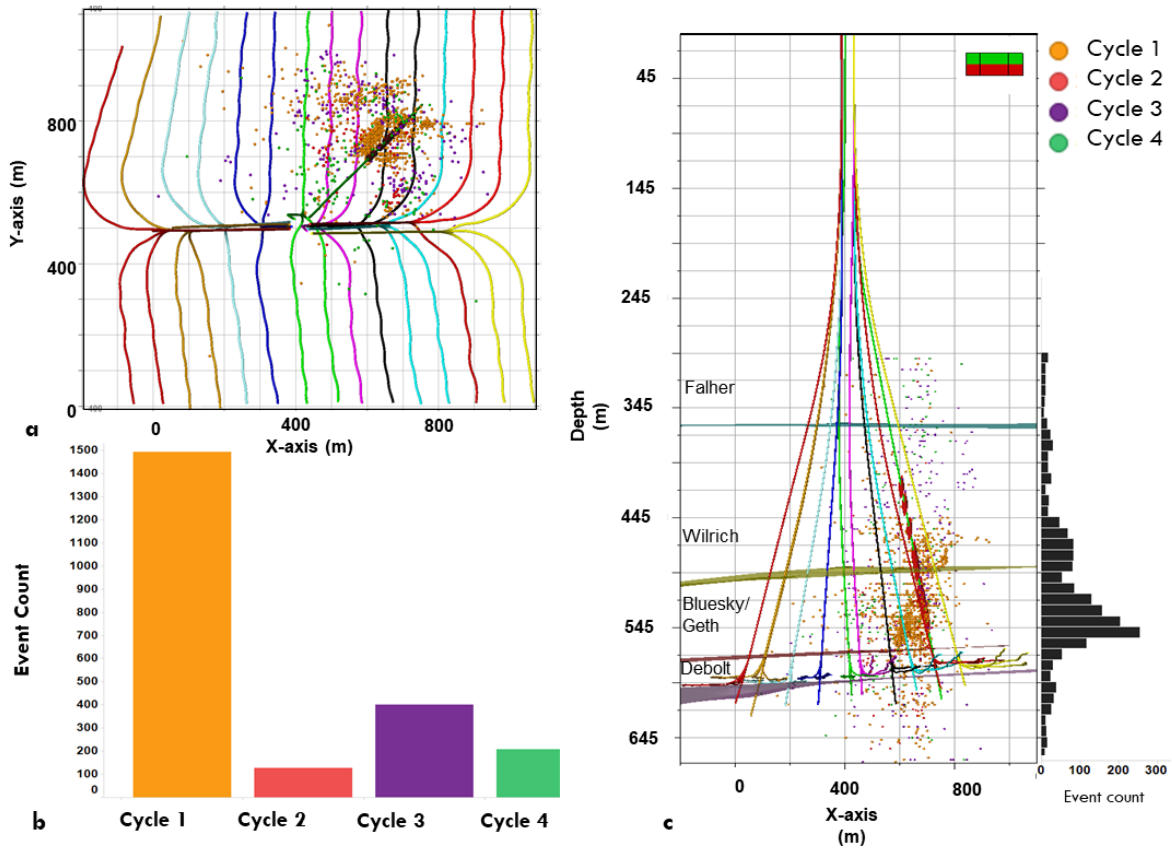


Figure 6-5: a) A map view of microseismic event location over the pad, b) Histogram of event count for each injection cycle, and c) Cross-section view and depth histogram of microseismic event distribution across the pad, horizontal colored lines indicate geological formations of interest, e.g., Falher Member, Wilrich Member, Bluesky, and Debolt Formations are shown as blue, yellow, red and purple colors, respectively. Microseismic events are colored based on their time of occurrence. Events that occurred during cycle 1, 2, 3, and 4 are colored as solid yellow, red, purple, and green circles, respectively.

The microseismic event locations used in this chapter are obtained from chapter 5. Over 2000 microseismic events were recorded during the four cycles of injection/production. Figure 6.5 shows the obtained locations, both in map view, East-West cross-section, and histogram, summarizing the event count per cycle. Several key observations can be made from the visual inspection of Figure 6.5. The histogram of event count per cycle indicates that most of the microseismicity was triggered during the first cycle, and lesser events were recorded during cycle 2, 3 & 4. The map view of event locations shows that large numbers of events are concentrated in the NE portion of the pad, forming a NE-SW trend close to the monitoring well. The majority of these events are clustered in the overburden (Wilrich and Falher Member), and a few are in the reservoir section (Bluesky Formation). The temporal trend of microseismic activity shows that 70% of events are recorded during the first injection cycle. When compared to spatial locations, these early locations are found to be tightly clustered. The microseismic activity recorded after the first cycle is relatively scattered around the monitoring well (Figure 6.5).

6.4.2 Moment magnitude

The moment magnitude is calculated to compare the intensity of microseismic activity. Figure 6.6 shows the histogram plot of moment magnitudes for all four cycles; a different color histogram is used for the comparison. The magnitude histogram of each cycle appears to follow the Gaussian distribution approximately. The magnitudes of the detected events vary from -3.8 to -0.6 (Figure 6.6), and events of magnitude -1.93 are most probable to occur.

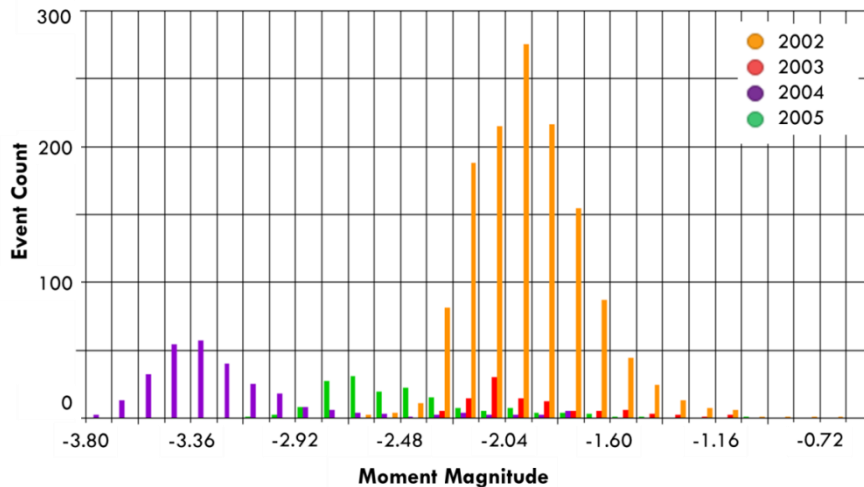


Figure 6-6: Histogram of calculated moment magnitudes of events recorded over four years. Different colors are used to show data from each cycle.

Interestingly, it is observed that the magnitude distribution is similar for the first two cycles and shifted towards lower values for the last two cycles. This is also evident from the mean magnitude values for each cycle. The mean magnitude values for four cycles are found to be -1.95, -1.93, -3.17, and -2.45, respectively. Note in Figure 6.6 that events with a magnitude less than -3 are only recorded for the third injection cycle, and events greater than -2.2 are detected during all cycles.

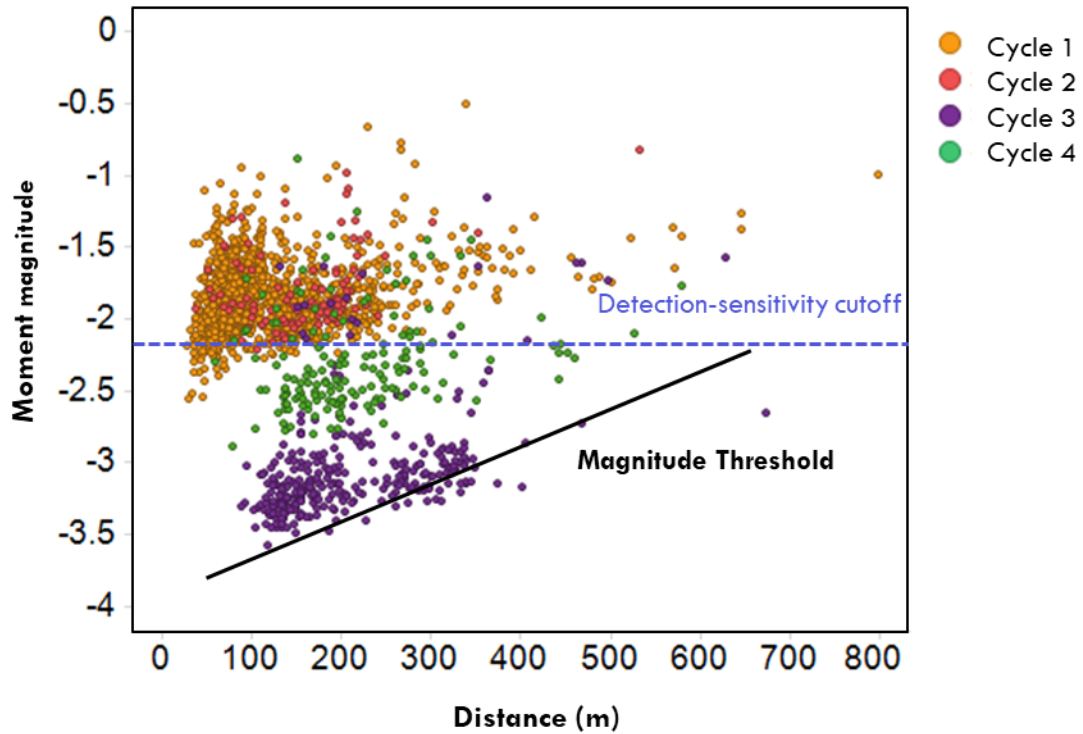


Figure 6-7: Magnitude versus distance plot for all data. The black line defines the magnitude detection limit for the data set, and the blue line indicates the detection-sensitivity cutoff.

To further analyze the moment magnitudes, it is a common practice to generate the magnitude versus distance plot. In the magnitude versus distance plot, smaller magnitude events are detected at distances of less than 200 m from the monitoring well, and large magnitude events are detected at all distances. Interestingly, when all the magnitudes are plotted together, it forms two separate clouds (Figure 6.7), indicating a shift in moment magnitudes (and possibly detection threshold) from cycle two onward. Next, the same magnitude-distance plot is used to define a magnitude threshold and apply the detection sensitivity cut-off to the dataset. Although the data appear to be clustered into two different clouds, I treat all the data as one data set to define the

parameters. The black line on the magnitude-distance plot in Figure 6.6 indicates the magnitude threshold, and the blue dotted line defines the detection sensitivity cut-off. The detection sensitivity cut-off is found to be -2.2, and any events of smaller magnitudes than -2.2 are excluded from further interpretation to accommodate the detection bias.

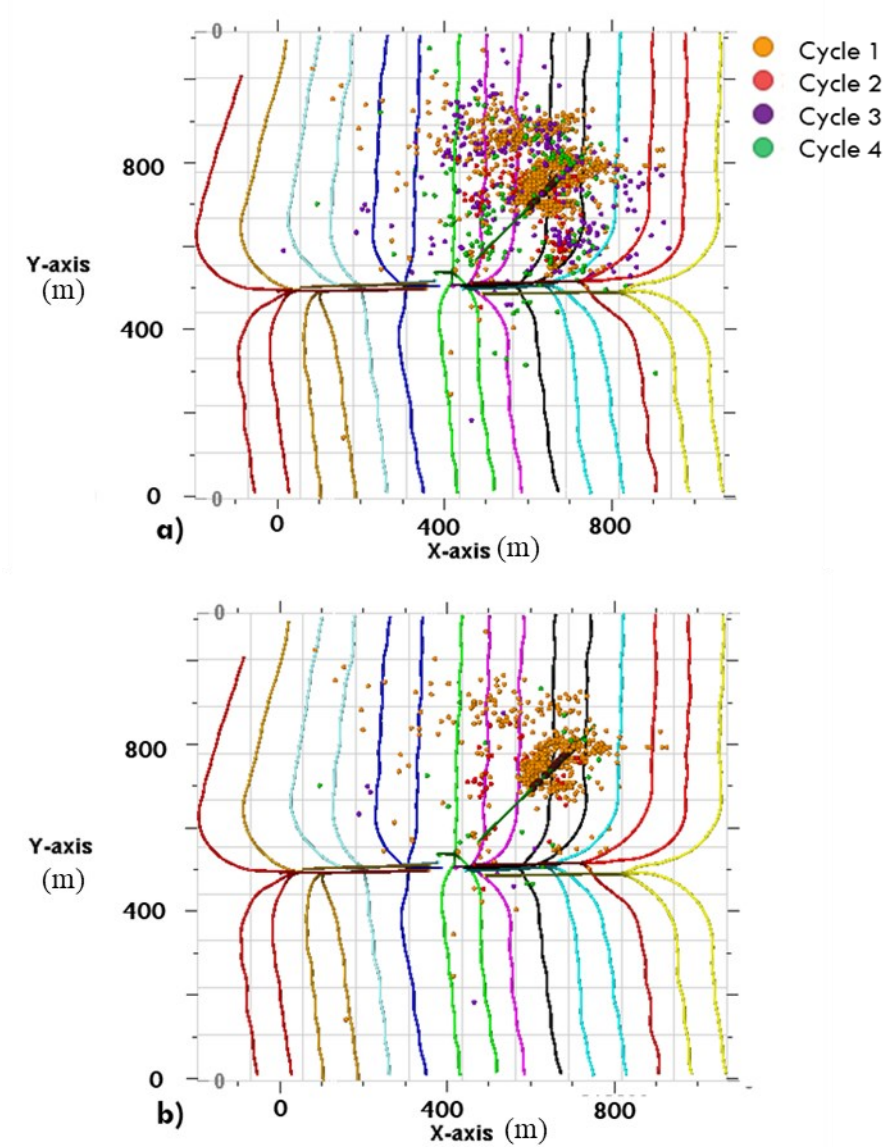


Figure 6-8: Map view of a) The magnitude biased event map and b) Magnitude-limited event map of the pad.

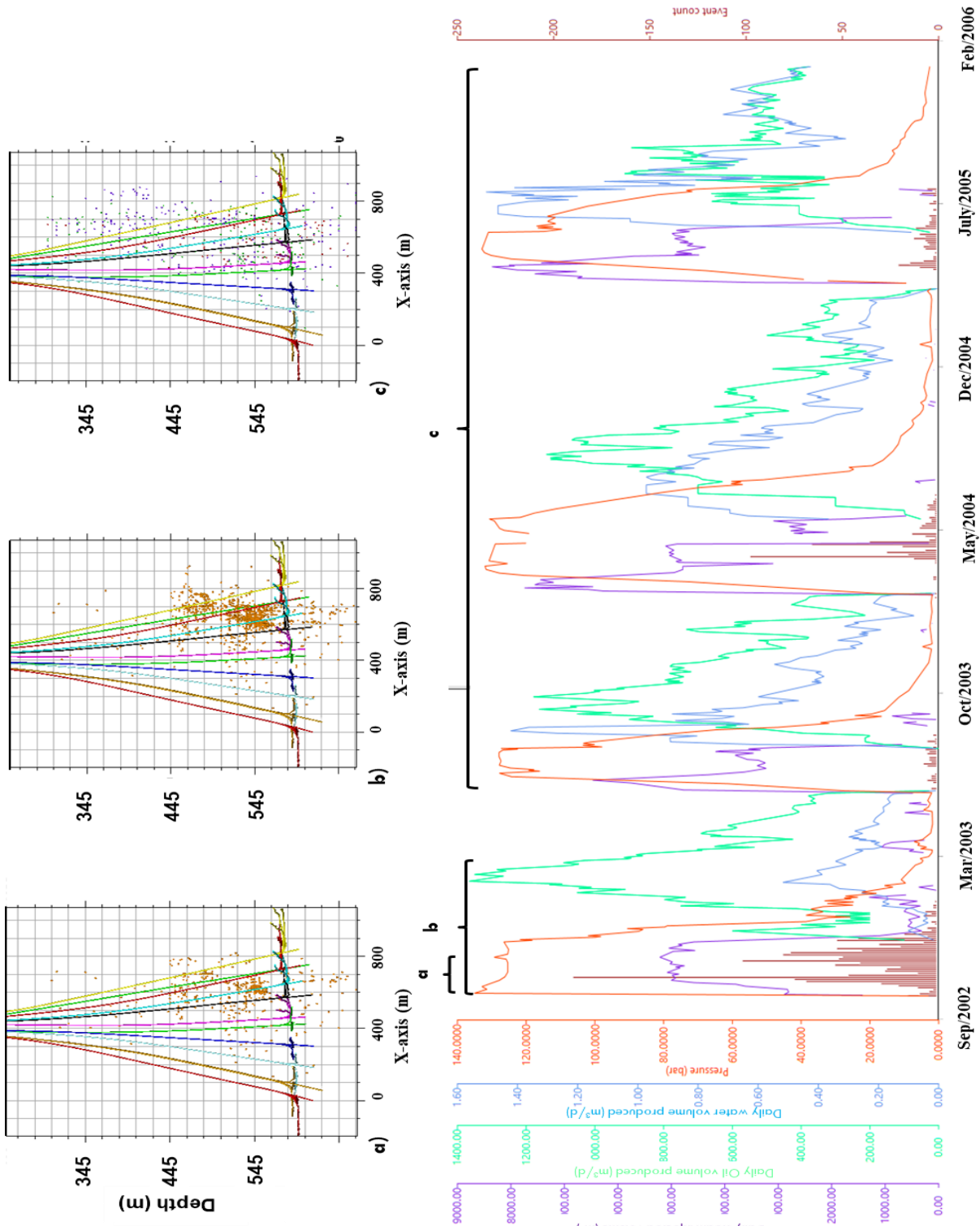


Figure 6-9: Time plot of injection pressure, microseismic event count, and production data over four years. The injected steam volume, water produced, oil produced, and injection pressure are shown in purple, blue, green, and red color, respectively. A dark red histogram shows the event frequency.

The effect of removing location bias is evident in Figure 6.8. The figure shows the map view of magnitude-biased versus magnitude-limited microseismic data over the pad. The magnitude-biased and magnitude-limited maps are substantially different. As expected, the number of events is reduced after removing the distance bias. The majority of the events removed from the data were recorded during cycles 3 and 4 and are minimally affecting the earliest recorded event count and trend. An important observation is that the spatial trend of the events does not change, and events are still found to be in the NE portion of the pad. This indicates that removing distance bias does not alter the spatial trend of event locations or affects the microseismic interpretation.

6.4.3 Integration of microseismic and engineering data

The microseismic data can be integrated with the engineering data, well configuration, and injection/production strategy to analyze any specific expression or anomalous trends in either data set.

The temporal trends of microseismic activity and engineering data can be seen in Figure 6.9. The steam injection volume and oil production curves are shown as purple and green. Microseismic events (dark red histogram) are detected during the steam injection phase, whereas silence is observed during the production phase; however, there appears to be no correlation between the injection volume and the resulting microseismicity.

The pressure profile reveals an interesting trend with the microseismic activity. At the start of the injection cycle, the injection pressure increases to the highest point (13.5 MPa). It is followed by the recording of the highest number of microseismic events. Then, injection pressure declines to 12.5 MPa, followed by a lower microseismic activity. The injection pressure then remains constant (12.5 MPa) throughout the injection cycles. The correlation between microseismic activity and pressure indicates a sudden increase in pressure and a noticeable increase in microseismic activity soon after the steam injection during the 1st cycle. The pressure and microseismicity activity then declined and never exceeded the previous peak value through the next injection/production cycles. This behavior indicates that the reduction in microseismicity after the 1st injection/production cycle may be related to the Kaiser effect.

Comparison of Figures 6.5 and 6.9 shows 75% of the microseismic events are recorded in the first steam injection and are confined to NE of the pad. This behavior of microseismic triggering may be characteristic of a fracture response (Maxwell, 2014) because of sudden triggering. It will be elaborated in detail in the next section

6.4.4 Brittleness index (BI)

The brittleness index is computed using equation 6.8. The depth profile of calculated rock properties, *BI* log, and event histogram are shown in Figure 6.10. A high value of *BI* indicates brittle rock. The high values of the Gamma-ray log (GR) above the reservoir indicate the presence of shale. The *BI* log shows smaller and mostly constant values within the reservoir interval as compared to the overburden. The *BI* values are mostly less than 0.5 in the reservoir interval, whereas a higher number of 0.6 to 0.7 is present in the overburden. The *BI* values can be roughly quantified into two groups, approximately 75% of microseismicity is associated with $BI > 0.5$, and the remaining is linked to $BI < 0.5$.

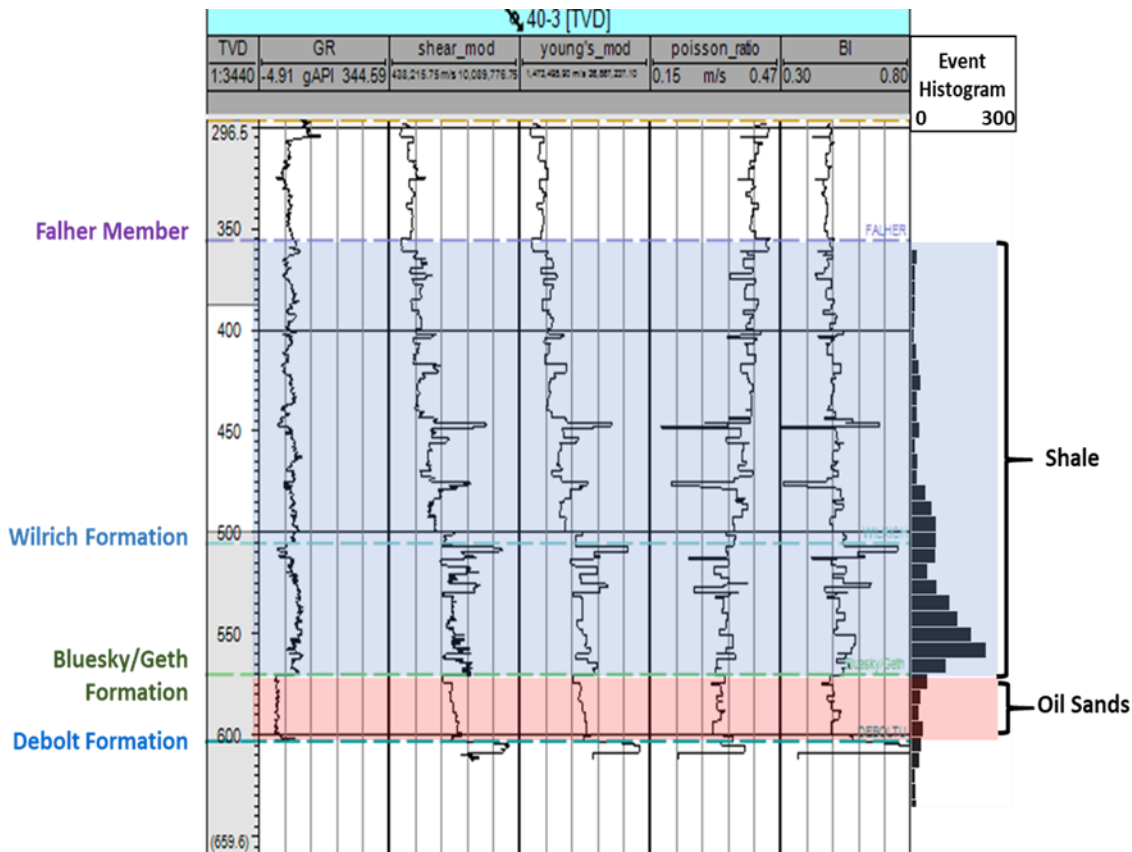


Figure 6-10: The GR log, calculated Shear modulus, Young’s modulus, Poisson’s ratio, and Brittleness Index log for well 40-3, located on the western side of the pad. The histogram on the right shows the microseismicity occurrence at different depths.

6.5 Discussion

The majority of the recorded microseismicity is found to be in the overburden; only a small number of events occurred within the reservoir interval. Although microseismicity in the overburden is not desirable, it does sometimes occur, raising questions about caprock integrity and fluid containment. In comparison with other thermal oil recovery monitoring experiments, a similar pattern of microseismicity is observed. For example, microseismic data from the Cold Lake CSS experiment revealed that microseismic events are clustered at shallow depths (200 to 400m). The peak of microseismic activity is at 400m depth, just above the Clearwater reservoir interval (Miyazawa et al., 2008). Urbancic & Jeziorski (2015) investigated data recorded over a heavy oil reservoir undergoing steam injection for approximately two months followed by a two-month soak cycle. During this time, microseismic events were observed to grow vertically upward into the caprock layers.

The map view of event locations (Figure 6.5) shows that microseismicity is confined in the north-eastern portion of the pad, very close to the monitoring well. The rest of the pad appears to be silent: no microseismic activity is recorded. Figure 6.5 shows the cross-sectional view of the pad from the south displaying a decrease in reservoir thickness from west to east. The top reservoir is seen to be dipping. The wells in the eastern half of the pad appear to be at a shallow depth compared to the western half of the pad. Could this be part of the reason why microseismicity is confined to a certain part of the pad? This possible correlation between microseismicity and geometry is confirmed by calculating the landing point/height across the pad.

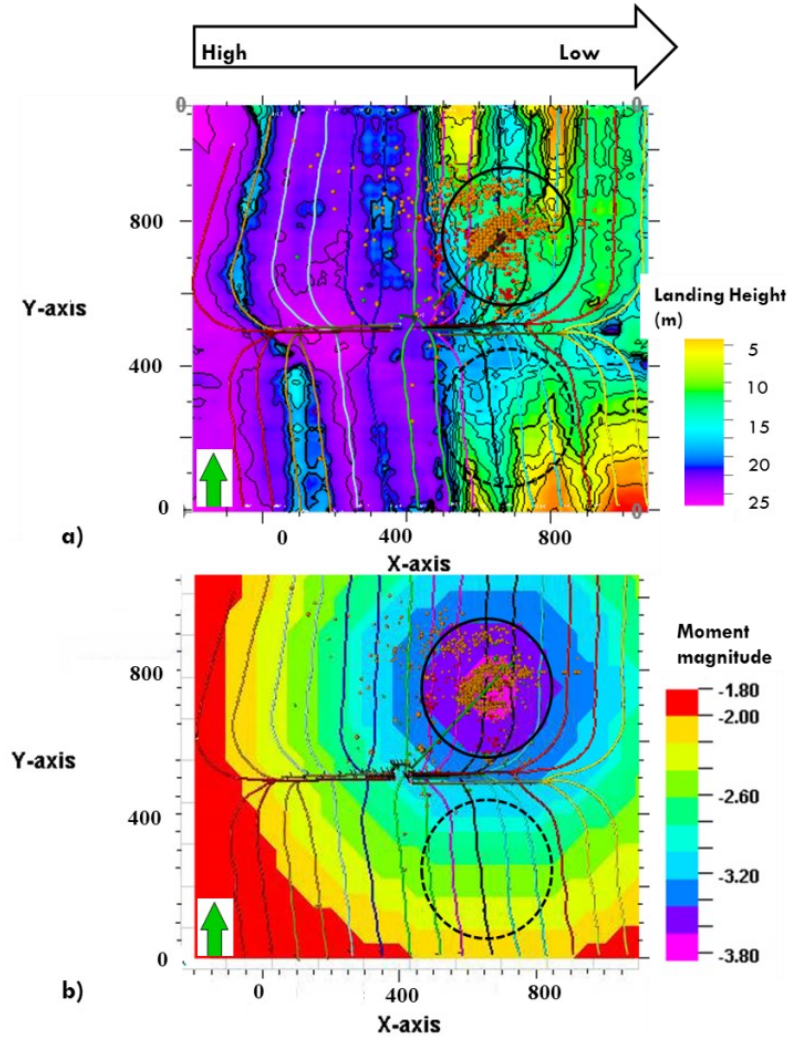


Figure 6-11: Map view of a) landing height and b) magnitude threshold limit overlain by the magnitude limited event map over the pad.

Figure 6.11a shows the landing height across the pad overlain by the well trajectories and microseismic event locations. The landing height varies between 3 to 25 m at the pad. The pad may be divided into the eastern and western half based on the landing height values (as clearly shown in figure 6.11a), and the microseismic event locations are all located on the northeastern side of the pad. On the other hand, the southeastern portion of the pad appears to be silent, although the landing height values are similar to the northeastern side of the pad.

The events must be threshold limited in terms of their magnitudes to achieve a reliable interpretation. This reduces the size of the data set, but it is necessary to remove the acquisition biases. Failure to apply the magnitude threshold to data can severely impact the qualitative and quantitative interpretation (length of fractures, size of the simulated zone). This is evident from the

simulation study by Grob & Van der Baan (2016) and observed by Pike (2014). The low magnitude events and S/N ratio can lower the detection limit, thus further reducing the size of the data set. Figure 6.11b shows the magnitude threshold map overlain by event locations corrected by the detection-sensitivity cut-off. The colored map shows the magnitude of events that can be detected at a certain distance. According to the threshold map, the events in the south-eastern portion of the pad must be of magnitude -2.2 and higher to be recorded by the monitoring array; however, there are no recorded events above the cut-off magnitude, indicating that the south-eastern portion of the pad did not have any microseismicity.

It must be noted that the threshold map is generated by incorporating all the events recorded during four cycles, even though events after cycle two are of very low magnitude and S/N ratio. It is not clear what may have caused the shift of magnitudes towards the lower values. But one possible reason may be the change in the acquisition set up after the second injection cycle; the operator reduced the number of receivers recording the data from ten to eight. The magnitude threshold and detection cut-off are defined by incorporating all the recorded data. On the other hand, excluding the low magnitude events from the analysis will increase the detection sensitivity cut-off, resulting in fewer events for further analysis. Nonetheless, most of the events are found to be on the northeast side of the pad. Hence, I anticipate that excluding smaller events from the analysis will not change the fracture interpretation.

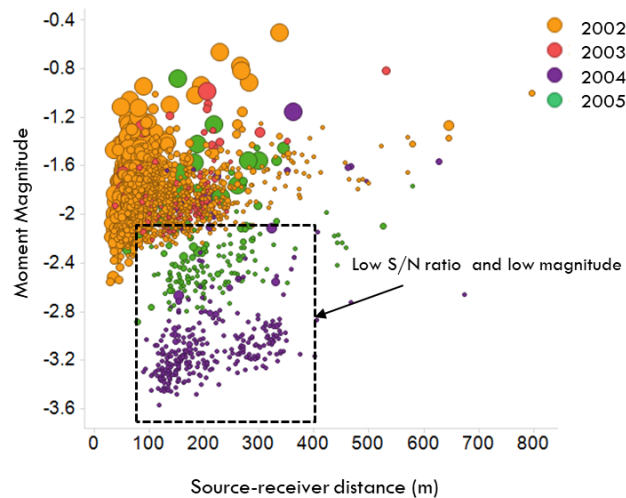


Figure 6-12: Magnitude-distance plot of all the recorded events, data points are shown by different colors and sizes to indicate the time of occurrence and S/N ratio. A smaller size indicates a low S/N ratio, and a larger size indicates a high S/N ratio event.

Next, it is necessary to understand why (90%) of microseismicity occurs above the reservoir as it is undesirable to have microseismic activity in the overburden. The absence of microseismicity in the heavy oil reservoir may be justified geomechanically. The heavy oil acts as viscoelastic, at room temperature heavy oil is solid, but as the temperature increases the viscosity of the oil decreases (Chopra et al., 2010). Moreover, it is highly unlikely to have brittle failure in fluid. Therefore, it is fair to hypothesize that new fracture creation is much easier in the shale than in the heavy oil sands. The hypothesis is tested by comparing the calculated *BI* values of the reservoir and overburden shale interval. The lower values of *BI* (<0.5) within the reservoir and higher values (>0.5) in the caprock shales indicate that the shales are more brittle and can result in more microseismic activity because of fracture creation. It must be mentioned here that the absence of microseismic activity within the reservoir interval is not always expected, but it depends on the brittle nature of the rock. Therefore, if the reservoir is more brittle (for example, carbonate) than the overlying shales, then a significant amount of microseismicity is expected. This has been observed during the thermal recovery of heavy oil from carbonate rocks in Oman (Al Hooti et al., 2019).

The majority (75%) of the microseismicity occurred during the first steam injection cycle, forming two clusters above the top Bluesky Formation and Wilrich Member. Therefore, it is essential to investigate the possible mechanism responsible for the temporal distribution of the clusters. In a hydraulic fracturing experiment, injection and pressure profiles along with microseismic event count are generally used to infer fracture initiation, as shown in Figure 6.13 (Maxwell, 2014). The sudden increase in microseismic activity immediately followed by higher injection pressure may be associated with fracture initiation (figure 6.13a), whereas constant microseismic activity throughout the process may be caused by uniform fracturing (figure 6.13b) because fracturing/faulting results in a sudden increase in the number and the magnitude of microseismic events. The same concept may be applied here to investigate the two clusters.

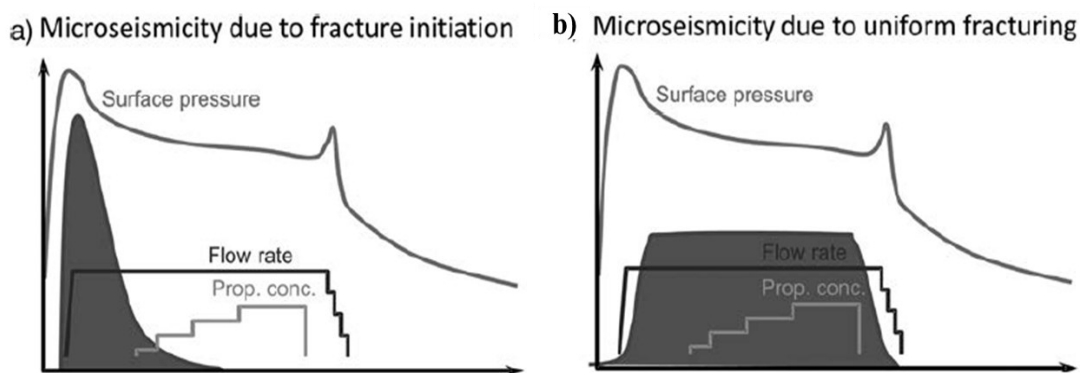


Figure 6-13: Schematic diagram showing two possible interpretations of microseismic event occurrence relative to surface pressure. The dark gray color shows the microseismic event histogram (reproduced with permission from Maxwell, 2014).

Figure 6.14 shows a plot of pressure and occurrence of the microseismic events for the first injection cycle. The three time intervals are marked on the chart as phase (a), (b), and (c) and corresponding time-stamped cross-sectional views of event locations.

Microseismic activity is recorded as soon as the injection pressure increases and reached a maximum count of about 200 events a day during phase (a). Then, the event distribution curve starts to decline, phase (b). Carefully inspecting the event locations in the cross-section reveals that during phase (a), the majority of microseismicity is triggered right above the reservoir, trending upward. Once the event count declines during phase (b), the microseismic cloud develops into two clusters, both at the boundary of the overburden geological formations. The pressure and event count curves in Figures 6.13 and 6.14 are nearly similar. Therefore, comparing both Figures (6.13 & 6.14) indicates that events recorded during phase (a) are associated with fracturing initiation, and events recorded during phase (b) are due to fault propagation. The microseismicity recorded after cycle one is relatively minimal and broadly scattered (Figure 6.9), indicating uniform and minimal fracturing. These event clusters are found to be associated with higher values of BI, as shown by the depth profile of the BI log.

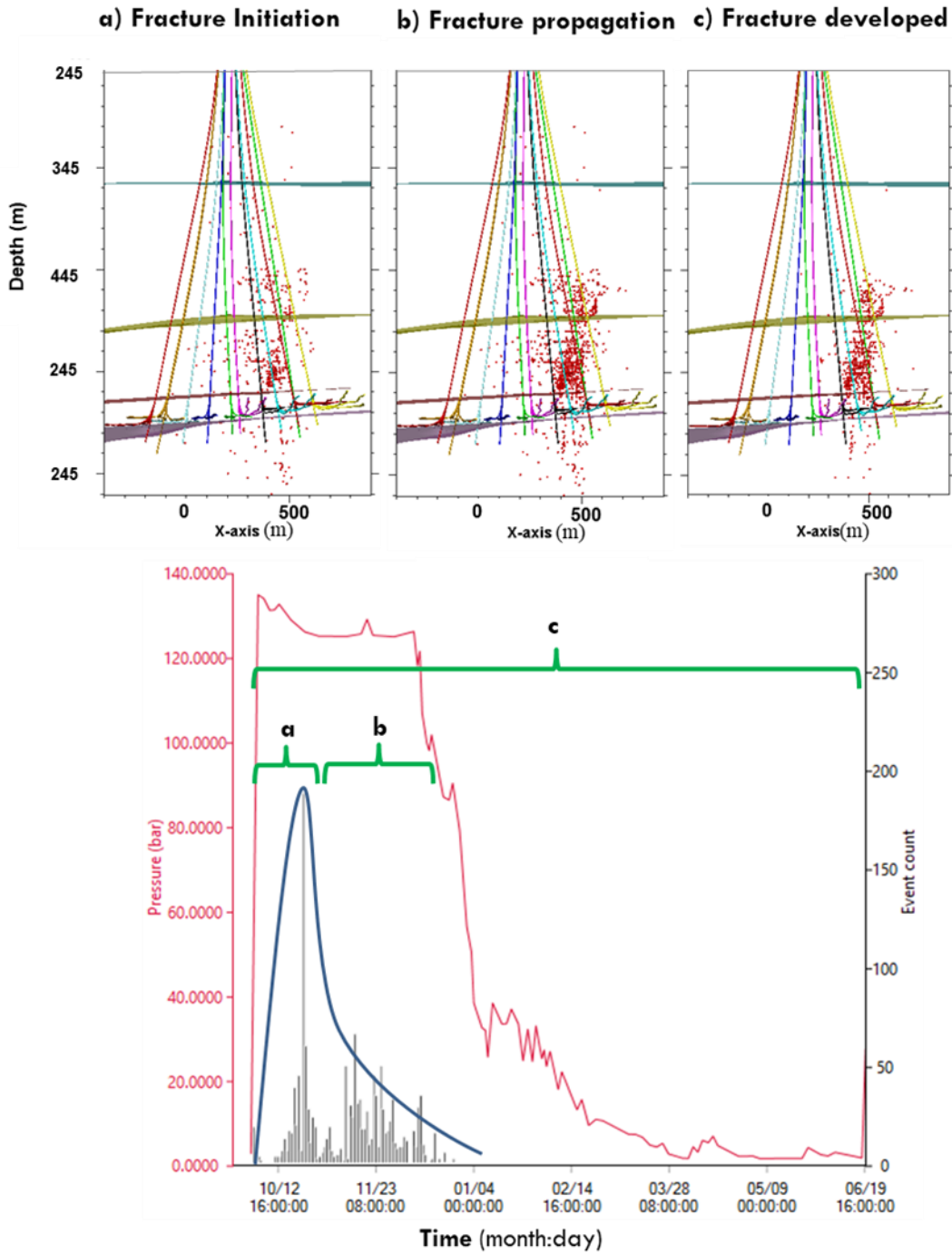


Figure 6-14: Time plot of simulation parameters (injection pressure, event count) and potential interpretation for cycle 1. The three time intervals are marked on the chart as phase (a), (b), and (c) (bottom) and corresponding time-stamped cross-sectional views of event locations (top). Pink line is the injection pressure, dark blue line shows the trend of microseismic histograms (light grey).

The two microseismic clusters are interpreted to be linked with two fracture planes (F1 and F2), trending in the NE-SW direction, having a dip of 10° (Figure 6.15). The fault F₁ is the shallow

and smallest of the two, just above the top Wilrich shale. F₂ is the largest and deeper fault, located above the top reservoir within the Wilrich shale. Fault F₂ initiated first, followed by fault F₁.

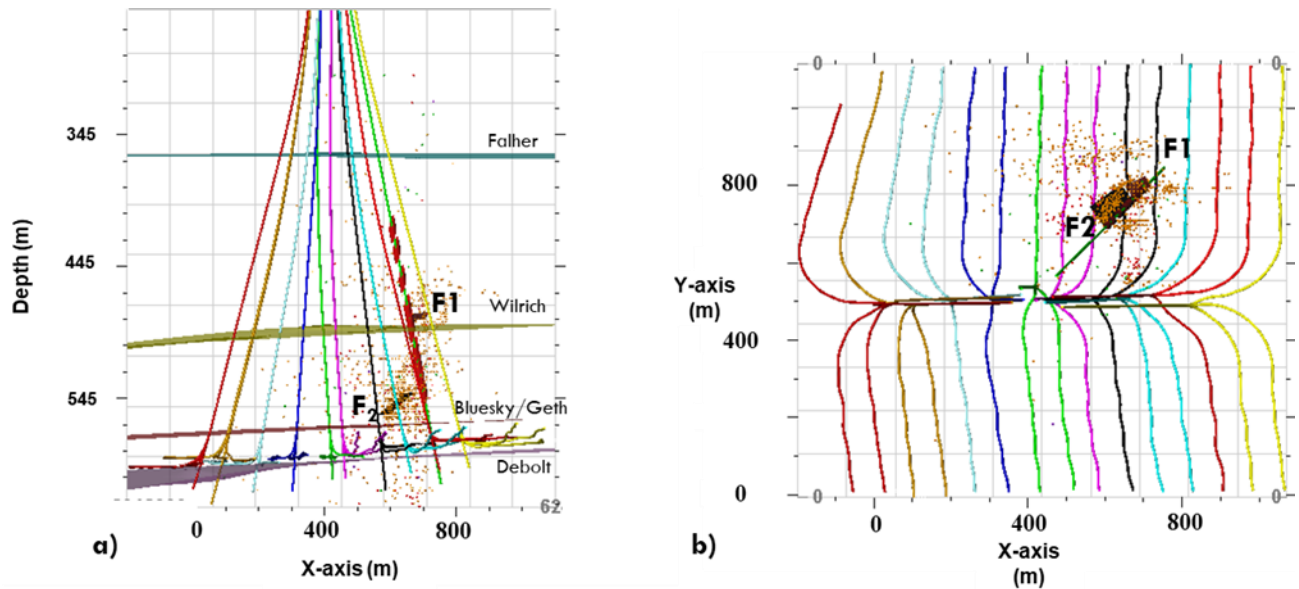


Figure 6-15: Interpreted fault/fracture planes in a) cross-sectional and b) map view overlay by the magnitude limited event locations.

The microseismic event clusters in the overburden may be due to fluid leakage or stress changes and must be investigated. In general, overburden clusters may suggest fluid leakage from the reservoir into the overburden and may concern future operations. An r-t plot (distance from injection point-time plot) is generated and analyzed, as shown in figure 6.16. The plot shows that most of the microseismic triggering occurred about 20 days after the steam injection, navigating vertically upward (encircled in figure 6.16) at a distance of 20 and 80 m above the reservoir zone. The time delay of 20 days between injection and microseismic triggering is sufficient for fluid migration. On the other hand, no pressure data or any incidences were reported to support the fluid leakage hypothesis, and steam injection continued for the rest of the cycles, although at a slightly lower pressure.

Having analyzed and interpreted the microseismic data, the next necessary step is to relate the findings with the predictions in chapter 3. One of the main findings of this chapter is the occurrence of microseismicity in the overburden shales. This observation validates my prediction that majority of the microseismic activity is expected in the overburden because of the brittle nature

of the caprock. However, most of the events occurred during the injection phase, and limited microseismicity activity occurred during the production cycles. Additionally, it was also assumed that reservoir fluid does not escape into the caprock. Based on the above data and observations derived from microseismic data alone, it is difficult to say with confidence if fluids may or may not have migrated into the caprock. It is also difficult to comment on the steam front evolution because of limited microseismic activity (only ~10%) within the reservoir. Therefore, seismic data will be analyzed in the next chapters to investigate 1) the presence of existing fractures, which may have provided a path for fluid migrations and, 2) the occurrence of any amplitude changes in the time-lapse seismic data, possibly due to the changes in fluid saturation in the overburden.

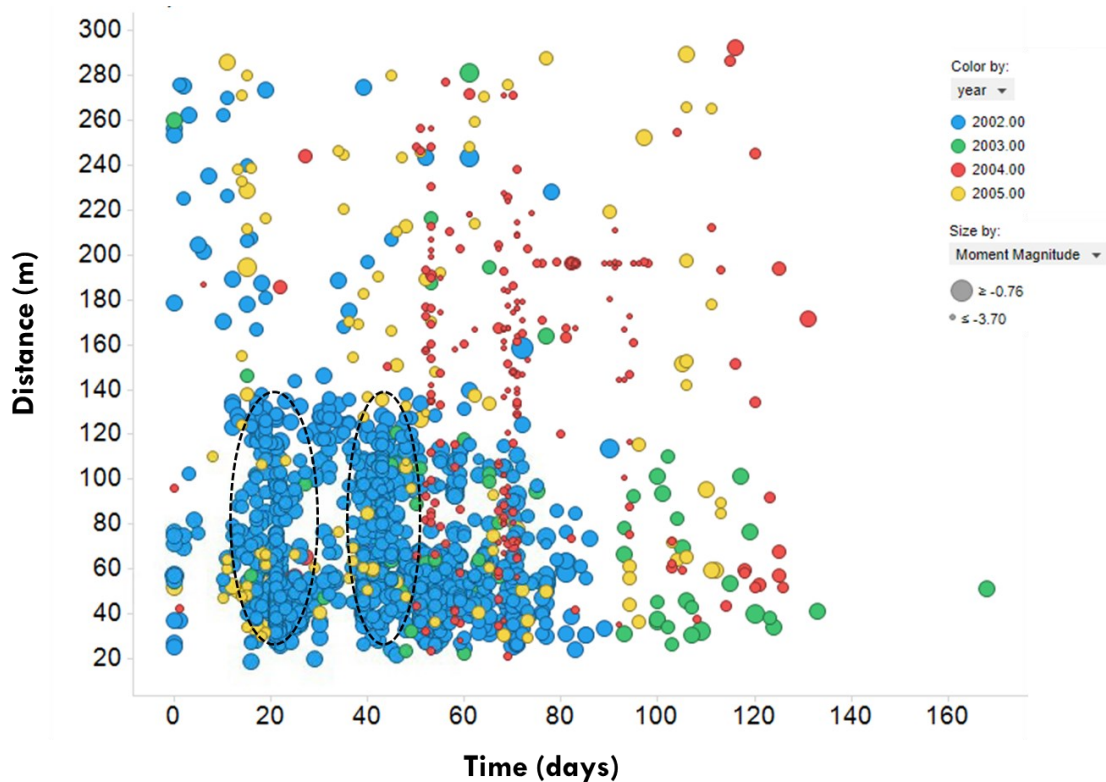


Figure 6-16: The r-t plot of induced microseismic data, different colors indicate data recorded during different cycles, and vertically extended events are encircled in black.

6.6 Conclusion

It is concluded that during the CSS experiment, the microseismic events are more likely to occur in the overburden than in the reservoir because of the brittle nature of shale in the overburden. This is supported by high *BI* values and microseismic clusters above the heavy oil reservoir. In addition to the rock physics properties, microseismic activity in the overburden is also

facilitated by low landing height. A low landing height will result in an injection point being very close to the top of the reservoir, thus possibly triggering microseismicity in the overburden. It is further concluded that microseismic monitoring proves to be a valuable tool in heavy oil monitoring experiments by providing detailed insight into the changes occurring in the overburden, as evident by the recording of an abundance of microseismicity. However, it is still unclear if fluid migration or stress changes caused microseismic triggering in the overburden. It may be possible to resolve this question after analyzing the seismic data and integrating all available observations for this field.

7 Time-lapse seismic data interpretation

7.1 Introduction

Time-lapse (4D) seismic monitoring is an effective technique to monitor the reservoir. It has been extensively used within the North Sea, where repeated marine streamer data have been acquired on fields with aquifer drive, e.g., the Gannet fields (Kloosterman et al., 2003; Staples et al., 2005), or water injection drive, e.g., Draugen (Koster et al., 2000). The technique is also proven to be applicable for monitoring of gas flood (e.g., Troll West; (Eikeberg & Elde, 2002)), solution gas breakout e.g., Foinaven oil field (Kristiansen et al., 2000), and steam injection e.g., Duri (Sigit et al., 1999). The main objective is to image the changes within the reservoir due to steam/water injection, oil/water/gas production, or CO₂ storage. For CSS operations, the objective is to identify areas impacted by steam, undergoing production, and areas not impacted by the injection/production operations.

The time-lapse seismic data used in this study consist of 2D seismic lines acquired over a pad undergoing CSS. The baseline survey was recorded before the start of the steam injection, and a monitor survey was acquired after four years (covering four cycles) of steam injection and production. The monitor data contain elevated temperatures due to the formation of steam chambers within the reservoir interval. A strong contrast is expected between the baseline and monitor surveys. The amplitude difference volume is calculated by subtracting the baseline survey from the monitor survey to analyze and interpret the changes. It is assumed that the changes are solely due to steam injection and oil production, but this is not necessarily true everywhere. Several other factors may also contribute to these changes, e.g., the difference in survey acquisition parameters, processing workflow, and near-surface velocity changes, affecting the phase and amplitude of the monitor survey. Therefore, it is important to understand and correct the monitor survey for these changes to avoid misinterpretation.

This chapter aims to understand the steam movement inside the reservoir and identify areas the steam may have bypassed. This will be achieved by applying a calibration workflow to the monitor survey to suppress the difference due to non-production-related factors and enhance the production-related changes. Then, a difference volume is calculated, which forms the foundation for the time-lapse seismic analysis.

7.2 Workflow: time-lapse analysis

The time-lapse seismic analysis followed in this study is broadly divided into three steps, well to seismic tie, data comparison, and difference volume.

7.2.1 Well to seismic tie

The first step is to interpret the temporal positions of the geological horizons on seismic data. The seismic data are in the time domain, and a well profile is always in the depth domain. To generate a synthetic seismogram, sonic and density logs are multiplied to obtain an impedance curve, which is then used to generate reflectivity series at the interface between contrasting velocities. Then the reflectivity series is convolved with the wavelet to generate a synthetic seismic trace. The wavelet may be extracted from the seismic data, or a synthetic wavelet can be generated. The synthetic seismogram may be bulk shifted or stretched/squeezed to match the prominent reflections with those on seismic data to achieve a good tie between synthetic seismogram and seismic data, to be able to trace horizons of interest at depth on seismic data in time (Badley, 1985).

7.2.2 Data comparison

Although both baseline and monitor data are acquired and processed identically, there are some differences between baseline and monitor data due to seasonal variation and noise level. Thus, before calibrating the monitor data, it is recommended to compare both datasets to understand how both datasets are different. It is done by calculating and comparing the cross-correlation, time shifts, and amplitude spectrums between baseline and monitor survey within the reservoir and overburden (caprock) strata.

7.2.2.1 Normalized RMS

The NRMS attribute, defined as the normalized root mean square of the difference between two datasets, is routinely used as a quality control measurement for time-lapse data. The NRMS difference is calculated by taking the difference between the two datasets on a sample-by-sample basis as

$$NRMS = \frac{2 * RMS(B-A)}{RMS(A)+RMS(B)} , \quad (7.1)$$

where A is the baseline survey, and B is the monitor survey, and RMS is the root mean square operator defined by Kragh & Christie (2002) as:

$$RMS = \sqrt{\frac{\sum_{t_1}^{t_2} (x_t)^2}{N}}, \quad (7.2)$$

where N is the number of samples in the time interval of t_2-t_1 , and NRMS is the normalized root means square. The NRMS measures the difference between the two surveys over a selected time interval. The NRMS values range between 0 to 200%, where 0 means identical and 200 means completely different data (Kragh & Christie, 2002). It is difficult to obtain 0% NRMS; rather typical values of NRMS after calibration is in the range of 10-30% or a little higher due to acquisition issues. Koster et al., 2000 documented an average value of 35%, whereas Kommedal & Barkved 2005 and Eiken et al. 2003 quoted much lower NRMS values, e.g., 14% and 6-12% respectively for the Draugen field. The variation in the calculated NRMS values is because of its sensitivity to small data changes, including noise, phase shifts, and amplitude differences (Kragh & Christie, 2002).

7.2.2.2 Cross-correlation

The cross-correlation attribute provides correlativity of two datasets, where similar or identical events will have a high correlation value and a lower value indicates dissimilar traces/data. Cross-correlation is a commonly applied processing technique, where a stationary trace (baseline) is matched to a corresponding sliding trace from the input (monitor) over a specified window. The process is described as shift, multiply, and add operation. For two given waveforms, $f(t)$ and $g(t)$, the cross-correlation function is defined as

$$(f * g)(\tau) = \sum_{-\infty}^{\infty} f^* g(t + \tau) dt, \quad (7.3)$$

where $*$ refers to complex conjugate, and τ is the time lag between the two signals. The calculated cross-correlation values are interpreted in conjunction with the computed time-shift values. The time-shift values display the time values (or lag) in msec required to produce the corresponding cross-correlation values.

7.2.3 Time-lapse calibration

Figure 7.1 shows the time-lapse calibration workflow applied in this study. The calibration was performed in six steps as follows 1) time and phase matching, 2) shaping filter, 3) static correction, 4) time-variant shifts, 5) amplitude matching, and 6) difference volume.

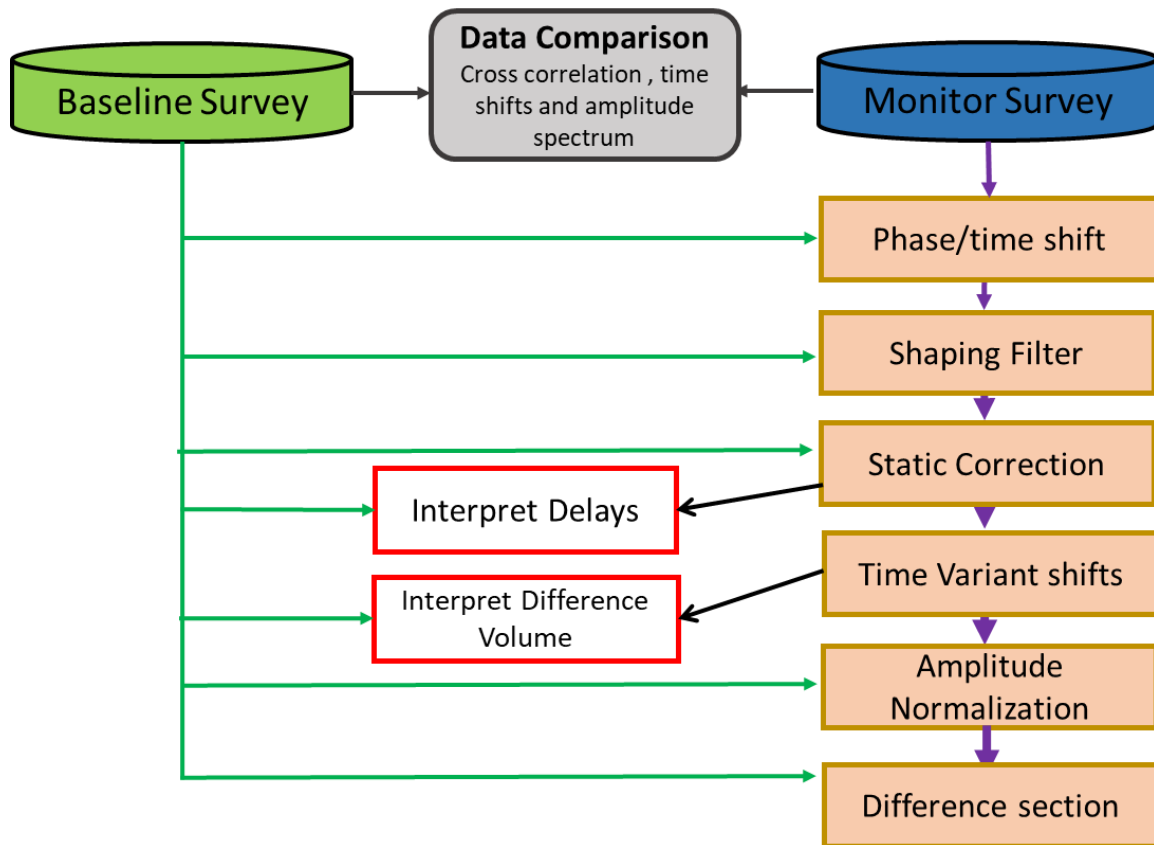


Figure 7-1: Flow chart showing the time-lapse calibration workflow followed in this study.

7.2.3.1 Phase/time shifts

The first step is to apply phase rotations and bulk time shifts to monitor survey while keeping the baseline survey as a reference. The step is necessary to remove nonproduction related changes from the monitor survey, ensuring both surveys are similar in terms of phase and time. The time shift is estimated by making a time pick on the envelope amplitude of the cross-correlation of the base to monitor survey. The phase shift is estimated by picking on the instantaneous phase of cross-correlation corresponding to the time of envelope maximum (Ng, 2005).

7.2.3.2 Shaping filter

This step derives and applies a shaping filter to the monitor survey. This process is used to match the wavelet and amplitude spectrum between the surveys to minimize the differences outside the area of interest. The filter adjusts the monitor survey wavelet to best match the wavelet of the baseline survey in a least-square sense (Rojas & Davis, 2009; Yilmaz, 2001). It is achieved by calculating the shaping filter (a_i) using the autocorrelation (r_i) of the monitor wavelet with the cross-correlation of baseline and monitor wavelet (g_i), as

$$\begin{pmatrix} r_0 & r_1 & \cdots & r_{n-1} \\ r_1 & r_2 & \cdots & r_{n-2} \\ \cdots & \cdots & \cdots & \cdots \\ r_{n-1} & r_{n-2} & \cdots & r_0 \end{pmatrix} \begin{pmatrix} a_0 \\ a_1 \\ \cdots \\ a_{n-1} \end{pmatrix} = \begin{pmatrix} g_0 \\ g_1 \\ \cdots \\ g_{n-1} \end{pmatrix} \quad (7.4)$$

The monitor and baseline wavelets are extracted by selecting a time window above the reservoir. The shaping filter estimates a function that matches the frequency, time, and average power of both datasets. The shaping filter a is then applied to the monitor data (Robinson & Treitel, 2000; Yilmaz, 2001).

7.2.3.3 Static corrections

It is desirable to process baseline and monitor surveys similarly; different static solutions were applied to both surveys due to the differences in acquisition parameters, seasonal variation, or any changes in the ground conditions (Tran et al., 2003). The shallow static step calculates the time shift by trace-by-trace cross correlating the monitor and baseline data above the reservoir; then, the time shift is applied to the monitor data to match the shallow reflector to those of baseline data. This step can spatially position the reflectors because of the difference in NMO and migration velocity functions between the two surveys (Rickett & Lumley, 2001).

This step is different from the phase and time shift as this calculates the time shifts trace by trace rather than as a global correction, which applies a one-time phase shift to all the data.

7.2.3.4 Time-variant shift

Time-variant statics are applied to compensate for the velocity related changes in the reservoir affecting the events beneath. It is similar to the previous steps except that more design windows are chosen so that data are matched above and below the reservoir. Thus, two time shifts are derived from the cross-correlation analysis, and time shifts between the two windows are interpolated. This step tries to match the base and monitor data in terms of time, above, within, and below the reservoir. After time deficiencies have been minimized, amplitudes can be compared.

7.2.3.5 Amplitude matching

The amplitude differences between baseline and monitoring surveys can be due to several reasons, e.g., scaling differences, differences in survey acquisition, data processing, and surface variations. On the other hand, amplitude differences between the baseline and monitor surveys

within the reservoir should be characteristic of steam injection and/or production. To correctly identify differences due to steam injection/production, the RMS amplitude of both surveys are matched and normalized via an amplitude scalar to balance the amplitudes statistically. The amplitude scalar is defined by calculating the RMS amplitude of baseline and monitor data within the defined window. The ratio of the RMS values is then applied to the monitor data, which defines the scalar.

7.2.3.6 Difference volume

The last step of time-lapse calibration calculates the difference volume by subtracting the calibrated monitor survey from the baseline survey. The difference volume is expected to remove all repeatable traces, highlighting amplitude anomalies within and around the reservoir due to steam injection and production.

7.3 Results

The above workflow was applied to the time-lapse 2D seismic data acquired over the heavy oil reservoir (Figure 7.2). The dataset consists of fifteen east-west trending 2D reflection seismic lines recorded before steam injection (baseline survey) and after four years of steam injection (monitor survey).

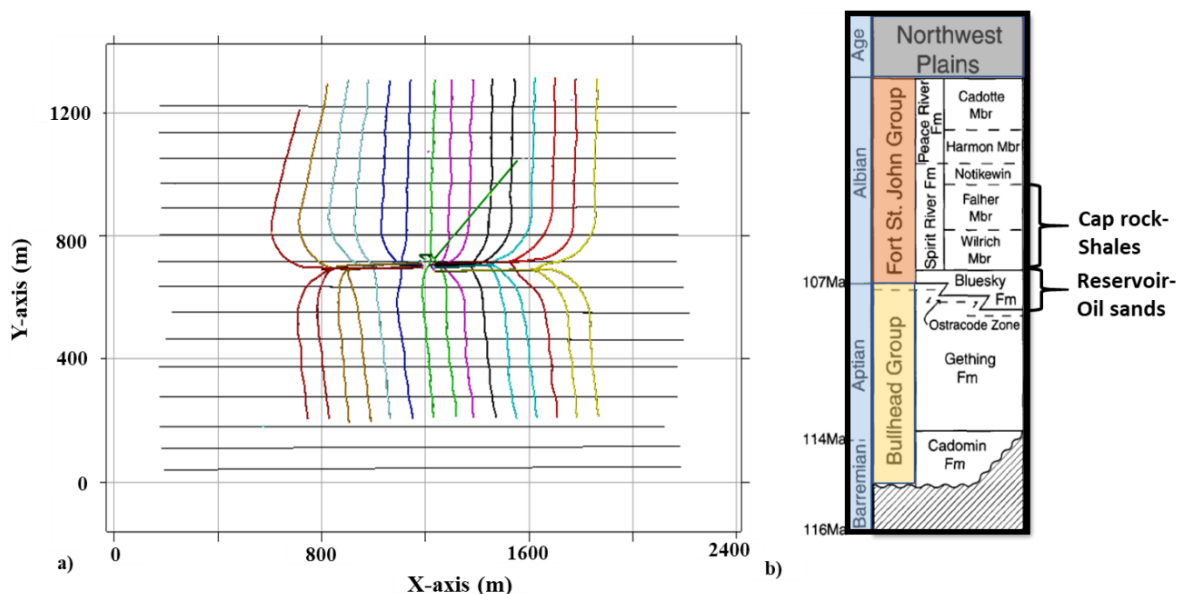


Figure 7-2: a) Basemap of the study area showing the location of seismic and well trajectories and b) stratigraphic section highlighting the geological formations of interest.

7.3.1 Horizon interpretation

Figure 7.3 shows the synthetic seismogram of well 40-3 and its tie to the seismic line. The synthetic seismogram was bulk shifted and stretched/squeezed to match the prominent reflections on the seismic data.

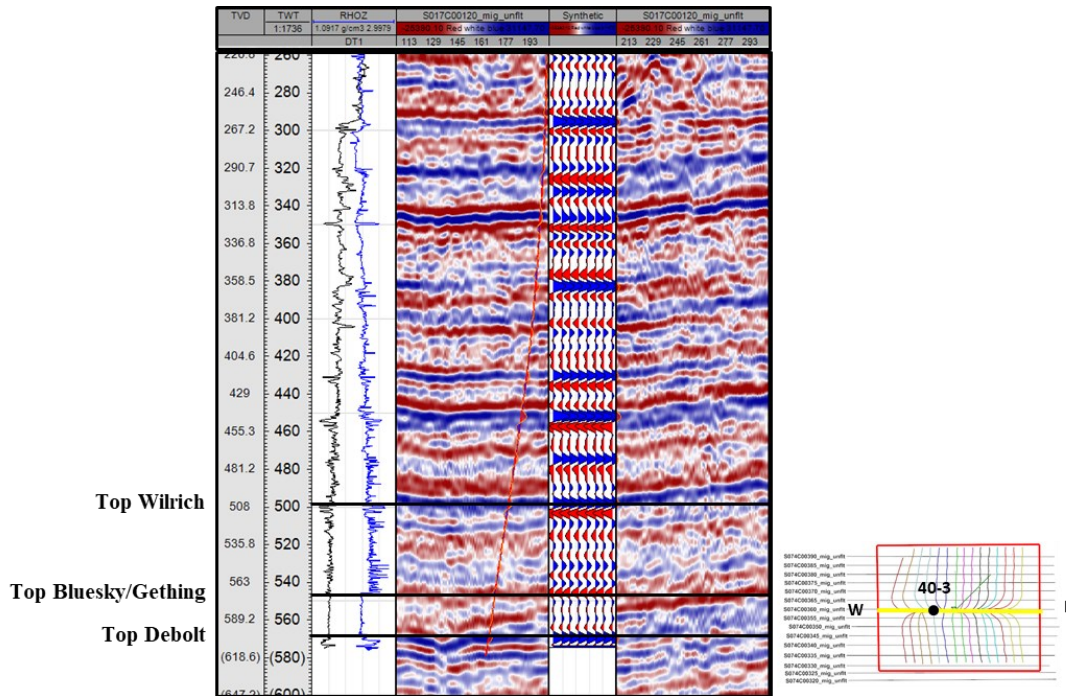


Figure 7-3: Well to seismic correlation of well 40-3 from pad 40, showing a match between seismic reflectivity and synthetic seismogram for the three geological horizons of interest. The red and blue colors on seismic and synthetic log indicate negative (trough) and positive (peak) amplitude.

Once a good match is achieved, geological horizons of interest are marked on the seismic line. The main geological units of interest are Wilrich Member of Spirit River Formation, Bluesky Formation of Lower Cretaceous age, and Mississippian carbonates of the Debolt Formation. Following the well to seismic tie, geological horizons of interest were picked on the baseline and monitor data and quality controlled at each seismic line before generating two-way time (TWT) maps. The picked horizons are shown on the east-west seismic line in Figure 7.4. In addition to the top reservoir and caprock, I also picked a continuous strong reflector on seismic data at around 340ms (approximately 200ms above the top reservoir). The general understanding is that steam injection and oil production in the reservoir should not impact the TWT of the shallow reflectors.

This assumption is used to quickly compare and correct any discrepancies in TWT between baseline and monitor surveys.

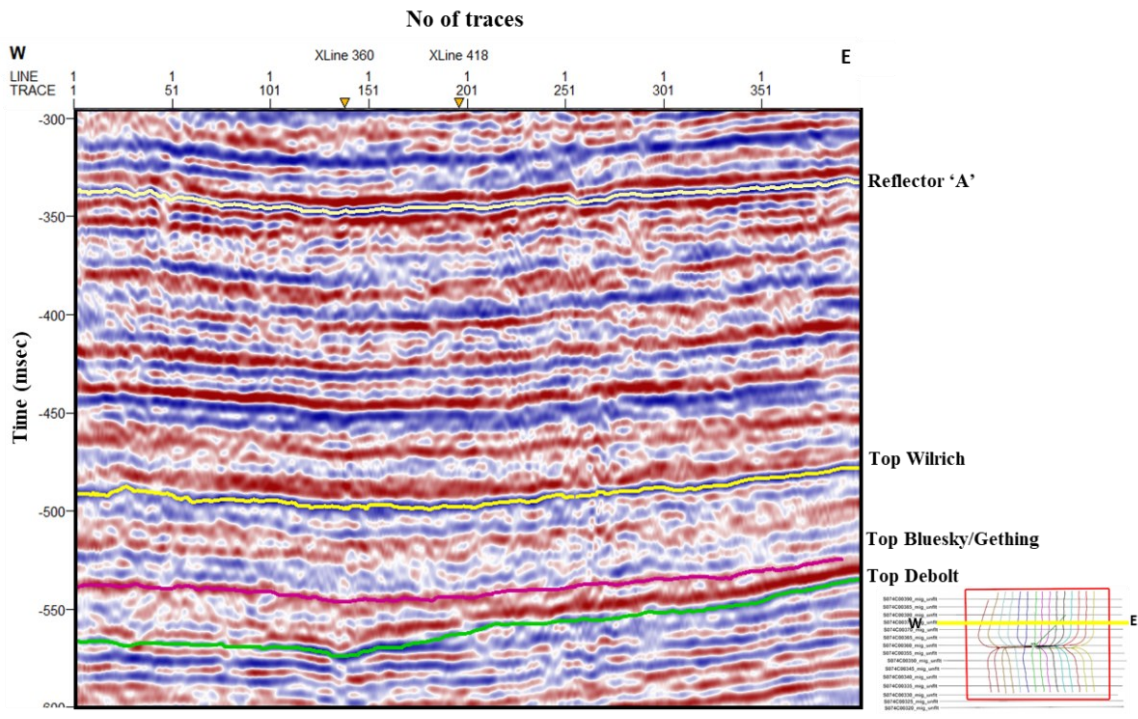


Figure 7-4: East-west 2D seismic section displaying the seismic character for the top and bottom of the reservoir (Bluesky/Geth and Debolt Formation), caprock (top Wilrich), and a reference reflector 'A'.

The difference between baseline and monitor TWT map of reflector 'A' is shown in figure 7.5. This map clearly indicates the differences between the baseline and monitor surveys at shallow level (200ms above reservoir), where no changes are expected. Therefore, both surveys must be calibrated before analyzing any difference between baseline and monitor survey; else, it will be misinterpreted. To analyze the TWT difference of the top (Top Bluesky) and bottom reservoir (Top Debolt), the TWT difference of reflector 'A' is subtracted from the TWT maps generated from the monitor survey.

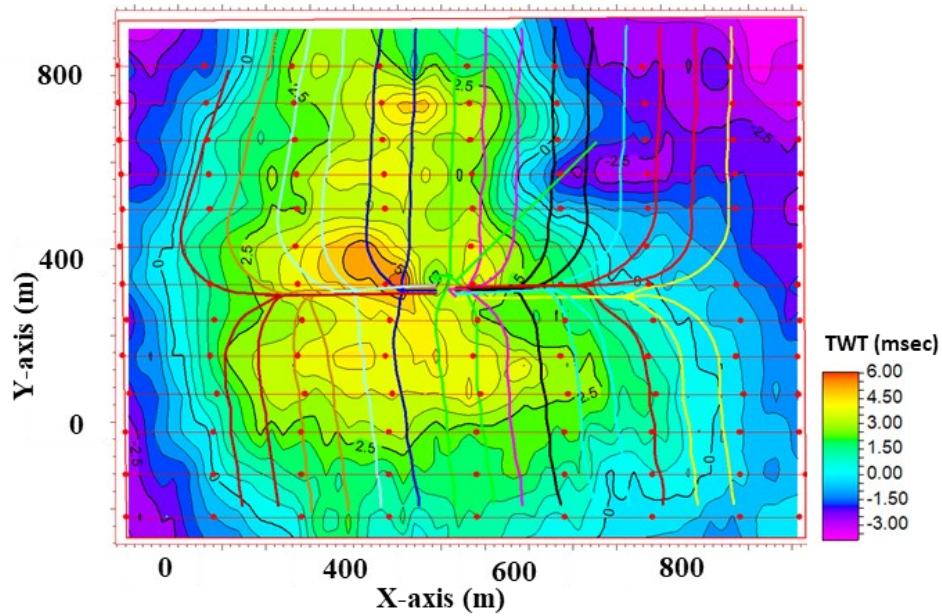


Figure 7-5: TWT difference map between monitor and baseline survey for reflector ‘A’ showing the time differences at shallow section (200ms above the reservoir). The horizontal lines are the seismic lines, and red dots are every 50th trace.

The TWT maps for top Bluesky/Gething and top Debolt Formations are displayed in Figure 7.6 for visual inspection and comparison. These maps are the earliest indications of areas changing due to steam injection/production. The TWT map of the top reservoir does not show much variation between baseline and monitor surveys, but a large variation is visible for top Debolt, possibly indicating that the zone impacted by the steam lies inside the reservoir. The mapping and comparison of TWT maps indicate changes in the monitor survey are injection/production-related, and processing differences likely exist. Next, I will inspect and remove any changes that are not production-related by calibrating the monitor survey to the baseline survey.

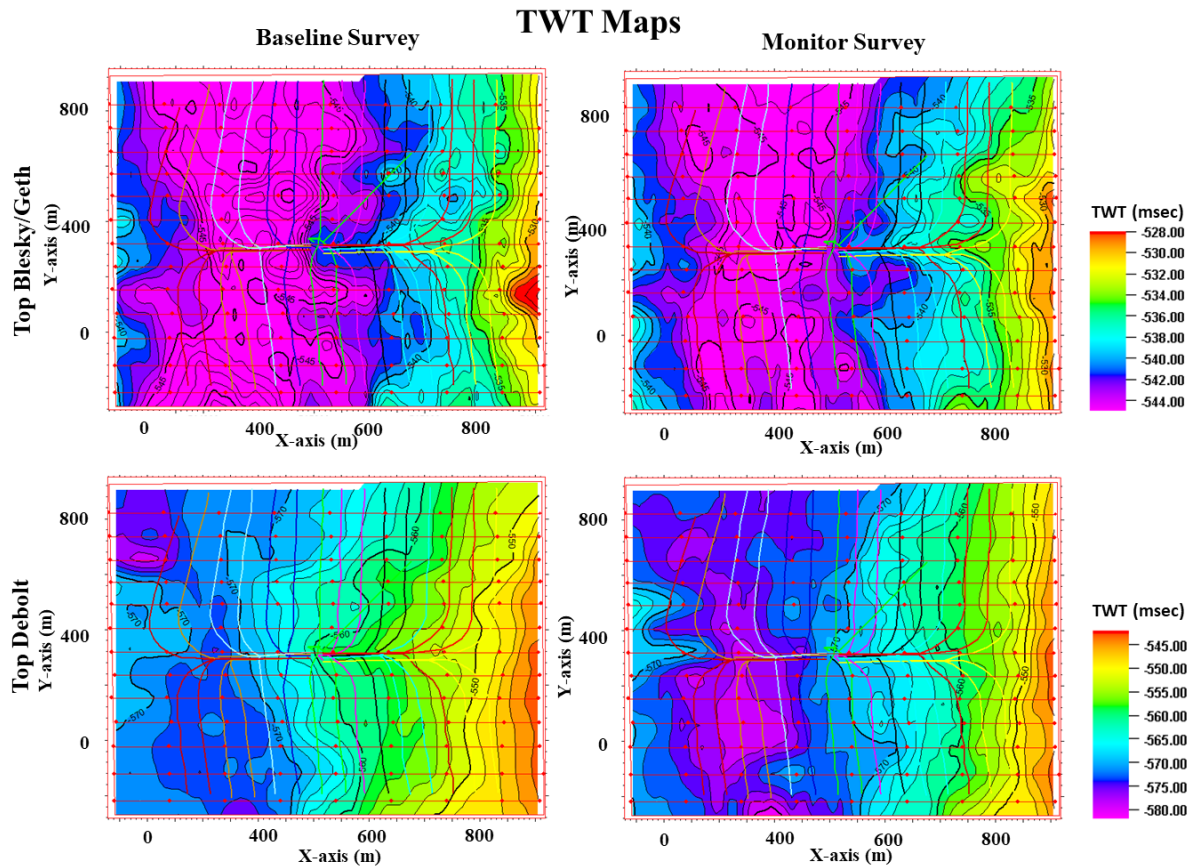


Figure 7-6: TWT maps for top Bluesky/Geth (top) and top Debolt (bottom) formation, generated from baseline (left) and monitor (right) surveys, highlighting the changes in TWT between the surveys.

7.3.2 Time-lapse calibration

Both surveys are compared by calculating the NRMS, cross-correlation, and time-shift values. Figure 7.7 shows the calculated attributes along an east-west 2D seismic line. The above attributes are calculated from the uncalibrated monitor and baseline seismic lines. Note the high NRMS values, especially above the reservoir ranging from 0.5 to 1.9, indicating considerable differences between both surveys. The cross-correlation values indicate that high correlation values (85% or more) above the reservoir interval can be obtained by applying time shifts of 1 to 4ms.

On the other hand, low cross-correlation values (50% to 75%) are found in the reservoir interval. The comparison further confirms the earlier observation that most of the changes are within the reservoir interval, and the slight deviation of cross-correlation from 100% in the overburden interval is likely not production-related.

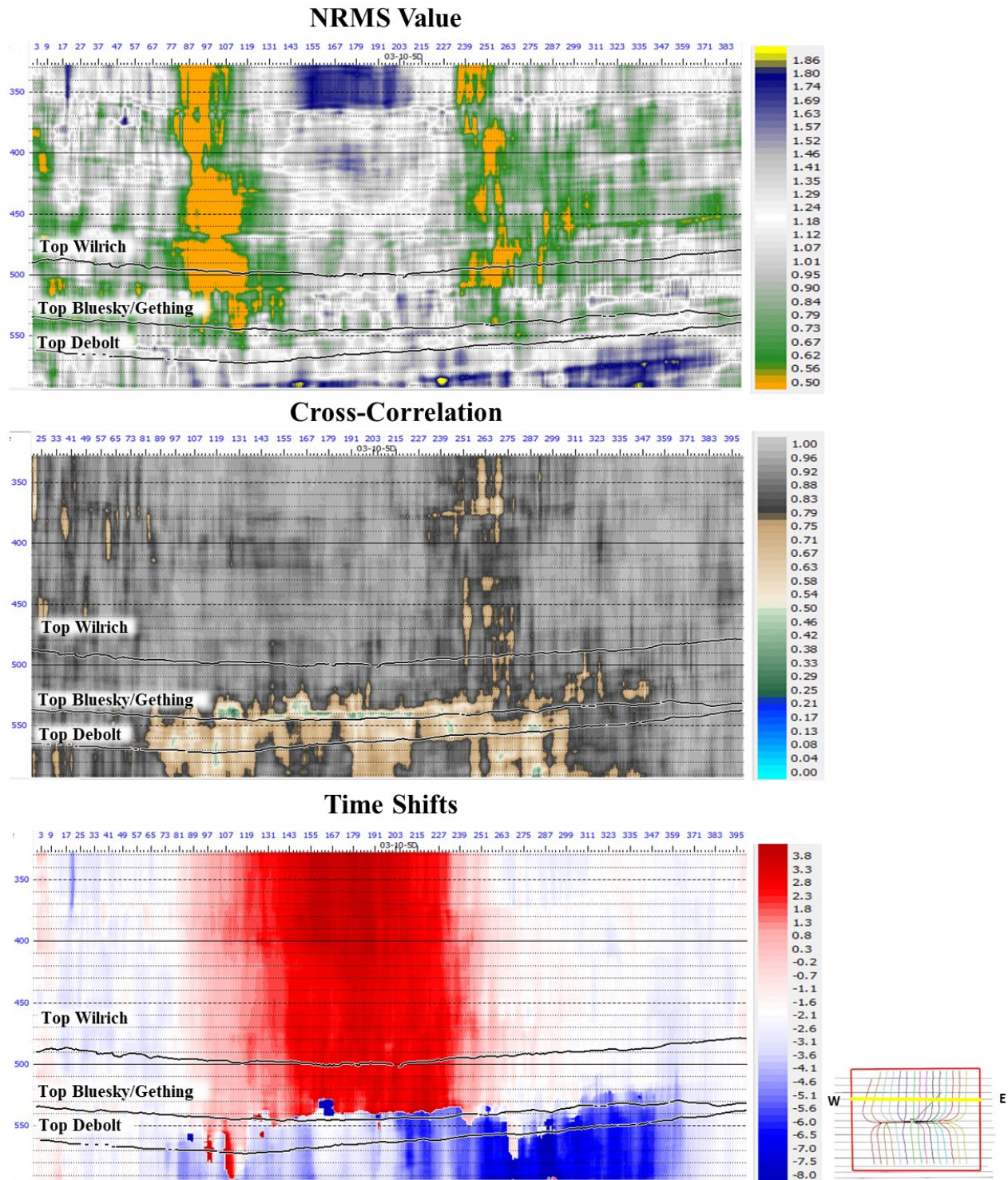


Figure 7-7: a) NRMS, b) cross-correlation, and c) time-shift values along a 2D section, calculated from the baseline and monitor surveys before calibrating the monitor data. The horizons of interest are overlaid for analysis purposes.

The monitor survey was calibrated by applying phase and time shifts, keeping the baseline survey as a reference. The phase and time shifts are calculated over a 200ms window, beginning from 300ms to the reservoir's top. The phase shift was calculated by restricting the maximum shift to 10ms and cross-correlation to 65%. These values are defined based on the initial comparison in Fig 7.7. The process was repeated for all the 2D seismic lines. The calculated and applied phase and time shifts are -8 to -12 degrees and -2 to -4ms, respectively. The improvement in the calibrated monitor survey is evaluated by calculating and comparing the NRMS attribute, as shown in Figure 7.9b. The improvement in the monitor survey because of applying phase and time shifts is indicated by low NRMS values (shown as green color) in the shallow section.

Then, a shaping filter was applied to the monitor data. The shaping filter was calculated over a 100ms window above the reservoir and then applied to all the monitor data. Figure 7.8 shows a comparison between the extracted baseline wavelet to the monitor wavelet before and after applying the shaping filter. The wavelet amplitude of baseline (blue) and monitor (green) surveys are slightly different, specifically at low frequencies (10-40 Hz) and higher frequencies (90-120 Hz) (Figure 7.8). After applying the shaping filter to monitor data, the resulting wavelet amplitude is very similar in shape at all the frequencies.

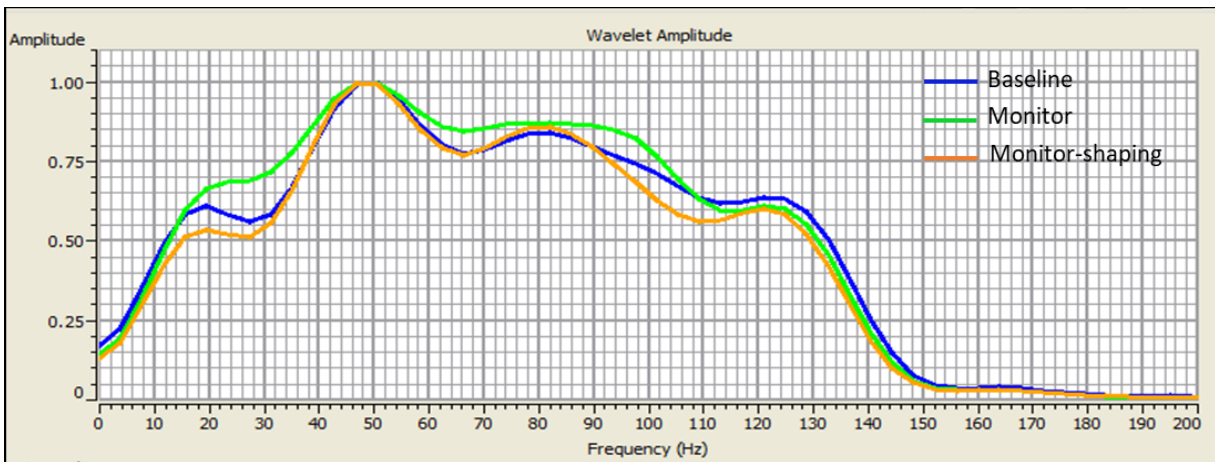


Figure 7-8: Amplitude spectra for the baseline (blue), monitor (green), and calibrated monitor data after the shaping filter (orange).

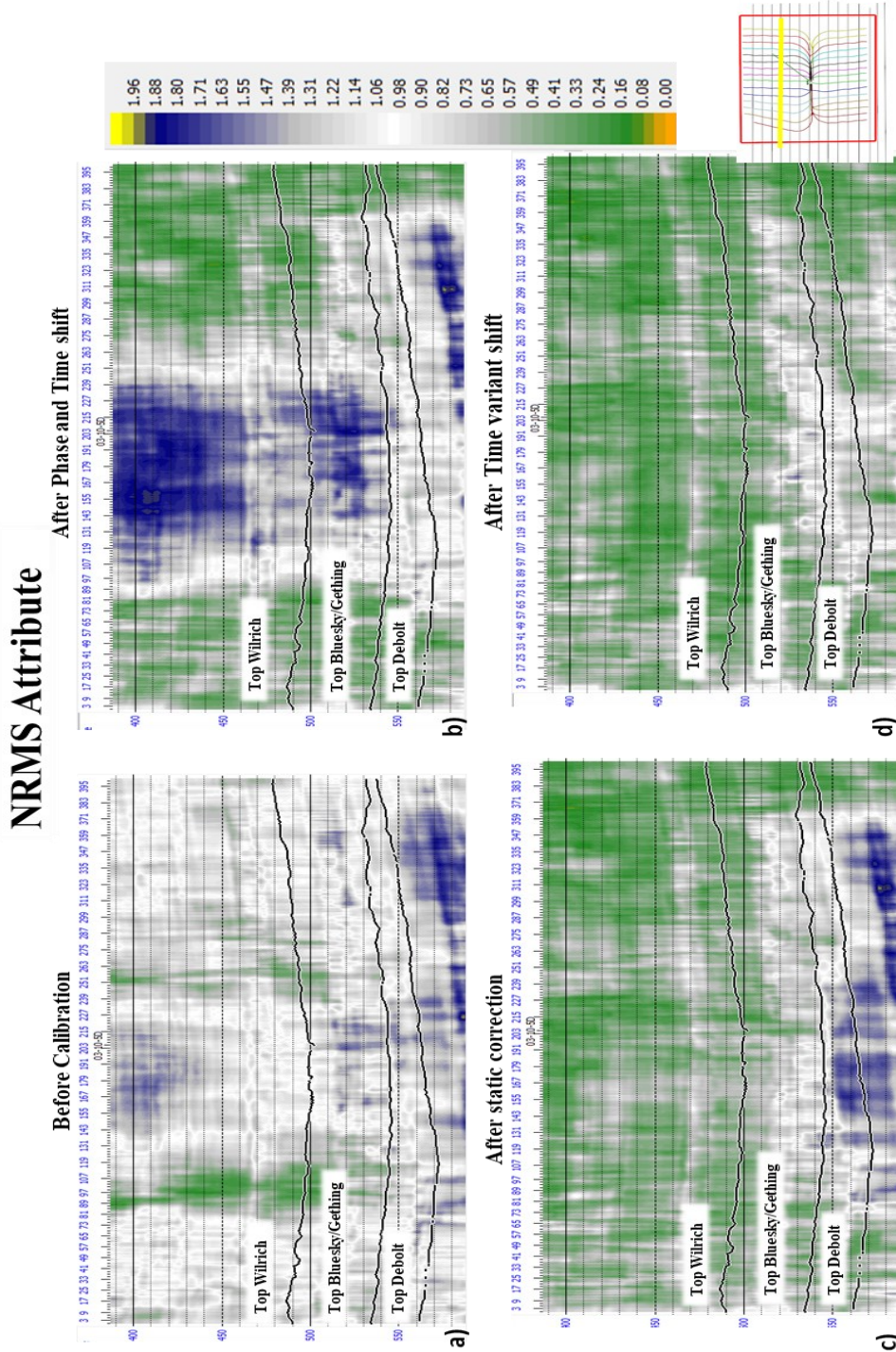


Figure 7-9: NRMS attributes a) before calibration, b) after phase and time shift, c) after statics correction, and d) after time-variant shifts, showing the improvement in NRMS attribute after each subsequent calibration step is applied.

The calibration process continued, and cross-correlation statics are calculated and applied to the shaping filtered monitor data. The statics analysis was run over a 100ms long window above the reservoir and applied to all the monitor surveys. As a result, the resemblance between the baseline and monitor survey is improved above the reservoir. This is shown by the calculating NRMS attribute after applying the statics correction (Figure 7.9c). The NRMS values are reduced from 1.7 (blue color) to 0.2 (green), especially above the reservoir, indicating that most of the discrepancies due to the shallow statics are eliminated.

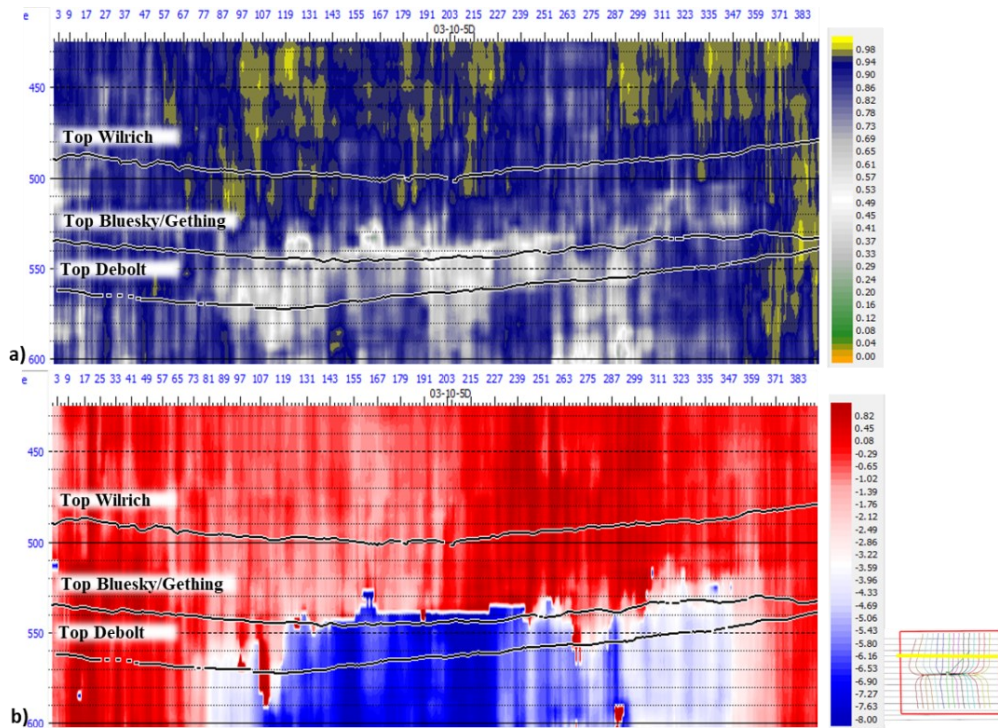


Figure 7-10: Cross-section showing the calculated a) cross-correlation coefficient and corresponding b) time shifts applied to the monitor data. The low cross-correlation values (0.5) and the largest time shifts (-7~-8ms?) are found to be within the reservoir interval.

The last step is to apply time-variant time shifts by selecting a 40ms window starting from the top of the reservoir, allowing a maximum time shift of 10ms. This step produces cross-correlation and time-shift values (Figure 7.10), which are then applied to monitor data. The monitor data are pushed down by approximately 6ms to obtain the maximum correlation between the monitor and baseline survey. Low cross-correlation values are still visible in the reservoir interval and are likely related to steam injection/production. The calculated time shifts are applied to the monitor data. Once done, the improvement is seen as indicated by lower NRMS values

(Figure 7.9d). Note the color change from blue to grey, indicating a decrease of NRMS from 1.5 to 1 inside and below the reservoir. The time-variant shift removed non-production related changes from above and below the reservoir. Thus, when the monitor survey is subtracted from the baseline survey, the difference in the amplitudes is largely related to steam injection/production changes, as shown in Figure 7.11.

The overall efficiency of the calibration workflow is evaluated by comparing the difference sections calculated before and after applying the calibration to the monitor data (Figure 7.11). Note the decrease of amplitude differences in the shallow section above the reservoir. The majority of amplitude differences of the shallow reflections overlying the reservoir have vanished after calibration; solely, the amplitude anomalies within the reservoir interval (525-570ms) remain evident. The amplitude anomalies are strongest at the top and bottom of the reservoir (as seen by the orange color in figure 7.11).

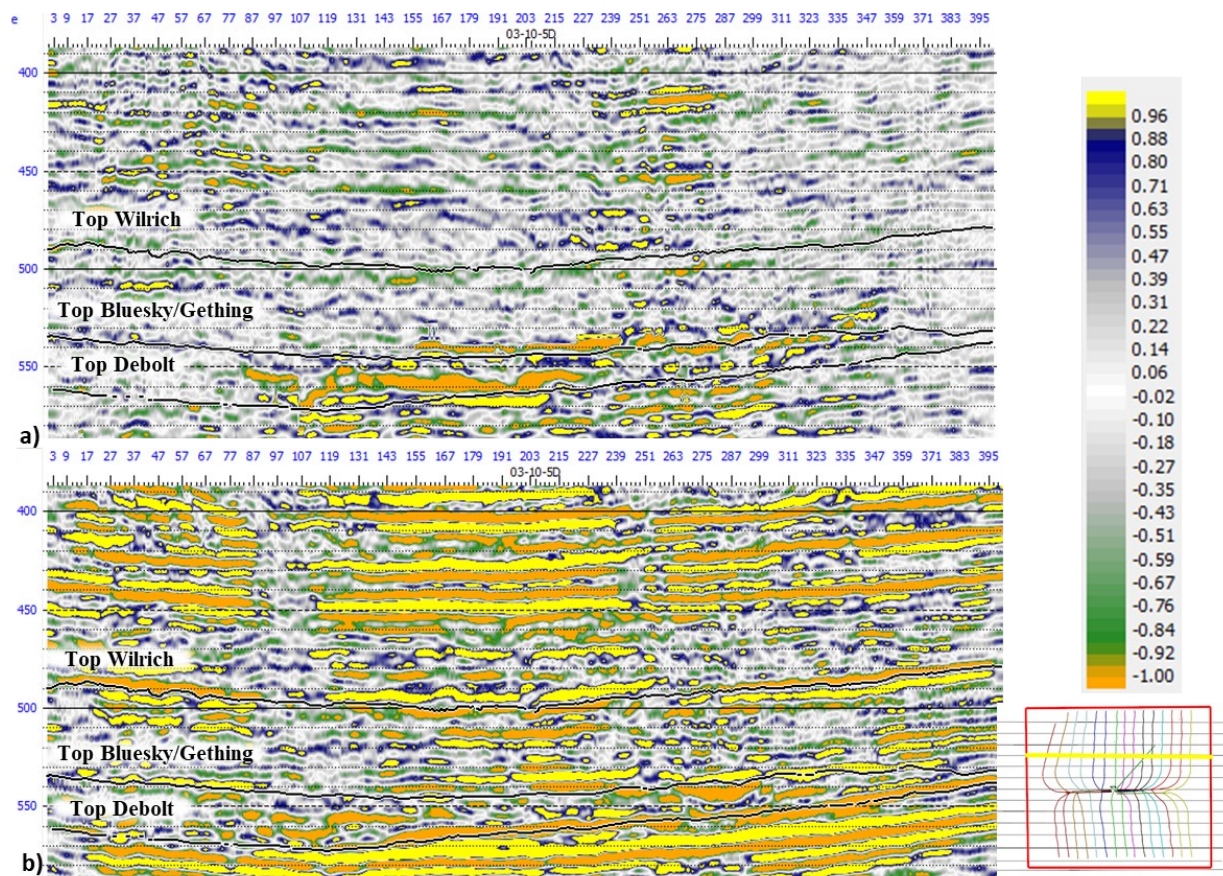


Figure 7-11: Difference section a) after and b) before applying the calibration workflow. After calibration, changes occur predominantly within the reservoir.

7.4 Time-lapse interpretation

The time-lapse interpretation is focused on the identification of travel time shifts and amplitude anomalies within the reservoir interval, primarily observed within the difference volume. Other techniques are also employed to support the observation and interpretation of amplitude anomalies, including isochrone analysis and RMS amplitude analysis.

7.4.1 Isochrone analysis

Isochrone maps display time variation between two seismic events. They can be thought of as time thickness maps, displaying the variation in travel time between two events (Eastwood et al., 1994; Isaac, 1998). These maps are robust and effective for identifying areas of increasing or decreasing travel time between baseline and monitor surveys. Isochrone maps are built over the reservoir interval, bounded by the top reservoir (Top Bluesky Formation) and bottom reservoir (Top Debolt Formation), on baseline and monitor surveys. The horizons are interpreted on 2D seismic lines and interpolated between the lines to generate the required maps. Figure 7.12 shows the isochrone maps of the reservoir calculated from the baseline and monitor surveys. There is significant travel time thickening at the center of the pad, enclosed by the red rectangle. These time delays are due to decreased P-wave velocity and/or increased reservoir thickness.

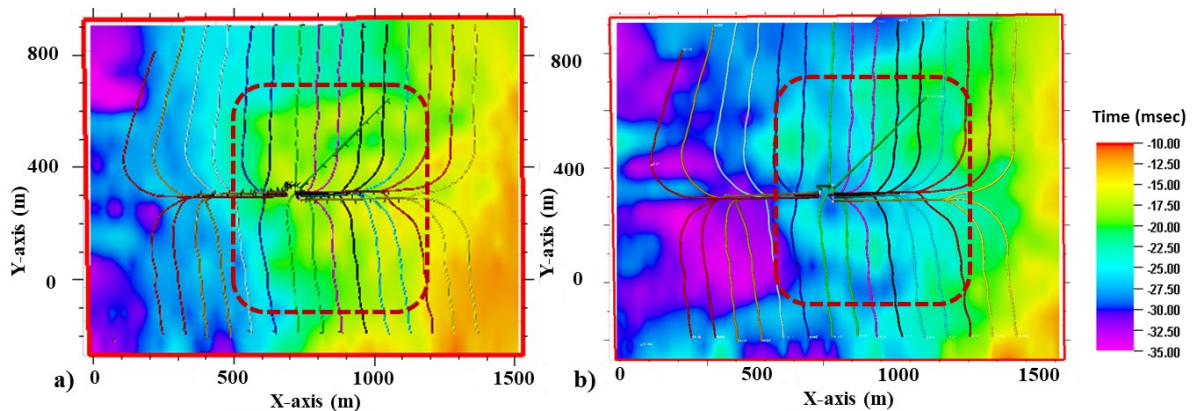


Figure 7-12: Reservoir isochrone maps generated from a) baseline survey and b) monitor survey. The dashed rectangle encloses the area with substantial changes.

7.4.2 Amplitude anomaly

Figure 7.13 shows an east west trending 2D seismic line from the baseline and monitor surveys. The zone of interest (Reservoir, Bluesky/Geth Formation) lies between 540 and 570ms.

The high amplitude anomalies are evident even on non-calibrated monitor seismic lines, between xline 140 and 235, and 240 to 320 within the interpreted reservoir interval marked by red and white arrows. The first amplitude anomaly is bounded by white arrows on the eastern side of the line, closer to the reservoir's top. The second anomaly is located on the western side of the line at the bottom of the reservoir, bounded by red arrows in Figure 7.13. Note that both amplitude anomalies appear to be isolated and at different depths. The first anomaly is much closer to the top of the reservoir, and the second anomaly is more towards the bottom of the reservoir.

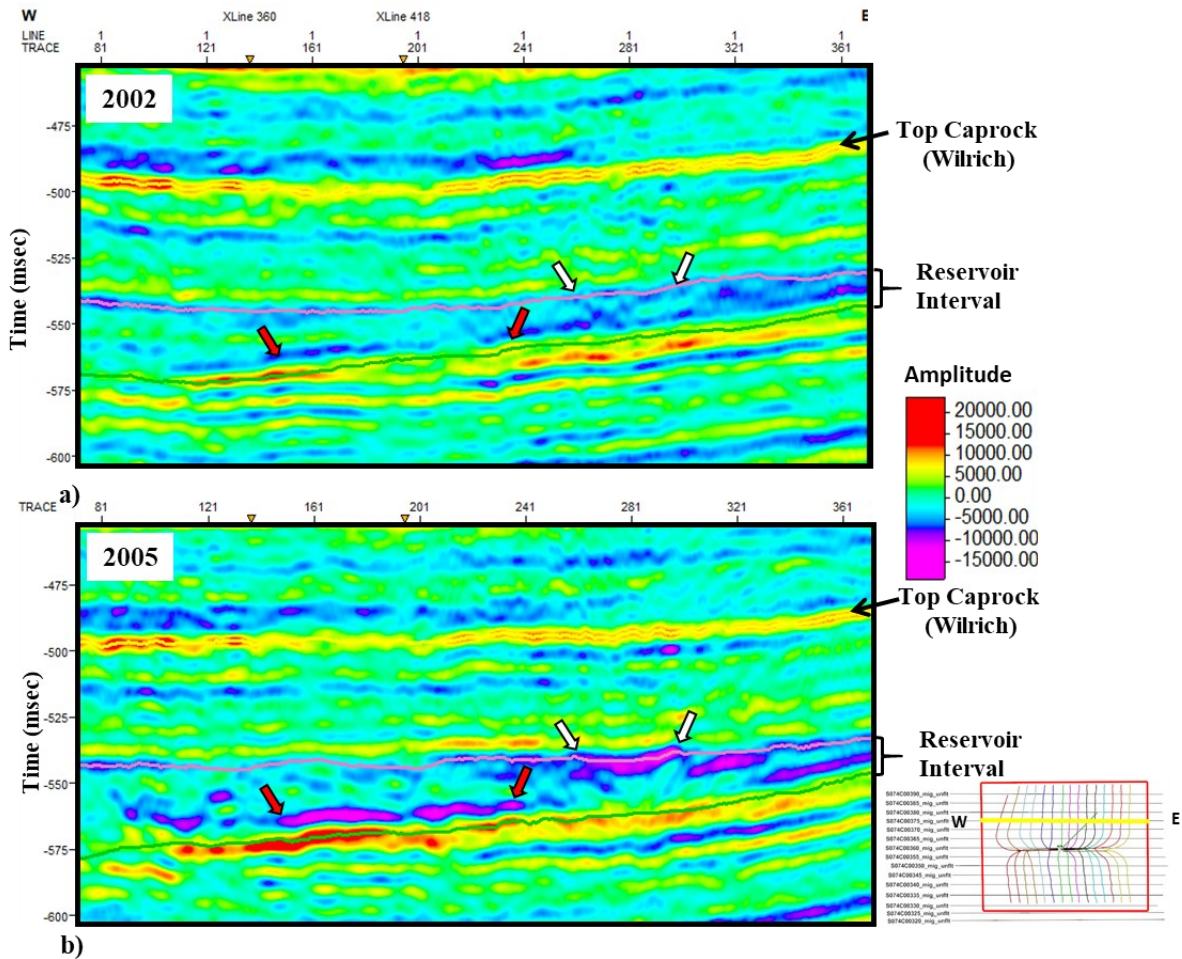


Figure 7-13: Comparison of a seismic line from the a) baseline and b) monitor surveys, highlighting areas undergoing amplitude changes.

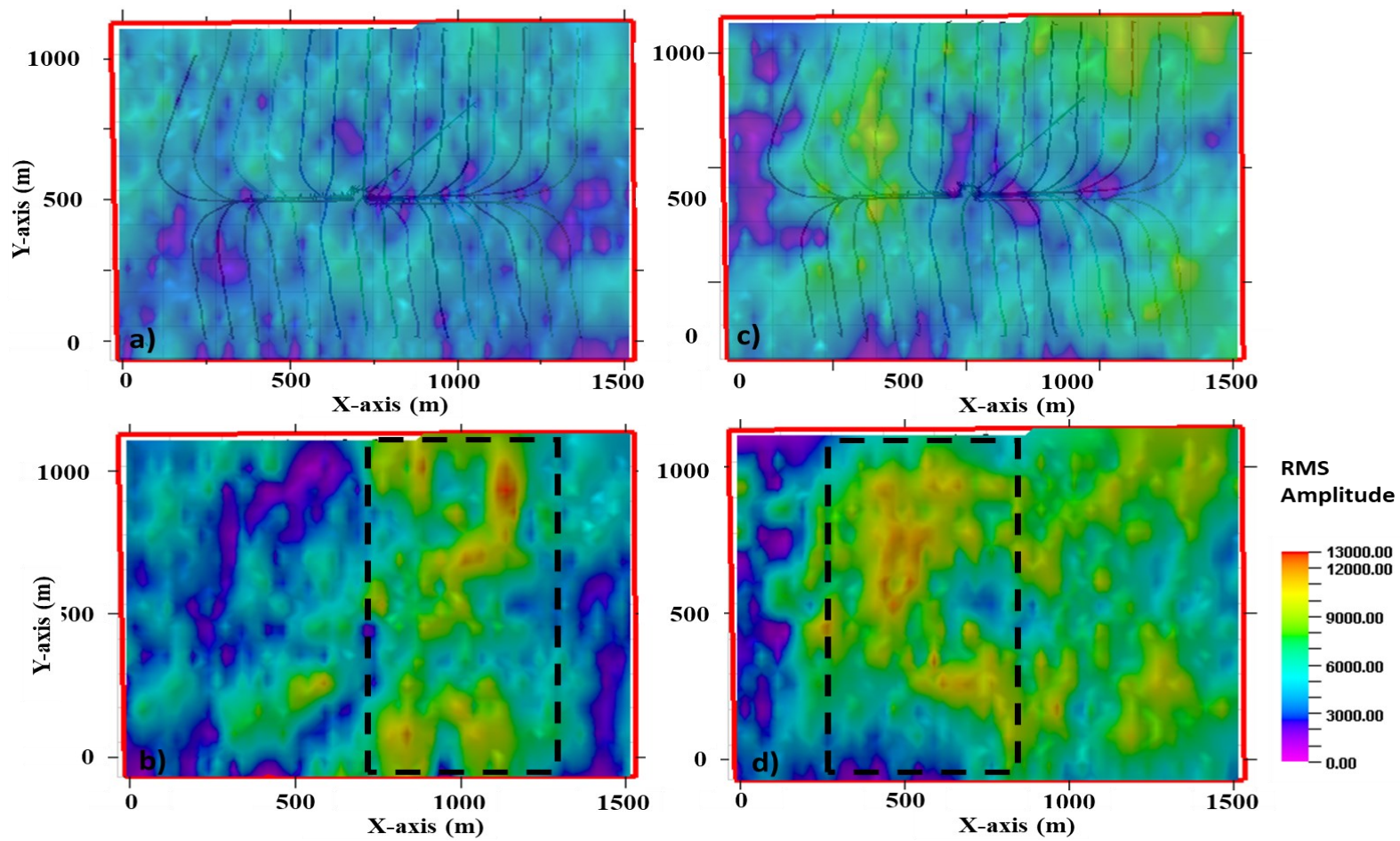


Figure 7-14: Comparison of RMS amplitude maps for a) Top Bluesky/Geth (baseline), b) Top Bluesky/Geth (monitor), c) Top Debolt (baseline), and d) Top Debolt (monitor).

Next, RMS amplitude is calculated from the baseline and monitor surveys for the top of Bluesky/Geth and Debolt formation, using equation 7.2. The resulting maps are shown in figure 7.14. An increase in the RMS amplitude values is observed for the top of Bluesky/Geth (figure 7.14b) and Debolt formation (figure 7.14d). This shows that an increase in amplitude for top Bluesky/Geth and Debolt is restricted to the east and west side of the pad, respectively, as indicated by the black rectangle.

7.4.3 Difference volume

After the calibration procedure, difference sections are created by subtracting the baseline data from the calibrated monitor data. The difference sections remove all repeatable traces, only leaving the physical differences between the two surveys.

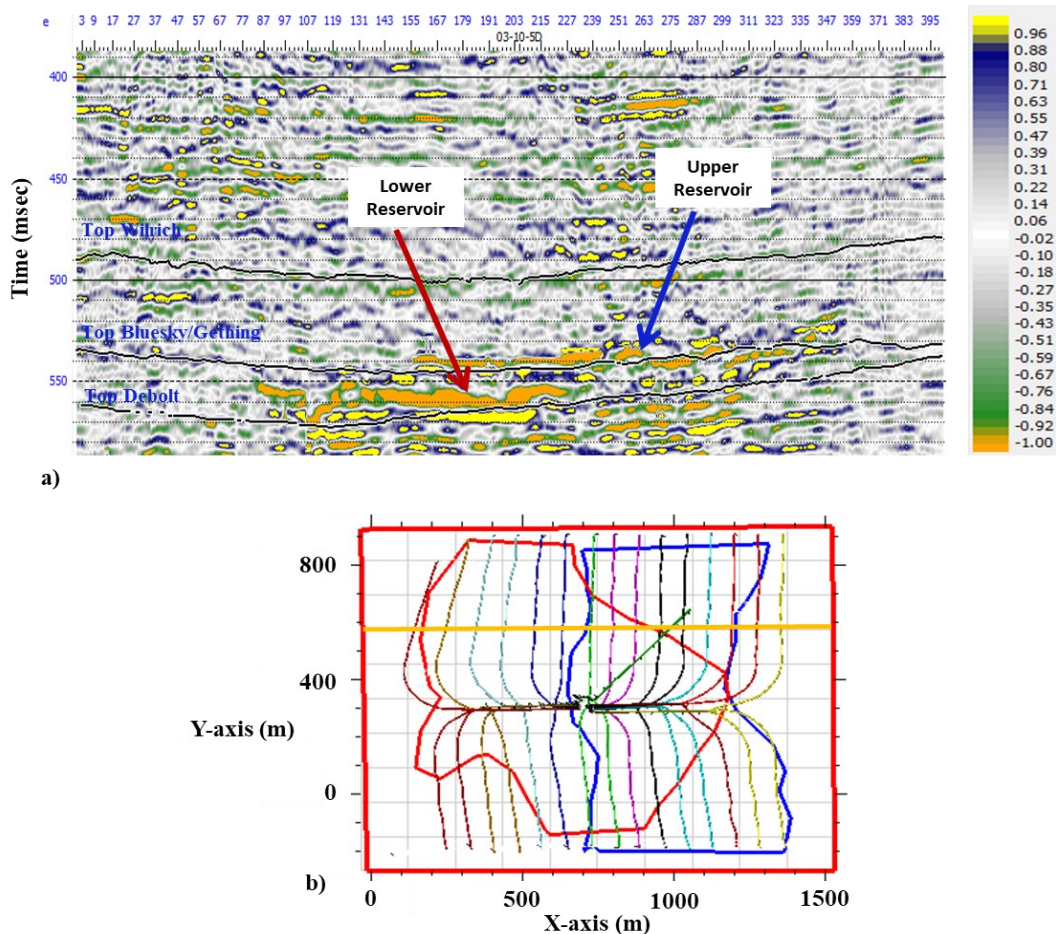


Figure 7-15: a) Amplitude difference section highlighting the changes within the reservoir and b) polygon showing the spatial trends of these changes over the pad. The blue and red polygons are representative of changes within the upper and lower reservoir interval, respectively.

Figure 7.15a shows the difference section from the northern side of the pad, as highlighted by the yellow line in Figure 7.15b. It can be seen that amplitude anomalies appear to be restricted in the upper and lower portion of the reservoir in the eastern and western sides of the section, respectively, shown by orange color on the section and indicated by blue and red arrows in Figure 7.15a.

The data available for this study consist of only 2D lines; it is difficult to produce a surface map of amplitude difference with high accuracy because of potential interpolation effects between 2D lines. Nonetheless, it is desirable to understand the spatial trends of the amplitude anomalies. Therefore, two separate polygons bordering the amplitude anomalies in the upper and lower reservoir are manually generated. The resulting polygons are shown as red and blue color in figure 17.b. The polygons display the spatial extent of amplitude anomalies in the upper and lower reservoir sections. Note the overlapping area of the two polygons in the middle of the pad.

7.5 Discussion

7.5.1 Time-lapse processing

The time-lapse calibration workflow is applied to the 2D seismic lines and well logs from a deviated well, located at an offset distance from the seismic line. The distance affected the match between seismic data and synthetic seismogram, and a perfect match was not obtained. However, the tie was sufficient to identify horizons of interest on seismic data and continue with the time-lapse calibration workflow and analysis. It is worth mentioning that there is no defined workflow to process time-lapse seismic datasets, and workflows are fields specific (Nguyen et al., 2015). One or more steps may be excluded depending on the repeatability of the monitoring and baseline survey. The workflow applied in this study is a generalized time-lapse workflow outlined by Kelly & Lawton (2012). However, the input parameters at each processing step are carefully selected to ensure the procedure's success. To evaluate the effectiveness of the calibration workflow, the NRMS attribute was calculated for calibration and quality control purposes (Kragh & Christie, 2002; Sheriff, 2002). Because of calibration, phase differences and time delays were removed from the overburden reflections. With every calibration step, the NRMS values are reduced above the reservoir reflector, indicating the effectiveness of each calibration step. The effectiveness of the calibration workflow is also demonstrated by comparing the difference section calculated before and after applying calibration to monitor data, as shown in figure 7.11. The majority of the difference in the shallow section vanished, thus only highlighting the differences due to heated

bitumen within the reservoir interval. The improvements in the calculated NRMS attribute and difference sections support the efficiency of the calibration workflow.

7.5.2 Additional observations

In addition to time-lapse seismic data, temperature logs and tiltmeter data images are also analyzed. The temperature data from the 3rd steam injection cycle recorded by two observation wells were made available, one from the east (40-A) and the other from the west end of the pad (40-B), as shown in figure 7.16. The reservoir temperature at 40-B well reaches 250C⁰, but the temperature at 40-A well does not exceed 40C⁰. The temperature difference at the pad is not due to the steam injection strategy because steam was injected at once in all the wells.

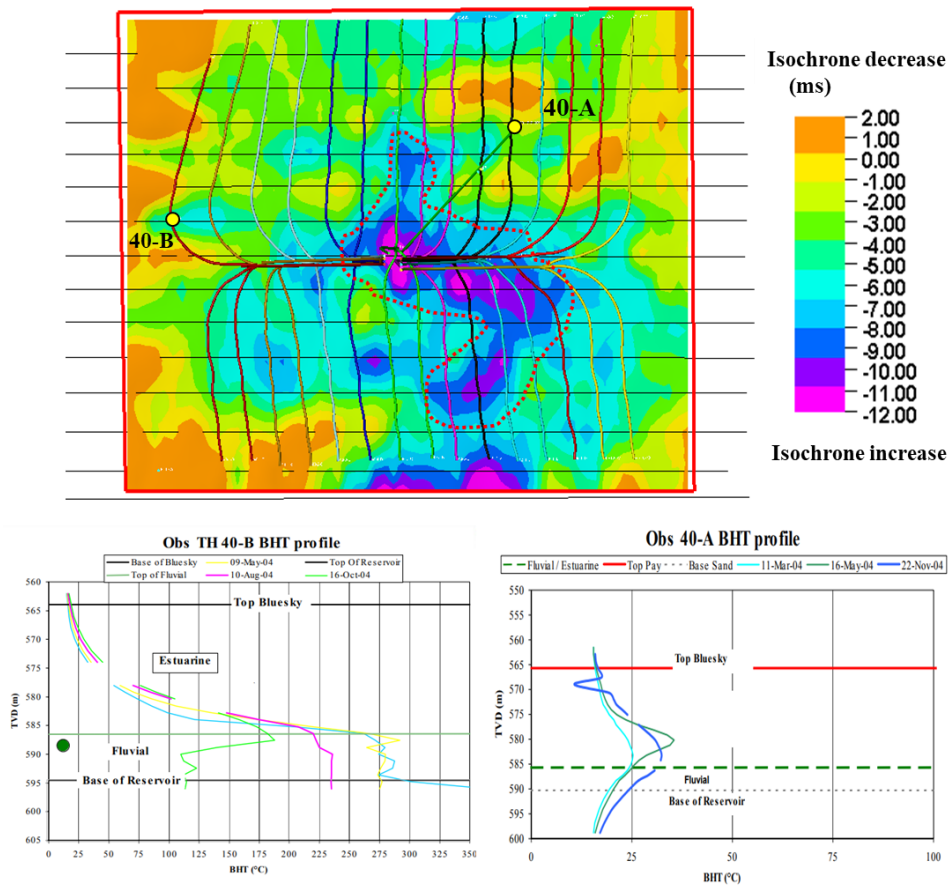


Figure 7-16: Isochrone difference map for the reservoir (top) and temperature profiles from two observation wells at the pad.

Additionally, tiltmeter data from the 2nd injection/production cycle are also available. During steam injection, the ground heave of up to 100mm is recorded, but as soon as production starts, partial subsidence of the ground is recorded, especially on the southern side, where subsidence is

relatively negligible (Figure 7.17). When comparing my results to other thermal heavy oil extraction experiments, it is common to record surface heave (Maxwell et al., 2007); however, the size of surface heave is of critical importance and must be monitored.

The findings from surface tiltmeter data are consistent with the predictions from chapter 3. It was predicted that steam injection and hydrocarbon production would cause the reservoir to expand and shrink, and this should be evident from the surface tiltmeter measurements. The tiltmeter data observations combined with the temperature profile indicate that the pad response to steam injection and production is distinct in different parts of the pad.

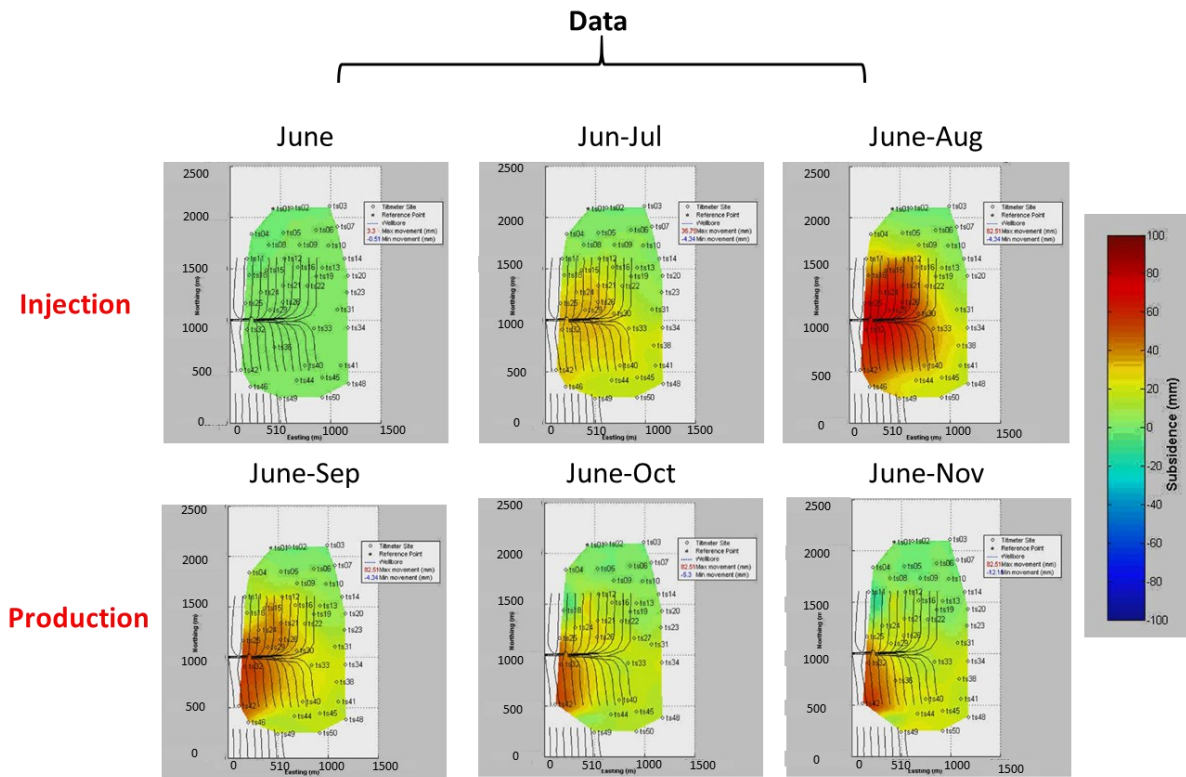


Figure 7-17: Subsidence values recorded by tiltmeter during the 2nd cycle of steam injection (top) and production (bottom) between June 2004 to November 2004. The steam was injected from June to August 2004, and production started in September and continued till the end of November 2004.

7.5.3 Time-lapse interpretation

The detailed analysis of the baseline and monitor surveys indicates a non-homogenous lateral and vertical distribution of steam in the reservoir section, seen by analyzing the amplitude differences, isochrone variations, and time delays. The earliest observation of differential steam movement became prominent as soon as the horizons of interest were picked, and seismic reflection amplitudes were compared between baseline and monitor seismic data, before

calibrating the seismic monitor survey. The 2D seismic lines in Figure 7.13 show the changes in reflection amplitude, especially in the reservoir interval indicated by the white and red arrows. The increase in reflection amplitude is seen as a dark purple color in the monitor survey (indicated by red and white arrows). The higher amplitudes on the eastern side are closer to the top of the reservoir and on the western side are closer to the bottom of the reservoir, perhaps highlighting the areas where steam has reached. It is supported by RMS maps at the top of the reservoir and Debolt formation, as shown in Figure 7.14. The reason why I computed amplitude differences at the top Debolt instead of the bottom reservoir reflector is that the bottom reservoir reflector is not strong and continuous. The Debolt formation is right below the reservoir and is expected to represent amplitude changes at the reservoir's bottom. These maps clearly show that amplitude changes are restricted to the eastern portion of the pad for the top reservoir and the western portion of the pad for the top Debolt formation. These findings are consistent with the amplitude difference polygons generated from the difference amplitude section in Figure 7.15. It is promising to see consistency in the spatial distribution of amplitude differences identified before and after monitor survey calibration, thus further confirming the initial interpretation of non-homogenous steam distribution.

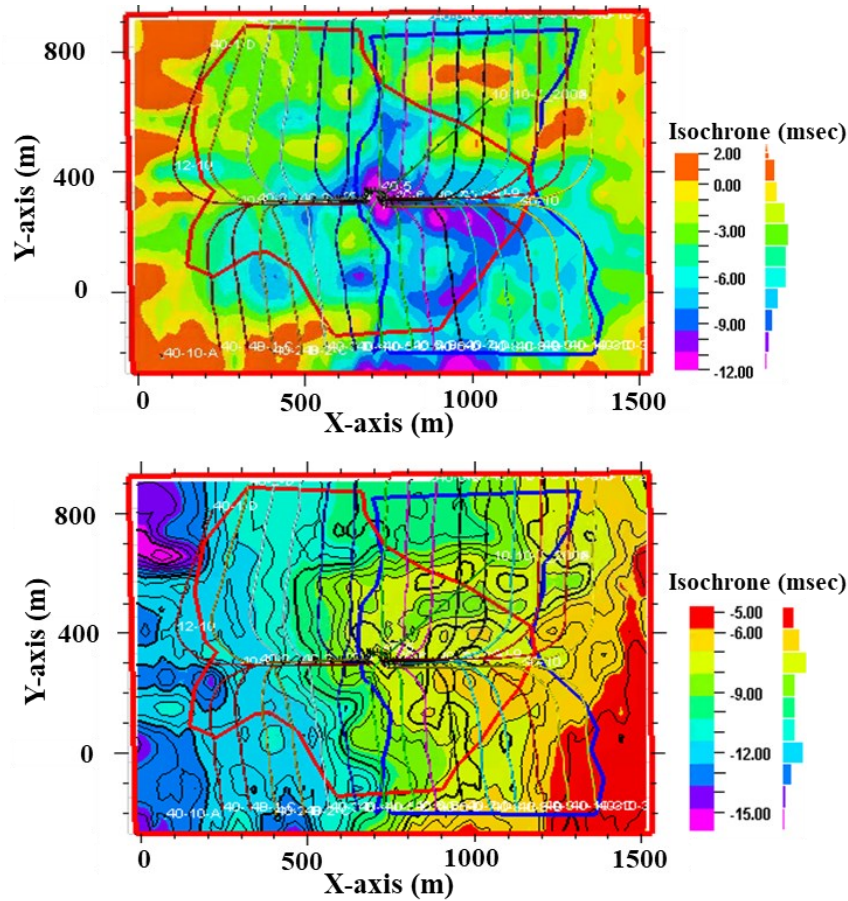


Figure 7-18: a) Observed and b) theoretical isochrones difference map for the reservoir interval, overlain by polygons bounding the changes in the upper (blue) and lower (red) reservoir interval.

Furthermore, the isochrone difference map can also highlight changes due to steam distribution. The isochrone difference map overlain by the amplitude difference polygons shows that high values of the time difference (about 12ms) are restricted to the southeast side of the pad (figure 7.18).

According to Kato et al. (2008), the P-wave velocity may slow down by 30% at higher temperatures (260°C). To analyze the isochrone differences, I model the expected isochronal changes due to a 30% reduction in P-wave velocity, assuming that injected steam is equally distributed inside the reservoir. The P-wave velocity from the sonic log and the isochrone thickness from seismic data is used to calculate the thickness of the reservoir in meters using

$$\text{Reservoir thickness (m)} = \text{velocity (m/sec)} * \text{isochrone} / 2 \quad (7.5)$$

The above equation is rearranged to calculate the isochrone thickness with a 30% reduced velocity within the reservoir. The expected (figure 7.18.b) and observed isochrone difference maps (figure 7.18.a) are significantly different. The mismatch between the observed and theoretical isochrone differences may be attributed to the non-homogenous steam distribution in the reservoir. The observed isochrone difference values are higher than theoretical isochrone difference values, specifically at the center of the pad shown as blue-purple color (figure 7.18.a). At the center of the pad, 30% velocity slowness (due to temperature increase) can be responsible for the isochrone difference of -8msec, but the observed value is -11msec. The difference of -3 msec possibly indicates that other factors also contribute to isochrone thickness. The remaining -3 msec of isochrone difference may be because of 1) reservoir dilation and 2) fluid substitution changes. According to Dusseault (2011), sandstones have a coefficient of thermal expansion of about 10^{-5}C^{-1} , and a 30 m thick reservoir can cause a 60 mm uplift on the surface if the reservoir temperature increases to 200°C. The -3msec isochrone difference roughly translates to reservoir expansion of 3m, which is unrealistic and not justifiable by the observed surface uplift value of 5 cm at the pad. The other possible parameter responsible for producing -3msec isochrone difference is fluid substitution. During steam injection, if the reservoir temperature ($>150\text{C}^{\circ}$) reaches the bubble point, then free gas is evolved (Batzle et al., 2006). And the presence of free gas in the heavy oil can drastically decrease the P-wave velocity (Batzle et al., 2006), thus causing isochrone thickening and possibly responsible for the remaining -3msec difference between observed and theoretical isochrone difference (Figure 7.18a&b).

Furthermore, a comparison of the amplitude difference map/polygon and isochrone difference map reveals that zones of high isochrones differences are consistent with the amplitude polygons (Figure 7.18a). The zone of isochrone differences may be interpreted as a reservoir zone where steam has effectively reached, resulting in velocity reduction and reservoir expansion. The temperature data over the pad correlates with the isochrone difference map, minimal changes are seen close to the well 40-A, but a difference of -6ms is observed at 40-B.

The changes in seismic attributes (two-way arrival time, amplitude, and isochrone) due to velocity slowness imply that steam is confined to reservoir interval. On the contrary, no changes in seismic attributes are observed in the overburden, thus confirming that steam is confined to the reservoir only. The above findings agree with the predictions made in chapter 3 and demonstrate the applicability of seismic attributes to outline the steam-affected zones.

The time-lapse seismic data analysis combined with temperature and tiltmeter data indicates a non-homogenous steam movement at the pad area. I divide the pad into four zones labeled as A, B, C, and D (D1 and D2) in figure 7.19, based on the analysis of amplitude, isochrone, temperature, and tiltmeter data. Zone A indicates the area where steam has only affected the lower reservoir, and zone C outlines the spatial extent where steam only reached the upper reservoir. At the center of the pad, the steam chamber appears to be well developed and extends into the upper and lower reservoir. The area on the northeast side of the pad appears to be least impacted by the steam, labeled as D1 and D2. It is supported by negligible temperature and isochrone variations.

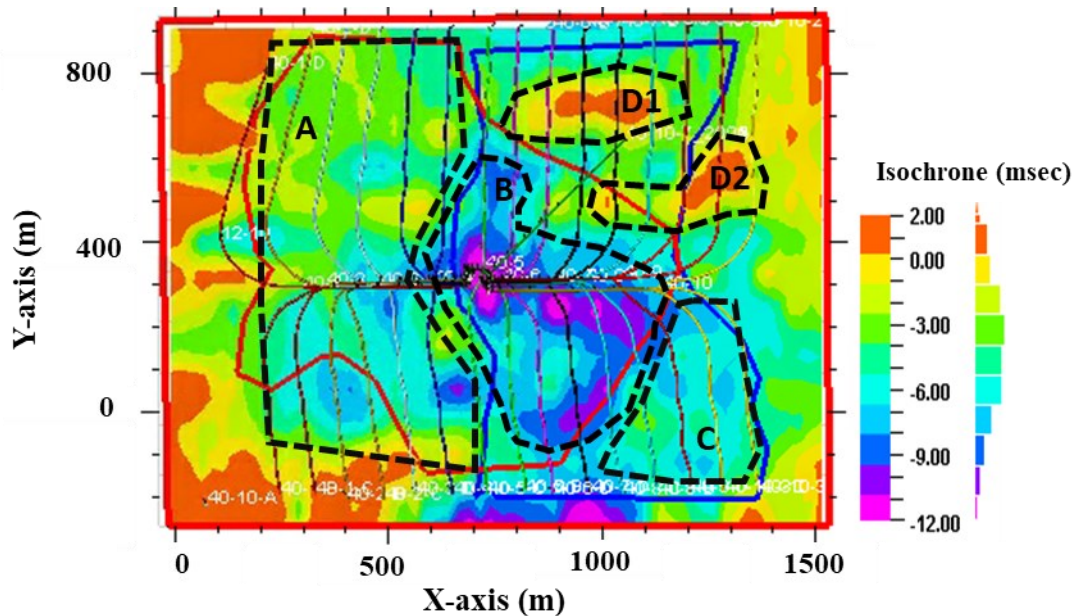


Figure 7-19: Figure showing observed isochrone difference map overlain by the amplitude polygons (red and blue) and several interpreted zones (A, B, C, and D), where steam migrated vertically into different zones of the reservoir.

The objective of using multiple horizontal injectors is to ensure the maximum steam distribution in the reservoir, but it is not always achieved. Figure 7.19 shows that the steam distribution in the reservoir is non-homogenous and appears to be well developed in the central portion of the pad within the reservoir, and no changes in seismic attributes (seismic amplitude and travel time) are observed in the caprock. A similar conclusion was reached by Kelly & Lawton (2012), and two anomalous zones were interpreted qualitatively by analyzing the changes in seismic travel time, isochrones, and amplitude attributes. However, Tanaka et al. (2010)

quantitatively analyze the changes in seismic time-lapse data recorded during the SAGD experiment. The study formulated and incorporated a petrophysical model to mark the boundary of the steam chamber and calculate the bitumen volume in the steam chamber. Additionally, it must be mentioned here that the focus of all the above-mentioned time-lapse studies is to analyze the changes within the reservoir interval.

The non-homogenous steam movement and development of hot and warm zones inside the reservoir could have been confirmed by analyzing hydrocarbon production per well. However, I only have cumulative production logs for each well (which has three horizontal arms in north and south both directions) rather than production logs of each horizontal well discretely.

It must be pointed out that time-lapse seismic interpretation is based on 2D seismic lines. Therefore any attribute map (amplitude, isochrones, and TWT) generated from the 2D data will have some uncertainty associated with it because 2D lines are all in E-W direction separated by 60 m. This uncertainty may be reduced by incorporating 3D seismic to improve the accuracy of the calculated attributes by providing more detailed images of the subsurface changes. However, this would come at a significant extra cost. The management may also consider acquiring other geophysical data, e.g., time-lapse gravity data over the pad, to identify zones of density changes. The observations can be correlated with the surface tiltmeter data and seismic reflection data for an integrated analysis. It must be kept in mind that the cost of gravity data acquisition is much less than other geophysical data acquisition.

The qualitative interpretation of seismic time-lapse data is limited to identifying areas of impedance change from quiet areas. The data can help judge the gross efficiency, location of pressure boundaries, and reservoir compartmentalization. However, a detailed analysis of fluid efficiency and estimation of fluid changes is not possible because the observed impedance is not a simple function of one physical property. Especially in the reservoir region where both water saturation and effective stress have changed, but impedance remains the same may occur. However, the analysis may be extended by incorporating additional well logs, rock physics models, and prestack seismic data to perform a time-lapse AVO analysis. This may help separate impedance changes in the anomalous zones.

7.6 Conclusion

The 2D time-lapse seismic data from a heavy oil field in Alberta are analyzed to investigate the steam distribution inside the reservoir. It is concluded that changes in several seismic attributes,

e.g., amplitude, travel time maps, and isochrone maps, can help to identify changing zones because of steam injection and/or production, such as reservoir expansion, temperature, and saturation changes. The time-lapse seismic integrated with temperature and tiltmeter data have shown steam distribution in the reservoir is non-homogenous vertically and spatially. Several zones have been interpreted where steam has migrated. It is also found that most of the isochrone and amplitude anomalies are located at the center of the pad, possibly indicating the reservoir zone where most steam may have migrated, thus affecting the reservoir temperature and fluid saturation. However, it is difficult to quantify the impact of temperature and fluid changes separately at this point.

The time-lapse analysis is useful for investigating the changes within the reservoir interval, but much cannot be said about the impact of steam injection and hydrocarbon production on the overburden. The caprock integrity is of great importance in such operations. It is also not clear how the steam moves (mechanism of steam distribution) inside the reservoir. To answer the above, time-lapse observations will be integrated with microseismic observations and engineering data in the next chapter.

8 Geomechanical behavior of the Peace River reservoir

8.1 Introduction

This research is aimed to analyze and integrate multidisciplinary geophysical data to investigate and better understand the impact of steam injection/oil production on the reservoir-caprock system. The research is initiated by putting forward a set of predictions in chapter 3; the predictions highlight the expected geomechanical deformation and seismic observations within and around the reservoir during both steam injection and oil production cycles. It is expected that seismic reflection data will highlight the changes at the reservoir level, and microseismic data will give a detailed picture of changes in the overburden; combining both data types is likely to give a detailed insight into reservoir-caprock response to the steam injection. Additionally, it is believed that the analysis of each data type in isolation may not give a complete subsurface image and result in biased interpretation.

To achieve the research objective, I have first analyzed the microseismic data in conjunction with the engineering data recorded during the four steam injection and production cycles. The intent was to investigate the spatial and temporal trends of microseismic activity and its correlation with the engineering parameters in chapter 6 and make a plausible clarification of the observed trends. Next, chapter 7 shows the time-lapse analysis of 2D surface seismic data to understand the steam movement inside the reservoir based on variations in the seismic properties. Each dataset was analyzed independently from the rest of the data. In this chapter, I will integrate the findings from each chapter to validate the set of predictions (outlined in chapter 3) and investigate the potential physical mechanisms responsible for the changes. I will divide the data observations associated with steam injection and hydrocarbon production for reservoir and caprock intervals. Next, data observations are integrated with the expected theoretical changes to understand the complete picture and validate the initial model.

8.2 Reservoir response to steam injection

8.2.1 Observations

The cyclic process of steam injection and hydrocarbon extraction disturbs the reservoir rock matrix causing changes in the physical properties of the reservoir. The analysis of time-lapse and microseismic data resulted in several key observations, highlighting the impacted areas. The first

observation came from the recorded microseismic data (2002 to 2005), showing limited to no microseismicity within the reservoir interval (Figure 8.1).

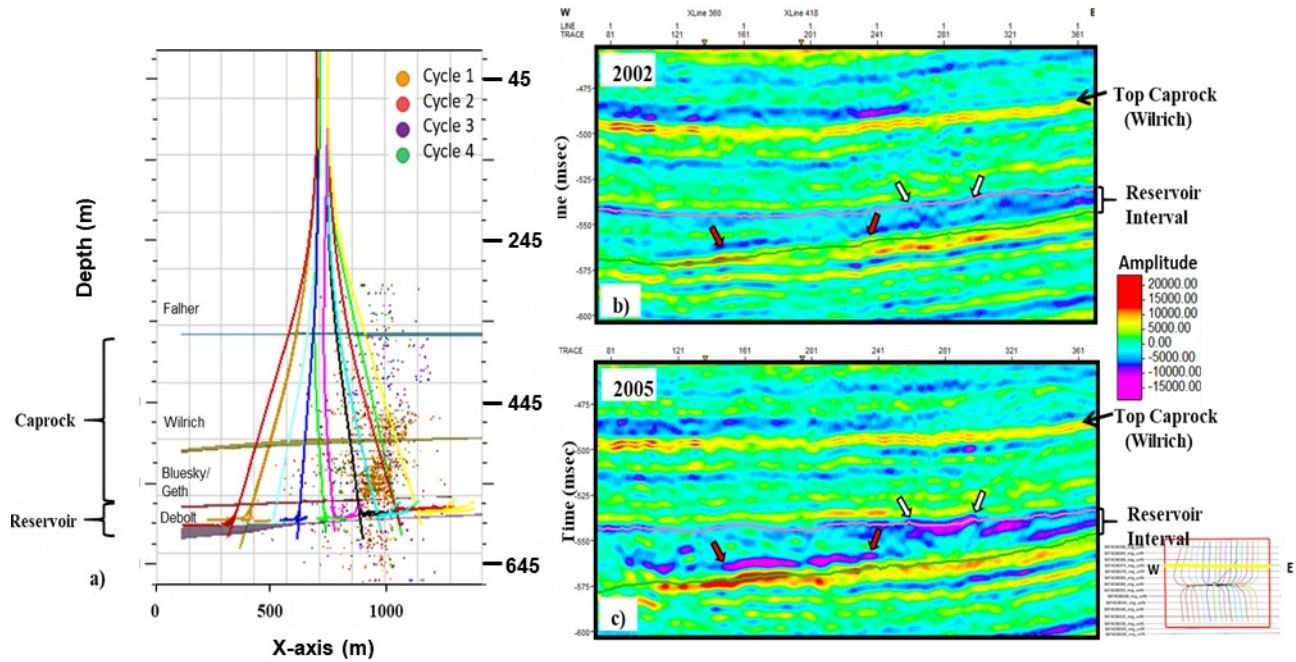


Figure 8-1: a) The cross-sectional view showing production-related microseismic event distributions across the pad. Horizontal colored lines indicate geological formations of interest. The Falher, Wilrich, Bluesky, and Debolt Formations are shown as blue, yellow, red, and purple colors, respectively. Microseismic events are colored based on their time of occurrence. Events that occurred during cycle 1, 2, 3, and 4 are colored as solid yellow, red, purple, and green circles, respectively. b,c) Comparison of a seismic line from the b) baseline and c) monitor surveys, highlighting areas undergoing amplitude changes.

On the other hand, analysis of time-lapse seismic data shows that most of the observed amplitude changes are limited to the reservoir interval (Figures 8.1 b & c). Figure 8.2 shows the isochrone difference map for the reservoir interval (colors) overlain by the blue and red polygons, highlighting the amplitude changes in the upper and lower reservoir interval, respectively. The isochrone difference map indicates reservoir thickening in terms of two-way travel times across the pad. These observations together indicate that different parts of the pad are impacted differently spatially and vertically due to steam injection. This is further confirmed from the temperature logs of the two observation wells, 40-A and 40-B (Figure 8.2, bottom). The temperature data was recorded at different times during the 3rd cycle of steam injection and production, as indicated by different colors of curves (figure 8.2 b & c). The temporal variation in temperature shows that temperature at the start of injection (March 2004) is low (~25°C) as recorded by well 40-A. The

temperature then starts to rise as the steam injection continues. Both wells record this, however, the temperature rise is minimal at 40-A (~35°C), but a substantial increase in temperature is recorded for 40-B (~275°C). The comparison of temperature changes and isochrone difference at both observation well locations indicates that both have similar isochrone difference values, contrary to the temperature measurements. This may be because the isochrone difference map is generated from the reservoir isochrone generated before steam injection and after four cycles of steam injection and production; thus, the isochrone difference map shows the cumulative changes in reservoir thickness after four cycles.

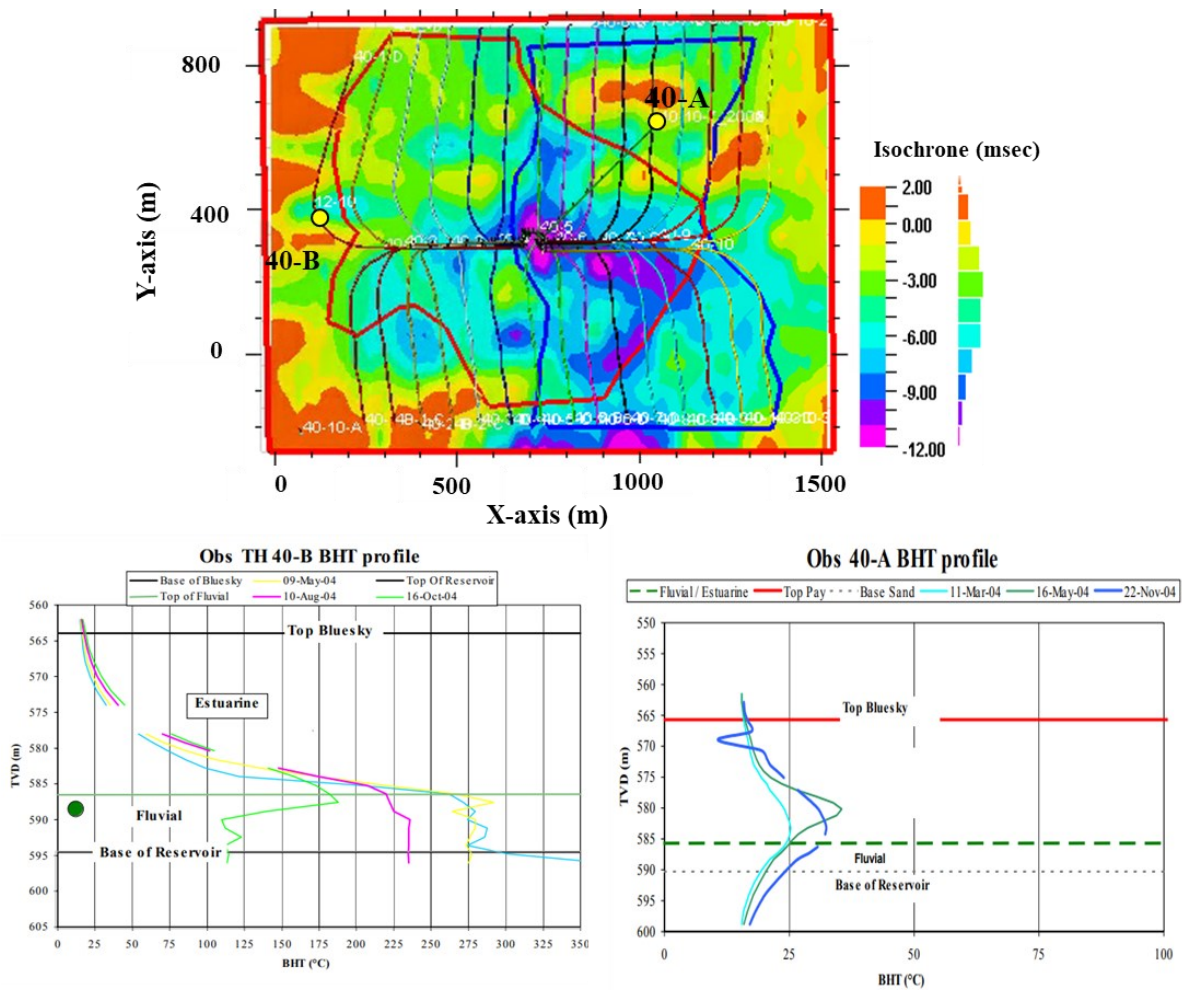


Figure 8-2: Isochrone difference map for the reservoir (top) and temperature profiles from two observation wells at the pad. Different colors in the bottom indicate temperature values recorded at different times.

The surface tiltmeter data shows surface uplift during steam injection, as seen in Figure 8.3. The Figure shows snapshots of the cumulative measured surface deformation during the 2nd cycle of steam injection (June-Aug 2004). The positive values indicate uplift, and the negative values are indicating subsidence. It is interesting to note that during the injection, surface uplift is seen throughout the pad, possibly due to reservoir dilation in response to steam injection.

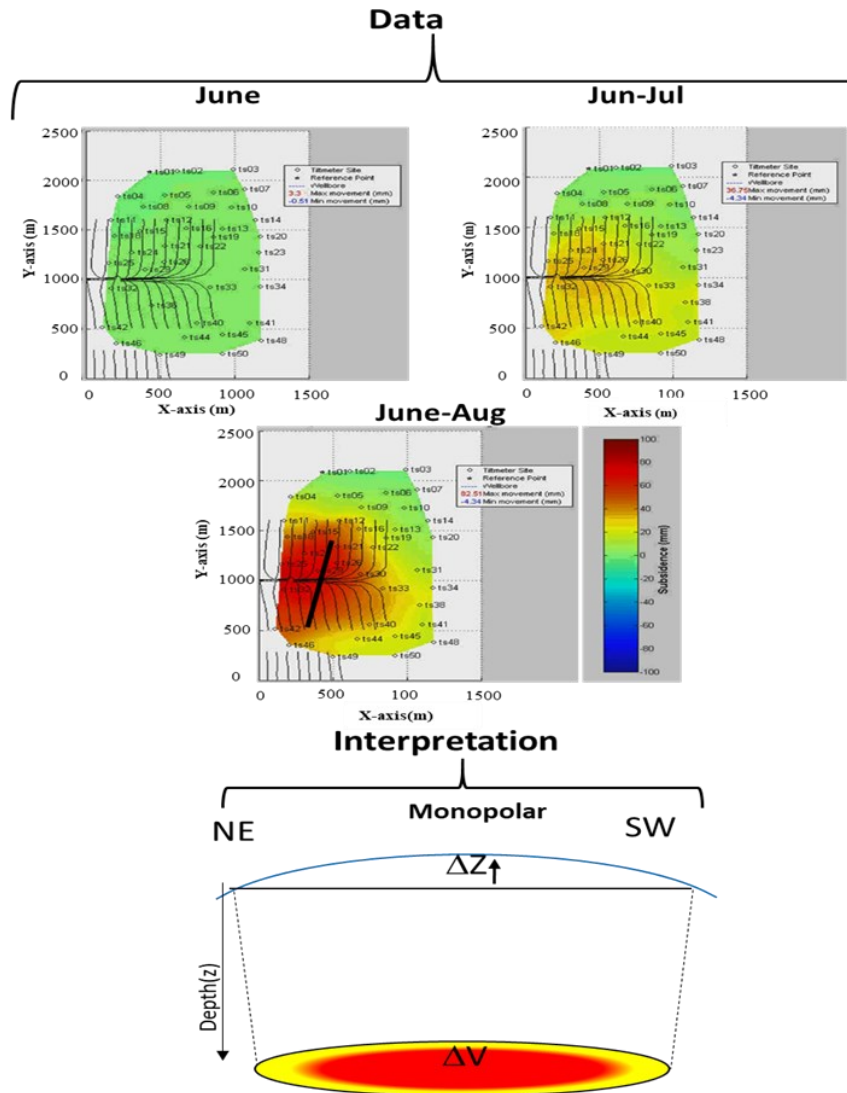


Figure 8-3: Subsidence values recorded by tiltmeters during the 2nd cycle of steam injection. The steam was injected from June to August 2004. The schematic diagram at the bottom shows the possible interpretation of the surface uplift during the injection cycle.

8.2.2 Theoretical analysis

It is discussed in Chapter 3 that steam injected at high temperatures and pressure reduces the viscosity of the heavy oil to facilitate hydrocarbon production. The high temperature inside the

reservoir reduces the density and P-wave velocity, thus decreasing the acoustic impedance. The decrease in acoustic impedance within the heated reservoir will result in higher impedance contrast between the reservoir and the surrounding rock. This will increase the seismic reflection amplitude. The decrease in P-wave velocity within the heated reservoir will increase the travel time (TWT). This should be visible on the isochrone difference map of the reservoir.

The steam injection at high temperatures also dilates the reservoir (Figure 8.4), exerting stresses in front of the propagating reservoir. The induced stresses are expected to cause shearing, but due to the ductile nature of the heavy oil reservoir, no or limited fracturing and microseismic activity are expected in the reservoir interval.

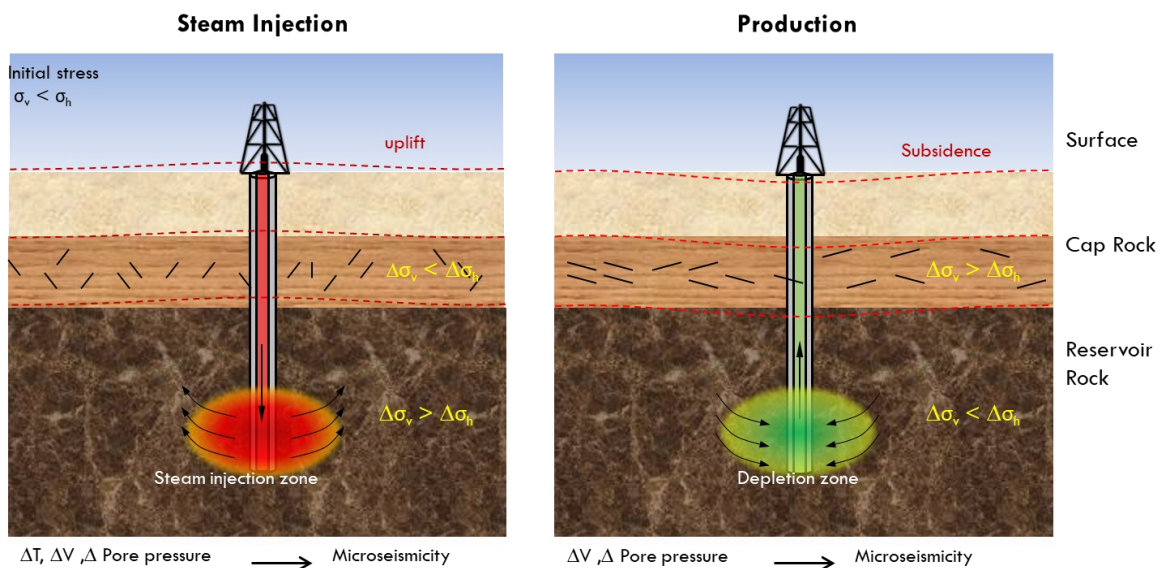


Figure 8-4: Showing stress changes (σ) in response to the pore pressure, temperature (T), and volumetric (V) changes during steam injection (left) and hydrocarbon production (right).

8.2.3 Comparison of observations and theory

The above field observations indicate that the reservoir is changing during steam injection, and the set of proposed predictions needs to be validated by the observations. The time-lapse seismic data consisted of a baseline and monitor survey, the baseline survey was recorded before steam injection, and the monitor survey was acquired after four cycles of steam injection and production. Therefore, the observed changes recorded by the time-lapse seismic data are the cumulative result of four steam injection and production cycles. It may be difficult to separate the observations into injection and production-related changes, but these data can still be interpreted

and analyzed. Microseismic data are recorded continuously; therefore, the resulting events can be confidently characterized as injection or production-related.

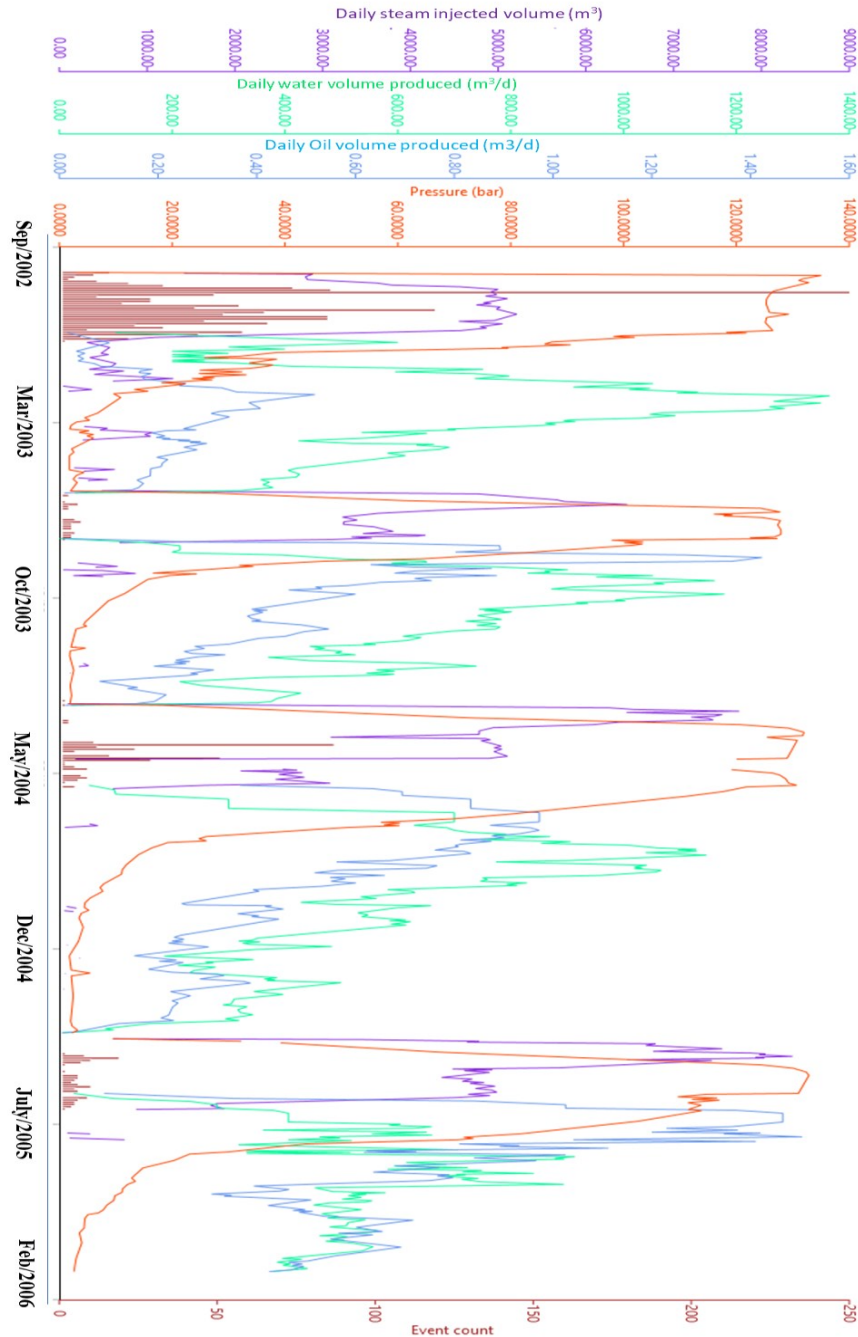


Figure 8-5: Time plot of injection/production data volumes microseismic activity recorded during the steam injection cycles. The steam injection, hydrocarbon, and water production are shown in red, green, and purple colors. The microseismic event count is shown as dark red bars.

Limited to no microseismic activity is found to be in the reservoir interval due to steam injection. This indicates a lack of fracturing and faulting, supporting the theory that the heavy oil reservoir behavior is ductile, thus validating the prediction. It is worth mentioning here that the thickness of the reservoir varies between 25 and 35 meters at the pad, and the expected depth uncertainty for event locations (base on uncertainty analysis in chapter 4) is approximately 20m. If it is assumed that, the current locations may be off in depth by 20m, this may place some of the locations into the reservoir interval, but the spatial trend of the locations remains the same. Therefore, it can be said with confidence that the reservoir remains relatively aseismic during the steam injection. The increased reservoir temperature and pressure reduce the viscosity and density of the reservoir, thus ultimately decreasing the P-wave velocity. The P-wave will take longer to travel through the heated reservoir zone. These zones are identified by comparing the reservoir isochrone values from the baseline and monitor surveys. To confirm the above, isochrone difference maps and amplitude changes are also analyzed, as shown in Figure 8.2. The isochrone difference map shows substantial thickening at the center of the pad, highlighting the reservoir zone with substantial velocity reduction due to steam injection (Figure 8.2). The decrease in density and velocity at the top reservoir reflector results in increased seismic amplitude (Figure 8.1c). The isochrone thickening is interpreted as the combined effect of velocity reduction and reservoir dilation.

The surface uplift during steam injection (Figure 8.3) supports this theory and the above interpretation that the reservoir dilates to accommodate the high temperature and pressure. The comparison of isochrone difference (Figure 8.2a) and surface uplift map (Figure 8.3) reveal different spatial patterns, and no correlation is found between both. This is possibly because the isochrone map shows cumulative changes from four injection and production cycles, whereas the surface uplift map is from a single injection cycle. The steam front in the reservoir can be interpreted based on the isochrone difference map and amplitude polygons (Figure 8.2a). I interpret that the steam has probably impacted the center and south side of the pad, indicating higher isochrone difference values (blue-purple color area).

Conversely, steam may not have reached the corner of the pad with very low isochrone difference values (yellow to greenish color areas). The above observations combined support the non-homogenous movement of steam inside the reservoir. The next section discusses the caprock response to steam injection.

8.3 Caprock response to steam injection

8.3.1 Observations

The steam is injected into the heavy oil reservoir, but its impact may be observed in the surrounding cold reservoir and the overburden. The first observation at the pad was the recording of an abundance of microseismicity in the caprock as soon as the injection began in September 2002 (Figure 8.1). Approximately 98% of the recorded microseismicity occurred during the injection cycles, of which 90% of the microseismicity occurred in the overburden. Moreover, the brittleness (Figure 8.6) calculated from the well logs indicate a higher value within the caprock than in the heavy oil sands.

On the other hand, the analysis of time-lapse seismic reflection data does not provide any evidence of pre-existing faults or activation of new faults due to injection. Similarly, the isochrone difference map and amplitude analysis also reveal minor changes in the caprock.

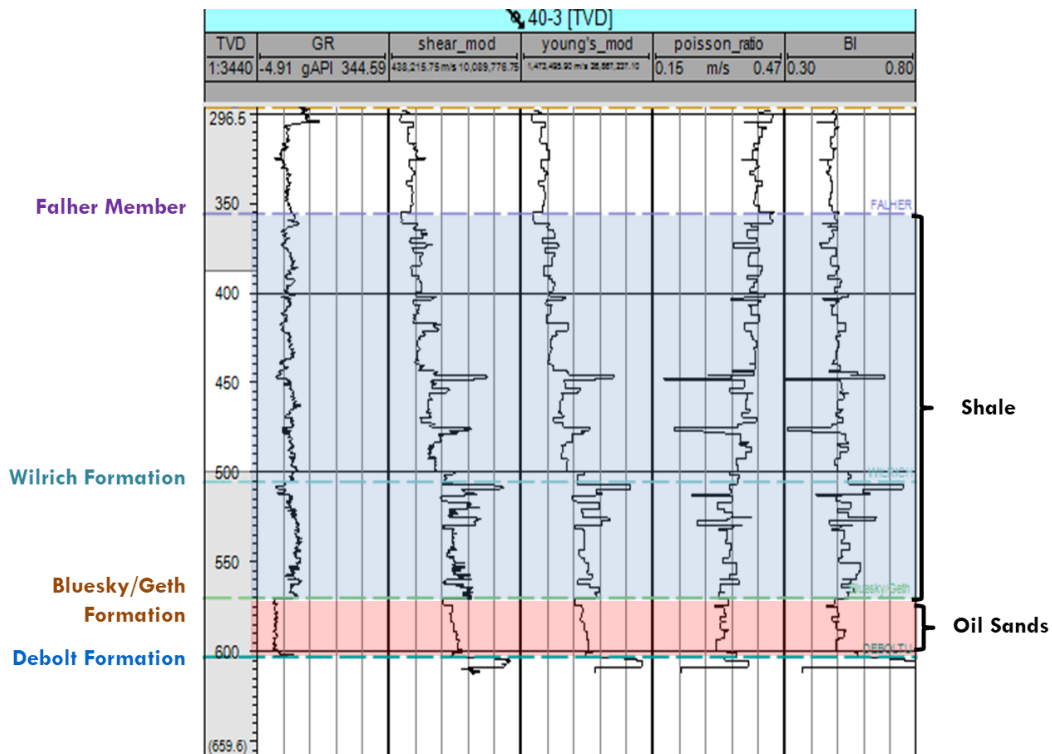


Figure 8-6: The GR log, calculated Shear modulus, Young's modulus, Poisson ratio, and Brittleness index log for well 40-3, located on the western side of the pad.

8.3.2 Theoretical Analysis

The shales above the heavy oil reservoir are impermeable. The steam injection at high temperature and pressure causes the reservoir to dilate. However, above the steam chamber, the horizontal stresses inside the caprock drops (Shafiei & Dusseault, 2013). If the injection pressure (P_{inj}) becomes higher than the min horizontal stress (σ_h) then vertical fractures may develop and propagate upward into the caprock (Shafiei & Dusseault, 2013). These cracks may also act as a pathway for reservoir fluid to leak into the caprock. If this happens, then the pore pressure in the overburden increases. This will move the Mohr's circle to the left, causing failure in the overburden (figure 8.7 c). This can affect the integrity of the steam front leading to loss of heat, and in extreme cases, may cause a gas or steam blow out.

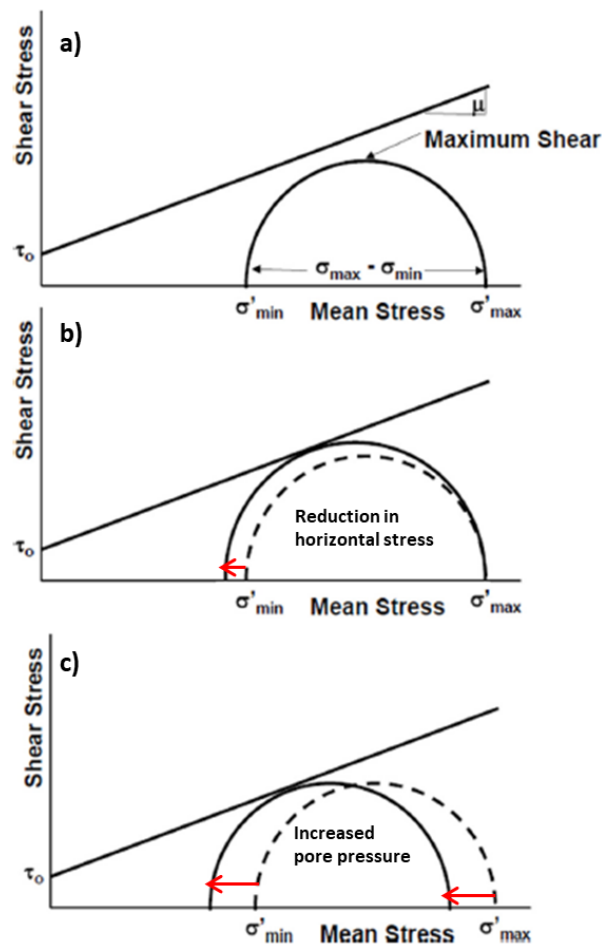


Figure 8-7: Mohr's circle plot showing a) initial stresses, b) reduction in minimum stress because of reservoir dilation, and c) increase in pore pressure in the overburden, causing slip failure. (reproduced with permission from Maxwell et al. (2015)).

Another effect on the caprock due to thermal simulation is the shrinkage of the shale barrier. When the temperature exceeds 125°C, absorbed water from the shales is stripped off the clay minerals causing the shale to dry and shrink (Shafiei & Dusseault, 2013). As the shrinkage occurs, the horizontal stress is reduced and may eventually drop below the pressure of the pore fluid (steam-oil-water-gas) in the reservoir, so vertical hydraulic fractures are generated. The reduction in horizontal stress can be visualized as the size of Mohr's circle grows, getting closer to the failure envelope, thus resulting in rock failure (Figure 8.7b). The same may be observed at the caprock-reservoir interface due to the concentration of shear stresses because of differential thermal stresses. These are enough to cause shear slippage at the interface (Shafiei & Dusseault, 2013). If the steam front reaches the caprock shale and condenses to a liquid state, it may be absorbed by the shales. This can cause shale to swell, thus reducing the Young's modulus and the peak strength (Bashbush et al., 2009). Therefore, shale swelling will also facilitate shale breakage by decreasing the cohesion and friction angle. In summary, the microseismicity in the caprock is expected during steam injection due to pore pressure and stress changes resulting in fracture initiation or reactivation.

8.3.3 Integrated Analysis

According to the data observations, the majority (90%) of the microseismic events are located in the overburden (Figure 8.1a), thus validating the prediction that microseismic activity is expected in the brittle shale. A variety of processes may result in microseismic activity or failure in the overburden, as discussed above and one must investigate the cause.

The first possible mechanism is reservoir fluid leakage into the caprock (also known as wet events or wet cracks). This could also happen if the high temperatures reach the caprock causing it to dehydrate and create microfractures. The reservoir fluid may enter the caprock through these mini fractures. If this is true, then the temperature in the overburden must increase and should be evident from the temperature logs, but no such change is recorded (Figure 8.2b&c). The fluid leakage into the caprock will alter the fluid saturation in the caprock, thus impacting the seismic amplitude, which may be evident in the time-lapse seismic data (Kato et al., 2008). Reservoir fluid leakage into the caprock is also possible if pre-existing fractures or faults are present. However, the interpretation of baseline seismic data does not support any pre-existing faults, nor does the monitor seismic data indicate any evidence of amplitude variations in the overburden, for instance,

due to fluid substitution. An r - t plot was also generated and analyzed, as shown in Figure 6.16 (chapter 6). The plot shows that most of the microseismic triggering occurred about 20 days after the steam injection, navigating vertically upward (encircled in Figure 6.16, chapter 6) at a distance of 20 and 80 m above the reservoir zone. The time delay of 20 days between injection and microseismic triggering is sufficient for fluid migration. But no pressure data or any incidences were reported to support the hypothesis of fluid leakage.

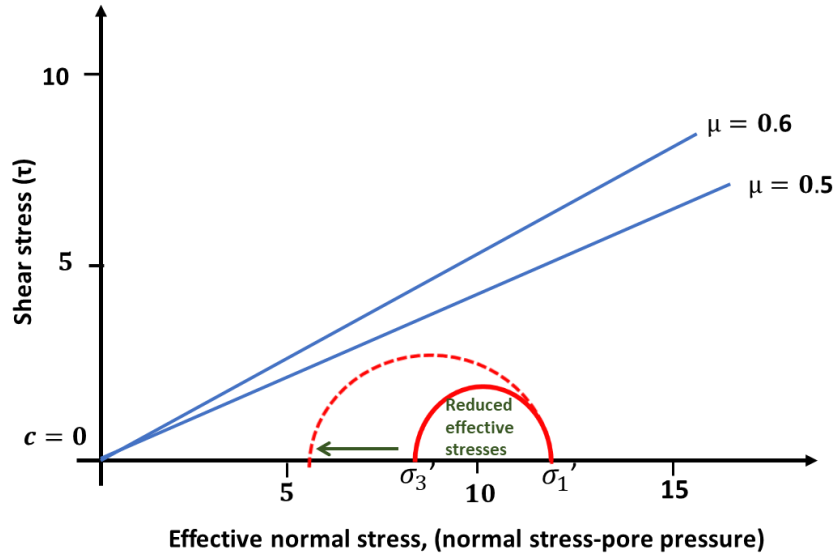


Figure 8-8: Possible Mohr circle changes responsible for microseismicity in the overburden during steam injection in the study area. The increased Mohr circle (dotted red) is caused by induced stress in the overburden due to steam injection into the reservoir. The solid blue lines are the failure criterion with a coefficient of friction (μ) 0.5 and 0.6 and cohesion (c) of 0 MPa.

The second possible mechanism responsible for triggering microseismicity in the overburden may be caused by induced stresses (also known as dry events or dry cracks). If the steam touches the caprock, it will condense to liquid and be absorbed by the shale. This will cause the shale to swell, reducing the Young's modulus and the strength of the caprock, thus making it easier to fail. The caprock may also experience shearing because of reservoir dilation, causing the effective horizontal stress to decrease in the overburden, thus inducing microseismic activity in the overburden (Figure 8.7b). As mentioned earlier, temperature data do not indicate that steam may have reached the caprock; therefore, it is reasonable to interpret that recorded microseismicity is caused by the induced stresses in the study area. This can be visualized by plotting the Mohr circle and estimate the failure criteria of the caprock for the study area (Figure 8.8). The initial

stress state in the Peace River area is shown as a solid red circle in the caprock. The minimum stress magnitude is estimated from a reported stress test, and vertical stress is estimated from well logs. The caprock compaction due to reservoir expansion is likely to reduce the effective horizontal stress. This will cause the Mohr circle to enlarge and move closer to the failure envelop (dotted red line, figure 8.8). In addition to the induced stresses, other factors also appear to favor the occurrence of microseismicity in the overburden, e.g., a higher brittleness index (Figure 8.6) and low landing height (Figure 6.11 a, chapter 6). The latter may facilitate stress transfer in areas where the wells are closer to the top reservoir interface.

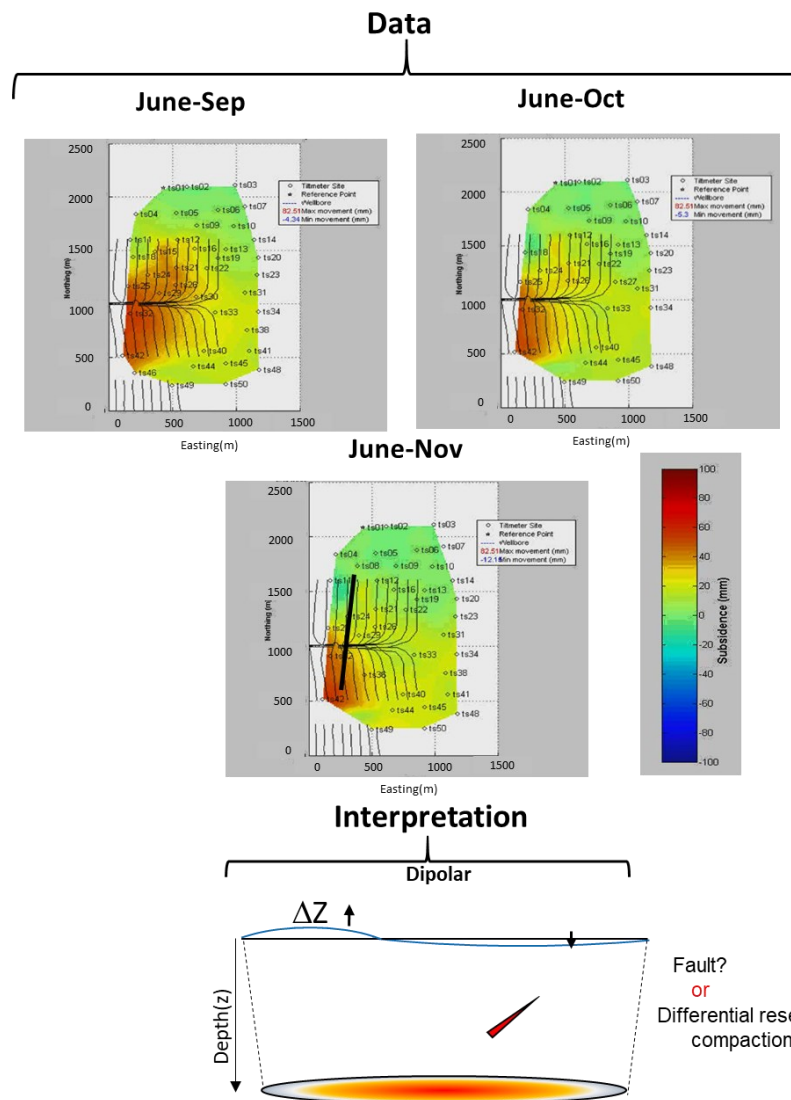


Figure 8-9: Surface heave values recorded by tiltmeters during the 2nd cycle of hydrocarbon production. The hydrocarbon extraction was from September to November 2004. The schematic diagram at the bottom shows the possible interpretation of the surface subsidence during hydrocarbon production.

8.4 Caprock-reservoir response to production

8.4.1 Observations

As soon as production starts, a drastic decrease in microseismic activity is observed, as shown in Figure 8.10. The recorded microseismicity is scattered and minimal. The most significant production-related observation came from the surface tiltmeter data, which was continuously recorded during the injection and production phases. Figure 8.9 shows obvious asymmetrical surface subsidence over the pad. The north side of the pad undergoes surface subsidence of 12 mm, whereas the south side of the pad is still uplifted (85mm). The asymmetrical surface heave may be due to 1) faulting in the subsurface or 2) differential hydrocarbon production. The negligible amount of recorded microseismicity contradicts the possibility of faulting during production. Therefore, the asymmetrical surface heave is possibly due to differential production at the pad.

The seismic data were recorded before steam injection and after four cycles of steam injection and production. Therefore, it is difficult to separate the seismic observations into injection and production portions. The comparison of seismic reflection changes (isochrone thickness and amplitude changes) with the tiltmeter data shows a spatial correlation between both. The surface subsidence is restricted to the north of the pad, where isochrone thickness changes are minimal. In contrast, the maximum isochrone thickness changes are located in the central and southern sides of the pad, where no surface subsidence is recorded. However, the surface is still uplifted due to the previous production cycle. There appears to be a correlation between the seismic reflection observations and tiltmeter data, but as mentioned earlier, the seismic data were recorded before steam injection and after four cycles of steam injection and production. Therefore, it is difficult to comment confidently if the variation in seismic parameters is due to steam injection or hydrocarbon production.

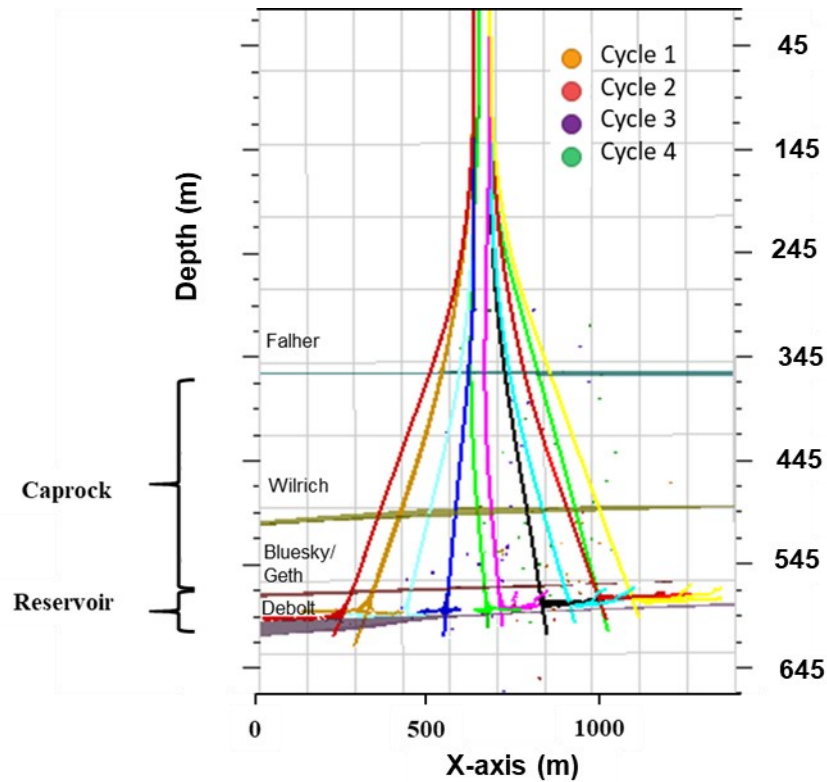


Figure 8-10: The cross-sectional view is showing production-related microseismic event distributions across the pad. Horizontal colored lines indicate geological formations of interest. The Falher, Wilrich, Bluesky, and Debolt formations are shown as blue, yellow, red, and purple colors, respectively. Microseismic events are colored based on their time of occurrence. Events that occurred during cycle 1, 2, 3, and 4 are colored as solid yellow, red, purple, and green circles, respectively.

Additionally, it is observed from the engineering data that the hydrocarbon production gradually decreases from the first cycle onward, despite increasing the injected steam volume.

8.4.2 Theoretical Analysis

The processes of hydrocarbon extraction or depletion can significantly impact both the reservoir and the surrounding rock. The depletion may cause faulting in the subsurface and surface deformation, as illustrated in Figure 8.11. During fluid/hydrocarbon extraction, the reservoir is compacted, and pore pressure decreases. As a result, the effective vertical stress (σ_v') decreases in the reservoir and increases in the overburden. The fluid extraction decreases pore pressure; thus, extraction should increase the effective confining stresses and prohibit fault slip. However, pieces of evidence suggest that fluid extraction can also induce microseismicity in the overburden by contracting the reservoir rock, deforming the surrounding rock, thus altering the stress field (Segall 1989; Yerkes and Castle 1976).

The schematic cross-section in Figure 8.11 summarizes the expected changes in response to hydrocarbon extraction. Extraction of fluid may result in surface subsidence, and both normal and reverse faults may accompany the extraction. Normal faults may develop at the margins of the subsidence (adjacent to the heated zone in the reservoir), and reverse faults may develop in the central region (caprock and below the reservoir). As a result, microseismic activity may be recorded above, below, and within the reservoir (adjacent to the depleted zone). However, due to the ductile nature of the heavy oil reservoir, limited or no microseismic activity is expected within the reservoir interval. It is anticipated that reservoir compaction may cause 1) surface subsidence and 2) microseismic activity in the overburden.

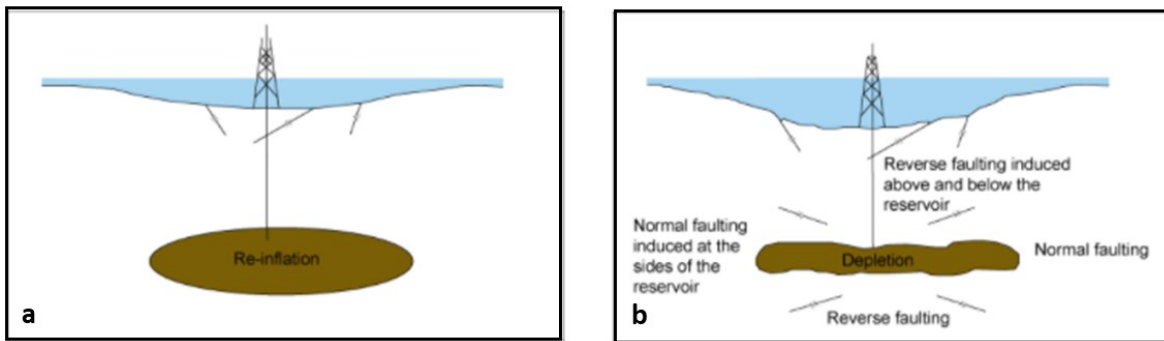


Figure 8-11: Schematic diagram showing the reservoir a) before depletion and b) after reservoir depletion and expected faulting and fracturing in the surrounding of the depleted reservoir (reproduced with permission from Segall, 1989).

8.4.3 Integrated Analysis

In response to the fluid extraction from the reservoir, the pore pressure is expected to decrease, and the reservoir shrinks, thus possibly resulting in faulting around the depleted reservoir and surface subsidence. The observed surface subsidence (Figure 8.9) supports the mechanism of reservoir depletion, but microseismic activity is absent during the production cycles (Figure 8.10). The absence of microseismicity during the fluid extraction phase may be due to the rate and duration of fluid extraction, presence, or absence of pre-existing weakness (Shapiro et al., 2006). The absence of microseismicity during the extraction thus may be related to the rate and duration of the extraction cycle as this will perturb the pore pressure, and a positive pore pressure perturbation is required to trigger microseismicity (Shapiro et al., 2006), which was possibly not achieved during the fluid extraction cycles in the study area.

Additionally, the observed surface subsidence during fluid extraction is only observed in the north section of the pad, which appears to be spatially correlatable to minimal isochrone thickness changes (Figure 8.2). This may also indicate that not all the wells are contributing equally to hydrocarbon production.

8.5 Comparison of predictions with observations

8.5.1 Lessons Learned

In this section, I compare the set of predictions from chapter 3 with the actual observations from chapters 6 and 7 to assess the validity. The schematic diagram in figure 8.12 shows the key features of the reservoir-caprock response after four cycles of steam injection and hydrocarbon production.

- a) The abundance of microseismicity in the overburden during injection and production agrees with the prediction that microseismicity is expected in the brittle shales and less likely in the ductile reservoir interval. The absence of microseismic activity in the reservoir signifies that fracturing is not responsible for hot fluid transfer within the reservoir to facilitate heat transfer to the cold unproduced reservoir. Rather, it is likely that the primary mechanism of heat transfer within the unproduced or cold reservoir is predominantly through conduction and fluid flow.
- b) The variation in seismic attributes within the reservoir interval due to steam injection agrees with the prediction in chapter 3. The increased seismic amplitude at the top and bottom of the reservoir (time-lapse data, chapter 7) and substantial thickening of the reservoir isochrones varies throughout the pad. The fluctuation in seismic attributes is due to the changes in several parameters, e.g., density, velocity, temperature, and fluid saturation. These observations combined support heterogeneous steam movement spatially and vertically, and some of the reservoir zones may not have been fully produced as desired. The heterogeneous steam movement is also supported by temperature data, which indicates the presence of hot and cold zones.
- c) As anticipated, because of the brittle nature of shales, most of the microseismicity is recorded in the overburden shales. The majority of the microseismicity is recorded during the injection phase. The occurrence of microseismicity is the earliest indication of fracturing/faulting or reactivation. The microseismicity in the overburden is not

desired and may be associated with stress variation (dry cracks) or pore pressure variation because of the reservoir fluid leakage into the overburden (wet cracks) and must be investigated. The r-t plot analysis (chapter 6), combined with the absence of seismic amplitude changes in the overburden, negate the possibility of reservoir fluid leakage (wet cracks) and microseismic activity in the burden that may be associated with the induced stresses (dry cracks). The presence of dry cracks (in the overburden) combined with the surface uplift and subsidence during the injection and production cycle can be interpreted as non-reversible changes in the subsurface (reservoir and overburden) due to reservoir dilation and compaction.

- d) As expected, surface tiltmeter data showed surface uplift and subsidence during steam injection and production cycles, respectively. This confirms reservoir dilation and shrinkage, thus causing the overlying layers to uplift and subside.

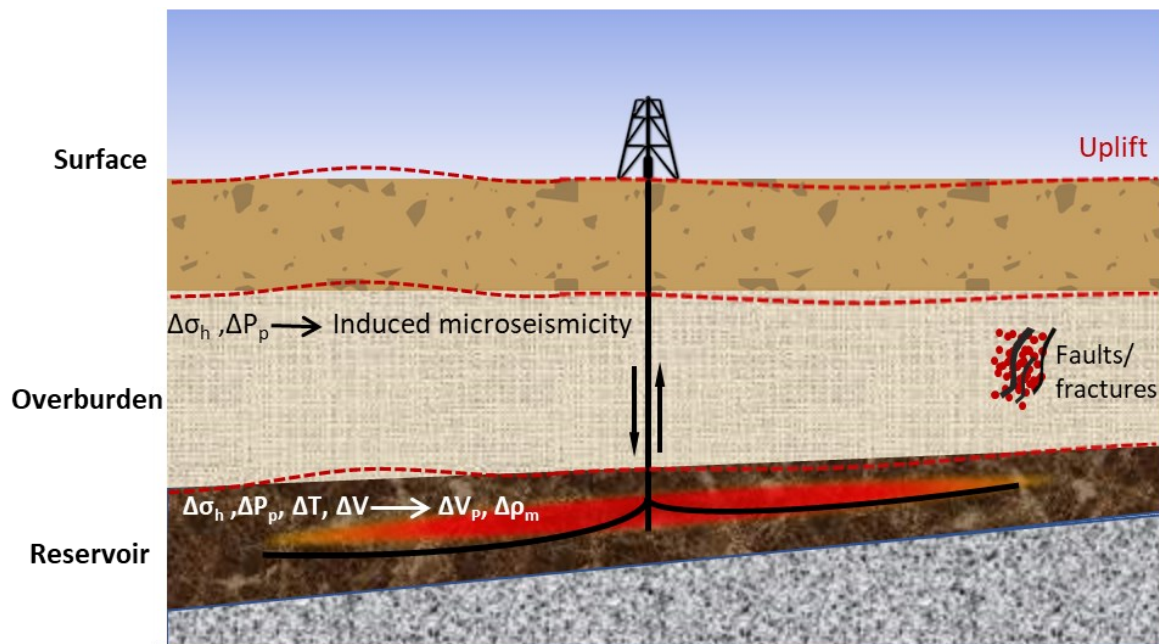


Figure 8-12: Schematic of the observed changes in the reservoir and overburden after four steam injection cycles and production at the pad.

The time-lapse seismic reflection data give better insight into the changes occurring within the reservoir zone. In contrast, microseismic data provide a more detailed picture of the changes in the overburden. By integrating both data types with other geophysical observations (e.g., surface

tiltmeter data) and engineering data, a more detailed understanding of the processes occurring during production and injection is achieved.

The importance of this multidisciplinary geophysical integration study could be emphasized by highlighting the probable interpretation if each dataset was interpreted independently. The analysis based on microseismic data alone could have been interpreted as reservoir fluid leaking into the overburden, thus compromising the caprock integrity, which is of concern during the steam-assisted heavy oil recovery operations. This may have easily resulted in misinterpretation of the microseismic data. Although it is known that this may not be the only reason for microseismic activity in the overburden, yet additional data are needed to investigate all possible mechanisms responsible for triggering microseismic activity.

Similarly, time-lapse reflection data only highlights steam-assisted changes within the reservoir zone but fails to show the impact of steam injection and hydrocarbon extraction on the surrounding rocks, e.g., small-scale fracturing in the overburden, responsible for triggering of microseismicity, thus resulting in a partial interpretation of the bigger picture.

8.5.2 Comparison with other models

Significant work has been done by Maron et al. (2005) to investigate and understand the steam movement and associated geomechanical processes in and around the reservoir. It must be pointed out that my results do not replicate the previous work. The main difference between both models is the mechanism of steam movement within the reservoir. According to Maron's model, the steam transfer into the unproduced reservoir occurs under fracturing conditions. This is because Maron interpreted significant microseismic activity in the reservoir interval during injection, which is believed to be associated with fracture creation or opening.

The results presented in this study are based on the data observations. As expected, the microseismic activity is essentially located in the caprock, and very limited microseismicity is triggered in the reservoir, contrary to the results shown by McGillivray (2005) and Maron et al. (2005), where all the events are located inside the reservoir zone. Their proposed model was based on these locations (provided by the vendor). I did not have event locations processed by the vendor. Therefore, I have performed extensive testing and quality control (synthetic analysis, manual inspection of time picks, azimuth, and event locations). The microseismic event locations in the overburden in my results are justified by higher values of the brittleness index of caprock than heavy oil sands (Figure 8.6). The reasoning is also supported by the conceptual model of Dusseault

& Collins (2010), which states that stiffer rock ahead of the heated zone can attract higher stresses and eventually will be forced into its yielding condition. This means that all the rock in advance of the propagating steam front will shear at low confining stresses. This also creates a large concentration of stresses between the reservoir and overlying impermeable non-expanding caprock. As a result, effective stresses decrease in the caprock, causing the shear failure, resulting in microseismic activity.

The observations and results presented in this study disagree with Maron's model because they do not consider the induced stresses inside and around the heavy oil reservoir due to steam injection at high pressure, which is the possible mechanism behind microseismic activity in the overburden. Although the authors incorporated several types of surveillance data acquired over the pad, the focus was to analyze the changes within the reservoir interval to track the steam movement and interpret the steam front.

It must be mentioned that it is a common practice to keep the injection pressure of steam below the fracture pressure during the steam-assisted recovery operation to avoid fracturing/faulting of the caprock. However, several studies have shown that it is common to record microseismicity in the overburden, indicating fracturing. The modeling study by Khan et al. (2011) demonstrated that keeping the injection pressure lower than the fracture pressure does not guarantee caprock integrity. This is supported by several published studies where the majority of the microseismic activity is observed in the overburden (Miyazawa et al., 2008; Parotidis et al., 2004, 2005; Shapiro & Dinske, 2009; Walters & Zoback, 2013). I also compare my results with Walters & Zoback (2013) and Miyazawa et al. (2008), where most of the microseismic event locations are found to be in the overburden (400m and 250 m depth) during heavy oil extraction from Cold Lake, Alberta. The majority of the microseismic events were clustered above the reservoir (at 400m and 250 m depth), and very few events were located inside the reservoir, possibly indicating that the reservoir may be an aseismic region. Miyazawa et al. (2008) used a simple geomechanical model and found that the size and distribution of microseismicity agrees with the Mohr circle. Their paper also mentions that the induced microseismicity is likely caused by stress changes associated with reservoir expansion rather than pore pressure changes due to steam penetrating into the overburden; this supports the conclusion drawn from my work. However, the model by Miyazawa et al. (2008) fails to explain the microseismicity at the depth of

230 m and does not include time lapse seismic data, which may have helped identify any existing faults, above the reservoir interval.

Walters & Zoback (2013) analyzed the microseismic event locations and surface deformation to understand better how both are spatio-temporally related. But, their study did not attempt to incorporate time-lapse surface seismic data and production data. However, it is still unclear what could be the potential mechanism behind microseismic activity in the unconsolidated reservoir (Walters & Zoback, 2013).

The results in this study are based on the experimental setup and data observations from the CSS technique, but it can easily be applied to other thermal recovery techniques, e.g., SAGD because both CSS and SAGD procedures involve the injection of steam at high temperature and pressure into the reservoir. Therefore, caprock and reservoir are expected to respond similarly to the CSS experiment. The only difference is in the acquisition setup (number of injectors and injection strategy).

8.6 Conclusions

The observations from the analysis of the multidisciplinary data agree with the predictions from chapter 3. This demonstrates the importance of linking geomechanical changes with the geophysical observables to ground truth and calibrate any proposed models. The results show that steam injection not only changes the physical properties (velocity, density, volume) of the reservoir but also affects the geomechanical properties (stresses and rock strength) of the reservoir and the surrounding rock. This is supported by the substantial amount of microseismicity in the overburden. The presence of microseismicity in the overburden does not necessarily represent fluid migration into the caprock but may be due to the stress transfer into the overburden because of stress/strain changes associated with reservoir expansion during steam injection.

Additionally, combining ground deformation, seismicity, time-lapse reflection, and engineering data to validate the predictions provides a powerful tool to improve our understanding of the relationships between fluid injection, extraction, and reservoir-caprock system dynamics, which in turn may lead to better containment strategies.

9 Conclusion

9.1 Conclusion

Buried heavy oil deposits are actively undergoing enhanced oil thermal recovery processes such as cyclic steam stimulation (CSS) for economic production. It is crucial to have a good understanding of how steam moves and affects the reservoir-caprock system to enhance the efficiency of the recovery processes. This is only possible by monitoring the steam injection and movement over time. In this research, multidisciplinary data recorded during the CSS experiment are used to understand the dynamics of the CSS operation and investigate the influence/impact of steam injection on the reservoir-caprock system.

In order to study this, time-lapse surface seismic survey and continuous microseismic data were analyzed along with log information, injection, and temperature data for four steam and production cycles. Before analyzing the recorded data, a synthetic study was performed to evaluate different location techniques and understand the expected location uncertainty in the recorded microseismic data. This was followed by processing and quality control of event locations. The obtained microseismic event locations provided detailed insight into the geomechanical response of the reservoir and caprock during steam injection and production. The spatial and temporal analysis of microseismic event locations revealed that 95% of the events occurred in the overburden during the steam injection. The detailed analysis of the locations resulted in the interpretation of two possible faults in the overburden, but microseismic data alone were insufficient to confirm if the microseismic activity was due to pre-existing faults or reservoir fluid leakage into the overburden. The analysis also concludes that microseismic data do not provide much information about the changes within the reservoir zone.

Next, time-lapse seismic data were incorporated to dig deeper into the changes at the reservoir level. The data were processed and analyzed for amplitude anomaly and isochrone thickening across the pad at the reservoir and caprock level. Contrary to the microseismic data, the time-lapse data revealed a much more detailed image of the changes within the reservoir zone. The isochrone thickness map appeared to be an important attribute to monitor the changes at the reservoir level. The changes in the amplitude and isochrone thickness maps integrated with the temperature observations indicated a non-homogenous movement of steam vertically and spatially in the reservoir. However, the data did not show any changes in the seismic attributes at the caprock

level, indicating that most likely; no pre-existing faults are present in the overburden. The amplitude and isochrone changes were restricted to the reservoir interval; therefore, it was concluded that no reservoir fluid leakage occurred during the injection and production.

Next, observations from each data were integrated to understand the complete picture of changes occurring in the subsurface and possible causes of microseismic activity in the overburden. The microseismic data were integrated with time-lapse changes to investigate the possibility of wet versus dry cracks as a possible cause of microseismicity in the overburden. Due to the absence of any evidence to support the possibility of pre-existing faults (from seismic data) and fluid migration (seismic amplitude changes in the overburden), it was concluded that microseismic activity in the overburden is the result of induced stresses (due to reservoir dilation) and caprock integrity was not compromised during the experiment. The reservoir dilation was also confirmed by incorporating isochrone changes and surface tiltmeter data.

It was also found that reflection seismic data observations highlighted the changes occurring at the reservoir interval, whereas microseismic data revealed the changes in the caprock. However, a complete picture of subsurface changes was only visible once the data observations from each geophysical data were integrated.

The main results of the research study may be listed as

1. The synthetic study demonstrated that microseismic event location uncertainty is associated with two commonly used event location methods (P- and SP- method), using synthetic data from a geophone array placed in a single deviated borehole.
2. A complete event location and quality control workflow for the case of a single deviated observation well is presented and successfully applied to produce a reliable event location catalog for further interpretation. A multidisciplinary data analysis approach helped understand the geomechanics of heavy oil reservoirs undergoing cyclic steam stimulation and relate the data observation to responsible physical mechanisms.
3. The research has highlighted the unique information extracted from each geophysical data resulting in successfully evaluating the changes in and around the heated reservoir.
4. It was found that seismic data observations highlighted the changes occurring at the reservoir interval, whereas microseismic data revealed the changes in the caprock.

However, a complete picture of subsurface changes was only visible once the data observations from each geophysical data were integrated.

9.2 Recommendation for future work

1. The data observations support the proposed predictions. However, the work can be extended by performing a coupled geomechanical-fluid simulation modeling study to match the data observations and use it for future prediction and optimization of future thermal operations.
2. Similarly, solely a qualitative interpretation is performed. It would be highly interesting to perform a quantitative interpretation by inverting observed amplitude changes into actual fluid saturation, temperature, and stress changes.
3. Furthermore, additional constraints could be obtained from the existing data, for instance, by performing a time-lapse analysis of amplitude-variations with offset (AVO).

Finally, additional data could have been acquired, such as multiple vintages of seismic reflection data, at closer time intervals, to better separate the production and injection changes. This would require substantial capital investments by the operator.

Bibliography

- Adams, J., & Bell, J. S. (1991). Crustal stresses in Canada. *Neotectonics of North America*, 1, 367–386.
- Aki, K., and Richards, P. G. (2009). *Quantitative seismology*. 2nd ed., corr. Print., Sausalito, Calif., Univ. Science Books, 2009, XVIII + 700 pp., ISBN 978-1-891389-63-4 (see http://www.ldeo.columbia.edu/~richards/Aki_Richards.html).
- Akram, J., D. W. Eaton, and A. St. Onge, 2013, Automatic event-detection and time picking algorithms for downhole microseismic data processing: 4th EAGE Passive Seismic Workshop, PSP07, doi: 10.3997/2214-4609.20142372
- Akram, J., 2014, Downhole microseismic monitoring: Processing, algorithms and error analysis: Ph.D. thesis, University of Calgary.
- Al-Aulaqi, T., Grattoni, C., Fisher, Q., Musina, Z., Al-Hinai, S., 2011. Effect of temperature, oil asphaltene content, and water salinity on wettability alteration. In: Paper SPE # 149071 presented at the SPE/DGS Saudi Arabia Section Technical Symposium and Exhibition held in Al-Khobar, Saudi Arabia, 15–18 May, 2011.
- Al-Hadhrami, H.S., Blunt, M.J., 2000. Thermally induced wettability alteration to improve oil recovery in fractured reservoirs. In: Paper SPE # 59289 presented at the 2000 SPE/DOE Improved Oil Recovery Symposium held in Tulsa, Oklahoma, 3–5 April, 2000.
- Al Hooti, K., Kendall, M., Al Harrasi, O., Al Azri, S., Al Siyabi, Q., & Verdon, J. (2019). Microseismic Monitoring of Thermally Assisted Gas Oil Gravity Drainage in a Heavy Oil Field in Oman. 81st EAGE Conference and Exhibition 2019, 2019(1), 1–5.
- Alberta Energy Regulator. (2015). Alberta's energy reserves 2014 and supply/demand outlook 2015–2024. In *Statistical Series (ST) 2015–98*.
- Albright, J. N., and R. J. Hanold, 1976, Seismic mapping of hydraulic fractures made in basement rocks: Proceedings of the ERDA Symposium on Enhanced Oil and Gas Recovery, Tulsa, 2, C–8, 1–13.
- Allen, R. V. (1978). Automatic earthquake recognition and timing from single traces. *Bulletin of the Seismological Society of America*, 68(5), 1521–1532.
- Arrowsmith, S. J., & Eisner, L. (2006). A technique for identifying microseismic multiplets and application to the valhall field, north sea identifying microseismic multiplets. *Geophysics*, 71(2), V31–V40.
- Artman, B., Podladtchikov, I., & Witten, B. (2010). Source location using time-reverse imaging. *Geophysical Prospecting*, 58(5), 861–873.
- Badley, M. E. (1985). *Practical seismic interpretation*.
- Baer, M., & Kradolfer, U. (1987). An automatic phase picker for local and teleseismic events. *Bulletin of the Seismological Society of America*, 77(4), 1437–1445.
- Baig, A., & Urbancic, T. (2010). Microseismic moment tensors: A path to understanding frac growth. *The Leading Edge*, 29(3), 320–324.
- Baisch, S., Bohnhoff, M., Ceranna, L., Tu, Y., & Harjes, H.-P. (2002). Probing the crust to 9-km depth:

- fluid-injection experiments and induced seismicity at the KTB superdeep drilling hole, Germany. *Bulletin of the Seismological Society of America*, 92(6), 2369–2380.
- Bashbush, J. L., Fernández, E., Rodriguez, A., Piña, J. A., & Ruiz, J. (2009). SAGD performance in the Orinoco Belt. *World Heavy Oil Congress 2009 Proceedings*. Paper, 549.
- Batzle, M. L., Han, D.-H., & Hofmann, R. (2006). Fluid mobility and frequency-dependent seismic velocity—Direct measurements. *Geophysics*, 71(1), N1–N9.
- Bayer, B., Kind, R., Hoffmann, M., Yuan, X., & Meier, T. (2012). Tracking unilateral earthquake rupture by P-wave polarization analysis. *Geophysical Journal International*, 188(3), 1141–1153.
- Behura, J., Batzle, M., Hofmann, R., & Dorgan, J. (2007). Heavy oils: Their shear story. *Geophysics*, 72(5), E175–E183.
- Bell, J. S., & Bachu, S. (2003). In situ stress magnitude and orientation estimates for Cretaceous coal-bearing strata beneath the plains area of central and southern Alberta. *Bulletin of Canadian Petroleum Geology*, 51(1), 1–28.
- Bell, J. S., Price, P. R., & McLellan, P. J. (1994). In-situ stress in the western Canada Sedimentary Basin. *Geological Atlas of the Western Canada Sedimentary Basin*, 439–446.
- Billings, S. D., Sambridge, M. S., & Kennett, B. L. N. (1994). Errors in hypocenter location: picking, model, and magnitude dependence. *Bulletin of the Seismological Society of America*, 84(6), 1978–1990.
- Brisco, C. D. (2018). *An Integrated Model of Shear Wave Anisotropy in the Vicinity of a Hydraulic Fracture*. University of Alberta.
- Brune, J. N. (1970). Tectonic stress and the spectra of seismic shear waves from earthquakes. *Journal of Geophysical Research*, 75(26), 4997–5009.
- Butler, R. M. (1987). Rise of interfering steam chambers. *Journal of Canadian Petroleum Technology*, 26(03).
- Castellanos, F., & van der Baan, M. (2012). High-accuracy relative event locations using a combined multiplet analysis and the double-difference inversion. In *SEG Technical Program Expanded Abstracts 2012* (pp. 1–5). Society of Exploration Geophysicists.
- Castellanos, F., & van der Baan, M. (2013). Microseismic event locations using the double-difference algorithm. *CSEG Recorder*, 38(3), 26–37.
- Chalaturnyk, R.J., Scott, J.D., Yang, G., 1991. Geomechanical Modeling of Phase A at the AOSTRA Underground Test Facility. In: *CIM Petroleum Society Annual Conference Paper 91-7*.
- Chmiel, M., & Bardainne, T. (2014). Tomography of a Velocity Model and Location of Microseismic Events with P, Sv and Sh Waves. *76th EAGE Conference and Exhibition 2014*, 2014(1), 1–5.
- Chopra, S., Lines, L. R., Schmitt, D. R., & Batzle, M. L. (2010). Heavy oils: reservoir characterization and production monitoring. *Society of Exploration Geophysicists*.
- Civan, F. (2004). Temperature dependence of wettability related rock properties correlated by the Arrhenius equation. *Petrophysics*, 45(04).
- Collins, P.M., Carlson, M.R., Walters, D.A., Settari, A., 2002. Geomechanical and thermal reservoir

- simulation demonstrates SAGD enhancement due to shear dilation. In: Paper SPE # 78237 Presented at the SPE/ISRM Rock Mechanics Conference held in Irving, Texas, 20–23 October, 2002.
- Collins, PATRICK M. (2007). The false lucre of low-pressure SAGD. *Journal of Canadian Petroleum Technology*, 46(01).
- De Meersman, K., Kendall, J.-M., & Van der Baan, M. (2009). The 1998 Valhall microseismic data set: An integrated study of relocated sources, seismic multiplets, and S-wave splitting. *Geophysics*, 74(5), B183–B195.
- De Waal, J. A., & Smits, R. M. M. (1988). Prediction of reservoir compaction and surface subsidence: Field application of a new model. *SPE Formation Evaluation*, 3(02), 347–356.
- Dusseault, M. B. (2002). CHOPS: Cold Heavy Oil Production with Sand in the Canadian heavy oil industry. Alberta Department of Energy.
- Dusseault, M. B. (2011). Geomechanical challenges in petroleum reservoir exploitation. *KSCE Journal of Civil Engineering*, 15(4), 669–678.
- Dusseault, M. B., & Collins, P. M. (2010). Geomechanics effects in thermal processes for heavy oil exploitation. *Heavy Oils: Reservoir Characterization and Production Monitoring*, 287–291.
- Dusseault, M. B., Yin, S., Rothenburg, L., & Han, H. (2007). Seismic monitoring and geomechanics simulation. *The Leading Edge*, 26(5), 610–620.
- Earle, P. S., & Shearer, P. M. (1994). Characterization of global seismograms using an automatic-picking algorithm. *Bulletin of the Seismological Society of America*, 84(2), 366–376.
- Eastwood, J. (1993). Temperature-dependent propagation of P-and S-waves in Cold Lake oil sands; comparison of theory and experiment. *Geophysics*, 58(6), 863–872.
- Eastwood, J., Lebel, P., Dilay, A., & Blakeslee, S. (1994). Seismic monitoring of steam-based recovery of bitumen. *The Leading Edge*, 13(4), 242–251.
- Eaton, D. W. (2014). Magnitude, scaling, and spectral signature of tensile microseisms. EGU General Assembly Conference Abstracts, 16.
- Economides, M. J., & Martin, T. (2007). *Modern fracturing: Enhancing natural gas production*. Tribune Publishing, Inc., Houston, Texas. 509.
- Eikeberg, O. A. E., & Elde, R. M. (2002). 1D Modelling-a Quantitative Tool in 4D Analysis on Troll West Oil Province? 64th EAGE Conference & Exhibition, cp-5.
- Eiken, O., Haugen, G. U., Schonewille, M., & Duijndam, A. (2003). A proven method for acquiring highly repeatable towed streamer seismic data. *Geophysics*, 68(4), 1303–1309.
- Eisner, L., Duncan, P. M., Heigl, W. M., & Keller, W. R. (2009). Uncertainties in passive seismic monitoring. *The Leading Edge*, 28(6), 648–655.
- Eisner, L., Thornton, M., & Griffin, J. (2011). Challenges for microseismic monitoring. In *SEG Technical Program Expanded Abstracts 2011* (pp. 1519–1523). Society of Exploration Geophysicists.
- Finol, A., & Ali, S. M. (1975). Numerical simulation of oil production with simultaneous ground subsidence. *Society of Petroleum Engineers Journal*, 15(05), 411–424.

- Font, Y., Kao, H., Lallemand, S., Liu, C.-S., & Chiao, L.-Y. (2004). Hypocentre determination offshore of eastern Taiwan using the Maximum Intersection method. *Geophysical Journal International*, 158(2), 655–675.
- Gajewski, D., Anikiev, D., Kashtan, B., Tessmer, E., & Vanelle, C. (2007). Localization of seismic events by diffraction stacking. In *SEG Technical Program Expanded Abstracts 2007* (pp. 1287–1291). Society of Exploration Geophysicists.
- Gassman, J., & Smit, D. C. (1951). Some aspects of elastic wave propagation in uid saturated porous solids. *Geophysics*, 16, 673–685.
- Gates, I. D., & Larter, S. R. (2014). Energy efficiency and emissions intensity of SAGD. *Fuel*, 115, 706–713.
- Geiger, L. (1912). Probability method for the determination of earthquake epicenters from the arrival time only. *Bull. St. Louis Univ*, 8(1), 56–71.
- Geller, R. J., & Mueller, C. S. (1980). Four similar earthquakes in central California. *Geophysical Research Letters*, 7(10), 821–824.
- Gentili, S., & Michelini, A. (2006). Automatic picking of P and S phases using a neural tree. *Journal of Seismology*, 10(1), 39–63.
- Gibowicz, S. J. (1994). *An Introduction to Mining Seismology* (pp. 24–38). Academic Press. San Diego.
- Got, J., Fréchet, J., & Klein, F. W. (1994). Deep fault plane geometry inferred from multiplet relative relocation beneath the south flank of Kilauea. *Journal of Geophysical Research: Solid Earth*, 99(B8), 15375–15386.
- Grieser, B., Bray, J., 2007. Identification of production potential in unconventional reservoirs. *SPE Pap.* 106623, 6.
- Grob, M., & Van der Baan, M. (2016). Influence of acquisition geometry on event cloud asymmetry and on b-value analysis. *CSEG Recorder*, 41(5), 30–35.
- Haldorsen, J. B. U., Brooks, N. J., & Milenkovic, M. (2013). Locating microseismic sources using migration-based deconvolution. *Geophysics*, 78(5), KS73–KS84.
- Han, D., Zhao, H., Yao, Q., & Batzle, M. (2007). Velocity of heavy-oil sand. *SEG Technical Program Expanded Abstracts 2007*, 1619–1623.
- Hanks, T. C., & Kanamori, H. (1979). A moment magnitude scale. *Journal of Geophysical Research: Solid Earth*, 84(B5), 2348–2350.
- Hicks, W. G., & Berry, J. E. (1956). Application of continuous velocity logs to determination of fluid saturation of reservoir rocks. *Geophysics*, 21(3), 739–754.
- Hubbard, S. M. (1999). *Sedimentology and ichnology of brackish water deposits in the Bluesky Formation and Ostracode Zone, Peace River oil sands, Alberta*. University of Alberta.
- Isaac, J. H. (1998). *Seismic methods for heavy oil reservoir monitoring*. University of Calgary.
- Jaeger, R., N. Cook, and N. Zimmerman, 2007, *Fundamentals of rock mechanics*, 4th ed.: Blackwell Publishing Ltd.

- Jones, G. A., Kendall, J., Bastow, I., Raymer, D. G., & Wuestefeld, A. (2014). Characterization of fractures and faults: a multi-component passive microseismic study from the Ekofisk reservoir. *Geophysical Prospecting*, 62(Vertical Seismic Profiling and Microseismicity Frontiers), 779–796.
- Jones, G. A., Raymer, D., Chambers, K., & Kendall, J.-M. (2010). Improved microseismic event location by inclusion of a priori dip particle motion: a case study from Ekofisk. *Geophysical Prospecting*, 58(5), 727–737.
- Kaiser, E. J. (1959): A study of acoustic phenomena in tensile test. Doctoral Thesis, Technische Hochschule München.
- Kalantzis, F., Kanasevich, E. R., Vafidis, A., & Kostykevich, A. (1996). Seismic reflection modelling and imaging of a thermal enhanced oil recovery project at Cold Lake, Canada. *First Break*, 14(3).
- Kalantzis, F., 1994, Imaging of reflection seismic and radar wave fields: monitoring of steam-heated oil reservoirs and characterization of nuclear waste repositories: Ph.D. thesis, University of Alberta.
- Kanamori, H. (1977). The energy release in great earthquakes. *Journal of Geophysical Research*, 82(20), 2981–2987.
- Karyampudi, R. S. and Rao, D. N. 1995. Improved Wettability Determination Using DDDC Technique at Elk Point Heavy Oil Field. Paper 95-22 Presented at the 46th Annual Technical Conference of CIM. May14–171995, Banff, Alberta.
- Kato, A., Onozuka, S., & Nakayama, T. (2008). Elastic property changes in a bitumen reservoir during steam injection. *The Leading Edge*, 27(9), 1124–1131.
- Kelly, B., & Lawton, D. C. (2012). Processing and interpretation of time-lapse seismic data from a heavy oil field, Alberta, Canada. *SEG Technical Program Expanded Abstracts 2012*, 1–5.
- Khan, S., Han, H., Ansari, S., Vishteh, M., & Khosravi, N. (2011). Caprock integrity analysis in thermal operations: an integrated geomechanics approach. Paper WHOC11-609 Presented at the World Heavy Oil Congress, 14, 17.
- Khazaei C (2016) Microseismic response of rock masses for assessment of caprock integrity (Doctoral dissertation). University of Alberta, Edmonton
- King GE. Thirty years of gas shale fracturing: what have we learned? In: SPE annual technical conference and exhibition: society of petroleum engineers; 2010.
- Kloosterman, H. J., Kelly, R. S., Stammeijer, J., Hartung, M., Van Waarde, J., & Chajecski, C. (2003). Successful application of time-lapse seismic data in Shell Expro's Gannet Fields, Central North Sea, UKCS. *Petroleum Geoscience*, 9(1), 25–34.
- Kocon, K., & van der Baan, M. (2012). Quality assessment of microseismic event locations and traveltimes using a multiplet analysis. *The Leading Edge*, 31(11), 1330–1337.
- Kommedal, J. H., & Barkved, O. I. (2005). 4D repeatability beyond twice—using variance. *SEG Technical Program Expanded Abstracts 2005*, 2526–2529.
- Koster, K., Gabriels, P., Hartung, M., Verbeek, J., Deinum, G., & Staples, R. (2000). Time-lapse seismic surveys in the North Sea and their business impact. *The Leading Edge*, 19(3), 286–293.
- Koster, K., Gabriels, P., & Horvei, A. (2000). Reservoir Monitoring of the Draugen Field Through Time-

Lapse Seismic and It's Business Impact. Abu Dhabi International Petroleum Exhibition and Conference. SPE 87300

Kragh, E. D., & Christie, P. (2002). Seismic repeatability, normalized rms, and predictability. *The Leading Edge*, 21(7), 640–647.

Kristiansen, P., Bouska, J., Thorogood, E., O'Donovan, A., & Christie, P. (2000). Foinaven 4D-Towed Streamer and Buried Sea-Bed Detectors in Deep Water for 4D Seismic. 62nd EAGE Conference & Exhibition, cp-28.

Kumar, R., Verma, S.K., 2010. Determination of wettability and its effect on oil recovery in a carbonate rock of an offshore field under ambient and elevated temperature. In: Paper SPE # 128545 Presented at the SPE Oil and Gas India Conference and Exhibition Held in Mumbai, India, 20–22 January 2010

Kurita, K., & Fujii, N. (1979). Stress memory of crystalline rocks in acoustic emission. *Geophysical Research Letters*, 6(1), 9–12.

Lee, W. H. K., & Lahr, J. C. (1972). HYPO71: A computer program for determining hypocenter, magnitude, and first motion pattern of local earthquakes (p. 100). US Department of the Interior, Geological Survey, National Center for Earthquake Research.

Lee, W. H. K., and S. W. Stewart (1981). Principles and applications of microearthquake networks, *Adv. Geophys. Suppl.* 2, 293 pp

Lockner, D. A. (1998). A generalized law for brittle deformation of Westerly granite. *Journal of Geophysical Research: Solid Earth*, 103(B3), 5107–5123.

Machel, H. G. (2010). The Devonian Petroleum System of the Western Canada Sedimentary Basin—with Implications for Heavy-Oil Reservoir Geology. In *Heavy oils: Reservoir characterization and production monitoring* (pp. 131–154). Society of Exploration Geophysicists.

Maron, K. P., Bourne, S., Wit, K., McGillivray, P., & Brissenden, S. (2005). Integrated reservoir surveillance of a heavy oil field in Peace River, Canada. 67th EAGE Conference & Exhibition, cp-1.

Mavko, G., T. Mukerji, and J. Dvorkin, 1998, *The rock physics handbook: Tools for seismic analysis in porous media*: University of Cambridge.

Maxwell, S. (2009). Microseismic location uncertainty. *CSEG Recorder*, 34(4), 41–46.

Maxwell, S. (2014). Microseismic imaging of hydraulic fracturing: Improved engineering of unconventional shale reservoirs. Society of Exploration Geophysicists.

Maxwell, S C, Mack, M., Zhang, F., Chorney, D., Goodfellow, S. D., & Grob, M. (2015). Differentiating wet and dry microseismic events induced during hydraulic fracturing. *Unconventional Resources Technology Conference*, San Antonio, Texas, 20-22 July 2015, 1513–1524.

Maxwell, Shawn C, Du, J., Shemeta, J. E., Zimmer, U., Boroumand, N., & Griffin, L. R. (2007). Monitoring SAGD steam injection using microseismicity and tiltmeters. *SPE ATCE*, Anaheim, 11–14.

Maxwell, Shawn C, & Urbancic, T. I. (2001). The role of passive microseismic monitoring in the instrumented oil field. *The Leading Edge*, 20(6), 636–639.

McGillivray, P. (2005). Microseismic and time-lapse seismic monitoring of a heavy oil extraction process at Peace River, Canada. *CSEG Recorder*, January, 5–9.

<https://www.cseg.ca/publications/recorder/2005/01jan/jan05-microseismic.pdf>

Mehrotra, A. K., & Svrcek, W. Y. (1986). Viscosity of compressed Athabasca bitumen. *The Canadian Journal of Chemical Engineering*, 64(5), 844–847.

Miyazawa, M., Venkataraman, A., Snieder, R., & Payne, M. A. (2008). Analysis of microearthquake data at Cold Lake and its applications to reservoir monitoring Analysis of induced microseismicity. *Geophysics*, 73(3), O15–O21.

Mossop, G. D. (1988). Geological Atlas of the Western Canada Sedimentary Basin. *Geoscience Canada*, 15(2).

Mossop, G. D., & Shetsen, I. (1994). Introduction to the geological atlas of the Western Canada Sedimentary Basin. *Geological Atlas of the Western Canada Sedimentary Basin*, edited by: Mossop, GD and Shetsen, I., Canadian Society of Petroleum Geologists and Alberta Research Council, Alberta, 1-11.

Mummery, R. C. (1985). Quantitative application of seismic data for heavy oil projects. *SEG Technical Program Expanded Abstracts 1985*, 393–394.

Muntendam-Bos, A. G., & Fokker, P. A. (2009). Unraveling reservoir compaction parameters through the inversion of surface subsidence observations. *Computational Geosciences*, 13(1), 43.

Nanayakkara, A. S., & Wong, R. C. K. (2009). How far does surface heave propagate? a discussion on analytical and numerical modeling of the surface heave induced by subsurface fluid injection. *KSCE Journal of Civil Engineering*, 13(4), 297–303.

Ng H, Monitoring Fluid Injection Using Seismic Time-Lapse Analysis: A Rainbow Lake Case Study, thesis. Faculty of Graduate Studies Department of Geology and Geophysics University of Calgary, Calgary, Alberta (2005).

Nguyen, P. K. T., Nam, M. J., & Park, C. (2015). A review on time-lapse seismic data processing and interpretation. *Geosciences Journal*, 19(2), 375–392.

O’connell, S. C., Mossop, G. D., & Shetsen, I. (1994). Geological history of the Peace River arch. In *Geological atlas of the Western Canada sedimentary basin (Vol. 28, pp. 431–440)*. chapter.

Pacey, K. (2013). *Geoscience of Climate and Energy 11. Ambient air quality and linkage to ecosystems in the Athabasca Oil Sands, Alberta*. *Geoscience Canada*, 40(3), 182–201.

Parotidis, M., Shapiro, S. A., & Rothert, E. (2004). Back front of seismicity induced after termination of borehole fluid injection. *Geophysical Research Letters*, 31(2).

Parotidis, M., Shapiro, S. A., & Rothert, E. (2005). Evidence for triggering of the Vogtland swarms 2000 by pore pressure diffusion. *Journal of Geophysical Research: Solid Earth*, 110(B5).

Pavlis, G. L. (1986). Appraising earthquake hypocenter location errors: A complete, practical approach for single-event locations. *Bulletin of the Seismological Society of America*, 76(6), 1699–1717.

Pearson, C. (1981). The relationship between microseismicity and high pore pressures during hydraulic stimulation experiments in low permeability granitic rocks. *Journal of Geophysical Research: Solid Earth*, 86(B9), 7855–7864.

Pike, K. A. (2014). *Microseismic Data Processing, Modeling and Interpretation in the Presence of Coals: A Falher Member Case Study*. Calgary, Alberta, Canada: University of Calgary

- Poiata, N., Satriano, C., Vilotte, J.-P., Bernard, P., & Obara, K. (2016). Multiband array detection and location of seismic sources recorded by dense seismic networks. *Geophysical Journal International*, 205(3), 1548–1573.
- Porter, J. W., Price, R. A., & McCrossan, R. G. (1982). The western Canada sedimentary basin. *Philosophical Transactions of the Royal Society of London. Series A, Mathematical and Physical Sciences*, 305(1489), 169–192.
- Poupinet, G., Ellsworth, W. L., & Frechet, J. (1984). Monitoring velocity variations in the crust using earthquake doublets: An application to the Calaveras Fault, California. *Journal of Geophysical Research: Solid Earth*, 89(B7), 5719–5731.
- Prugger, A. F., & Gendzwil, D. J. (1988). Microearthquake location: A nonlinear approach that makes use of a simplex stepping procedure. *Bulletin of the Seismological Society of America*, 78(2), 799–815.
- Rastin, S. J., Unsworth, C. P., Benites, R., & Gledhill, K. R. (2013). Using real and synthetic waveforms of the Matata swarm to assess the performance of New Zealand GeoNet phase pickers. *Bulletin of the Seismological Society of America*, 103(4), 2173–2187.
- Rentsch, S., Buske, S., Luth, S., & Shapiro, S. A. (2007). Fast location of seismicity: A migration-type approach with application to hydraulic-fracturing data. *Geophysics*, 72(1), S33–S40.
- Rickett, J. E., & Lumley, D. E. (2001). Cross-equalization data processing for time-lapse seismic reservoir monitoring: A case study from the Gulf of Mexico. *Geophysics*, 66(4), 1015–1025.
- Rickman, R., Mullen, M. J., Petre, J. E., Grieser, W. V., & Kundert, D. (2008). A practical use of shale petrophysics for stimulation design optimization: All shale plays are not clones of the Barnett Shale. *SPE Annual Technical Conference and Exhibition*. SPE115258
- Robinson, E. A., & Treitel, S. (2000). *Geophysical signal analysis*. Society of Exploration Geophysicists.
- Rojas, N., & Davis, T. L. (2009). Spectral decomposition applied to time-lapse seismic interpretation, Rulison Field, Colorado. In *SEG Technical Program Expanded Abstracts 2009* (pp. 3845–3849). Society of Exploration Geophysicists.
- Rowe, C. A., Aster, R. C., Phillips, W. S., Jones, R. H., Borchers, B., & Fehler, M. C. (2002). Using automated, high-precision repicking to improve delineation of microseismic structures at the Soutz geothermal reservoir. In *The Mechanism of Induced Seismicity* (pp. 563–596). Springer.
- Ruiz, S., Aden-Antoniow, F., Baez, J. C., Otarola, C., Potin, B., del Campo, F., Poli, P., Flores, C., Satriano, C., & Leyton, F. (2017). Nucleation phase and dynamic inversion of the Mw 6.9 Valparaíso 2017 earthquake in Central Chile. *Geophysical Research Letters*, 44(20), 10–290.
- Rutledge, J. T., & Phillips, W. S. (2003). Hydraulic stimulation of natural fractures as revealed by induced microearthquakes, Carthage Cotton Valley gas field, east Texas. *Hydraulic Stimulation of Natural Fractures*. *Geophysics*, 68(2), 441–452.
- Schembre, J. M., Tang, G.-Q., & Kovscek, A. R. (2006). Wettability alteration and oil recovery by water imbibition at elevated temperatures. *Journal of Petroleum Science and Engineering*, 52(1–4), 131–148.
- Schön, J. H. (2015). Geomechanical properties. In *Developments in Petroleum Science* (Vol. 65, pp. 269–300). Elsevier.

Schoofs, S., Al-Lawati, M. H. A., Engen, G., Al Salmi, K., Al Quseimi, I., Al Kindy, F., Marsden, C., Ita, J., Van Der Heyden, F., & Bauer, A. (2010). Integrated Usage of Surveillance Data for Estimating Cap Rock Integrity and Heat Distribution during Steam Injection in a Fractured Carbonate Reservoir. SPE EOR Conference at Oil & Gas West Asia.

Scott, J. D., Proskin, S. A., & Adhikary, D. P. (1994). Volume and permeability changes associated with steam stimulation in an oil sands reservoir. *Journal of Canadian Petroleum Technology*, 33(07).

Segall, P. (1989). Earthquakes triggered by fluid extraction. *Geology*, 17(10), 942–946.

Shafiei, A., & Dusseault, M. B. (2013). Geomechanics of thermal viscous oil production in sandstones. *Journal of Petroleum Science and Engineering*, 103, 121–139.

Shapiro, S. A., & Dinske, C. (2009). Fluid-induced seismicity: Pressure diffusion and hydraulic fracturing. *Geophysical Prospecting*, 57(2), 301–310.

Shapiro, S. A., Kummerow, J., Dinske, C., Asch, G., Rothert, E., Erzinger, J., Kümpel, H., & Kind, R. (2006). Fluid induced seismicity guided by a continental fault: Injection experiment of 2004/2005 at the German Deep Drilling Site (KTB). *Geophysical Research Letters*, 33(1).

Sigit, R., Morse, P. J., & Kimber, K. D. (1999). 4-D seismic that works: A successful large scale application, Duri Steamflood, Sumatra, Indonesia. In *SEG Technical Program Expanded Abstracts 1999* (pp. 2055–2058). Society of Exploration Geophysicists.

Singhal, A. K., Ito, Y., & Kasraie, M. (1998). Screening and design criteria for steam assisted gravity drainage (SAGD) projects. SPE International Conference on Horizontal Well Technology. SPE 50410, Nov. 1998, 1-7.

Sleeman, R., & Eck, T. Van. (1999). Robust automatic P-phase picking: an on-line implementation in the analysis of broadband seismogram recordings. *Physics of the Earth and Planetary Interiors*, 113(1–4), 265–275. <http://www.sciencedirect.com/science/article/pii/S0031920199000072>

Smith, R. J., N. S. Alinsangan, and S. Talebi, 2002, Microseismic response of well casing failures at a thermal heavy oil operation: Proceedings, Society of Petroleum Engineers/International Society for Rock Mechanics SPE/ ISRMConference, Paper 78203

Sondergeld, C., K. E. Newsham, J. T. Comiski, M. C. Rice, and C. S. Rai, 2010a, Petrophysical considerations in evaluating and producing shale gas: Society of Petroleum Engineers Unconventional Gas Conference, Pittsburgh, Pennsylvania, February 23–25, 2010, SPE Paper 131768, 34 p., doi:10.2118/131768-MS

Spence, W. (1980). Relative epicenter determination using P-wave arrival-time differences. *Bulletin of the Seismological Society of America*, 70(1), 171–183.

Staples, R., Hague, P., Weisenborn, T., Ashton, P., & Michalek, B. (2005). 4D seismic for oil-rim monitoring. *Geophysical Prospecting*, 53(2), 243–251.

Stark S. Increasing Cold Lake recovery by adapting steamflood principles to a bitumen reservoir. In: Paper presented at SPE enhanced oil recovery conference, 19e21 july, kuala lumpur, Malaysia. Imperial Oil Resources Ltd; 2011. ISBN: 978-1-61399-138-0.

Stein S, Wyssession M (2003) An Introduction to Seismology, Earthquakes and Earth Structure (Blackwell, Oxford)

- Talebi, S., & Boone, T. J. (1998). Source parameters of injection-induced microseismicity. *Pure and Applied Geophysics*, 153(1), 113–130.
- Tanaka, M., Endo, K., & Onozuka, S. (2010). Estimation of Steam Chamber Extent Using 4D Seismic. *Journal of Canadian Petroleum Technology*, 49(5), 50–55.
- Tanimoto, K., Nakamura, J., & Fudo, R. (1978). Application of acoustic emission in in-situ test. Proc., 10th Int. Conference on Soil Mechanics and Foundation Engineering, 2, 573–576.
- Thurber, C. H., & Engdahl, E. R. (2000). Advances in global seismic event location. In *Advances in seismic event location* (pp. 3–22). Springer.
- Tran, H. T., Bentley, L. R., & Krebs, E. S. (2003). Using time-lapse analysis to predict reservoir changes in a carbonate pool: a case study of the Rainbow B pool. *Crews Research Report*, 15. p 1-21
- Urbancic, T., & Jeziorski, K. (2015). Microseismic Monitoring Applications in Heavy Oil Reservoirs. *CSEG Recorder*, 40(01).
- Verdon, J. P., Kendall, J.-M., Stork, A. L., Chadwick, R. A., White, D. J., & Bissell, R. C. (2013). Comparison of geomechanical deformation induced by megatonne-scale CO₂ storage at Sleipner, Weyburn, and In Salah. *Proceedings of the National Academy of Sciences*, 110(30), E2762–E2771.
- Walters, R., & Zoback, M. D. (2013). Microseismicity and surface deformation of a heavy-oil reservoir undergoing cyclic steam stimulation. In *SEG Technical Program Expanded Abstracts 2013* (pp. 2218–2222). Society of Exploration Geophysicists.
- Wang, H., Li, M., & Shang, X. (2016). Current developments on micro-seismic data processing. *Journal of Natural Gas Science and Engineering*, 32, 521–537.
- WILLIAMS, G. D. and BURK, JR., C. F., 1964. Upper Cretaceous. In: R. G. McCROSSAN and R. P. GLAISTER (Editors), *Geological History of Western Canada*. Alberta Soc. Petrol. Geologists, Calgary, Alta, pp.169-189.
- Wright, G. N., McMechan, M. E., Potter, D. E. G., & Holter, M. E. (1994). Structure and architecture of the Western Canada sedimentary basin. *Geological Atlas of the Western Canada Sedimentary Basin*, 4, 25–40.
- Yerkes, R. F., & Castle, R. O. (1976). Seismicity and faulting attributable to fluid extraction. *Engineering Geology*, 10(2–4), 151–167.
- Yilmaz, Ö. (2001). *Seismic data analysis: Processing, inversion, and interpretation of seismic data*. Society of exploration geophysicists. Society of Exploration Geophysics., Tulsa.
- Zang, A., Wagner, F. C., Stanchits, S., Janssen, C., & Dresen, G. (2000). Fracture process zone in granite. *Journal of Geophysical Research: Solid Earth*, 105(B10), 23651–23661.
- Zhang, D., Ranjith, P. G., & Perera, M. S. A. (2016). The brittleness indices used in rock mechanics and their application in shale hydraulic fracturing: A review. *Journal of Petroleum Science and Engineering*, 143, 158–170.
- Zhang, W., & Zhang, J. (2013). Microseismic migration by semblance-weighted stacking and interferometry. In *SEG Technical Program Expanded Abstracts 2013* (pp. 2045–2049). Society of Exploration Geophysicists.

- Zhou, H. (1994). Rapid three-dimensional hypocentral determination using a master station method. *Journal of Geophysical Research: Solid Earth*, 99(B8), 15439–15455.
- Zhou, R., Huang, L., & Rutledge, J. (2010). Microseismic event location for monitoring CO₂ injection using double-difference tomography. *The Leading Edge*, 29(2), 208–214.
- Zhou, W., Wang, L., Guan, L., Guo, Q., Cui, S., & Yu, B. (2015). Microseismic event location using an inverse method of joint P–S phase arrival difference and P-wave arrival difference in a borehole system. *Journal of Geophysics and Engineering*, 12(2), 220–226.
- Zimmer, U. (2011). Microseismic design studies. *Geophysics*, 76(6), WC17–WC25.
- Zoback, M. Lou, & Zoback, M. (1980). State of stress in the conterminous United States. *Journal of Geophysical Research*, 85(B11), 6113–6156.
- Zoback, M. D. (2010). *Reservoir geomechanics*. Cambridge University Press.
- Zoback, M. D., & Harjes, H. (1997). Injection-induced earthquakes and crustal stress at 9 km depth at the KTB deep drilling site, Germany. *Journal of Geophysical Research: Solid Earth*, 102(B8), 18477–18491.